Tempering of a Mixture of Bainite and Retained Austenite

By
Arijit Saha Podder
St. John's College, Cambridge

University of Cambridge
Department of Materials Science and Metallurgy
Pembroke Street, Cambridge CB2 3QZ

A dissertation submitted for the
degree of Doctor of Philosophy at the
University of Cambridge
January 2011

PREFACE

This dissertation is submitted for the degree of Doctor of Philosophy at the University of Cambridge. The research reported herein was conducted under the supervision of Professor H. K. D. H. Bhadeshia in the Department of Materials Science and Metallurgy, University of Cambridge, between October 2007 and January 2011.

This work is to the best of my knowledge original, except where acknowledgment and references are made to previous work. This dissertation is the result of my own work and includes nothing which is the outcome of work done in collaboration except where specifically indicated in the text. Neither this, nor any substantially similar dissertation has been, or is being, submitted for any other degree, diploma, or other qualification at any other university. This dissertation does not exceed 60,000 words in length.

Some of the work described herein has been published:

- A Saha Podder and H K D H Bhadeshia, Thermal Stability of Austenite Retained in Bainitic Steels, *Materials Science and Engineering A*, 527:2121-2128, 2010.

Arijit Saha Podder

January 2011

ACKNOWLEDGMENTS

I would like to express my sincere gratitude to my supervisor Professor Harshad Kumar Dharamshi Hansraj Bhadeshia for all his support, guidance, inspiration and encouragement during the work and my stay here.

I would like to thank Professor A. L. Greer for the provision of Laboratory facilities in the Department of Materials Science and Metallurgy at the University of Cambridge.

I earnestly acknowledge financial support from Cambridge Commonwealth Trust as Nehru-Cambridge Commonwealth Scholarship for providing me the opportunity to pursue research at the University of Cambridge. I also express my gratitude to the Hinduja Foundation and British Petroleum (BP plc) for financial support. I am indebted to Tata Steel Ltd., India for providing me study leave to pursue research at Cambridge.

I would like to thank every member of the Department for being very kind to me. I am grateful to Dr Mary Vickers for numerous fruitful discussions. I wonder if this work would have been at all possible without Mr Kevin Roberts, Mr Andrew Moss, Mr Dave Nicol and Mr Frank Clarke. I would like to thank Dr Ivan Lonardelli for his assistance in carrying out collaborative work using synchrotron radiation.

I shall cherish for long the memory of being with the PT-group and I thank every member of the group for help and friendship. I would like to thank especially Mathew J. Peet. and Ashwin Pandit for being with me in every difficult situation. All the help from Hala Salman Hassan, Andrew Barrow, Aseel Hamideny, Amir Shirazdi, David Bombač, Pei Yan, Steve Ooi, Stéphane Forshik, Radu Dimitriu and other group members is also gratefully acknowledged.

The support from St John's College, including the fantastic accommodation and the fabulous food at the buttery and Hall, made my life a really enjoyable one. The association with many friends in the College and the Department has been beneficial.

I am greatly indebted to my parents and my wife, Nilanjana, for their support, devotion and understanding.

ABSTRACT

Concern about the fuel economy of automobiles has stimulated the development of bainitic steels. A high strength to weight ratio together with good ductility may be achieved by this endeavour if a number of metallurgical issues can be resolved. Strong bainitic steels are alloyed with silicon in order to avoid the deleterious effect of cementite which otherwise forms in association with bainite. This strengthens the steels and also enhances the toughness because the carbon that is usually precipitated as brittle cementite instead partitions into the residual austenite, allowing the latter to be retained. The amount of retained austenite in the steel can, in principle, be optimised by heat treatment. Substantial work has, in the past, been carried out on the nature of the bainite transformation. However, this is not the case when it comes to the decomposition of the retained austenite during tempering. This is important because applications such as the galvannealing of automotive steel involves subjecting it to temperatures as high at 475°C.

The goal of the work initiated in this thesis was to gain a detailed understanding of the thermal decomposition of retained austenite. Systematic characterisation experiments have been undertaken to demonstrate the progress of the tempering process as a function of time and temperature. High resolution dilatometry was carried out to distinguish quantitatively between the two competing processes of austenite decomposition and tempering of martensite. Based on these studies a new theory has been proposed for the decomposition of retained austenite during and after the tempering process. In essence, the austenite is rendered unstable to martensitic transformation during cooling from the tempering temperature even though the fraction of precipitation is minute.

The evolution of microstructure during the progress of tempering has been captured using *in situ* transmission electron microscopy. This study provides strong evidence of the austenite decomposition model. The fact that the process does not involve nucleation of new ferrite, but rather the growth of existing ferrite at the expense of austenite, has been confirmed by direct observation. High-energy synchrotron X-ray radiation has been used for *in situ* experiments which revealed the structural changes during the tempering process with a particular focus on the change in lattice parameters and carbon content of the film and blocky types of austenite. More importantly, it verified the instability of the austenite to the cooling process. The tempering behavior of Mn and Ni-containing bainitic steels has been compared and it has observed that the process is faster in the latter case. These experiments provided critical data in the validation of kinetic theory. The non-uniform strains and dislocation densities were estimated from X-ray measurements during the progress of tempering process.

An attempt has been made to predict the overall transformation kinetics of the decomposition of retained austenite subjected to the tempering treatment, based on the simultaneous transformations of ferrite and cementite. This helped confirm that it is not tenable to argue that new ferrite forms by reconstructive nucleation and growth during tempering.

Contents

Chapter 1

General Introduction

Steels could be argued to be the most important and useful of all materials because of their relatively low price and the wide range of desirable properties which can be controlled by changing the chemical composition and processing parameters. Steel remains the most successful of all materials, with 1.3 billion tonnes being consumed annually in improving the quality of life. The mechanical properties depend to a reasonable extent on the microstructure, which is influenced in part by precipitation reactions. Phase transformations are therefore important in designing the microstructures for specific applications. Several techniques are used by steel manufacturers to make high performance steels. These include grain refinement, work hardening, precipitation hardening and heat treatment. Using these techniques, sheet steels can be developed with an ideal combination of formability and strength for specific automotive applications.

Bainite, considered to be the epicentre for automotive steels research, is an aggregate of phases which was identified first by Davenport and Bain [1] as a result of systematic isothermal transformation experiments. They reported the discovery of the new microstructure consisting of an 'acicular, dark etching aggregate' which formed in the temperature range between pearlite and martensite and was unlike either of those microstructures. The new microstructure was found subsequently to exist in two main variants: lower and upper bainite. It was not until low-alloy, low-carbon steels, containing small amounts of boron and molybdenum to suppress proeutectoid ferrite were developed that the potential for commercial exploitation became realistic [2]. Bainite has been associated with the latest breakthrough technologies because of tremendous developments in phase transformation theory and the fact that combinations of properties, including toughness and strength, achievable using this phase mixture can be comparable to those of quenched and tempered martensitic steels. The introduction of dual phase steel with ferrite and bainite being the major components led to very high strength steel with adequate ductility [3]. With these improved mechanical properties and low manufacturing cost, bainitic steel is being used increasingly in a number of industrial applications, such as rail steel [4] and armour steel [5].

The carbon that is partitioned from bainitic ferrite following isothermal transformation, stabilises the residual austenite, enabling it to be retained at ambient temperature. Cementite precipitation becomes possible when its carbon concentration exceeds the solubility limit given by the extrapolated $\gamma/(\gamma+\theta)$ phase boundary [6]. This is depicted in Figure 1.1, where the shaded area illustrates austenite that is unstable to the precipitation of cementite. If the transformation temperature falls below T_c, carbide precipitation is inevitable.

Interesting microstructures can be obtained when silicon is added to steel in concentrations of about 2 wt%. Silicon is generally present in steels as an aftermath of the deoxidation reactions involved in the steelmaking process. However, it also retards the formation of cementite from austenite, making it possible to obtain a carbide-free microstructure of just bainitic ferrite and carbon enriched austenite [7]. In silicon-rich steels cementite does not form in association with bainitic ferrite even after holding at the isothermal transformation temperature for many hours [8, 9]. For the same reason, the precipitation of cementite during the tempering of martensite is retarded significantly by the presence of silicon [10, 11]. The morphology of the retained austenite is important in this context. The phase can be present in the microstructure in two forms: blocky and film type. The best elongation behaviour has been observed when the austenite is in the form of films between the subunits of bainite rather than as blocks between sheaves of bainitic ferrite [12, 13]. The blocks of austenite tend to transform into martensite in the early stages of deformation and consequently lead to early fracture [12]. The film austenite is fine in scale and stabilised by carbon enrichment. A typical transmission electron micrograph of the isothermally transformed material is shown in Figure 1.2. A microstructure of this kind has many advantages. The absence of cementite reduces the chances of cleavage or void nucleation.

Unlike martensite, the bainite does not derive its strength from dissolved carbon, which means that it is more resistant to tempering. The films of austenite, intimately dispersed between the ferrite, are buffers to the propagation of cracks. Very high strength can be achieved by refining the structure; strength up to 2.5 GPa has been achieved using a bainitic microstructure with the individual plates reduced down to 50 nm in thickness [14].

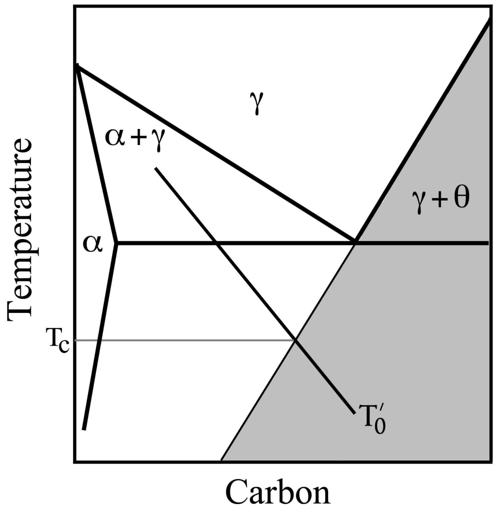

Figure 1.1: Thermodynamic condition which must be satisfied before cementite can precipitate from austenite [6]. α, γ and θ denote ferrite, austenite and cementite respectively.

1.1 Scope of the Research

Tempering is historically associated with the heat treatment of martensite in steels. It improves the toughness of virgin martensite but lowers the strength. The most important structural change is the formation of various distributions of iron and alloy carbides as the supersaturation of the as-quenched martensite is relieved and the equilibrium state is approached. The tempering process has been researched since the 1960s and there is an impressive collection of literature in the context of martensite, for example, [15–22]. Although bainitic steels have been the subject of particular interest over the last two decades, only limited work has been reported on tempering reactions. There is literature describing the precipitation of carbides during the bainite transformation in steels [6, 23–30], but hardly any information on the stability of retained austenite during the tempering of mixtures of bainitic ferrite and retained austenite [31, 32]. Transformation induced plasticity (TRIP) steels, known for their high strength, improved formability and crash

Figure 1.2: Transmission electron micrograph showing bainite ferrite (α_b) with retained austenite films (γ_f) entrapped between the ferrite plates (From present work).

worthiness, have received considerable interest from the automotive industries for the application in body-in-white. The stability of retained austenite controls the transformation rate during deformation and strongly influences the formability and mechanical behaviour [33]. As a consequence, the mechanical stability of retained austenite during processing of these steels has become topic of research in recent years [34–41]. The corresponding thermal stability of retained austenite has not been similarly scrutinised. That is the subject of this thesis.

The tempering of bainite and retained austenite has numerous industrial implications because modern steels are coated with zinc, by the process of galvanizing/ galvannealing, after cold rolling, to make them suitable for automotive applications. Coated steels are becoming ever more popular for the outer panels of passenger cars. There is demand for this Zn-coated steel for the white-goods industries, such as in the manufacture of refrigerators, washing machines etc. During coating, the steels are heated in the range of 400°C to 500°C to facilitate the coating process, so that some tempering is then inevitable. The stability of the retained austenite therefore becomes important. Another important area is the development of shafts for aircraft engines, where transient temperatures of about 400°C are reached. It is in this context that the evolution of the microstructure during the heat treatment of structures containing retained austenite has been studied in order to provide mechanistic details which can help design more stable phase mixtures involving carbon enriched austenite.

Chapter 2

Literature Survey: Tempering of Bainite

2.1 Bainitic Transformation

'Bainite', named after E. C. Bain [1], is the generic term for fine aggregates of ferrite platelets (or laths) and associated cementite particles. The transformation occurs from austenite at temperatures between those at which pearlite and martensite form. The structure can be generated either through isothermal transformation or continuous cooling heat treatment below the bainite-start (B_S) temperature.

2.1.1 Transformation Mechanism

Considerable research has been carried out on the mechanism of the bainite transformation. One school of thought holds the view that the transformation is displacive [8, 9, 42, 43] whereas another argues that the diffusion plays a major role [28, 44]. The former mechanism implies the existence of an atomic correspondence across the transformation interface whereas the later is associated with an uncoordinated movement of atoms which destroys any such correspondence. Given the large collection of observation available in the literature and reviewed extensively [45–47], the first theory is a more plausible explanation for the growth of the bainite. According to this theory bainite grows by the propagation of discrete martensitic sub-units at all stages of transformation and this explanation is consistent with the existence of the so-called incomplete reaction phenomenon [48]. The bainitic ferrite in this scenario partitions carbon into the residual austenite soon after formation [43].

The thermodynamic description of the bainite reaction is linked to its mechanism of growth and depends on the behaviour of solute atoms during transformation. By far the largest contribution to the stored energy of bainite is due to the experimentally observed invariant-plane strain shape deformation. The contributions from interfacial area are by comparison negligible during the growth stage [42].

The dislocation density in bainite is found to be higher than that in allotriomorphic ferrite even when these two phases form at similar temperatures, and the dislocation density increases as the transformation temperature is reduced [49, 50]. This is often attributed to the fact that bainite forms by a shear mechanism. If the shape deformation accompanying the displacive transformation is accommodated, at least partially, by plastic relaxation of the adjacent austenite, then the resulting dislocations introduced into the austenite can be inherited by any bainite that forms subsequently [51, 52]. Direct observations [52] reveal the plastic relaxation in the austenite adjacent to a plate of bainite, as illustrated schematically in Figure 2.1.

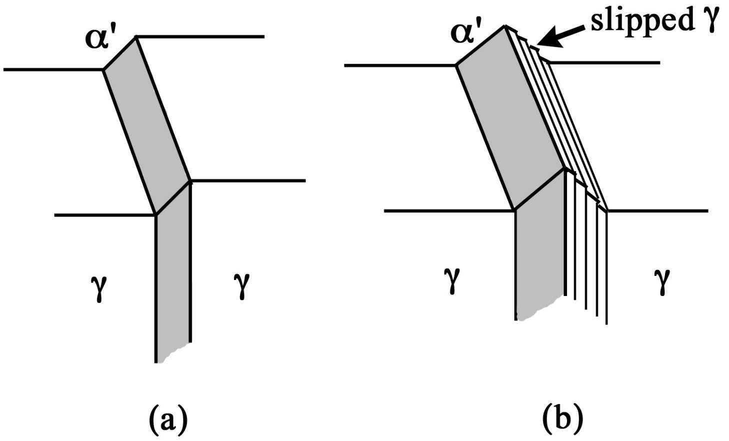

Figure 2.1: Schematic illustration of (a) a perfect invariant-plane strain surface relief and (b) one where plastic relaxation of the shape change occurs in the adjacent matrix [6].

Substitutional solutes do not partition at all during the bainite reaction. Their primary effect is through their influence on the relative thermodynamic stabilities of the austenite and ferrite phases. The ratio of the iron to substitutional solute atoms remains constant everywhere during the formation of bainite. This is expected due to displacive character of the transformation and the low diffusivity of substitutional atoms at the temperatures where bainite forms. The trapping of solutes in the bainite raises its free energy [6].

After the displacive transformation, the bainitic ferrite is supersaturated with carbon, with its carbon content equal to that of the parent austenite. However, given the temperatures involved, much of the excess carbon is able to partition into the austenite [42]. Some carbon remains within the ferrite, either trapped at dislocations or other defects. Atomic scale observations show that the amount of carbon retained in the bainitic ferrite is increased with the decrease in transformation temperature because of lower diffusivity of carbon at low temperatures [53].

2.1.2 Incomplete Reaction Phenomenon

During isothermal transformation below the B_S temperature, the austenite decomposes to bainite and the maximum degree of reaction increases from zero at the B_S temperature to some other finite value at lower temperatures, which is always less than would be expected from an application of the lever rule to the equilibrium or paraequilibrium [†] phase diagram. This effect is termed the 'incomplete reaction phenomenon' [6, 42, 48].

Bhadeshia and Edmonds [8, 42] explained this observation by incorporating the T_0 concept, the temperature at which both bainitic ferrite and austenite of similar composition have identical free energy, as shown in Figure 2.2. The T_0 curve represents the locus of all points on a plot of temperature versus carbon concentration, where austenite and ferrite of the same chemical composition also have identical free energies. On the other hand, the paraequilibrium ($\alpha + \gamma/\gamma$) phase boundary is represented by the Ae'_3 curve *i.e.*, the composition of austenite which is in equilibrium with ferrite subject to the constraint that the substitutional lattice is configurationally frozen. Any austenite with a carbon concentration in excess of that defined by the T_0 curve, cannot transform without a change in composition between the parent and product phases. Thus, any displacive transformation involving a full supersaturation of carbon, can occur only below the appropriate T_0 temperature [42].

To summarise, the diffusionless growth of bainite has to occur at a temperature just

---

[†] Paraequilibrium is a state of equilibrium in which the substitutional alloying elements are unable to partition, although carbon, which is a fast diffusing interstitial element, redistributes between the phases until its chemical potential is uniform throughout.

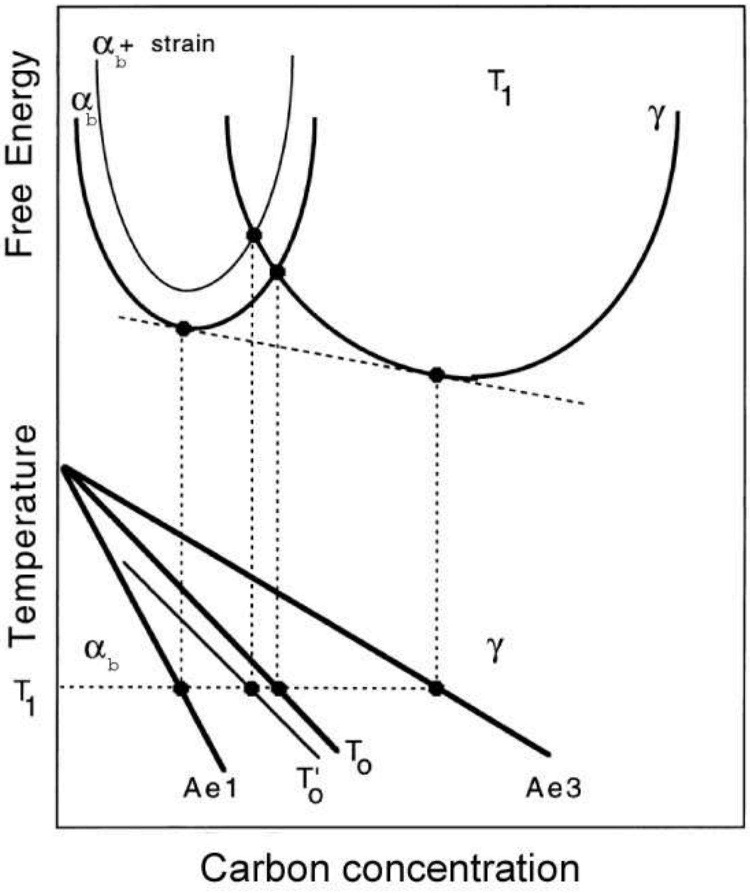

Figure 2.2: Schematic illustration of the T_0 and $T_0^{'}$ curves. The $T_0^{'}$ curve incorporates a strain energy term for the ferrite due to the displacive mechanism of transformation. α_b corresponds to bainitic ferrite. T_1 is the temperature corresponding to the free energy curves. Ae_3 denotes the temperature separating the $\alpha + \gamma$ and γ. Ae_1 is the minimum temperature at which austenite exists [6].

below T_0, when the free energy of bainitic ferrite falls below that of austenite of the same composition, as shown in Figure 2.2. With decreasing temperature the austenite can tolerate successively greater amounts of carbon before the formation of supersaturated ferrite stops. Experimental evidence of the incomplete reaction phenomenon has been reported by many but most recently by Caballero [54], who measured the carbon distribution in austenite through X-ray diffraction and atom-probe tomography. These results are consistent with a mechanism in which the bainite grows without diffusion and with the excess carbon partitioned into austenite immediately after isothermal transformation.

The growth of bainite is accompanied by a change in shape which is characterised as an invariant plane-strain with a large shear component. The elastic strain caused in the austenite as it accommodates this shape deformation is associated with an estimated 400 J mol^{-1} of strain energy [6]. This is less than the corresponding term for martensite, which is 600 J mol^{-1} because bainite plates usually have a smaller aspect ratio. The shear and dilatational components of the shape change are similar for martensite and bainite. The T_0 curve modified to account for this strain energy is called the $T_0^{'}$ curve. Thus the transformation to bainite stops when the carbon concentration of the residual austenite reaches the $T_0^{'}$ boundary [6, 8].

The incomplete transformation allows films of austenite to be retained between bainite plates. It has been observed that the thickness of these austenite films can be estimated by assuming that the carbon diffusion field around an existing plate of ferrite prevents the close approach of another parallel plate [55]. This is because the regions of austenite with the highest carbon concentration are unable to transform to bainite. This theory predicts a dependence of film thickness on the bainite plate thickness since the net quantity of carbon partitioned into the austenite must increase with the thickness of the bainite plate.

Application of the lever rule allows the estimation of the permitted fraction of bainite ($V_{\alpha_b}^{max}$) at any temperature [4]:

$$V_{\alpha_b}^{max} = \frac{c_{T_0} - \bar{c}}{c_{T_0} - c_{\alpha_b}} \tag{2.1}$$

where c_{T_0} is the austenite carbon content given by the T_0 boundary, $\bar{c}$ is the average carbon concentration of alloy and c_{α_b} is the carbon concentration of the bainitic ferrite after the excess has been partitioned into the residual austenite.

2.2 Morphology of Bainite

Bainite consists of aggregates of fine plates of ferrite, separated by regions of residual phases. These consist of untransformed austenite or cementite which forms subsequent to the growth of bainitic ferrite. The aggregates of plates are designated ‘sheaves’ whereas individual plates are sometimes called 'sub-units' which are connected in three dimensions [56]. There is reduction in the width of the platelets with decreasing temperature; as a consequence the number density of platelets increases within a sheaf as the transformation temperature is reduced [32]. It is also established that there is small misorientation between the plates within any given sheaf. Where they touch, adjacent plates are separated by low-misorientation grain boundaries. The microscopic shape of a sheaf is that of a wedge-shaped plate [57]. The sheaves appear to nucleate on the austenite grain boundaries and the thicker end of the wedge begins at the initial nucleation site [6].

Two kinds of bainite are formed from austenite depending on transformation temperature and can be differentiated depending on the precipitation: (i) upper bainite and (ii) lower bainite. Upper bainite forms as an aggregate of lath like ferrite plates with carbides precipitated parallel to the long axis, while in lower bainite the ferrite plates form with carbides also precipitated internally at some angle to the major axis of the plate. Figure 2.3 shows the mechanism of growth and development of the two classical forms of bainite. It has been established that both upper and lower bainite need not form in the same steel [58]. The precipitation of carbides in upper bainite is a secondary process, not essential to the mechanism of formation of bainitic ferrite except that it depletes the carbon content in the austenite, thereby promoting further transformation. Silicon can prevent the precipitation of cementite from the austenite between the plates of bainitic ferrite, but has only a limited effect on precipitation from supersaturated ferrite where the driving force for cementite formation is much larger [59]. It is possible in high carbon steels to avoid the formation of upper bainite completely so that after pearlite the austenite decomposes directly into lower bainite as the transformation temperature is reduced [58]. Similarly, in low carbon steels, it is possible that upper bainite formation is followed by martensite transformation, without any intervening lower bainite.

Another type of bainite designated 'granular' has been also reported in some alloy steels cooled continuously in the bainitic temperature range [60]. Granular bainite forms by continuous cooling transformation rather than isothermal treatment and appears to consist of relatively coarse ferritic regions in a mixture of retained austenite and martensite and contains no carbides. This structure is formed only in certain alloy steels. It has been established that granular bainite is not different from conventional bainite in its mechanism of transformation. The unusual morphology is a consequence of two factors: continuous cooling transformation and a low carbon concentration [61].

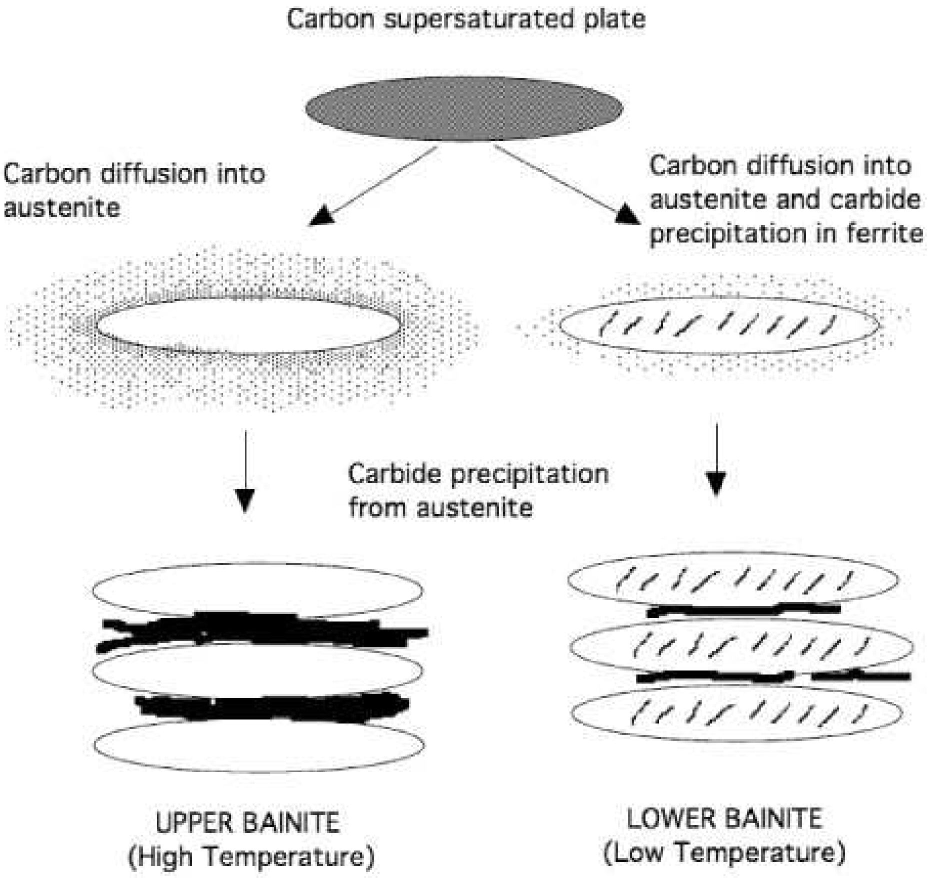

Figure 2.3: Illustration of upper and lower bainite showing the main differences in carbon partitioning and precipitation [58].

The low carbon concentration ensures that any films of austenite or regions of carbide that might exist between sub-units of bainite are minimal, making the identification of individual platelets within the sheaves rather difficult using light microscopy [6].

2.3 Effect of Transformation Temperature

The degree of transformation to bainite increases with supercooling, from zero at the upper limit, which is generally known as the B_S temperature. The carbon that partitions into the austenite after the formation of bainite changes its composition, until it eventually becomes thermodynamically impossible for the austenite to transform and the reaction stops [6]. For a given alloy, a larger undercooling below T_0 would allow more bainite to form before diffusionless growth becomes impossible. A decrease in transformation temperature increases the volume fraction of bainite as can be seen in Figure 2.4. The ferrite regions are, in general, coarser at higher transformation temperatures. Very fine plates of ferrite can be achieved by reducing the transformation temperature. It is reported that bainite plates can be as low as 35 nm when the transformation temperature was reduced to 200°C [62]. The bainite plate thickness will be discussed in details in the subsequent section.

2.4 Effect of Alloying Elements

2.4.1 Significance of Silicon

It is known that silicon increases the resistance to softening on tempering by suppressing cementite formation [64]. Gordine and Codd [65] have shown that the presence of $\sim$1.5 wt%Si appreciably increases the resistance to softening on tempering in a 0.6 wt%C steel by entering into the ϵ-carbide. This stabilizes ϵ-carbide so that it persists to higher tempering temperatures. Owen [10] suggested that silicon postpones the final stage of tempering because, in the presence of sufficient silicon ($>$1 wt%), the tempering reaction is controlled by the diffusion of silicon instead of carbon.

Silicon is also added in bainitic steels to suppress cementite precipitation [66]. When cementite forms under paraequilibrium conditions, the silicon is trapped inside the cementite lattice. The resulting reduction in the free energy slows down the kinetics of precipitation [59]. So the carbon, that is partitioned into the residual austenite after bainitic transformation, does not precipitate as cementite but remains there to make the

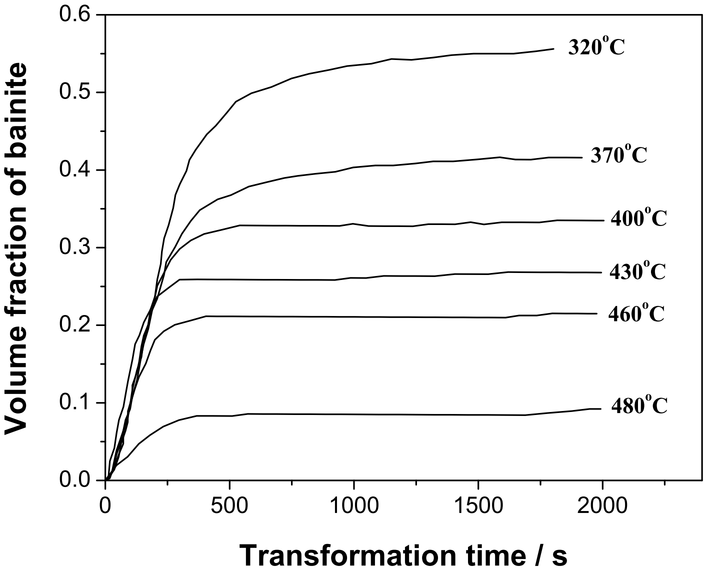

Figure 2.4: Effect of isothermal temperature on volume fraction of bainite in C-Mn-Si steel [63].

austenite stable at ambient temperature [7, 67, 68]. In contrast, under equilibrium conditions the solubility of silicon in cementite is negligible due to the partitioning into the austenite, so its concentration hardly affects the phase fraction. As a consequence, elevated temperature transformation involving cementite, such as the diffusional formation of pearlite, are not affected by addition of small concentrations of silicon [59]. Moreover, silicon is also ineffective in retarding the precipitation of cementite if the parent phase is significantly supersaturated with carbon because the driving force for the reaction is large even for paraequilibrium precipitation.

The microstructure, obtained in silicon rich steel, consists of fine plates of bainitic ferrite separated by carbon enriched regions of austenite. There are some potential advantages of this microstructure such as:

(a) Cementite is responsible for initiating fracture in high strength steels. Its absence is expected to make the microstructure more resistant to cleavage failure and void formation.

(b) The microstructure derives its strength from the fine grain size of the ferrite plates, which are less than 1 μm in thickness.

(c) The ductile films of austenite, which are intimately dispersed between the plates of ferrite, have a crack blunting effect. They further add to toughness by increasing the work of fracture as the austenite is induced to transform to martensite under the influence of the stress field of a propagating crack. This is the TRIP or transformation-induced plasticity effect [69–71]. In TRIP-aided steel, silicon also contributes to the solid solution strengthening of ferrite.

Silicon increases the temperature of all transformations of carbon steel but has relatively little effect on the rate of transformation; consequently both the *Ac* and *Ar* transformations of nickel steels may be raised by increasing silicon as shown in Figure 2.5.

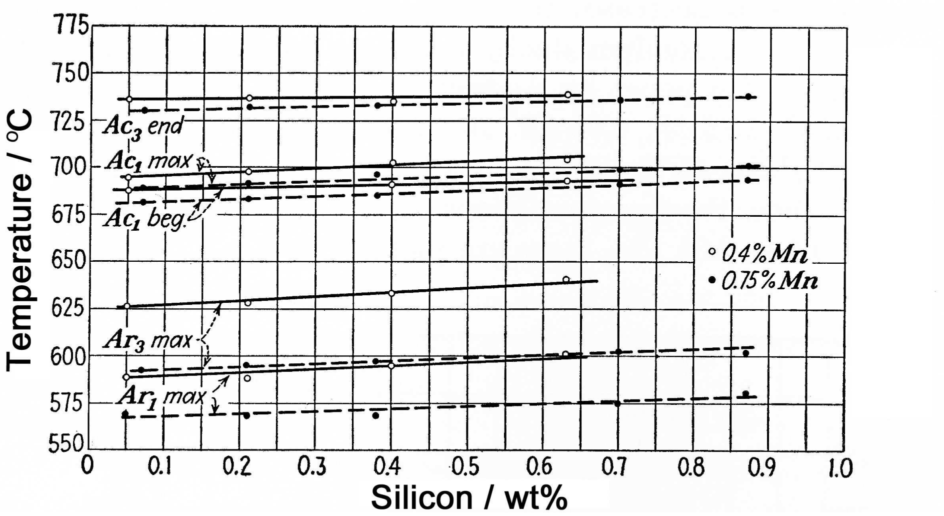

Figure 2.5: Effect of silicon on the transformation temperature of steels containing 0.4 wt% carbon, 4 wt% nickel and 0.4 or 0.75 wt% manganese. A_3 is the temperature at which sample becomes fully austenite and A_1 is the eutectoid temperature. *c* and *r* denote for heating and cooling respectively [72].

2.4.2 Effect of Manganese and Nickel

Manganese plays an important role during steelmaking, by helping in deoxidation of the melt by forming MnO and through modification of sulphides present by forming MnS [73]. Manganese is a major alloying element in steels, has complex interactions with carbon and influences hardenability. Manganese refines the grain size and thereby improves the tensile strength. Manganese and nickel both increase tensile and yield strengths with nickel being slightly more effective than manganese [74]. Nickel lowers the critical temperatures of steel, widens the temperature range for effective quenching and tempering, and retards the decomposition of austenite [75]. Increasing the manganese content decreases ductility and weldability, but less than carbon. Manganese lowers the ductile-to-brittle impact transition temperature due to the grain-refinement ability. Manganese has a significant effect on the hardenability of steel as can be observed from Figure 2.6a [76] and is much more effective in increasing hardenability, per weight percent added, than nickel. Manganese is the most effective alloying addition for lowering the M_S temperature after carbon [77]. It therefore promotes the retention of austenite [40]. In the context of the bainitic transformation, the decrease in carbon concentration of any austenite remaining untransformed is caused by the reduction of T_0 temperature with the addition of manganese [12]. Manganese also decelerates the pearlite reaction because of its slow diffusivity even through the moving interface [66].

2.5 Bainite Plate Thickness

The thickness of the bainite plate depends on the temperature, yield strength of austenite, the free energy change accompanying transformation, rate of nucleation *etc.* Quantitative analysis proves that temperature has only a small independent effect on the thickness of bainite plates whereas strong austenite and high driving forces lead to finer plates [78]. A systematic study by Chang [63] showed that temperature appears to have a strong influence essentially because it affects the chemical free energy and the strength of the austenite. The former leads to a higher nucleation rate which encourages grain boundary and subsequent autocatalytic nucleation. The plates are expected to become thicker at high temperatures because the yield strength of the austenite is expected to be lower [78]. Dynamic recovery at high temperatures may further weaken the austenite and lead to coarser plates.

Transmission electron microscopy is used to determine the true plate thickness t by measuring the mean linear intercept $\overline{L}_T = \pi t/2$ in a direction normal to the plate length. The plate thickness t is also related to the mean linear intercept measured using randomly oriented test lines, $\overline{L} = 2t$ [79]. However, $\overline{L}_T$ is easier to measure since it is rare in transmission electron microscope observations that entire plates of bainite can be imaged [78]. For a given thickness t, the strength contribution due to the size of

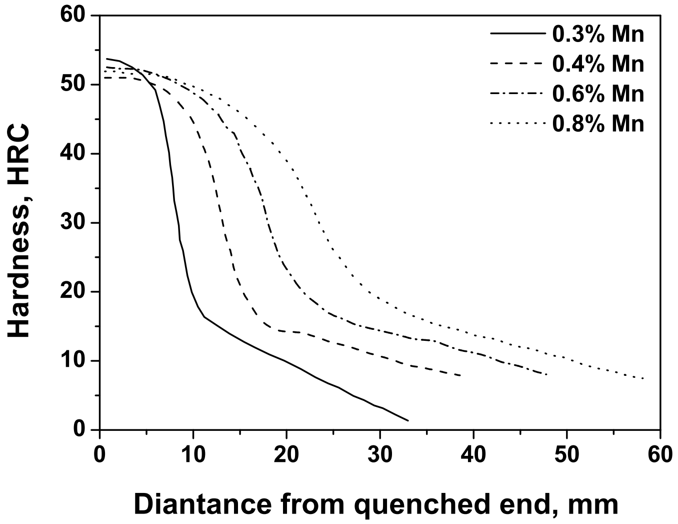

(a)

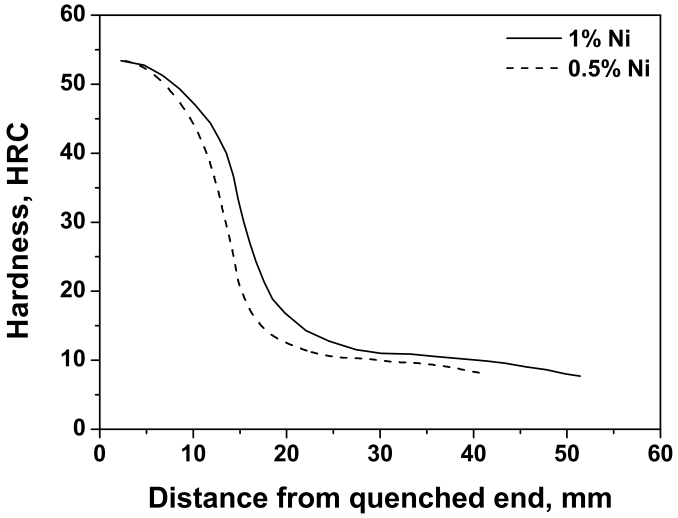

(b)

Figure 2.6: Jominy curves for ductile irons containing various quantities of (a) manganese and (b) nickel [76].

the plates is given by $\Delta\sigma \approx 115(\overline{L})^{-1}$ MPa where $\overline{L}$ is in micrometers [80]. It follows that $\Delta\sigma \simeq 311$ MPa for plates of thickness 185 nm, whereas $\Delta\sigma \simeq 1643$ MPa for plates of thickness 35 nm. The transmission electron micrograph in Figure 2.7 illustrates the carbide-free bainitic structure formed at 200°C. The bainitic plates in this steel are long and thin, giving an elegant fine-scale mixture of austenite and bainitic ferrite. The plates have an apparent width less than 50 nm, with each plate separated by films of retained austenite. Very high hardness (in excess of 600 HV) and an ultimate strength of about 2.3 GPa are achieved because of the fine scale of the bainite plates.

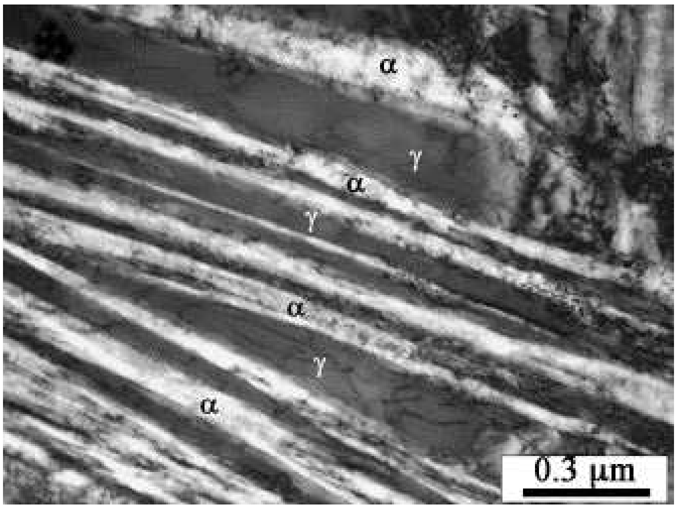

Figure 2.7: Transmission electron micrograph of structure obtained at 200°C for 240 h [53].

2.6 Precipitation During Bainitic Transformation

Carbides can precipitate (during the bainitic transformation) either from austenite or bainitic ferrite. There is a variety of factors which can influence any subsequent changes in carbide chemical composition and morphology during tempering or during service at elevated temperatures.

One difference between the transformation of austenite to pearlite from that of bainite is that the latter does not involve cooperative growth of bainitic ferrite and carbides. The ferritic component of bainite forms first, the excess carbon from the thermodynamically unstable, supersaturated bainitic ferrite is then removed by either of two competing process [81]. These are the partitioning of carbon into the residual austenite or its precipitation (in the form of carbides) within the bainitic ferrite. At relatively high temperatures, the rejection of carbon into the residual austenite is rapid, so that any carbide precipitation occurs from the carbon-enriched residual austenite and the final microstructure obtained is upper bainite. The sequence of reactions can be summarised as follows, with θ representing cementite:

$$\begin{aligned}\gamma &\longrightarrow \gamma + \alpha_{b,supersaturated}\\ &\longrightarrow \alpha_{b,supersaturated} + \gamma_{enriched}\\ &\longrightarrow \alpha_{b,supersaturated} + \alpha + \theta\end{aligned}$$

This contrasts with the cooperative growth of cementite and ferrite during formation of pearlite in plain carbon steels: $\gamma \longrightarrow \alpha + \theta$

There is practically no difference between upper and lower bainite when the precipitation of carbides from the carbon-enriched austenite is considered. However, in lower bainite some of the excess carbon precipitates in the ferrite, thus reducing the quantity partitioned into the austenite [44]. At lower temperatures, carbide precipitation within bainitic ferrite is predominant. The precipitation reactions for lower bainite can be summarised as follows:

Case I: High dislocation density

$$\begin{aligned}\gamma &\longrightarrow \gamma + \alpha_{b,supersaturated}\\ &\longrightarrow \theta_{inferrite} + \alpha_{b,supersaturated} + \gamma_{enriched}\\ &\longrightarrow \alpha_{b,supersaturated} + \alpha + \theta_{betweenferriteplates} + \theta_{inferrite}\end{aligned}$$

Case II: Low dislocation density

$$\begin{aligned}\gamma &\longrightarrow \gamma + \alpha_{b,supersaturated}\\ &\longrightarrow \epsilon_{inferrite} + \alpha_{b,supersaturated} + \gamma_{enriched}\\ &\longrightarrow \alpha_{b,supersaturated} + \epsilon_{inferrite} + \alpha + \theta_{betweenferriteplates}\\ &\longrightarrow \alpha_{b,supersaturated} + \theta_{inferrite} + \theta_{betweenferriteplates} + \alpha\end{aligned}$$

It is generally accepted that the precipitation of upper bainitic carbide takes place in the austenite as a consequence of the partitioning of carbon from the bainitic ferrite to the austenite. In general there is little known about the formation of cementite in austenite during this process [31, 32].

2.7 Stability of Retained Austenite

The untransformed austenite that is present in the microstructure at room temperature is designated to be retained. It is necessary to consider both its mechanical and thermal stability. When the austenite decomposes under the influence of stress the resulting high carbon, untempered martensite will be brittle and may crack depending on the size of the plate of martensite [82]. There is plenty of evidence that the austenite retained to ambient temperature after isothermal formation of bainitic ferrite, particularly the larger blocky austenite, can be stimulated to decompose to martensite even at relatively small stresses [83–85]. The mechanical stability of retained austenite is therefore important in obtaining good toughness in bainitic steels. Miihkinen and Edmonds [86] have reported that mechanical stability of retained austenite decreases with an increase in isothermal transformation temperature.

The thermal decomposition of retained austenite is a tempering process in the temperature range of 200°C to 300°C [87], the details of which will be discussed in a subsequent section. In general retained austenite transforms into mixtures of ferrite and cementite in this stage of tempering. The activation energy for this process is about $115\,\mathrm{kJ\,mol^{-1}}$ [88], which is consistent with the activation energy for the diffusion of carbon in austenite [89]. In TRIP steels the characteristics of austenite in the final microstructure are determined during intercritical annealing when fine regions of austenite appear along the boundaries of ferrite grains. During subsequent quenching and holding at the bainite transformation temperature, the reaction proceeds by the growth of bainitic ferrite plates resulting in further carbon enrichment and modification of the morphology of residual austenite.

In silicon-rich bainitic steels the retained austenite is present: as thin films between the subunits of a given sheaf of bainite, and as coarser blocks between different sheaves. Both are enriched in carbon but the films more so because of their geometrical isolation between plates of ferrite [42].

The blocky morphology of austenite has already been stated to be detrimental to the toughness of the steel. On the other hand, austenite films which have a higher carbon content are much more stable and remain untransformed until the later stages of deformation and hence enhance toughness via the TRIP effects [34, 36, 90, 91]. A large film/blocky austenite ratio should therefore result in better toughness. Bhadeshia and Edmonds [7] have established that the ratio of films to blocky austenite should exceed about 0.9 for optimum properties:

$$(V_{\gamma-f}/V_{\gamma-B}) = V_{\alpha_b}/(6-7.7V_{\alpha_b}) > 0.9 \tag{2.2}$$

where $V_{\gamma-f}$ and $V_{\gamma-B}$ are the volume fractions of film and blocky morphologies respectively and V_{α_b} is that of bainite.

The carbon content of retained austenite c_γ can be estimated, after rearranging Equation 2.1, using [42]:

$$c_\gamma = \bar{c} + V_{\alpha_b}(\bar{c} - c_{\alpha_b})/(1 - V_{\alpha_b}) \tag{2.3}$$

where $\bar{c}$ is bulk carbon content and c_{α_b} is the final carbon content in the bainitic ferrite.

Bhadeshia has expressed the stability factor of austenite in terms of the ratio of martensite (formed during quenching from the isothermal transformation temperature to room temperature) and residual austenite [7]. Figure 2.8 shows the variation of austenite stability parameter as a function of austenite carbon content for 0.43C-3Mn-2Si (wt%) steel transformed at 270°C and 363°C. While the microstructure of the steel transformed at 363°C comprised bainitic ferrite, retained austenite and some martensite, the steel transformed at 270°C additionally contained some carbides with the bainitic ferrite. Figure 2.8 demonstrates an enhanced austenite stability as a result of the finely divided austenite remaining after partial transformation to bainite as compared to the plain carbon steels.

The blocky austenite in the structure arises because the bainite reaction stops before equilibrium is reached [4]. Diffusionless growth cannot be sustained once the carbon concentration of the austenite reaches the T_0 curve of the phase diagram, i.e., c_{T_0} (Figure 2.2). The thermodynamic limit (T_0) can be manipulated to minimise the amount of blocky retained austenite: the substitutional solute content can be altered to shift the T_0 to higher c_{T_0}; the transformation temperature (T) can be reduced to increase c_{T_0}; the average carbon concentration $\overline{c}$ of the steel can be reduced to increase the fraction of bainite and hence consume the blocks of retained austenite. The alloy design philosophy is therefore simple: V_{α_b} must be increased (refer Equation 2.1) such that the blocks of austenite cease to control the toughness.

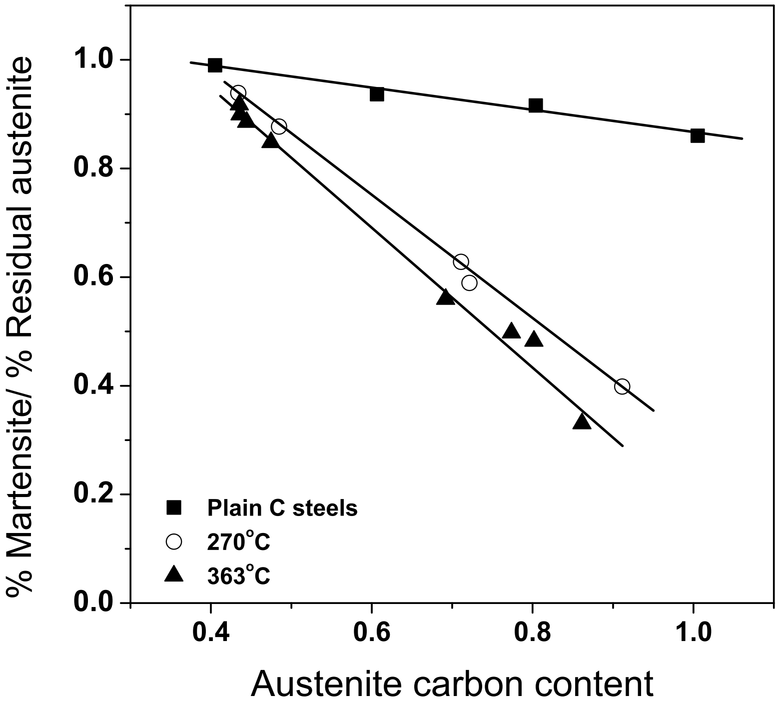

Figure 2.8: The austenite stability parameter as a function of carbon content, in wt% [7].

2.8 Tempering of Steel

The tempering of steel essentially involves heating of the material to elevated temperatures in order to enhance properties such as ductility. The tempering of martensite has been the subject of many research and review articles [17, 21, 87, 88, 92–95]. Even now in the midst of 21st century, martensite is referred to in the context of the tempering process.

The major purpose of tempering is to reduce the brittleness imparted by excessive hardening and to introduce the degree of ductility and toughness necessary for a given application while preserving as much as possible the strength and hardness of the as-quenched martensitic microstructure. Severe internal stresses may reside in the material due to rapid cooling from the austenite state. These stresses can, in principle, be relieved by tempering. The steel of course softens as a result. That is true for all steels except under appropriate circumstances, high-speed steel. Tempering increases the hardness of high-speed steel provided it is tempered at a high temperature (about 450°C) where carbides rich in substitutional solutes can precipitate [96].

Tempering may be performed at any temperature up to the lower critical temperature (Ae_1) to produce a wide variety of structure and properties in any given steel. The rate of cooling from the tempering temperature normally has no significant effect on the steel. Steel parts are usually cooled in still air after being removed from the tempering furnace. However, there are a few types of steel that must be quenched from the tempering temperature to prevent brittleness. This phenomenon is caused due to the segregation of certain impurity elements such as P, As, Sb, Sn, N *etc*, which reduce the inter-granular cohesion of iron [97]. The presence of Mn and Ni enhances the embrittlement because of interaction with the impurities. These interactions lead to co-segregation of alloying elements and impurity elements at the grain boundaries [98].

The mechanisms associated with the structural changes produced by tempering are best grouped into stages, many of which overlap and develop concurrently. Early work has established, at least loosely defined, four tempering stages associated with carbide formation in martensite [20, 87, 99], as follows:

- Stage I: The formation of a transition carbide and the lowering of the carbon content of the martensite.
- Stage II: The transformation of retained austenite to ferrite and cementite.
- Stage III: The replacement of transition carbide and low carbon martensite by cementite and ferrite and
- Stage IV: The development of alloy carbides or secondary hardening in alloy steels.

These definitions, to some extent, emphasise development of various carbides in the tempering ranges used in commercial practice. Other work, however, has shown that considerable structural rearrangement of carbon atoms occurs prior to the development of the first identifiable carbide. According to Olson and Cohen [94], regimes of structural change prior to conventional stages of tempering are generally termed as aging, which has two different stages. The first corresponds to the clustering of carbon atoms. In as-quenched martensite, carbon atoms are trapped in randomly distributed and separated c-axis octahedral sites. Mössbauer spectroscopy has provided evidence for such clustering in as-quenched martensite [100]. The first stage of aging thus develops as carbon atoms cluster to adjacent octahedral sites in the martensite. The second stage consists of a fine modulated tweed microstructure containing elastically distorted carbon-deficient regions, which are sufficiently coarse to yield a separable X-ray diffraction peak [101, 102].

Table 2.1 summaries the reactions and stages of structural changes which occur during the tempering of martensitic steels, iron carbon alloys and iron nickel carbon alloys. The temperature ranges are only approximate and usually based on 1-hour treatments. However alloy carbide formation, ferrite boundary rearrangements and segregation phenomenon may take much longer.

Temperature Range (°C)	Reaction	Comments
25 to 100	Carbon segregation to dislocations and boundaries; precipitation clustering and ordering	Clustering predominant in high-carbon steels
100 to 200	Precipitation of transition carbides as aligned 2 nm diameter particles	Carbides may be $\epsilon(\mathrm{Fe_{2.4}C})$ or $\eta(\mathrm{Fe_2C})$
200 to 350	Transformation of retained austenite to ferrite and cementite	Associated with tempered martensite embrittlement
350 to 550	Segregation and co segregation of impurity and substitutional alloying elements	Responsible for temper embrittlement
250 to 700	Formation of ferrite and cementite; eventual development of well spherodised carbides in a matrix of equiaxed ferrite grains	Lath structure maintained
500 to 700	Formation of alloy carbides in Cr, Mo, V and W containing steels. The mix and composition of the carbides may change significantly with time	The alloy carbides produce secondary hardening and pronounced retardation of softening during tempering or long time service exposure around 500°C

Table 2.1: Tempering reactions in steels

There are notable differences in the tempering behaviours of bainite and martensite, because the former autotempers during transformation. Bainite forms at comparatively higher temperatures ($B_S > M_S$, where M_S is martensite-start temperature) so autotempering becomes an unavoidable part of the transformation. The redistribution of carbon from the supersaturated ferrite into the residual austenite, and the precipitation of carbides during the bainitic reaction, occur rapidly and are genuine autotempering effects.

Unlike martensitic steels, the tempering of bainite is not highly sensitive to small variations in the carbon content. The strength of martensite drops rapidly as carbon leaves solid solution. However, with bainite the carbon is present mostly as coarse carbides which contribute little to strength. Bainitic steels containing strong carbide forming elements undergo secondary hardening during annealing at high temperatures, as finer and more stable alloy carbides form at the expense of cementite.

As compared with martensite, bainite grows at relatively high temperatures where the microstructure undergoes recovery during transformation. In low carbon bainite annealed at high temperatures (700°C for 1 h), there is only slight increase in recovery and little change in the density of carbide particles [2].

The hardness and tensile strength of fully bainitic microstructures decrease during tempering, with the rate of change being largest for lower bainite, which has the highest starting value. The high strength steels demonstrate large changes in strength during tempering.

2.9 Precipitation of Carbides During Tempering

When high carbon martensite is tempered, the first carbide to form is usually a transition phase such as ϵ-carbide, which is replaced eventually by the thermodynamically more stable cementite [25, 87, 103]. The temperature for this transformation is usually in the range of 100°C to 200°C. Si additions can retard the replacement of the ϵ-carbide even upto 400°C [65]. Similarly, when lower bainite forms in high carbon steels, ϵ-carbide forms first and transforms subsequently into cementite during prolonged holding at the isothermal transformation temperature [23, 104]. However, ϵ-carbide cannot form during the tempering of martensite in steels containing 0.2 wt% carbon or less [88, 103]. Most of the carbon in these steels is at dislocation sites. Most of these sites have a lower energy than those available in ϵ carbide, so there is little driving force for precipitation [16]. Before precipitation can occur some dislocations must be removed by recovery, but the presence of carbon strongly inhibits recovery.

ϵ-carbide is a transition iron carbide with an approximate chemical formula of Fe_2C. It has a hexagonal close-packed arrangement of iron atoms with carbon atoms located in the octahedral interstices (Figure 2.9). According to Jack [105] the lattice parameters are $a = 2.735$ and $c = 4.339$ Å. This carbide precipitates as plates which are approximately 6-20 nm thick and 70-400 nm long [6] and possesses a rigged interface with the matrix. The precipitation of this carbide depends on the transformation temperature [29].

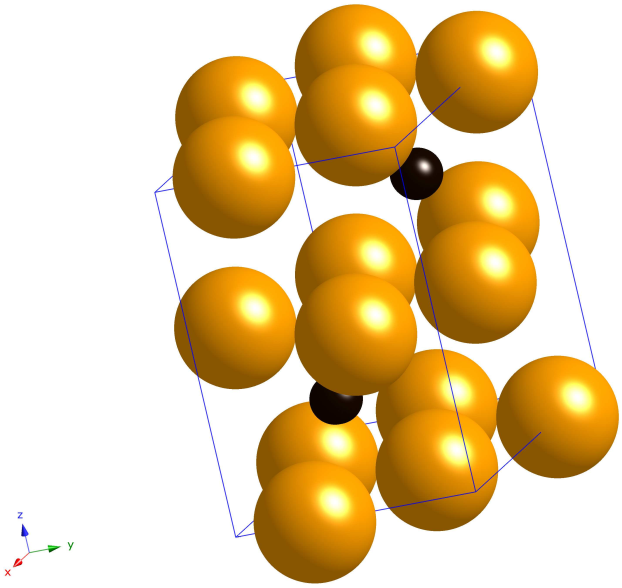

Figure 2.9: The crystal structure of epsilon carbide containing 6 iron atoms (yellow) and 2 carbon atoms (black). The carbon atoms occupy $\frac{1}{3}, \frac{2}{3}, \frac{3}{4}$ and $\frac{2}{3}, \frac{1}{3}, \frac{1}{4}$ positions [105].

The most common carbide to form in bainitic steels is cementite [23], the crystal structure of which is shown in Figure 2.10. In silicon rich steels, orthorhombic carbides and c-carbide, also transition carbides, such as κ-carbide and various orthorhombic forms are stimulated because they are easier to nucleate [6]. Eventually these carbides transform into cementite as tempering continues. Studies on lower bainite have established that the precipitation of cementite is not related to the lattice invariant shear itself, but to the relief of the overall strain energy associated with the shape deformation of lower bainite [24].

Previous studies have revealed that sufficient carbon for ϵ-carbide formation during the bainite reaction is only available when the average carbon content of the steel is above approximately 0.55 wt% [26–28]. ϵ-carbide has also been reported to precipitate in retained austenite in untempered steels [29, 104, 107]. Most of the literature indicates

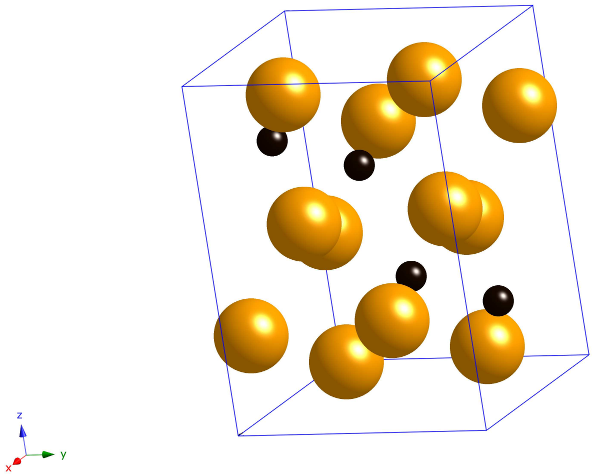

Figure 2.10: The crystal structure of cementite containing 12 iron atoms (yellow) and 4 carbon atoms (black). The carbon atoms occupy the 0.43 -0.13 0.25 positions [106].

that ϵ-carbide precipitates in lower bainite during isothermal transformation [29, 107] but their presence in upper bainite has not been confirmed. A thorough study is required to corroborate the nucleation and growth aspects of this carbide in retained austenite.

Jha and Mishra [104] have reported another type of carbide upon tempering of retained austenite and is designated as η-carbide. This has an orthorhombic crystal structure with lattice parameters $a = 2.74$, $b = 4.60$ and $c = 4.37$ Å and can be characterized by an Fe_2C stoichiometry (Figure 2.11). Sandvik has reported a new type of carbide from austenite, which is different from cementite [32]. This study revealed a new orientation relationship between bainitic ferrite and the carbide. It has also suggested that the lattice stress associated with the bainitic ferrite affects the nucleation of the Fe_2C.

Carbides other than ϵ, η and θ require long range diffusion and can form during tempering or during prolonged holding at the isothermal transformation temperature. The crystal structures of carbides in bainite or tempered bainite are listed in Table 2.2.

The volume fraction of cementite precipitation as a function of time and temperature can be represented by an Avrami type equation with rate constants k and n [58]:

$$\xi\{t\} = 1 - \exp\{-kt^n\} \tag{2.4}$$

where $\xi\{t\}$ is the volume fraction of cementite normalised by its equilibrium volume

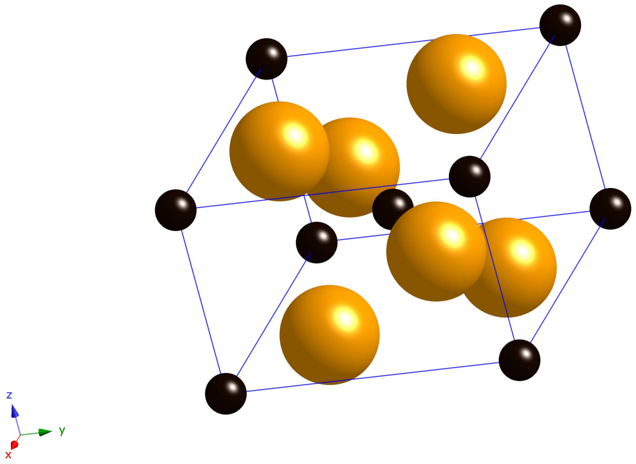

Figure 2.11: The crystal structure of η carbide containing 4 iron atoms (yellow) and 2 carbon atoms (black). The carbon atoms occupy at 0,0,0 and $\frac{1}{2},\frac{1}{2},\frac{1}{2}$ [105].

fraction at the reaction temperature and k and n are rate constants determined from experimental data. It has been assumed that $\xi\{t\}$, the normalised fraction, is related empirically at any time t to the hardness of the martensite, $H\{t\}$, by:

$$\xi\{t\} = \frac{H_0 - H_{\{t\}}}{H_0 - H_F} \tag{2.5}$$

where H_0 is the hardness of the as-quenched virgin martensite, H_F is the hardness when all the carbon has precipitated but before any significant recovery, recrystallisation or coarsening has occurred. This implicitly assumes that the amount of carbon precipitated is related linearly to the change in hardness during the initial stages of tempering.

The rate constant k can be related to the temperature T and an activation energy Q by:

$$k = k_0 \exp\left\{-\frac{Q}{RT}\right\} \tag{2.6}$$

where R is the gas constant and k_0 is the pre exponential factor.

Carbide	Crystal System	Fe, M/C
κ	Hexagonal $a = 6.9$ $c = 4.8$ Å	1.37
ϵ	Hexagonal $a = 2.735$ $c = 4.339$ Å	2.4-3
χ	Monoclinic $a = 11.563$ $b = 3.573$ Å $c = 5.058$ $\beta = 97.44°$	2.2 or 2.5
η	Orthorhombic $a = 4.704$ $b = 4.318$ $c = 2.830$ Å	2
Fe_3C	Orthorhombic $a = 4.525$ $b = 5.087$ $c = 6.743$ Å	3.0
M_7C_3	Orthorhombic $a = 4.526$ $b = 7.010$ $c = 12.142$ Å	7/3
(Fe,Si)C_x	Orthorhombic $a = 8.8$ $b = 9.0$ $c = 14.4$ Å	
(Fe,Si)C_x	Orthorhombic $a = 6.5$ $b = 7.7$ $c = 10.4$ Å	
(Fe,Si,Mn)C_x	Orthorhombic $a = 14.8$ $b = 711.4$ $c = 8.5$ Å	
$M_{23}C_6$	Cubic F $a = 10.621$ Å	23/6
M_6C	Cubic F $a = 11.082$ Å	6
C	Triclinic $a = 6.38$ $b = 5.05$ $c = 4.59$ Å $\alpha = 90°$ $\beta = 70.1°$ $\gamma = 84.7°$	

Table 2.2: Carbides in bainite or tempered bainite. Fe, M/C is the ratio of metal to carbon atoms [6, 108]

2.10 Summary

A final microstructure of bainitic ferrite and retained austenite can be achieved by selecting proper isothermal temperature and addition of sufficient silicon. The mechanical stability of retained austenite depends on the morphology. Among the film and blocky type of retained austenites, the former is more stable under deformation but similar information is yet to be available under thermal load. The decomposition of retained austenite has been discussed previously in conjunction with martensite tempering in the context of martensitic steels. However, less attention has been paid to the study of retained austenite as a separate phase although the final properties of the bainitic steel depends largely on the decomposition product of retained austenite. In the present work, an attempt has been made to study the progressive decomposition of retained austenite during the tempering process using different characterisation techniques and to understand the structural changes that occur due to this transformation.

Chapter 3

Literature Survey: Overall Transformation Kinetics

3.1 Introduction

The theory used to estimate the overall transformation kinetics of the decomposition of retained austenite is described in this chapter. This includes a consideration of nucleation and growth and the interactions between particles growing from different locations. A discussion about simultaneous transformation kinetics involving both cementite and ferrite is also included in this chapter.

3.2 Classical Theory of Nucleation

3.2.1 Homogeneous Nucleation

Consider the homogeneous nucleation of spherical precipitates of β in an α matrix assuming negligible volume strain energy. When a spherical embryo with a radius, r, is created by a thermal fluctuation, the change of free energy, ΔG, is given by

$$\Delta G = \frac{4}{3}\pi r^3 \Delta G_V + 4\pi r^2 \sigma_{\alpha\beta} \tag{3.1}$$

where, $\Delta G_V = G_V^\beta - G_V^\alpha$ is the Gibbs free energy per unit volume (G_V^β and G_V^α are Gibbs free energies for the β and α phases respectively) and $\sigma_{\alpha\beta}$ is the interfacial energy per unit area, assumed to be isotropic. While the driving force, ΔG_V, for the phase change is negative (*i.e.* a reduction in free energy), the term with $\sigma_{\alpha\beta}$ is positive. The resulting variation in ΔG with radius r is illustrated in Figure 3.1. Initially when the particle is very small, ΔG increases with r. As r increases further, ΔG reaches a maximum and then decreases. In this situation the particle can, in principle, continue to grow. The value of ΔG corresponding to the maximum is sometimes referred to as the critical nucleation barrier G^*.

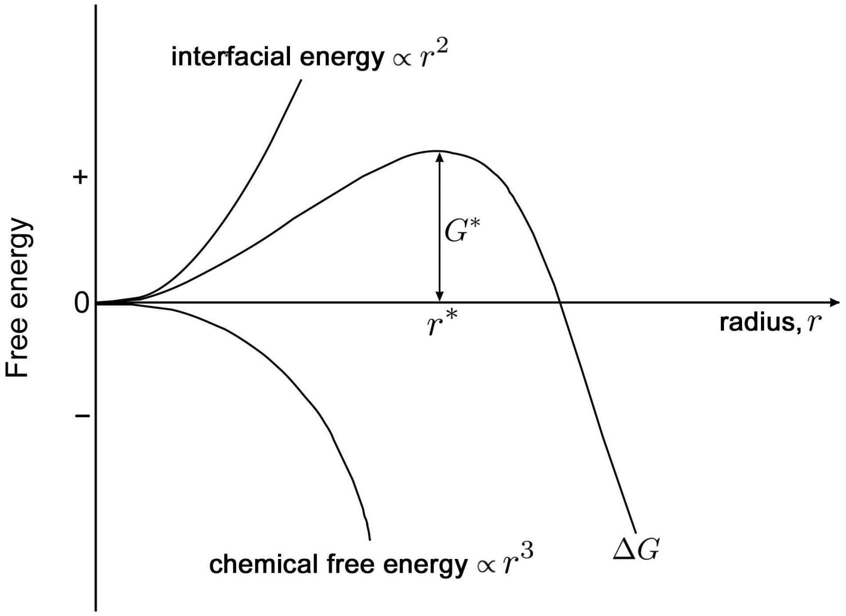

Figure 3.1: The free energy change associated with the formation of a particle as a function of radius r.

The maximum free energy occurs at a critical radius, r^*. If $r < r^*$ the system can lower its free energy by the dissolution of β, whereas when $r > r^*$ the free energy of the system decreases if the particle grows. The maximum of Equation 3.1 can be obtained by differentiating with respect to r and then equating to zero, which gives

$$G^* = \frac{16\pi\sigma_{\alpha\beta}^3}{3\Delta G_V^2} \tag{3.2}$$

The corresponding radius of the critical particle r^* is given by

$$r^* = -\frac{2\sigma_{\alpha\beta}}{\Delta G_V} \tag{3.3}$$

ΔG_V is zero at the equilibrium temperature, so $G^* = \infty$. When $\Delta G_V < 0$, the nucleation barrier becomes finite. With increasing driving force both the barrier and the critical radius decrease. The probability of the barrier to nucleation being overcome with the aid of thermal fluctuation is given by a universal gas constant and so the concentration of critical sized nuclei, N^*, will be given by

$$N^* = N_V \exp\left(\frac{-G^*}{RT}\right) \tag{3.4}$$

where N_V is the number of nucleation sites per unit volume. The nucleation rate depends on the attempt frequency, which can be written as kT/h, where h is the Planck constant, k is the Boltzmann constant, T is the absolute temperature and Q is the activation energy for the transfer of atoms across the embryo/matrix boundary. Thus the nucleation rate, I, per unit volume is given by

$$I = N_V \frac{kT}{h} \exp\left(-\frac{G^* + Q}{RT}\right) \tag{3.5}$$

Driving Force for Nucleation

In Equation 3.5, Q is the activation energy for solute diffusion and independent of temperature whereas G^* is strongly dependent on temperature. Figure 3.2 shows schematically the free energy curves of the matrix α. The free energy-composition diagram of the solute rich precipitate phase, β, is constant with a narrow range of solubility of this phase. The equilibrium compositions, $c^{\alpha\beta}$ and $c^{\beta\alpha}$, of the matrix and precipitate respectively can be determined by constructing a tangent which is common to both the free energy curves. The intercept of the tangent with the vertical axes gives the chemical potentials, which are identical for each species whatever the phase, by virtue of the fact that the tangent is common. Equilibrium precipitation causes the free energy of the system to decrease by ΔG_0, as shown in Figure 3.2. The corresponding free energy change per unit mole of equilibrium precipitate, ΔG_n, is, to a good approximation, given by [6]:

$$\Delta G_n = \Delta G_0 \frac{c^{\beta\alpha} - c^{\alpha\beta}}{\overline{c} - c^{\alpha\beta}} \tag{3.6}$$

3.2.2 Heterogeneous Nucleation

In the preceding section it has been assumed that the formation of nuclei can occur with equal probability throughout the parent phase. This is less likely in practical applications except where metals and alloys are extremely pure and contain very few inclusions, line

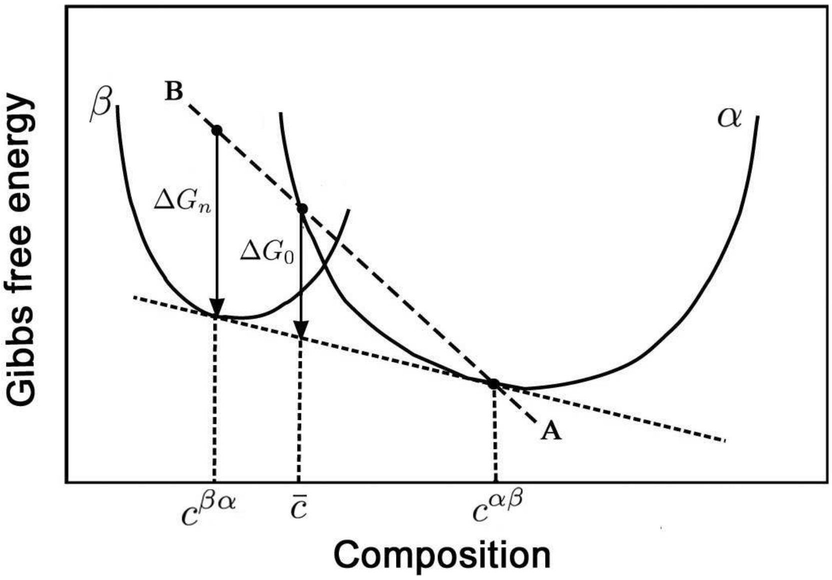

Figure 3.2: Free energy diagrams illustrating chemical free energy changes during nucleation and growth of β precipitates from a phase, α, of composition $\bar{c}$.

or surface defects. In general, metals and alloys for commercial applications contain many defects, which enable nuclei to form with a much lower activation energy. This heterogeneous nucleation occurs at sites such as grain boundaries, impurity particles and dislocations. Additionally the critical size or the number of atoms in the system to form a critical nucleus is also less than required for homogeneous nucleation. This is due to the fact that the formation of a nucleus will either relax lattice strain or destroy a defect, both of which release free energy, thus reducing the net free energy required to form a nucleus.

Nucleation on Grain Boundaries

Consider the grain boundary between two grains to be planar. Assuming that the interfacial energy of the α/β interface is isotropic, the new β particle will be bounded by spherical surfaces on both sides of the grain boundary, as shown in Figure 3.3. The contact angle, θ, between the particle and the grain boundary can be expressed by [109]:

$$\cos\theta = \frac{\sigma_{\alpha\alpha}}{2\,\sigma_{\alpha\beta}} \tag{3.7}$$

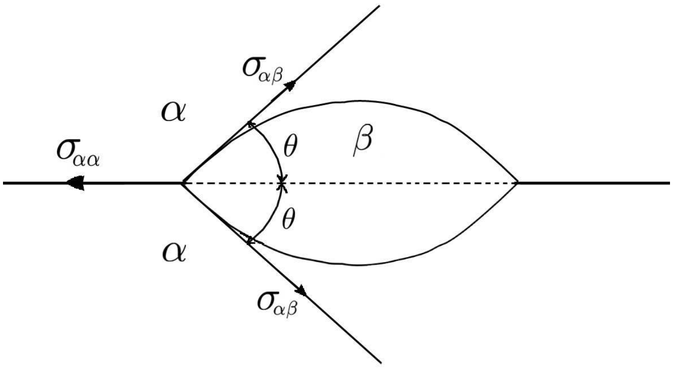

Figure 3.3: The shape of a nucleus on a planar grain boundary [109].

where $\sigma_{\alpha\alpha}$ and $\sigma_{\alpha\beta}$ are the interfacial energies of the α/α and α/β interfaces respectively. The free energy of formation of the β phase from the supersaturated α phase is

$$\Delta G = V^{\beta}\,\Delta G_V + A_{\alpha\beta}\,\sigma_{\alpha\beta} - A_{\alpha\alpha}\,\sigma_{\alpha\alpha} \tag{3.8}$$

where V^{β} is the volume of the embryo, $A_{\alpha\beta}$ is the spherical area of the α/β interface of energy, $\sigma_{\alpha\beta}$, created and $A_{\alpha\alpha}$ is the circular area of the α/α grain boundary of energy, $\sigma_{\alpha\alpha}$, destroyed during the process.

It can be shown that the critical radius of the spherical cap will be independent of the grain boundary and is given by

$$r^* = \frac{2\sigma_{\alpha\beta}}{\Delta G_V} \tag{3.9}$$

and the activation barrier for heterogeneous nucleation will be given by

$$\Delta G^*_{het} = \frac{16\pi}{3}.f(\theta).\frac{\sigma^3_{\alpha\beta}}{\Delta G^2_V} \tag{3.10}$$

where the function $f(\theta) = \frac{1}{2}\Big[2 - 3\cos\theta + \cos^3\theta\Big]$.

The activation energy for grain boundary nucleation and homogeneous nucleation can be correlated using the following equation considering similar interfacial free energy and ΔG_V

$$\frac{\Delta G^*_{het}}{\Delta G^*_{hom}} = f(\theta) \tag{3.11}$$

where ΔG^*_{het} and ΔG^*_{hom} are the free energies for heterogeneous and homogeneous nucleation respectively.

Figure 3.4 shows the dependency of $\Delta G^*_{het}/\Delta G^*_{hom}$ on $\cos\theta$ for various heterogeneous nucleation sites. The Figure shows nucleation at grain corners reduce the activation energy for nucleation and hence acts as preferred nucleation sites.

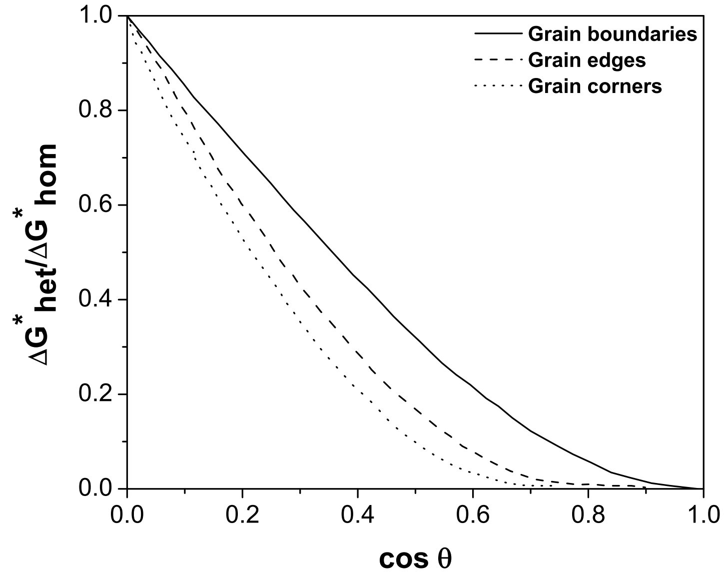

Figure 3.4: The effect of θ on the ratio of activation energy required to form a nucleus on various types of nucleation sites [110].

3.3 Growth Theory

In general two types of growth models are considered: one for diffusion-controlled growth and the other for interface controlled growth. The former can occur for phase transformations where long range compositional changes take place. In contrast interface-controlled growth can occur if the growth is determined by atomic processes in the immediate vicinity of the interface, as for example, massive austenite to ferrite transformation during cooling in substitutional binary Fe-Mn alloys [111] and also in some cases of crystallisation reactions of amorphous alloys [112].

3.3.1 Zener Model for Diffusional Growth

The first elucidation of diffusional growth during phase transformation was due to Zener [113, 114] who considered a spherical precipitate particle growing in an infinite solid solution of initially uniform composition. A key assumption of the theory that allowed Zener to solve Fick's diffusion equation is that the moving interface between parent phase and product phase is always in a state of local equilibrium. The variation of composition along a line normal to the interface during diffusional growth is illustrated in Figure 3.5. Consider x as the semi-thickness of plate or radius of a cylinder or sphere. When the boundary is in a position $x = x^I$ then the diffusion flux at the interface across unit area in a time, ∂t, is given by

$$D\left(\frac{\partial c}{\partial x}\right)_{x=x^I} \partial t \tag{3.12}$$

where the concentration, c, of solutes in the α phase is a function of x and t, and D is the diffusion coefficient. If during this time interval the interface advances a distance ∂x, the amount of solute which will be required is $(c^{\beta\alpha} - c^{\alpha\beta})\partial x$, where $c^{\beta\alpha}$ and $c^{\alpha\beta}$ are, respectively, the concentrations in the precipitate and in the matrix at the precipitate/-matrix interface. This solute can only come from the diffusion flow, so the two terms can be equated to derive the growth velocity, v, as follows:

$$v = \frac{dx^I}{dt} = \frac{D}{c^{\beta\alpha} - c^{\alpha\beta}}\left(\frac{\partial c}{\partial x}\right)_{x=x^I} \tag{3.13}$$

Zener [113] proposed the approximation where the concentration gradient ahead of the interface is assumed to be constant (Figure 3.6), in which case the concentration gradient $\partial c/\partial x_{x=x^I}$ can be represented as $(\overline{c} - c^{\alpha\beta})/x^D$ where x^D is an effective diffusion distance. Hence the expression for the growth rate becomes

$$v = \frac{\overline{c} - c^{\alpha\beta}}{c^{\beta\alpha} - c^{\alpha\beta}} \frac{D}{x^D} \tag{3.14}$$

where $\overline{c}$ is the concentration of the solute in the matrix far away from the precipitate. For precipitate growth during isothermal transformation, the dimensionless supersaturation, Ω, can be represented by

$$\Omega = \frac{\overline{c} - c^{\alpha\beta}}{c^{\beta\alpha} - c^{\alpha\beta}} \tag{3.15}$$

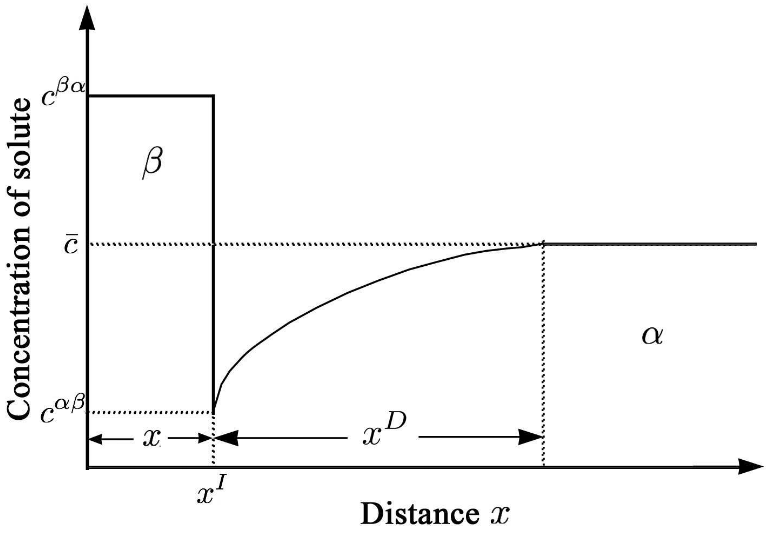

Figure 3.5: Schematic illustration of the variation of solute concentration at the interface between matrix, α, and precipitate, β. x^I is the position of the α/β interface.

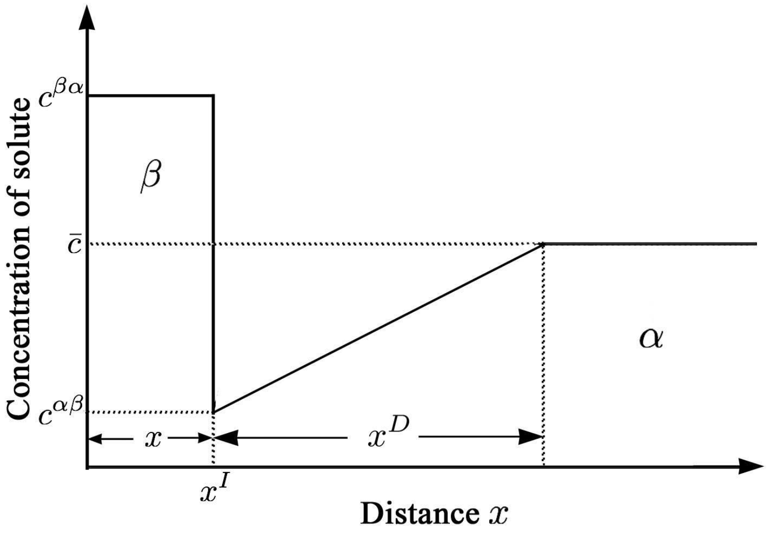

Figure 3.6: Schematic illustration of a constant concentration gradient at the interface between matrix, α, and precipitate, β.

It follows from Equations 3.13 to 3.15 that the growth rate can written as

$$v = \frac{D\Omega}{x^D} \tag{3.16}$$

The diffusion flux of solute towards the interface must equal the rate at which solute is incorporated in the precipitate. Hence by considering the overall conservation of mass, it can be written

$$(c^{\beta\alpha} - \overline{c})x^I = \frac{1}{2}x^D(\overline{c} - c^{\alpha\beta}) \tag{3.17}$$

so that

$$x^D = \frac{2(c^{\beta\alpha} - \overline{c})}{(\overline{c} - c^{\alpha\beta})}x^I \tag{3.18}$$

After substitution of x^D into Equation 3.14, the growth rate can be represented as

$$v = \frac{dx^I}{dt} = \frac{D}{2x^I}\frac{(\overline{c} - c^{\alpha\beta})^2}{(c^{\beta\alpha} - \overline{c})(c^{\beta\alpha} - c^{\alpha\beta})} \tag{3.19}$$

In many cases, $c^{\beta\alpha} \gg c^{\alpha\beta}$ and $c^{\beta\alpha} \gg \overline{c}$, so the concentration difference $(c^{\beta\alpha} - \overline{c}) \simeq (c^{\beta\alpha} - c^{\alpha\beta})$ and hence

$$\frac{dx^I}{dt} = \frac{D}{2x^I}\Omega^2 \tag{3.20}$$

Integrating this equation gives

$$2\int x^I \partial x^I = \Omega^2 D \int \partial t \tag{3.21}$$

so that

$$x^I = \Omega\sqrt{Dt} \tag{3.22}$$

The linear dimension of the precipitate therefore varies with the square root of diffusion coefficient and time. This is the parabolic law for one dimensional growth in a binary system. If all the linear dimensions change similarly, each dimension must be proportional to $\sqrt{Dt}$ and the growth is parabolic with the velocity proportional to $(D/t)^{1/2}$.

3.3.2 Growth of Spherical Particles

Zener [115] has given a solution for the precipitate growth in a spherical system. For spherical particles the growth is parabolic in all directions. Hence the relationship between the radius, r^I, of a spherical particle and time, t, can be expressed as

$$r^I = Ct^{\frac{1}{2}} \tag{3.23}$$

where C is a constant. The theory of parabolic growth can be solved by evaluating Equation 3.13. In order to obtain the value of C it is convenient to solve the general diffusion equation in the form of

$$\frac{\partial c}{\partial t} = D\left(\frac{\partial^2 c}{\partial r^2}\right) + (j-1)\frac{D}{r}\left(\frac{\partial c}{\partial r}\right) \tag{3.24}$$

where j= 1,2 or 3 for one, two or three dimensional growth respectively. The boundary conditions for this equation are

$$c(x,0) \ = \overline{c}, \ \ c(x,t) = c^{\alpha\beta}$$

Zener showed that the variation of concentration with distance can be obtained by solving Equation 3.24 and is represented by [116]:

$$c(x,t) = \overline{c} + (c^{\alpha\beta} - \overline{c})\frac{\phi_j[r/(Dt)^{0.5}]}{\phi_j[r^I/(Dt)^{0.5}]} \tag{3.25}$$

where $\phi_j(x)$ measures the degree of advancement of a moving interface and is given by

$$\phi_j(x) = \int_x^\infty \eta^{-2}\exp(-\eta^2/4)\, d\eta$$

where η is a variable of integration.

For parabolic growth, since $r^I \infty (Dt)^{0.5}$, so the term $r^I/(Dt)^{0.5}$ is a dimensionless function of the solute concentrations, which determines the growth velocity, α_j. This is also termed as the parabolic rate constant and can be derived from Equation 3.13 using the composition function of Equation 3.25:

$$\frac{1}{\Omega}\frac{dr^I}{dt} = \frac{(\alpha_j^{-2})}{\phi_j[\alpha_j]}\exp\left(\frac{-\alpha_j^2}{4}\right)D^{\frac{1}{2}}t^{\frac{1}{2}}$$

and hence

$$(\alpha_j)^j = \frac{2\Omega \exp\left(\frac{-\alpha_j^2}{4}\right)}{\phi_j[\alpha_j]} \tag{3.26}$$

This equation is an implicit expression for α_j in terms of the supersaturation. The growth law is given by:

$$r^I = \alpha_j (Dt)^{\frac{1}{2}} \tag{3.27}$$

Zener showed that it possible to derive simpler equations for α_j for one and three dimensional growth by using asymptotic expansions of $\phi_j[\alpha_j]$ valid in the range of $\alpha_j \ll 1$ and $\alpha_j \gg 1$. For one-dimensional growth, this gives,

$$\left.\begin{array}{lll} \alpha_1 = & \frac{2}{\pi^{\frac{1}{2}}}\Omega & (\alpha_1 \ll 1) \\ \alpha_1 = & \sqrt{2}\frac{(c^{\beta\alpha} - c^{\alpha\beta})^{\frac{1}{2}}}{(c^{\beta\alpha} - \overline{c})^{\frac{1}{2}}} & (\alpha_1 \gg 1) \end{array}\right\} \tag{3.28}$$

and for three-dimensional growth

$$\left.\begin{array}{lll} \alpha_3 = & (2\Omega)^{\frac{1}{2}} & (\alpha_1 \ll 1) \\ \alpha_3 = & \sqrt{6}\frac{(c^{\beta\alpha} - c^{\alpha\beta})^{\frac{1}{2}}}{(c^{\beta\alpha} - \overline{c})^{\frac{1}{2}}} & (\alpha_1 \gg 1) \end{array}\right\} \tag{3.29}$$

3.3.3 Growth of Plate Shaped and Needle Shaped Particles

Various theories have been developed to describe the diffusion-controlled growth of precipitates with shapes approximating to needles or plates. The most comprehensive one is due to Trivedi [117, 118]. His solution, based on Ivantsov's [119] treatment, included the effect of the nonisoconcentrate nature of the interface at the precipitate tip. The concentration at the tip can vary due to capillary effects and due to the interface kinetics effect. The principal approximations used by Trivedi were: (1) the steady state shape of the interface near the growing tip is a parabolic cylinder for the case of a plate like precipitate, (2) the elastic strain energy and anisotropy of surface properies can be neglected, (3) the concentration of solute in the matrix is such that the theory of capillary applicable to dilute solutions can be used and (4) the diffusivity is independent of concentration.

For the case in which the shape is a parabolic cylinder, i.e. an infinite plate, the Ivantsov theory gives the supersaturation, Ω_r, as being:

$$\Omega_r = (\pi p)^{1/2} \exp(p) \operatorname{erfc}(p)^{1/2} \tag{3.30}$$

where erfc(p) is the complementary error function, the Péclet number, p, for dimensional growth can be expressed as $p = vr/2D$, r is the radius of particle. To calculate the growth rate, it is necessary to evaluate the value of r. Zener assumed that the particle adopts a radius which gives maximum rate of growth, in this case at $r = r_c$. The growth rate is given by

$$v = \frac{D\Omega}{4C_1 r_c} \tag{3.31}$$

where C_1 is a constant. The critical radius, r_c, is given by Christian [116]:
For a plate,

$$r_c = \frac{2c^{\alpha\beta}\Gamma}{(\overline{c} - c^{\alpha\beta})} \tag{3.32}$$

For a needle,

$$r_c = \frac{c^{\alpha\beta}\Gamma}{(\overline{c} - c^{\alpha\beta})} \tag{3.33}$$

where Γ is the capillary coefficient [116]

$$\Gamma = \left(\frac{\sigma v^3}{kT}\right)\left(\frac{1 - c^{\alpha\beta}}{c^{\beta\alpha} - c^{\alpha\beta}}\right) \tag{3.34}$$

Hillert [120] has proposed a model for the diffusion problem of plate growth which assumes that concentration in the plane perpendicular to the plate has the form

$$c - c^{\alpha\beta} = C_2 \exp\left(\frac{-\pi {x_2}^2}{16m^2}\right) \tag{3.35}$$

where x_2 is the coordinate in the perpendicular direction and C_2 and m are arbitary constants. Using this assumption, the steady state growth rate is given by

$$v = \frac{D\Omega_r}{2} \frac{c^{\beta\alpha} - c^{\alpha\beta}}{c^{\beta\alpha} - \overline{c}} \frac{1}{m}\left(1 - \frac{m_c}{m}\right) \tag{3.36}$$

Trivedi has given an exact solution for the diffusion problem which allows the composition to vary along the interface of a plate but assumes that the shape remains that of a parabolic cylinder. His growth equation may be written in the form

$$\Omega_r = (\pi p)^{1/2} \exp(p) \operatorname{erfc}(p)^{1/2} \Big\{ 1 + \frac{r_c}{r} \Omega_r \, S(p) \Big\} \tag{3.37}$$

$S(p)$ is a function of p which Trivedi and Pound [121] estimated as $3[2p(1+2p)]^{-1}$. Trivedi calculated the $S(p)$ with values ranges ∼10 at $p = 0.07$ to ∼0.45 at $p = 10$.

3.4 Overall Transformation Kinetics

In the case of nucleation and growth reactions, an individual region may form after a time interval $t = \tau$. Different particles will therefore attain critical status at different times from the start of heat treatment. Assuming a product phase, β, is forming from a parent phase, α, and that any dimension of the β phase increases linearly with the time of transformation, the linear dimension, d, of the product phase after time t is

$$d = v(t - \tau) \tag{3.38}$$

For isotropic growth, a transformed region will have the shape of a sphere. The volume of such a region, V^β, will be zero at times shorter than the incubation time (i.e. before nucleation) after which it will be a function of the time elapsed since nucleation.

$$\left.\begin{aligned} V^\beta &= \frac{4\pi}{3} v^3 (t-\tau)^3 && (t > \tau) \\ &= 0 && (t < \tau) \end{aligned}\right\} \tag{3.39}$$

The number of new β phase regions nucleated in the time interval τ and $\tau + d\tau$ is $I_V V^\alpha d\tau$ where I_V is the homogeneous rate of nucleation per unit volume and V^α is the volume of the parent phase α. In the initial stages of the transformation, when $V^\alpha \gg V^\beta$, the nuclei are widely spaced and the interference between neighbouring nuclei is negligible. The transformed regions of the parent phase can grow independently of each other. The increase in the volume of the β phase, dV^β, due to particles nucleated in the time interval, $d\tau$, is given by

$$dV^\beta = \frac{4\pi}{3} v^3 (t-\tau)^3 I_V V d\tau \tag{3.40}$$

If the above equation is integrated between the limits $\tau = 0$ to $\tau = t$, this gives

$$f_V = \frac{V^\beta}{V} = \frac{\pi}{3} I_V v^3 t^4 \tag{3.41}$$

where V^β is the volume fraction of the product phase. This equation is valid only for short duration of transformation when $V^\beta \ll V^\alpha$. This is because individual regions will ultimately impinge upon each other at some stage of the transformation. Therefore, only those parts of the change in volume which remain in untransformed regions of the parent phase can contribute to the change in real volume of β. In reality, we must consider mutual interference of regions growing from separate nuclei. The problem posed by this has been solved by Avrami [122–124], who introduced the concept of extended volume. This phenomenon can be explained through Figure 3.7. Considering two particles that exist at time t, after a small interval dt, new regions marked a, b, c and d are formed, assuming that they are able to grow unrestricted in extended space whether or not the region into which they grow is already transformed. However, only those components of a, b, c and d which lie in previously untransformed matrix can contribute to a change in the real volume of the product phase (β). The real and extended (designated by subscript e) volumes are related by the following equation:

$$dV^\beta = \left(1 - \frac{V^\beta}{V}\right) V_e^\beta \tag{3.42}$$

This equation can be integrated to obtain the real volume fraction

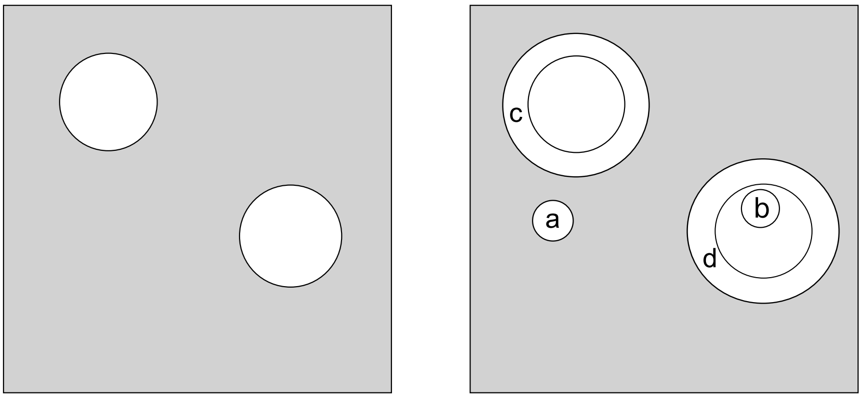

(a) time = t (b) time = t + △t

Figure 3.7: Schematic illustration of the concept of extended volume with time. Two precipitate particles have nucleated together and grown to a finite size in the time t. New regions c and d are formed as the original particles grow, but a and b are new particles, of which b has formed in a region which is already transformed.

$$V_e^{\beta} = -V \ln\left(1 - \frac{V^{\beta}}{V}\right) \tag{3.43}$$

so that

$$\frac{V^{\beta}}{V} = 1 - \exp\left(-\frac{V^{\beta}}{V}\right) \tag{3.44}$$

Similar to Equation 3.40 the change in extended volume over the interval τ and $\tau + d\tau$ is

$$dV_e^{\beta} = \frac{4\pi}{3} v^3 (t-\tau)^3 I_V V d\tau \tag{3.45}$$

After integration and substituting with Equation 3.43 gives

$$-\ln\left(1 - \frac{V^{\beta}}{V}\right) = \frac{4\pi}{3} v^3 \int_0^t I_V (t-\tau)^3 d\tau \tag{3.46}$$

By substituting with the volume fraction of precipitate ($f_V = V^{\beta}/V$) this expression becomes

$$-\ln\{1 - f_V\} = \frac{4\pi}{3} v^3 I_V \int_0^t (t-\tau)^3 d\tau \tag{3.47}$$

If the nucleation rate is constant, after integration, this gives

$$f_V = 1 - \exp\{-\pi v^3 I_V t^4/3\} \tag{3.48}$$

This equation is known as the Johnson-Mehl-Avrami equation and is based on the assumption that nucleation is random. This means if the system is divided into a number of small volume elements, the probability of forming a nucleus in unit time would be the same for all the elements. Avrami proposed a rather general form of the above equation for three dimensional nucleation and growth process:

$$f_V = 1 - \exp(-kt^n) \tag{3.49}$$

where n is a numerical exponent and the value varies from 1 to 4. n is independent of temperature provided that there is no change in the nucleation mechanism. k, on the other hand, depends on the nucleation and growth rates and is therefore sensitive to temperature. The specific values of k and n can be obtained from experimental data by plotting $\ln(-\ln\{1 - f_V\})$ versus $\ln\{t\}$. The isothermal transformation curves obtained by substituting $n = 1$ in the above equation is equivalent to that for a first order homogeneous reaction.

3.5 Kinetics of Simultaneous Transformation

Jones and Bhadeshia [125] developed a model for the simultaneous occurrence of two or more transformations. This was carried out by generalising the classical theory of the extended volume concept described in the previous section. This model was based on the modification of Avrami overall transformation kinetics theory for grain boundary nucleated phases.

3.5.1 Simple Simultaneous Reaction

Consider precipitates β and θ to form at the same time from the parent phase which is designated as α. It was assumed in the model that the nucleation and growth rates do not change with time and that the particles grow isotropically.

As discussed in the previous section, the increase in the extended volume due to particles nucleated in a time interval, $t = \tau$ to $t = \tau + d\tau$, can be given by:

$$d{V_e}^{\beta} = \frac{4\pi}{3}{v_\beta}^3(t-\tau)^3 I_\beta V d\tau \tag{3.50}$$

$$d{V_e}^{\theta} = \frac{4\pi}{3}{v_\theta}^3(t-\tau)^3 I_\theta V d\tau \tag{3.51}$$

where ${V_e}^{\beta}$ and ${V_e}^{\theta}$ are extended volumes of β and θ respectively. v_β, v_θ, I_β and I_θ are the growth and nucleation rates of β and θ respectively and V is the total volume of the system. The increase in real volumes of the two phases can be represented in terms of extended volumes using the following equations:

$$dV_\beta = \left(1 - \frac{V_\beta + V_\theta}{V}\right) d{V_e}^{\beta} \tag{3.52}$$

$$dV_\theta = \left(1 - \frac{V_\beta + V_\theta}{V}\right) d{V_e}^{\theta} \tag{3.53}$$

where V^β and V^θ are real volumes of β and θ respectively. In general, V^β is a complicated function of V^θ and it is not possible to analytically integrate these equations to find the relationship between the actual and extended volumes. However, in certain simple cases, it is possible to relate V^θ to V^β by multiplication with a suitable constant, μ, in which case $V^\theta = \mu V^\beta$. Hence Equations 3.52 and 3.53 can be written as:

$$dV_\beta = \left(1 - \frac{V_\beta + \mu V_\beta}{V}\right) dV_e{}^\beta \tag{3.54}$$

$$dV_\theta = \left(1 - \frac{V_\theta + \mu V_\theta}{\mu V}\right) dV_e{}^\theta \tag{3.55}$$

After rearranging, the volume fractions f_β and f_θ can be expressed as:

$$f_\beta = \frac{1}{1+\mu}\left[1 - \exp\left\{ - \frac{(1+\mu)}{3}\pi {v_\beta}^3 I_\beta t^4 \right\}\right] \tag{3.56}$$

$$f_\theta = \frac{1}{1+\mu}\left[1 - \exp\left\{ - \frac{(1+\mu)}{3\mu}\pi {v_\theta}^3 I_\theta t^4 \right\}\right] \tag{3.57}$$

These equations resemble the well known Avrami equation for single phase precipitation with extra factors to account for the presence of a second precipitating phase. Since the nucleation and growth rates were assumed to be constant, it is possible to calculate explicitly the value of μ, which is given by

$$\mu = \frac{V_\beta}{V_\theta} = \frac{I_\beta {v_\beta}^3}{I_\theta {v_\theta}^3} \tag{3.58}$$

3.6 Summary

The transformation which occurs during tempering involves nucleation and growth of many transformation products, because at the tempering temperature austenite can decompose into different precipitates and ferrite. These reactions may overlap and interact with each other either by hard impingement where the adjacent products touch each other or by soft impingement where their diffusion or thermal field overlap.

Nucleation of the transformation products have been discussed in terms of classical nucleation theory. In order to determine overall transformation kinetics both the nucleation and growth process are combined accounting for the different impingement effects.

The model for the overall transformation kinetics will require strong support from experimental results regarding the change in volume fraction of retained austenite with the progress of the tempering treatment and also about the nature of the precipitates.

Chapter 4

Experimental Procedure

4.1 Sample Preparation

The chemical compositions of the alloys, prepared as a 20 kg vacuum induction melts from high purity base materials, are given in Table 4.1. The ingots were hot forged and then hot rolled to 25 mm square cross section bars. The alloys contain sufficient silicon to prevent the precipitation of cementite during transformation to bainite, and about 3 wt% of manganese or 4 wt% of nickel for the purpose of hardenability. It should therefore be possible to isothermally transform to just bainitic ferrite leaving residual austenite. Bhadeshia and Edmonds found no evidence for carbide precipitation in silicon added steel even after 74 h at 350°C [42]. Cylindrical samples, 12 mm long and 8 mm diameter, were machined from this material to use on a *Thermecmaster* thermomechanical simulator. The equilibrium phase fractions have been calculated using National Physical Laboratory's Metallurgical and Thermodynamic Data Bank (MTDATA) [126] and TCFE database as presented in Figure 4.1. This package is capable of calculating phase equilibria for multi-component systems where many phases may be coexisting. It can predict the larger systems by combining experimentally determined data from the appropriate unary, binary and ternary sub-systems. The reliability of the predictions depends on the available data for corresponding sub-systems. MTDATA warns when certain data are missing to avoid misinterpreting the output. For any given system MTDATA can calculate the compositions and mass fractions of the phases present by minimising the Gibbs free energy along with the requirement for conservation of mass. It is possible to suppress the formation of any phase and recalculate the phase equilibria without that phase present. In this way it is possible to deduce the relative stabilities

Steel	C	Mn	Ni	Si
Fe-Mn-Si	0.22	3.0	-	2.03
Fe-Ni-Si	0.39	-	4.09	2.05

Table 4.1: Chemical compositions of the experimental steels in wt%

of the phases and determine likely precipitation sequences. MTDATA may be used to predict how changes in alloy composition and heat treatment affect the relative stability of the phases and is therefore an useful tool in the design of new alloys. Using MTDATA, it is possible to predict any system thermodynamically but it is unable to predict time dependence of microstructure, which requires kinetic modelling. Nevertheless, much useful information can be generated on the basis of thermodynamic calculations alone and some examples are provided in the Chapter 9.

4.2 Heat Treatment

All the heat treatments were carried out in a *Thermecmaster* thermomechanical simulator capable of monitoring the strain, load, time and temperature during the course of transformation. The machine is equipped with an environmental chamber which can be evacuated or filled with inert gas using a rotary and oil diffusion pump. The heat source is a radio frequency coil, and the temperature was measured with a 0.1 mm diameter Pt/Pt-10%Rh (Type S) thermocouple spot welded to the sample. A scanning laser beam is used to follow changes in the diameter of the specimen during testing. The specimen is seated centrally between Si_3N_4 dies. Heating is via a water-cooled induction coil surrounding the specimen. The maximum heating rate that can be achieved is around $50°C\,s^{-1}$ but this is dependent upon the material. Cooling was carried out by blowing a helium jet directly onto the specimen surface. The helium flow rate during cooling is controlled by a proportional servo valve. These devices ensure excellent efficiency in controlling the temperature and holding time of isothermal treatments, and fast cooling in quenching processes.

Austenitisation was carried out by heating the steels above the Ac_3 temperatures, which was calculated using Andrew's Equation [127]. For the Fe-Mn-Si steel, this temperature was 930±2°C, whereas for the Fe-Ni-Si steel this was 880±2°C. Both the steels were austenitised for 30 min in the vacuum chamber. The purpose of this treatment

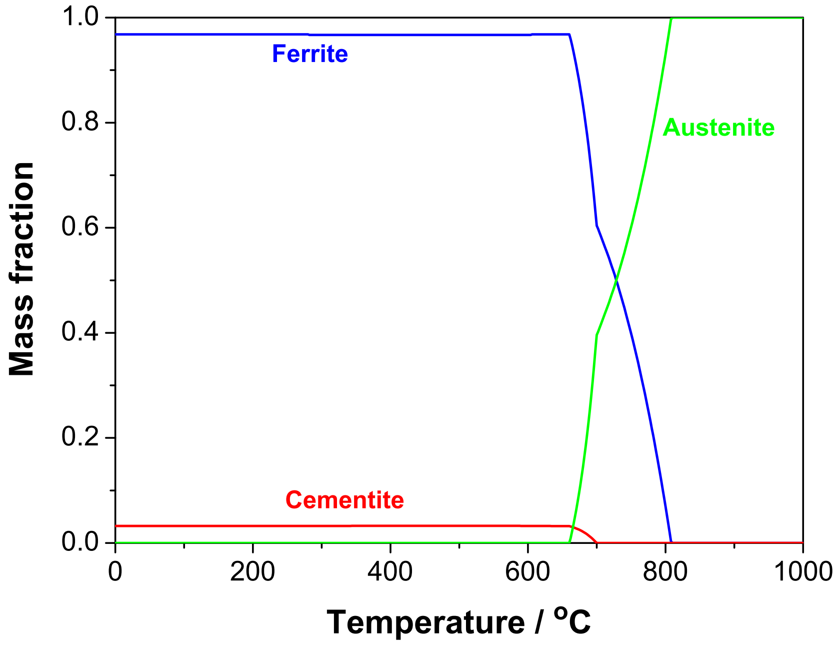

(a)

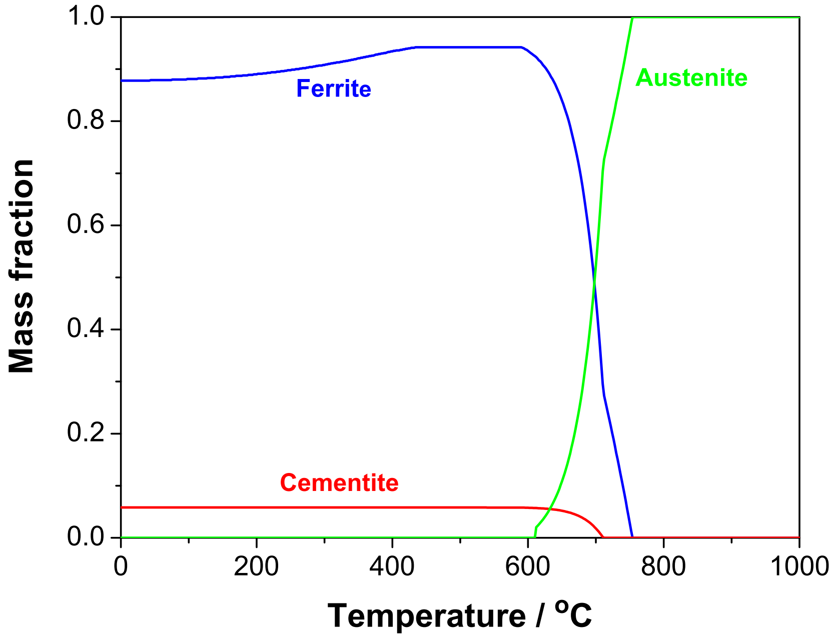

(b)

Figure 4.1: The evolution of equilibrium phase fractions for (a) the Fe-Mn-Si-steel and (b) the Fe-Ni-Si-steel, calculations were done using MTDATA where ferrite, austenite and cementite phases are permitted.

was to austenitise the sample. The time at the austenitisation temperature depends on the size as well as the initial microstructure of the sample [128]. The heating rate was maintained at 10°C s^{-1}. Samples were then cooled below the B_s temperature using a helium jet at a cooling rate of 10°C s^{-1}. The isothermal transformation temperatures for the Fe-Mn-Si steel and the Fe-Ni-Si steel were 390°C and 380°C respectively. One sample of the Fe-Mn-Si steel was also cooled at 30°C s^{-1} to compare the effect of cooling rate on the microstructure. The samples were held at the isothermal temperatures for 2 h. The B_S and M_S temperatures were calculated for the experimental steels using the algorithms described elsewhere [129–131]. The diameter change associated with the heat treatment was recorded to relate this to the volume change on transformation. After isothermal transformation the samples were quenched to room temperature at a cooling rate of 10°C s^{-1} using a helium jet. Figure 4.2 illustrates the heat treatments.

Specimens of the Fe-Mn-Si steel cooled to the isothermal temperature using two different cooling rates (10°C s^{-1} and 30°C s^{-1}) produced similar bainitic structures and no allotriomorphic ferrite was found in any of the samples. The hardness test results also support this conclusion, with 393±3 HV for the sample cooled at 30°C s^{-1} and 391±2 HV for the other sample. Due to the similarity in structure in both cases, all the further experiments were carried out using the 10°C s^{-1} cooling rate.

The temperatures selected for tempering were 400°C, 420°C, 450°C and 480°C for the Fe-Mn-Si steel, whereas for the Fe-Ni-Si steel the tempering temperatures were 400°C, 420°C and 450°C. The transformation kinetics are extremely fast at 480°C for Ni added steel, so it was not possible to capture the transformation stages. The tempering time was selected in the range of 2 min to 30 h depending on the temperature and materials. Only one sample was tempered at 250°C for 5 h in order to determine the contribution of martensite tempering to the cumulative dilation obtained after tempering at 450°C.

4.3 Measurement of Prior Austenite Grain size

The prior austenite grain boundary can be revealed by means of a thermal etching technique as described by Andrés [132]. To reveal and measure the prior austenite grain size, a special heat treatment was formulated. This was carried out in a *Thermecmaster* thermomechanical simulator, so the same sample dimensions were used, as described in Section 4.1. Prior to the heat treatment the sample was polished to a mirror finish

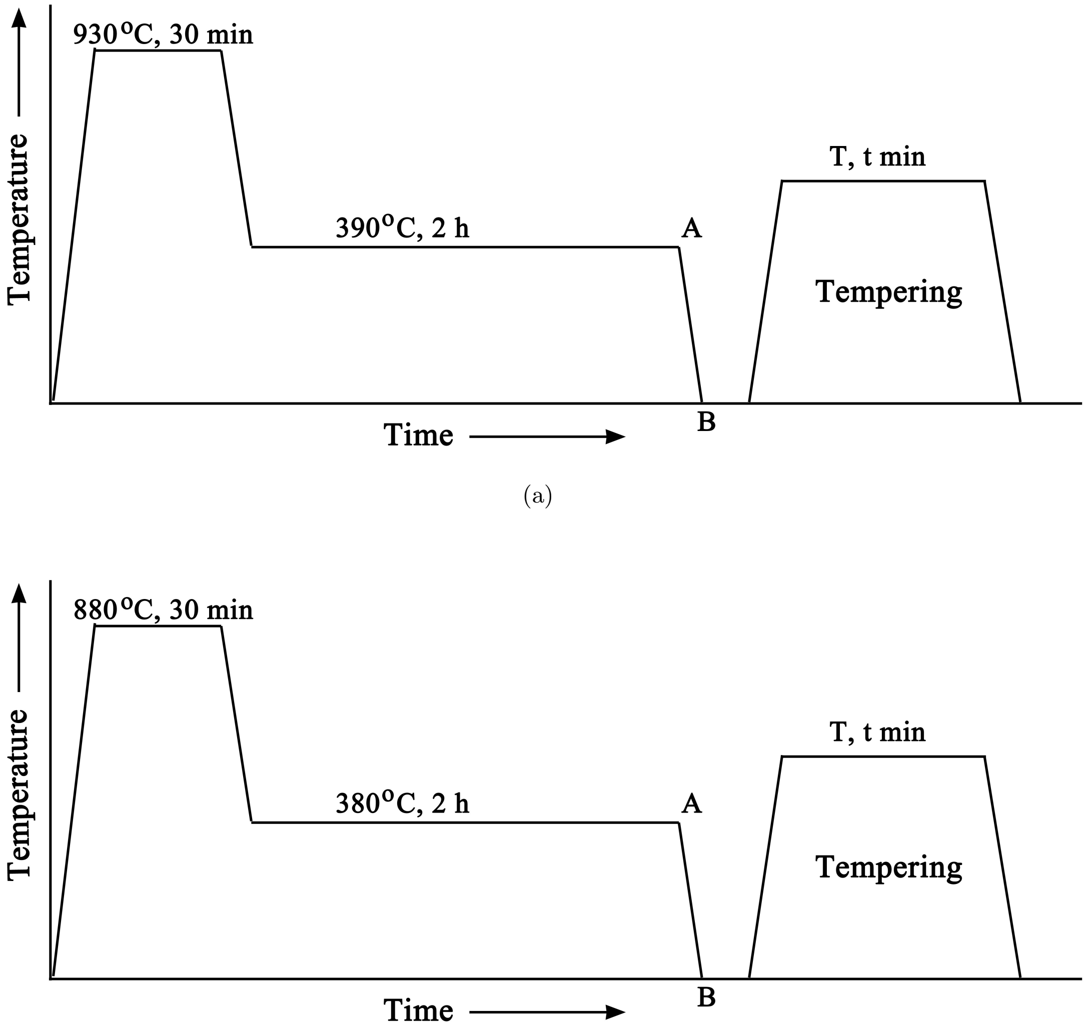

(a)

(b)

Figure 4.2: Schematic of the heat treatment for (a) the Fe-Mn-Si steel and (b) the Fe-Ni-Si steel. *T* stands for tempering temperatures in celsius and *t* for tempering duration.

using up to 1 µm diamond paste. Samples from the Fe-Mn-Si steel were austenitized at 930°C for 30min (similar austenisation treatment has been given to all the heat treated material). They were then cooled at $50°\mathrm{C\,s^{-1}}$ to 650°C, held at this temperature for 5 min, then cooled down to room temperature using the same cooling rate. Samples from the Fe-Ni-Si steel were austenitized at 880°C for 30 min. They were then cooled at $50°\mathrm{C\,s^{-1}}$ to 650°C and held at this temperature for 8 min, then cooled down to room temperature at $50°\mathrm{C\,s^{-1}}$. Prior austenite grain boundaries were revealed by this heat treatment (as shown in Figure 4.3) and the grain size was measured using the linear intercept method [133].

4.4 Hardness Testing

Hardness testing is a quick method of characterising the overall effect of tempering and provides valuable information of overall changes. The tests were carried out using a Vickers hardness testing machine, using a 30 kg load. The test was developed in 1924 by Smith and Sandland at Vickers Ltd as an alternative to the Brinell method. The Vickers hardness test is convenient since the measurement is independent of the size of the indenter, which can be used for all materials irrespective of hardness. Each quoted value represents the average of 10 values.

4.5 Optical Microscopy

The specimens were prepared for optical microscopy by hot mounting in conductive bakelite, then polished using 400, 600, 800 and 1200 grit silicon carbide emery paper and finally polished with 6 µm and 1 µm diamond paste in the polishing cloth. After that the samples were etched with 2% nital (2% Nitric acid and 98% Methanol). All the microscopic analyses were carried out using a ZEISS optical microscope.

4.6 Scanning Electron Microscopy

The scanning electron microscope (SEM) is one of the most versatile instruments for examination and analysis of the microstructural characteristics of materials. The primary reason for the SEM's usefulness is the high resolution; values to the tune of 5 nm are usually quoted for commercial instrument. The investigation of surface relief or topog-

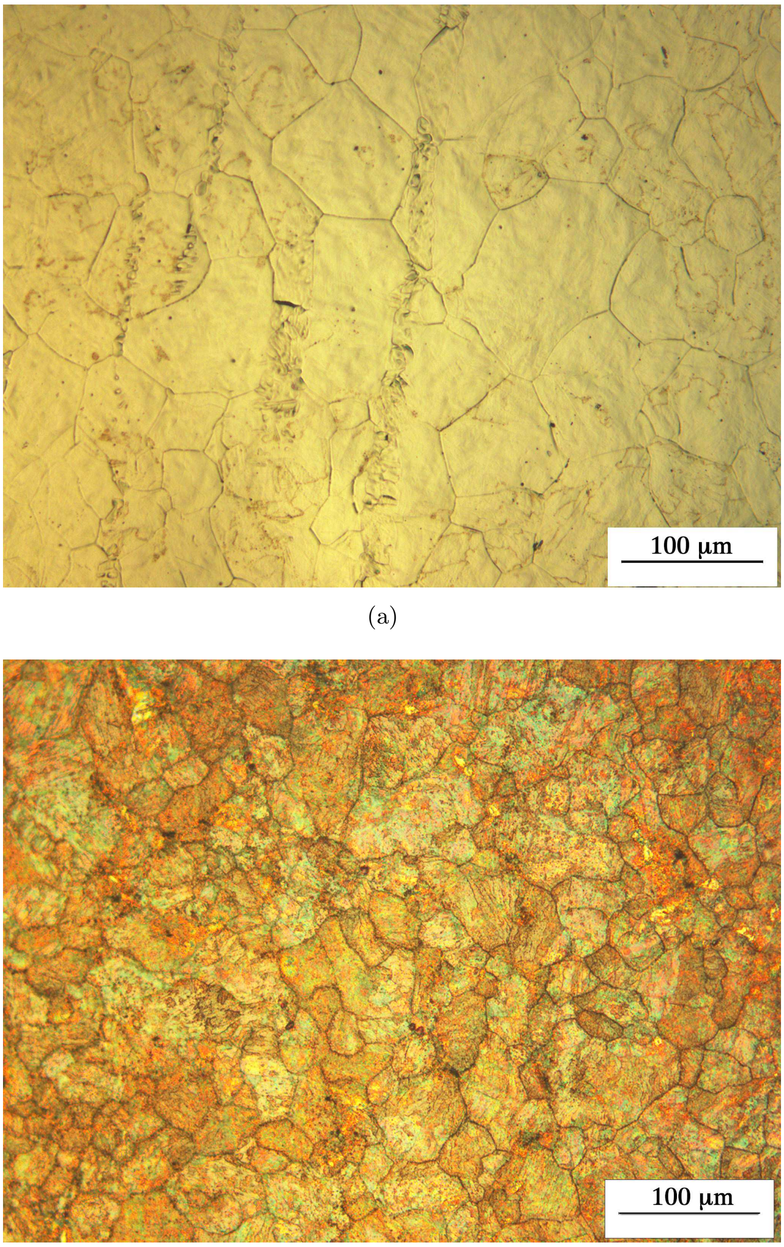

(a)

(b)

Figure 4.3: Prior austenite grain boundaries visible after thermal etching for (a) the Fe-Mn-Si steel and (b) the Fe-Ni-Si steel.

raphy is the most common application of SEM for materials. It is the high depth of field of the SEM that makes it so valuable for topographic studies. Another reason behind the wide applicability of SEM is the rich variety of interactions which the electron beam undergo within the specimen. The same specimens after observing in an optical microscope were used for scanning electron microscopy to explore more detailed features of the microstructure. High resolution scanning electron microscopy was carried out using a JEOL 6340F which has cold-tip field emission gun (FEGSEM).

4.7 Dilatometric Analysis

Dilatometry is useful in the study of steels, because it permits the real time monitoring of the evolution of transformations in terms of dimensional changes. When a material undergoes a phase change, the lattice changes and this is, in principle, accompanied by a change in a specific volume. All the dilatometric measurements were carried out in *Thermecmaster* thermomechanical simulator. The resolution of this instrument is $5\,\mu m$.

4.8 X–Ray Diffraction

X-rays are electromagnetic radiation of wavelength about 1 Å, which is about the same size as an atom. The discovery of X-rays in 1895 enabled scientists to probe crystalline structure at the atomic level. X-ray diffraction has been in use in two main areas, for the fingerprint characterization of crystalline materials and the determination of their structure. Each crystalline solid has its unique characteristic X-ray powder pattern which may be used as a 'fingerprint' for its identification. Once the material has been identified, X-ray crystallography may be used to determine its structure. X-ray diffraction is one of the most important characterization tools used in solid state chemistry and materials science. Using X-ray diffraction it is also possible to determine the size and shape of the unit cell for any compound.

4.8.1 Common Errors in Diffraction Analysis

- Instrument misalignment
- Specimen displacement
- Zero-shift

- Flat specimen
- Transparency

Amongst these, the specimen displacement and zero-shift errors are the most serious in lattice parameter determination. Figure 4.4 shows the magnitudes of the variety of common errors in counter diffractometry [134]. The specimen displacement error is a major source of error in diffraction data.

Specimen displacement error

Specimen-surface displacement from the goniometer axis of rotation causes peak shifts. A shift towards higher 2θ occurs if the specimen is within the focusing circle and *vice versa* [135]. The shift of peak's centre of gravity is given by [135]:

$$\Delta 2\theta = 2S\cos\theta / R_g \tag{4.1}$$

where $\Delta 2\theta$ is the peak shift in radians, S is the specimen displacement relative to the goniometer axis and R_g is the radius of the goniometer. It is difficult to measure the displacement, S, experimentally, so other means must be considered to correct the corresponding error.

Zero-shift error

Zero-shift or zero-angle calibration error can to a large extent be avoided via adjustment and calibration of the diffractometer. However, it cannot be eliminated completely due to inevitable inaccuracies in the diffractometer's mechanical movement [136].

Cohen's method

Systematic and random errors causing peak shifts were corrected using the least-squares method proposed by Cohen [137], implemented in the commercial software PHILIPS X'Pert HighScore Plus which uses the Rietveld method for crystal structure refinement.

The basic principle in Cohen's method is that if the errors, which depend on the Bragg angle, can be expressed in the form of a mathematical function, the combined systematic and random errors can be eliminated from the data using the linear least-squares method. The method has an advantage that it is also applicable to non-cubic crystal systems [138].

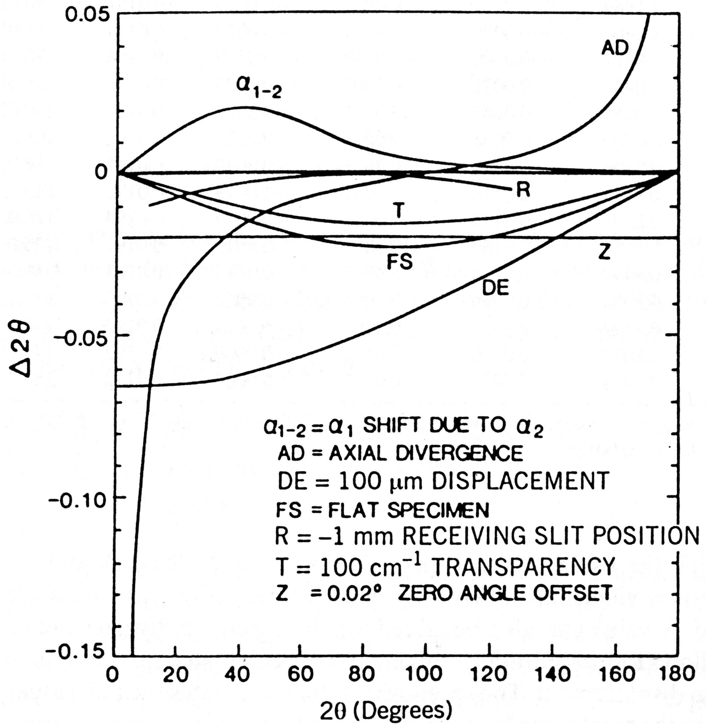

Figure 4.4: Common sources of peak shifts in X-ray diffraction. The flat specimen error was assessed by constantly illuminating 13 mm of the specimen length [134].

The quantities used in the least-squares refinement are:

$$Q_i = \frac{1}{d_i^2} = 4\left(\frac{\sin\theta_i}{\lambda}\right)^2 \tag{4.2}$$

where d_i is the interplanar spacing of the ith reflection, θ_i is its Bragg angle and λ is the wavelength.
Q_i can be written as a polynomial expression:

$$Q_i = \sum_{j=1}^{m_u} a_{ij}x_j \tag{4.3}$$

where a_{ij} is the jth term coefficient, x_j is an unknown parameter and m_u is the number of unknown cell parameters.

In a general case such as the triclinic system, for a reflection i with Miller indices hkl, a_{ij} may be written as:

$$a_{i1} = h^2, a_{i2} = k^2, a_{i3} = l^2, a_{i4} = 2kl, a_{i5} = 2lh, a_{i6} = 2hk \tag{4.4}$$

and the unknown parameter, in reciprocal-lattice coordinates, can be expressed as:

$$x_1 = a^{*^2}, x_2 = b^{*^2}, x_3 = c^{*^2}, x_4 = b^*c^*\cos\alpha^*, x_5 = c^*a^*\cos\beta^*, x_6 = a^*b^*\cos\gamma^* \tag{4.5}$$

where a^*, b^*, c^*, α^*, β^* and γ^* are the reciprocal-lattice constants.
It follows that, the minimisation function can be given as:

$$\Delta = \sum_{i}^{N} w_i[d^*(\text{observed})_i^2 - d^*(\text{calculated})_i^2]^2 \tag{4.6}$$

where N is the number of reflection lines, w_i is the weight assigned to each reflection line, $d^*(\text{observed})_i$ and $d^*(\text{calculated})_i$ are the observed and calculated interplanar spacings respectively. The scheme used herein was to assign the same weight for all observed reflections.

4.8.2 Rietveld Refinement

A crystallographic information file (CIF) contains information about approximate phase lattice parameter, space group, site occupation factor (taken as 1 for the iron atom in both α_b and γ) and parameters regarding the thermal displacements of atoms. Such a file, containing approximate lattice parameters of both crystal structures (α_b,γ), is compared with the observed reflections. Using Equation 4.6, new cell parameters are calculated from the new d$_i$ values of the observed reflection lines. This process is then repeated until there is no increase in the Figure of merit [139]:

$$F_N = \frac{1}{\overline{|\Delta 2\theta|}} \frac{N}{N_{\text{poss}}} \tag{4.7}$$

where $\overline{|\Delta 2\theta|}$ is the mean absolute difference between observed and calculated Bragg angles, N is the number of observed lines and N_{poss} is the number of possible reflection lines.

The analysis includes the following refinable parameters: (a) background; (b) scale factors; (c) zero-shift error; (d) lattice parameters; (e) profile parameters. u, v and w are peak width parameters and are related with full width at half maximum (FWHM) by $\text{FWHM}^2 = u\tan^2\theta + v\tan\theta + w$, only u and w are refined. The value of u is typically associated with strain broadening. No profile parameter are allowed to have a negative magnitude; (f) peak shape parameters. A single peak shape parameter was refined per phase. Peak width analysis for determining crystallite sizes and lattice effective micro strains is not performed using the Rietveld method; (g) asymmetry parameter was refined in some cases where peaks exhibited prominent asymmetry; and (h) preferred orientation parameters.

The refinement procedure has been carried out in a sequential manner to avoid trapping in a false minimum.

Mathematics and procedures

The diffraction pattern is collected as a numerical intensity value, y_i, at each of several thousand equal increments (steps), i, in the pattern. Depending on the method, the increments may be either in scattering angle, 2θ, or some energy parameter such as velocity (for time-of-flight neutron data) or wavelength (for X-ray data collected with an energy dispersive detector and an incident beam of 'white' radiation). For constant wavelength data, the increments are usually steps in scattering angle and the intensity, y_i, at each step, i, in the pattern is measured directly with a quantum detector on a diffractometer.

The best fit designates the best least-squares fit to all of y_i simultaneously and is carried out by minimisation of the residual, S_y [140].

$$S_y = \sum_i w_i (y_i - y_{ci})^2 \tag{4.8}$$

where w_i equals $1/y_i$, y_i is the total observed intensity at step i and y_{ci} is the calculated intensity at step i. This minimization process is performed over the entire scanned 2θ range simultaneously. The calculated intensities y_{ci} are determined from the $|F_K|^2$ values calculated from the structural model by summing of the calculated contributions from neighbouring (i.e. within a specified range) Bragg reflections in addition to the background. y_{ci} can be written as:

$$y_{ci} = s \sum_K L_K |F_K|^2 \phi_l (2\theta_i - 2\theta_K) P_K A + y_{bi} \tag{4.9}$$

where s is the scale factor, K represents the Miller indices (hkl) of a Bragg reflection, L_K is a factor which contains Lorentz-polarisation and multiplicity factors, ϕ_l is the function which represents the reflection-line profile, P_K is the preferred orientation function, A is the absorption factor and y_{bi} is the background intensity at step i.

Estimates of uncertainty

It has been established [140] that each parameter that is estimated reduces the sum of Figure 4.8 to 1, so that the sum of the n terms is n, each of which is the weighted square of the difference between an observed and an estimated model with p parameters, the weighted sum of squared residuals, is $n - p$. The weighted pattern R index, R_{wp}, is defined by [140]

$$R_{wp} = \left\{ \sum_{i=1}^{n} w_i [y_i - y_{ci}]^2 / \sum_{i=1}^{n} w_i {y_i}^2 \right\}^{1/2} \tag{4.10}$$

The numerator of the expression inside the braces is the sum of squared residuals and thus has expected value $n-p$. The expected R index, R_e, is accordingly defined as

$$R_e = \left\{(n-p)/\sum_{i=1}^{n} w_i {y_i}^2\right\}^{1/2} \tag{4.11}$$

The ratio of R_{wp}/R_e, sometimes referred to as the 'χ factor' (also called as the "goodness of fit", is a measure of how well the fitted model accounts for the data).

Quantitative phase analysis

Quantitative phase analysis can be carried out on a multi phase system using the method described by Hill and Howard [141]. According to this method, the weight of a phase in a mixture is proportional to the product of the scale factor, as derived by Rietveld analysis of the powder diffraction pattern, with mass and volume of the unit cell. Considering all the phases are identified and crystalline, the weight fraction, W_p, of phase, p, can be expressed by:

$$W_p = \frac{(SZMV)_p}{\sum_i (SZMV)_i} \tag{4.12}$$

where S, Z, M and V are the Rietveld scale factor, the number of formula unit per unit cell, the mass of the formula unit and the unit cell volume. i is an index for all the phases. Subsequently, the volume fraction of the individual phases, V_p, can also be derived using

$$V_p = \frac{(SV^2)_p}{\sum_i (SV^2)_i} \tag{4.13}$$

4.8.3 Experimental Details

X–ray diffraction tests were carried out using a Philips vertical diffractometer with unfiltered CuK$_\alpha$ radiation, and the instrument operated at 40 kV and 40 mA. A continuous scanning mode was chosen with the rate of 0.05° s^{-1} over the angular width of $2\theta =$ 30-150° with a collecting time of 16.65 s at each step. A secondary monochromator in the form of curved graphite was used to eliminate CuK$_\beta$ radiation. A divergent slit of

1° and a receiving slit of 0.2 mm were used. To identify the presence of carbides, low angle scanning was carried out where step scanning mode was chosen over an angular width of $2\theta = 36\text{-}52°$ with collecting time of 80 s at each step.

Four discs, each with a diameter of 8 mm, were sliced from the specimen after the heat treatments. Each sample was polished using the standard metallographic techniques and was etched with 2% nital and were used for X–ray analysis. Peak positions and phases were identified using X'Pert HighScore Plus® software. The fraction of retained austenite was evaluated using Rietveld refinement [140, 142].

4.8.4 Extraction of Precipitates

As the precipitates contribute only ∼1% of the volume of the sample, so X–ray diffraction on a bulk specimen is unlikely to provide accurate information about precipitates. A method commonly used to avoid this difficulty involves dissolution of the matrix, leaving residues which can be analysed by X–ray diffraction. Before extraction of the precipitates, the samples were cleaned using HCl acid and then washed with methanol. Specimens of 0.2 ∼ 0.3 gm were dissolved in a solution of 5% nital in about 3 months. The residues were filtered using a 0.1 μm membrane filter to extract the precipitates. To make the process faster, the filtration was done by suction with a vacuum pump. The filter was then allowed to dry for one day, and then placed in a X–ray diffractometer. Identification of the different phases was often made difficult because of overlapping peaks. An analysis was carried out to remove any peaks arising from the filter itself. This technique is useful when used in conjunction with other identification methods. The main advantages are that it should reveal all the precipitates present, the amount of materials investigated at once is far more than with most of the other methods (SEM, TEM etc.) and it can give, in principle, quantitative information. It is relatively easy to implement when compared to methods such as TEM for which the sample preparation can be much more time consuming. The disadvantages are that no information is obtained about the morphology, distribution or location of the precipitates. In practice, quantitative information can only be obtained from TEM regarding the finer precipitates of size less than 200 nm.

4.9 Electron Backscattered Diffraction Pattern

Orientation imaging of grains was carried out using the electron backscattered diffraction (EBSD) technique. EBSD technique works by positioning a beam of electrons on selected sampling points on the specimen surface. The resulting diffraction pattern provides crystallographic information which can be related back to its position of origin on the specimen. The most important application of EBSD is to generate an orientation map, which is a quantitative description of the microstructure of a region in terms of its orientation constituents. The diffraction lines obtained on a phosphor screen are characteristic of the grain orientation. The EBSD attachment is mounted on a CamScan MX2600 scanning electron microscope equipped with a field emission gun and operated at 25 kV. The specimen tilt was 70° during the measurements. Metallographic specimens were prepared in the usual way by grinding, polishing and etching (using 2% nital). Orientation imaging is sensitive to sample preparation and surface profile, so the metallographic samples were further polished using 0.25 μm colloidal silica. Measurement of EBSD was carried out for the isothermally transformed materials for both alloys and some specimens after tempering treatments.

4.10 Transmission Electron Microscopy

Transmission electron microscopy was carried out on thin foils and carbon replicas. The specimens for *in situ* TEM observation are originally from the isothermally transformed materials in a *Thermecmaster*, in the form of discs. After being mechanically cut into circular foils with 3 mm diameter and 40 μm thickness, the specimens were electro-polished by a twin-jet electro-polisher in a solution of 70% ethanol, 25% glycerol and 5% perchloric acid. The voltage and current settings for the twin jet polishing were 15 V and 10 mA respectively. Room temperature TEM was carried out in a JEOL 2000FX (200 kV) instrument. In the case of the *in situ* studies, specimens were heated up to the tempering temperature and held for different times to observe the change in the structure and then cooled to room temperature. For the *in situ* observations, a JEOL 200CX with an in-built hot stage was used.

4.10.1 Selected Area Diffraction Pattern (SADP)

One major advantage of TEM is that it is possible to take selected area electron diffraction patterns from a small chosen area of the thin foil in TEM. To obtain this, the selected area in the bright field or dark field image is brought to the centre of the screen and an intermediate aperture is inserted. The intermediate lens is then made to focus on the back focal plane of the objective lens to get the diffraction pattern, which can be seen by removing the objective aperture. Figure 4.5 shows the ray diagram for the formation of images and diffraction patterns in a TEM. An area of the order of 0.1-1 μm^2 across is selected by a diaphragm in the first intermediate image. The cone of diffracted electrons with an aperture of the order of a few tens of micro-radians can pass through the small polepiece bores of the final lenses only if the back focal plane of the objective lens that contains the first diffraction pattern is focused on the screen.

4.10.2 Camera Length

Figure 4.6 shows schematically the formation of a diffraction pattern from a thin foil specimen (without showing the lenses) in a TEM. The transmitted beam travels straight from its path whilst the diffracted beam is deflected by an angle 2θ from the principal axis (i.e. from the transmitted bream) of the lens. The distance between the transmitted spot and diffracted spot from *hkl* plane as measured on the screen is R_{hkl}. The distance from the specimen to the screen (it is the calculated value considering the magnification of various lenses, rather than the physical distance and can be altered by the operator) is commonly known as camera length (L).

Since θ is very small in electron diffraction (a small fraction of a degree), it may be assumed that

$$\tan 2\theta \cong \sin 2\theta = 2\sin\theta = D/L \tag{4.14}$$

From Bragg's equation,

$$2\sin\theta = \lambda/d_{hkl} \tag{4.15}$$

The above equations can be combined to give

$$\lambda/d_{hkl} = R_{hkl}/L \tag{4.16}$$

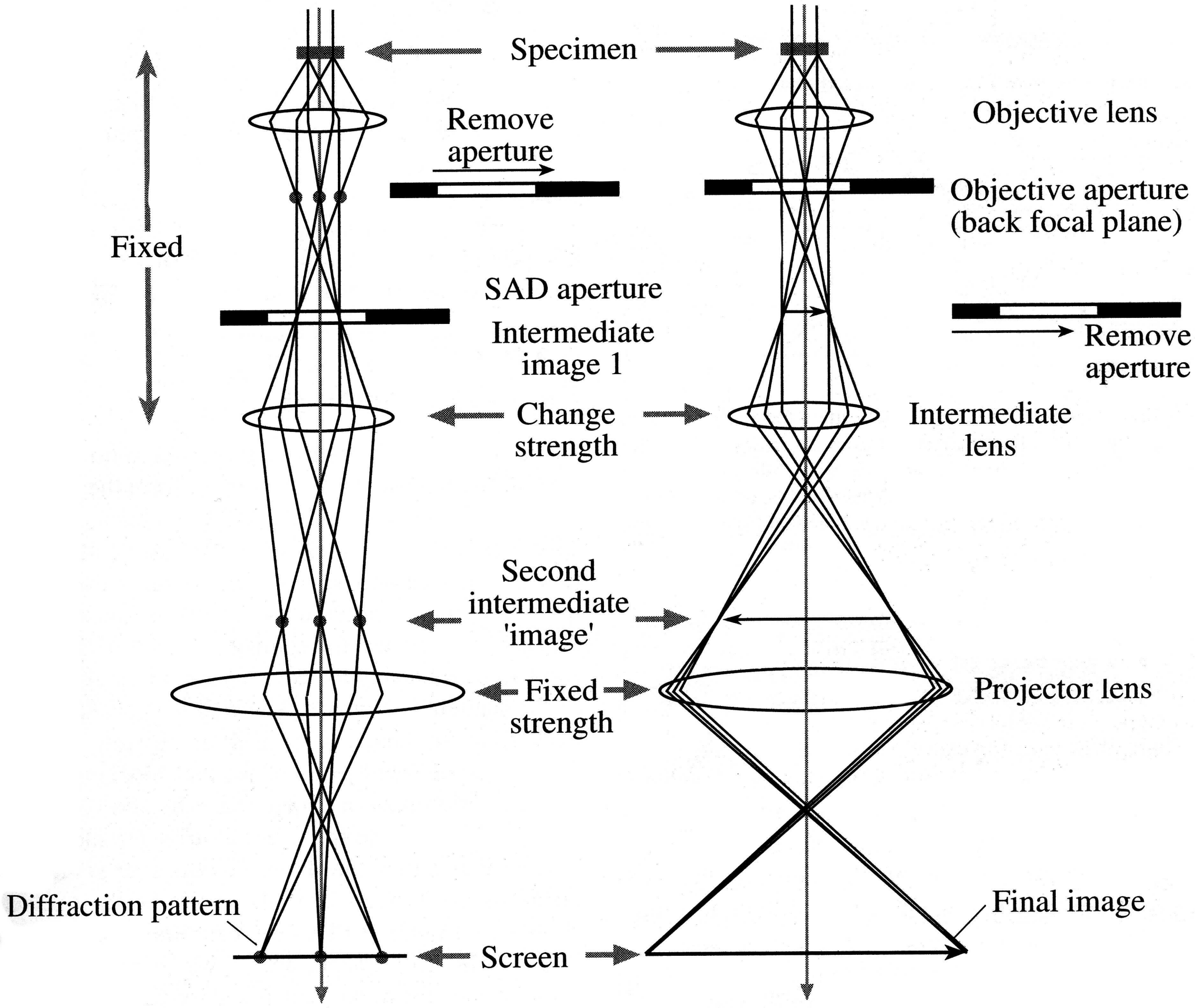

Figure 4.5: The basic operations of the TEM imaging system involve (a) projecting the diffraction pattern on the viewing screen and (b) projecting the image onto the screen [143].

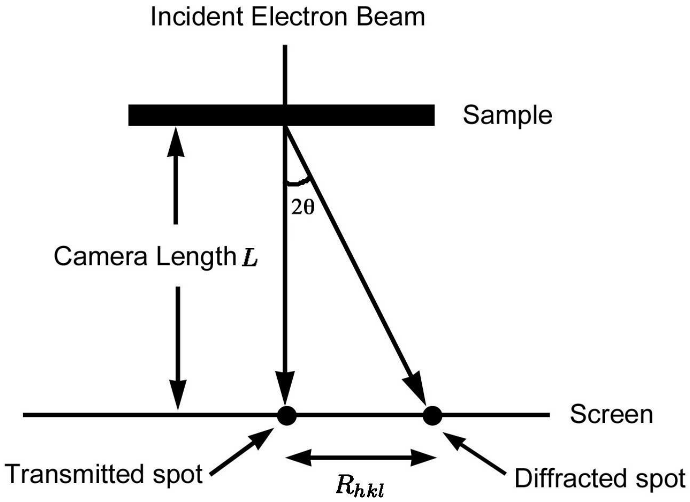

Figure 4.6: Schematic diagram of the geometry of diffraction in transmission electron microscopy. L, R_{hkl} and θ are the camera length, distance between the transmitted spot and the diffracted spot in the diffraction pattern and Bragg angle respectively.

or

$$\lambda L = d_{hkl} R_{hkl} \tag{4.17}$$

where d_{hkl} is the spacing of hkl planes. This term λL is the camera constant and is used as a calibration parameter in solving diffraction pattens. Once $d_{hkl}R_{hkl}$ is known, d_{hkl} value for any other R_{hkl} can be obtained. The wavelength, λ, is given by

$$\lambda = \frac{h}{\left[2m_e eV\left(1+\frac{eV}{2m_e c^2}\right)\right]^{1/2}} \tag{4.18}$$

where V is the accelerating voltage, c is the speed of light in vacuum, h is Planck's constant, e is the charge of the electron and m_e is the electron mass.

4.10.3 Carbon Replica Technique

For some samples, the carbon replica technique was used to characterize the precipitates. This technique has number of advantages over thin foil samples. The size and chemical composition of the carbides may be measured more accurately by eliminating the effect of the matrix. Working with a magnetic specimen in the electron beam may cause difficulties, which can be avoided. The samples for this technique were polished mechanically by the same method as for optical microscopy and chemically etched with 5% nital for a few seconds. A carbon coating of 20 ~ 30 nm (brown gold colour) was deposited in a vacuum of 10^5 torr onto the etched surface. This film was then scored with a blade to divide it into several smaller squares (about 1 mm^2). To strip off the carbon film, the sample was submerged in 10% nital for 5 min. The film was then rinsed with methanol and floated off in distilled water. Each sample yielded a few small squares of film which were mounted on copper grids and dried before examination in the TEM. Figure 4.7 shows a schematic drawing of the sample preparation procedures.

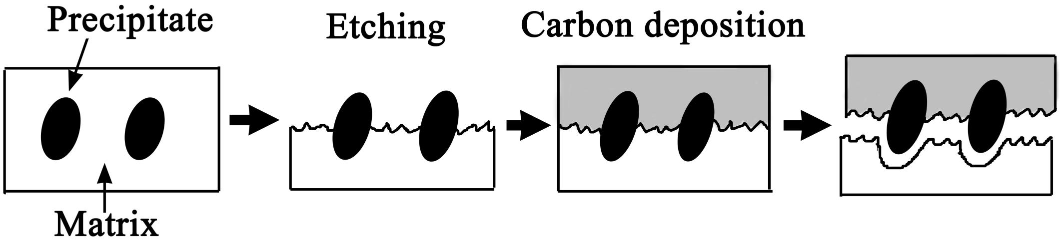

Figure 4.7: Schematic drawing of carbon replica extraction technique

Chapter 5

Thermal Stability of Retained Austenite

5.1 Introduction

It is known that in a tensile test, the onset of plastic instability can be delayed by the presence of austenite which gradually undergoes martensitic transformation during the course of elongation. The resulting transformation–induced plasticity is known as the TRIP effect [70, 144]. A cheap way of introducing austenite in the microstructure is by preventing the precipitation of iron carbides during the bainite transformation [26, 27]. The carbon that is partitioned from bainitic ferrite then stabilises the residual austenite. Silicon and aluminium additions can achieve this by affecting the chemical driving force for the precipitation of cementite from austenite [59]. Many commercially successful steel concepts have been developed based on such mixed microstructures of bainitic ferrite and carbon–enriched retained austenite, reviewed in [4, 145–148].

Steels with a microstructure consisting of a mixture of bainitic ferrite and carbon–enriched retained austenite are of interest in a variety of commercial applications because they have been shown to exhibit good combinations of strength, toughness and ductility. However, their use at temperatures moderately above ambient requires a knowledge of the thermal stability of the austenite. The microstructure consisting of bainitic ferrite and carbon–enriched retained austenite is not thermodynamically stable because the reaction stops when the latter phase reaches approximately a composition defined by the T_0 curve of the phase diagram, rather than when the much greater equilibrium concentration consistent with the Ae_3 curve is achieved [147, 149]. The T_0' curve accounts also for strain energy but the average carbon concentration at which the bainite reaction stops in the absence of carbide precipitation usually lies somewhere between T_0 and T_0' given the heterogeneous distribution of carbon in the austenite. A computer program and its associated documentation, for the calculation of such curves can be obtained from [150]. Given sufficient time at a high enough temperature, the retained austenite should therefore decompose into a mixture of ferrite and carbides. In this chapter, a detailed examination of the thermal stability of the microstructure given that many of the steels being developed either have to undergo transients into high temperature regimes (for example during galvanising) or have to serve at moderately high temperatures over long periods of time.

It is acknowledged that previous studies [151–153] investigated the stability of the retained austenite and bainite mixtures, but these were conducted as continuous heating experiments, did not consider the dilatometric effect of the tempering of martensite present in the initial microstructure, and did not consider the stability of the remaining austenite on cooling to ambient temperature.

5.2 Experimental Procedure

An Fe–0.22C–3Mn–2.03Si wt% alloy was prepared as a 20 kg vacuum induction melt from high purity base materials. The advantage of using this alloy is that a great deal is known about its transformation into a mixture of bainitic ferrite and retained austenite, including the T_0 curve and its validation [7, 85]. The ingot was hot–forged and then hot–rolled to 25 mm square cross section bars. All the heat treatments were carried out in a *Thermecmaster* thermomechanical simulator as described in Chapter 4.

Austenitisation was carried out by heating the sample at 10°C s^{-1} to 930°C, where it was held for 30 min under vacuum. Samples were then cooled to 390°C at 10°C s^{-1} using a jet of helium gas, for isothermal transformation to bainite for two hours in order to allow the maximum quantity of bainite consistent with the T_0 curve to form. The heat treatment schedule is illustrated schematically in Fig 4.2a.

The tempering temperature studied was 450°C, which is higher than the B_S, with the tempering time ranging from $\frac{1}{2}$ to 5 h. One sample was water quenched after austenitisation to establish the dimensional changes during subsequent tempering; this experiment helps to distinguish between the changes that accompany the decomposition of austenite.

Specimens for optical microscopy and transmission electron microscopy (TEM, JEOL 2000FX, 200 kV) were prepared using standard methods described in Chapter 4. X–ray diffraction with Cu K_α radiation was conducted using continuous scanning at $0.05^\circ\,\mathrm{s}^{-1}$ over $2\theta = 30 - 150^\circ$. The volume fraction of retained austenite was determined using Rietveld refinement [140, 142, 154, 155]. Specific step–scans over $2\theta = 36 - 52^\circ$ were carried out to characterise diffraction from the low–volume fractions of carbides expected on prolonged tempering.

5.3 Transformation Strain

Assuming that phase changes in polycrystalline samples cause isotropic strains on a macroscopic scale, the linear and volume strains are related as follows:

$$\frac{\Delta L}{L_0} = \frac{\Delta V}{3V_0} \tag{5.1}$$

where the subscript identifies the original dimensions. For austenite (γ) decomposing into a mixture of ferrite (α) and cementite (θ),

$$\frac{\Delta L}{L_0} = \frac{1}{3}\left[\frac{(2V_\alpha a_\alpha^3 + \frac{1}{3}V_\theta a_\theta b_\theta c_\theta) - V_{\gamma_0} a_{\gamma_0}^3}{V_{\gamma_0} a_{\gamma_0}^3}\right] \tag{5.2}$$

where V_{γ_0} is the initial volume fraction of austenite measured using X–ray diffraction; V_α and V_θ are the volume fractions of ferrite and cementite respectively. a_θ, b_θ and c_θ, a_α and a_γ are lattice parameters of the phases identified by the subscript, at the test temperature, calculated by correcting the values at room temperature with the appropriate expansion coefficient [156–158] (temperature in Kelvin):

$$\begin{aligned}
a_\theta &= 4.5165[1 + \{6.0 \times 10^{-6} + 3.0 \times 10^{-9}(T - 273) + \\
&\quad 1.0 \times 10^{-11}(T - 273)^2\}(T - 298)] \quad \text{Å} \\
b_\theta &= 5.0837[1 + \{6.0 \times 10^{-6} + 3.0 \times 10^{-9}(T - 273) + \\
&\quad 1.0 \times 10^{-11}(T - 273)^2\}(T - 298)] \quad \text{Å} \\
c_\theta &= 6.7475[1 + \{6.0 \times 10^{-6} + 3.0 \times 10^{-9}(T - 273) + \\
&\quad 1.0 \times 10^{-11}(T - 273)^2\}(T - 298)] \quad \text{Å}
\end{aligned} \tag{5.3}$$

$$\begin{aligned}
a_\alpha &= 2.8664 + \frac{(a_{Fe} - 0.279x_{\mathrm{C}})^2(a_{\mathrm{Fe}} + 2.496x_{\mathrm{C}}) - a_{\mathrm{Fe}}^3}{3a_{\mathrm{Fe}}^2} - 0.03x_{\mathrm{Si}} + \\
&\quad 0.06x_{\mathrm{Mn}} + 0.07x_{\mathrm{Ni}} + 0.31x_{\mathrm{Mo}} + 0.05x_{\mathrm{Cr}} + 0.096x_{\mathrm{V}} \quad \text{Å}
\end{aligned} \tag{5.4}$$

$$\begin{aligned} a_\gamma &= 3.5780 + 0.033w_{\mathrm{C}} + 0.00095w_{\mathrm{Mn}} - 0.0002w_{\mathrm{Ni}} + 0.0006w_{\mathrm{Cr}} + \\ &\quad 0.0056w_{\mathrm{Al}} + 0.0031w_{\mathrm{Mo}} + 0.0018w_{\mathrm{V}} \qquad \text{Å} \end{aligned} \tag{5.5}$$

The carbon concentration of the ferrite is assumed to be 0.025 wt%; x is the concentration in mole fraction and w in weight fraction. The thermal expansion coefficients of ferrite and austenite considered in these calculation were $e_\alpha = 1.244 \times 10^{-5}\,\mathrm{K}^{-1}$ and $e_\gamma = 2.065 \times 10^{-5}\,\mathrm{K}^{-1}$ respectively. For martensite, thermal expansion coefficient was same as ferrite.

The strain expected during the tempering of martensite is given by:

$$\frac{\Delta L}{L_0} = \frac{1}{3}\left[\frac{(2V_\alpha a_\alpha^3 + \frac{1}{3}V_\theta a_\theta b_\theta c_\theta) - 2V_{\alpha'} a_{\alpha'}^2 c_{\alpha'}}{2V_{\alpha'} a_{\alpha'}^2 c_{\alpha'}}\right] \tag{5.6}$$

where $V_{\alpha'}$ is the initial volume fraction of martensite and $a_{\alpha'}$ and $c_{\alpha'}$ are lattice parameters of martensite, measured using X–ray diffraction.

5.4 Results

Figure 5.1 shows the bainite sheaves in a matrix of martensite and retained austenite (grey–etching blocks), obtained by isothermal transformation at 390°C for 2 h. Retained austenite is present in silicon-rich bainitic steel in two forms: as thin films between the subunits within a given sheaf of bainite and as coarser blocks between different sheaves of bainite. Both are enriched in carbon but the films contain more carbon because of their isolation between plates of ferrite [42]. The austenite film can be clearly identified from Figure 5.2 after isothermal transformation. From these microstructures it is difficult to distinguish the martensite from the retained austenite, but some martensite must form during cooling from 390°C to room temperature, as is evident from the presence of martensitic twin (Figure 5.3). The amount of austenite remaining at the isothermal transformation temperature can be calculated using the T_0 curve of the phase diagram [42]. The curve determines the limiting concentration of carbon in the austenite at the point where the bainite reaction ceases, so by applying the lever rule to the T_0 curve, the quantity of residual austenite was estimated as $V_\gamma^{390} = 0.32$ for transformation at 390°C. Some of this may decompose to martensite, and this quantity can be estimated by applying the Koistinen and Marburger Equation [159]:

$$1 - V_{\alpha'} = \exp[-0.011(M_S - T_Q)] \tag{5.7}$$

where M_S and $T_Q = 20°\text{C}$ represent the martensite–start and room temperatures respectively. M_S is calculated [131] for the composition of the carbon–enriched austenite left untransformed at 390°C. The fraction of martensite was in this way calculated to be $V_{\alpha'}^{20} = 0.185$, thus leaving a fraction $V_{\gamma}^{20} = 0.135$ of austenite retained to room temperature. The thickness of the bainite plates was measured as described in [133, 160] and found to 300 ± 22 nm.

5.4.1 Microstructural Evolution During Tempering

Tempering at 450°C leads to significant changes in the optical microstructure (Figure 5.4) with the development of dark–etching regions in what was previously the blocky areas in the untempered sample. The dark regions grew in extent as the tempering time was increased. Higher resolution micrographs are presented in Figure 5.5a,b which reveal clearly that the dark regions are tempered martensite. There is, of course the possibility that some features identified as tempered martensite are due to the decomposition of retained austenite by a diffusional mechanism into a mixture of ferrite and carbides, but Figure 5.5c shows an experiment in which tempering was conducted at a temperature of 250°C, which is too low to permit the necessary diffusion. The observed structure in the blocky regions is identical to that of the samples tempered at 450°C, showing that the interpretation related to the tempering of martensite is correct.

Figure 5.6 shows the change in Vickers hardness as a function of the tempering time. The decrease in hardness due to tempering is minimal, about 30 HV over a period of 5 h at 450°C. The extent and rate of change of properties during tempering is expected to be small for bainite because there is little excess carbon in solution in the ferrite. The microstructure in effect tempers during the course of transformation with the partitioning of excess carbon into the residual austenite [6].

5.4.2 Dilatometric Analysis

The metallographic observations already described indicate that the initial changes are due to the tempering of martensite, followed by the decomposition of retained austenite into a mixture of ferrite and cementite. The former process should lead to a contraction as supersaturated martensite precipitates cementite, whereas the latter should be accompanied by an expansion of the sample at constant temperature, Section 5.3, [19]. Figs 5.7a–c show that the net tempering strain is negative for a time up to about 1 hour

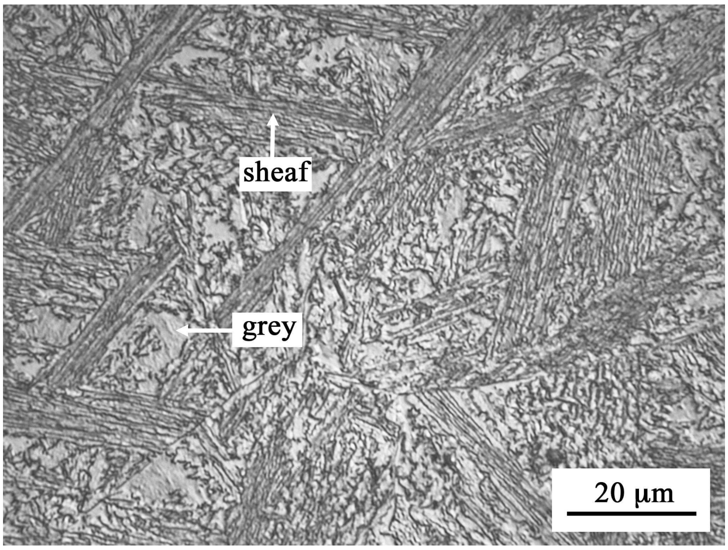

(a)

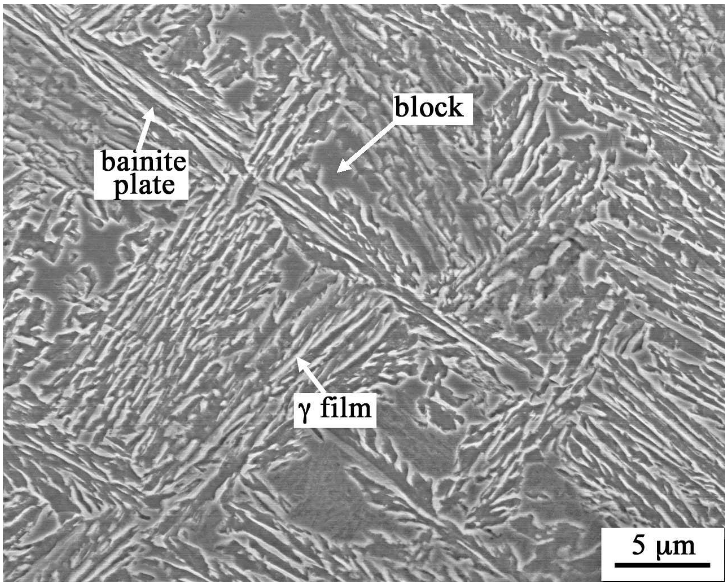

(b)

Figure 5.1: (a) Optical micrograph showing bainite sheaves embedded in a residue of martensite and retained austenite (grey). The steel was transformed isothermally at 390°C for 2 h. Calculations indicate that the volume fractions of bainitic ferrite, retained austenite and martensite are 0.68, 0.135 and 0.185 respectively. (b) Corresponding scanning electron micrograph.

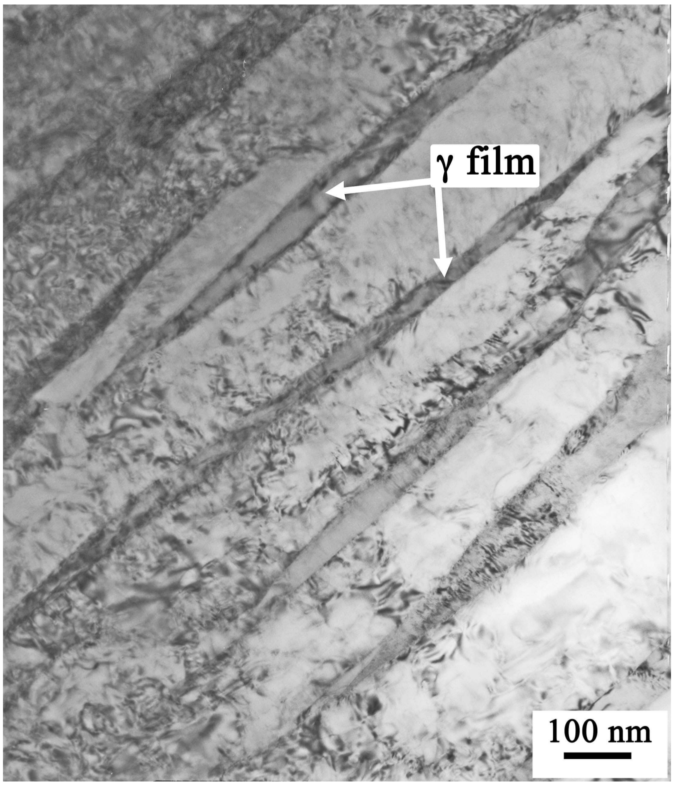

Figure 5.2: Transmission electron micrograph showing austenite film after isothermal transformation.

at temperature 450°C, followed by an increase in specimen dimensions. There was a increase in dimension as tempering progresses.

To further confirm this interpretation, a sample was tempered at 250°C, where austenite decomposition is most unlikely; Figure 5.7d shows that the decrease in strain is comparable to that obtained at the higher tempering temperature, proving that the contraction is due to the tempering of martensite. A sample quenched from the austenitising temperature in order to produce a fully martensitic sample was tempered, Figure 5.7e; a larger contraction consistent with the fact that the starting microstructure is just martensite, was observed, proving the role of martensite tempering in causing a contraction in sample dimensions.

The subsequent expansion seen in Figure 5.7c virtually compensates for the contraction accompanying the tempering of martensite, leaving the sample essentially unchanged in dimensions following prolonged tempering.

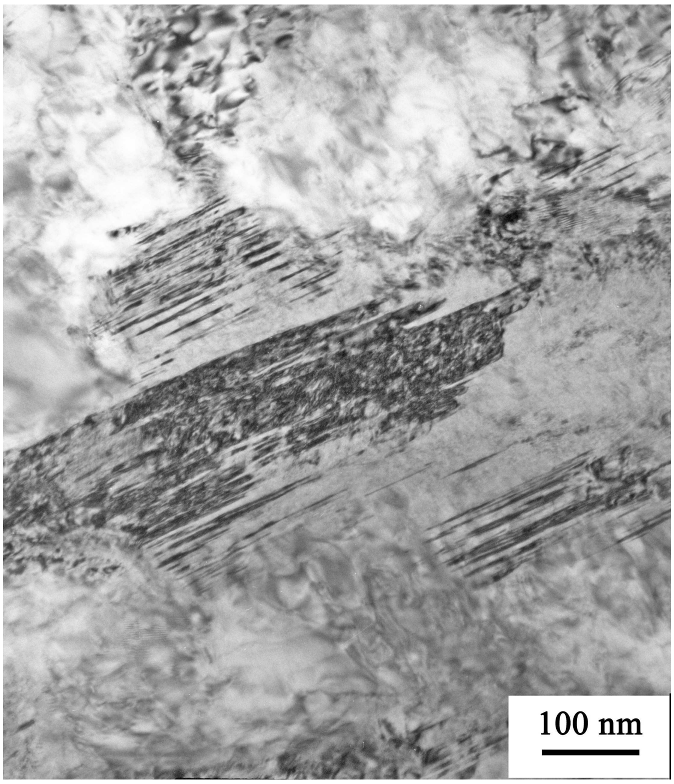

Figure 5.3: Micrograph showing twin structure as an evidence of martensite after isothermal transformation.

The strain for the austenite decomposition calculated using Equation 5.2 decreased as the tempering temperature was raised, as illustrated in Figure 5.8. The measured result (Figure 5.7c) is very much consistent with the calculated result. The strain due to tempering of martensite, calculated using Equation 5.6, taking account of same amount of martensite formed after isothermal transformation and the calculated strain, is close to the experimental result at 250°C, as depicted in Figure 5.7d. In case of fully martensitic sample the calculated strain (Figure 5.8) is slightly deviated from the experimental value (Figure 5.7e) because the calculated strain totally depends on the lattice parameter of martensite.

5.4.3 Quantitative Determination of Phase Fractions

The volume fractions of austenite retained following isothermal transformation and tempering were measured using X–ray diffraction. Figure 5.9 and Table 5.1 show the dra-

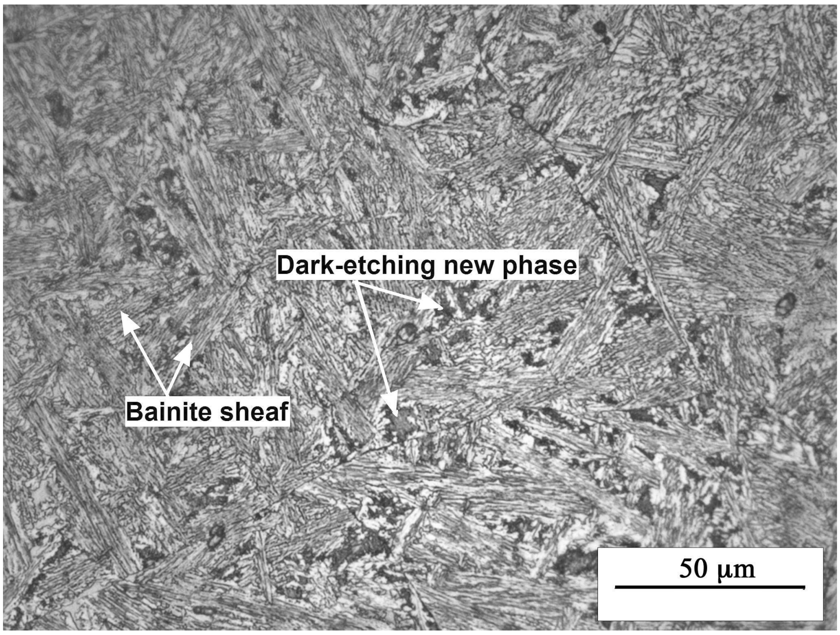
Dark-etching new phase
Bainite sheaf
50 µm

(a)

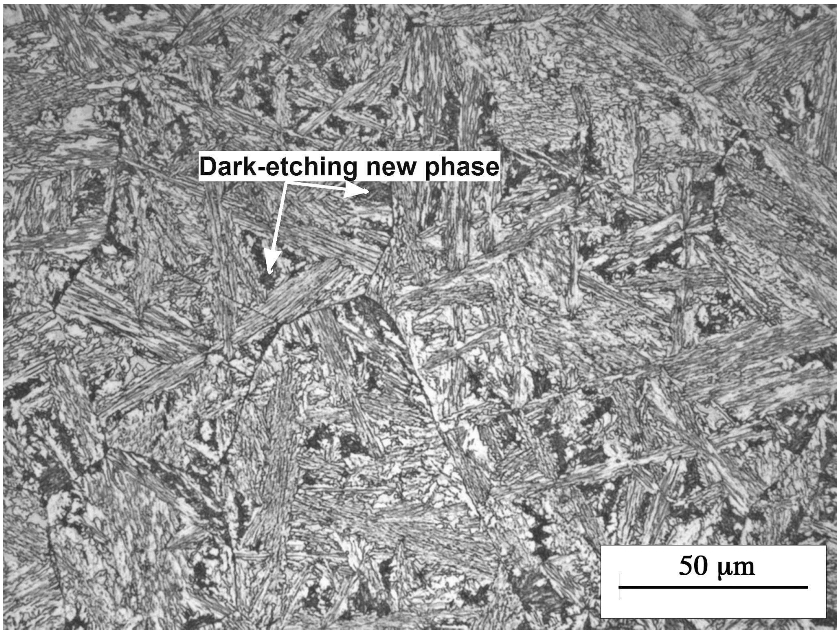
Dark-etching new phase
50 µm

(b)

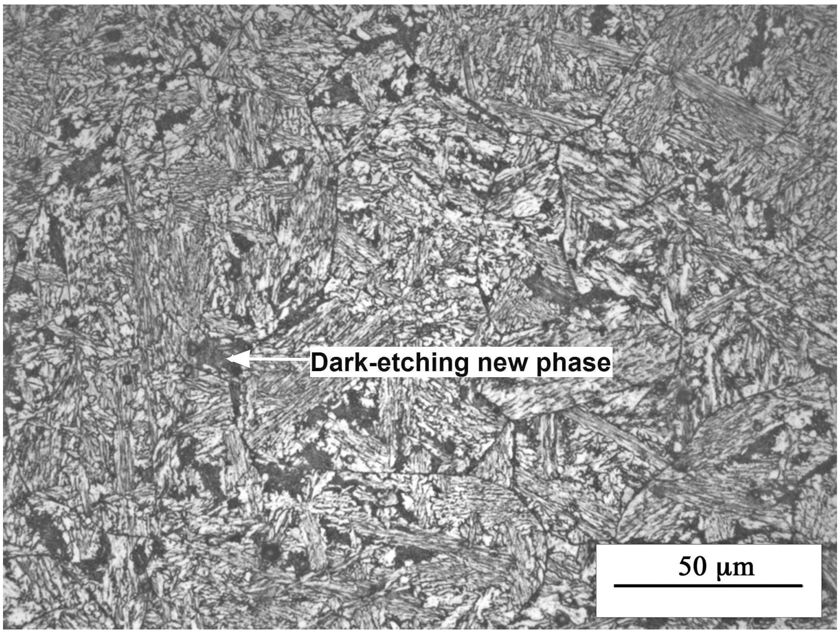

(c)

Figure 5.4: Optical micrographs of sample tempered at 450°C for (a) 30 min, (b) 1 h and (c) 2 h.

matic reduction in retained austenite content even after tempering at 450°C for 30 minutes. In contrast, the tempering at 250°C causes no change in the retained austenite content, Figure 5.10a. Prolonged tempering which leads to the decomposition of austenite confirms the emergence of cementite, Figure 5.10b.

The carbon content of the retained austenite after the isothermal transformation to bainitic ferrite was calculated using the T_0 curve temperature to be 0.7 wt% (Figure 5.11) whereas the carbon content of retained austenite measured from the X-ray diffraction was 0.67±0.1 wt%. The volume fraction of retained austenite calculated using Equation 5.7 was 0.135 and this result is consistent with the measured value from X-ray diffraction (Table 5.1).

The change in the carbon content of the retained austenite during tempering, determined from the measured lattice parameter of retained austenite, is presented in Figure 5.12. The fact that the concentration decreases even on tempering for 30 min implies that carbide precipitation from the austenite is quite rapid. Such carbides can only be detected using transmission electron microscopy, as reported later in this chapter.

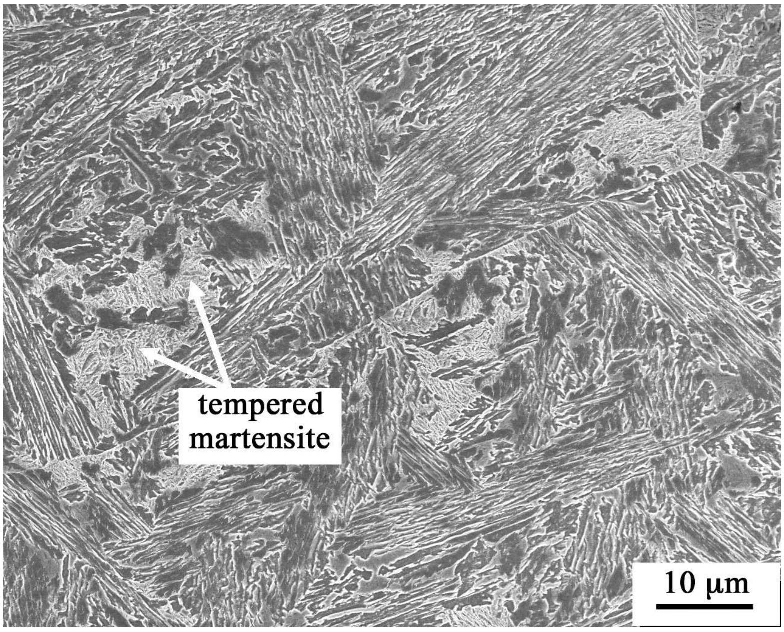

(a)

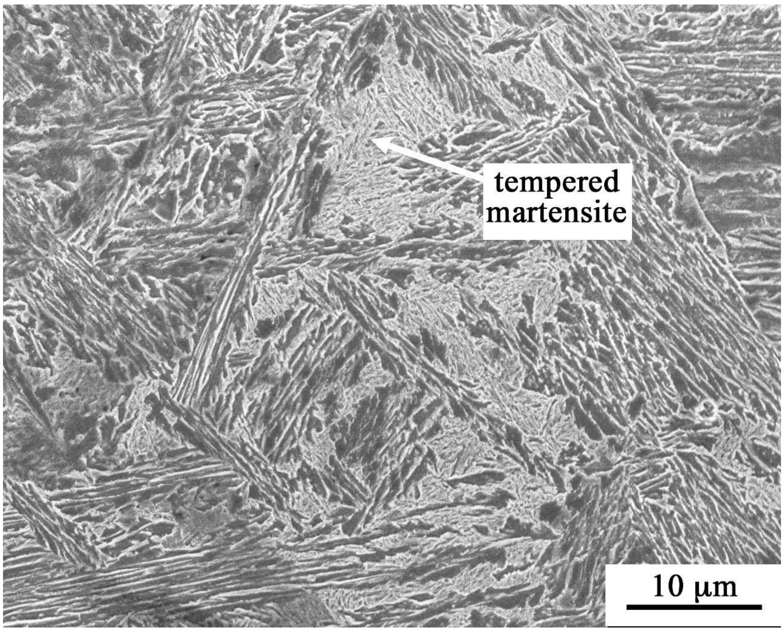

(b)

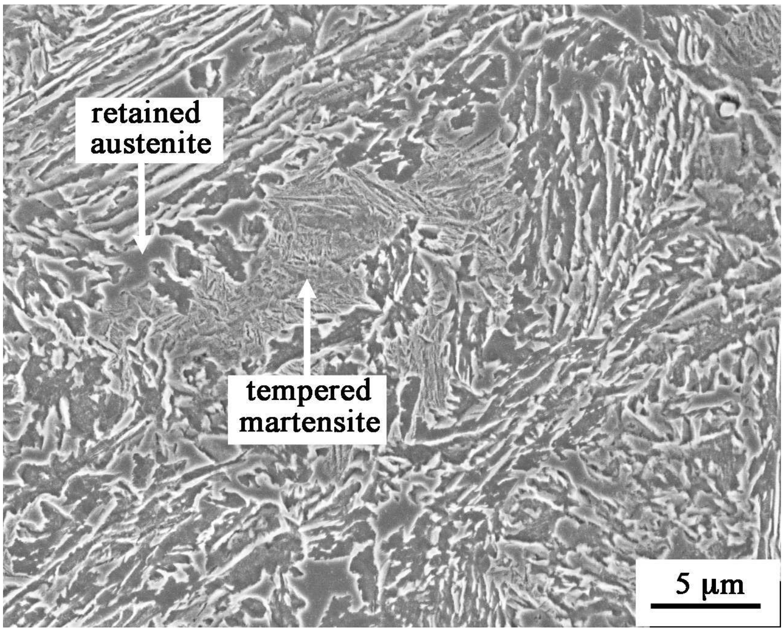

(c)

Figure 5.5: Scanning electron micrographs of samples transformed at 390°C for 2 h, and then tempered at (a) 450°C for 1 h, (b) 450°C for 2 h and (c) 250°C for 5 h.

The lattice parameter of "ferrite" is more difficult to interpret because it reflects that of both martensite and bainitic ferrite, but the trend is consistent with the tempering of martensite. Precipitation of cementite from martensite or bainitic ferrite would lead to a decrease in their lattice parameters; the somewhat slow decrease during tempering at 450°C is a known phenomenon [160] associated with the fact that carbon tends to be trapped at dislocations, where they have a lower energy than in the cementite lattice (Table 5.1) [16].

5.4.4 Transmission Electron Microscopy

Detailed observations revealed that fine carbide particles precipitated at all the time periods studied for tempering at 450°C. Figure 5.13 shows the presence of Morié fringes in the tempered specimen after tempering for 2 h. Morié fringes are produced when two crystals, which have differences in lattice parameter or orientation, overlap. In this case, contrast effects are produced by the carbide and the matrix. Using high resolution TEM, the lattice parameters and lattice plane of the overlapped crystal can be calculated from

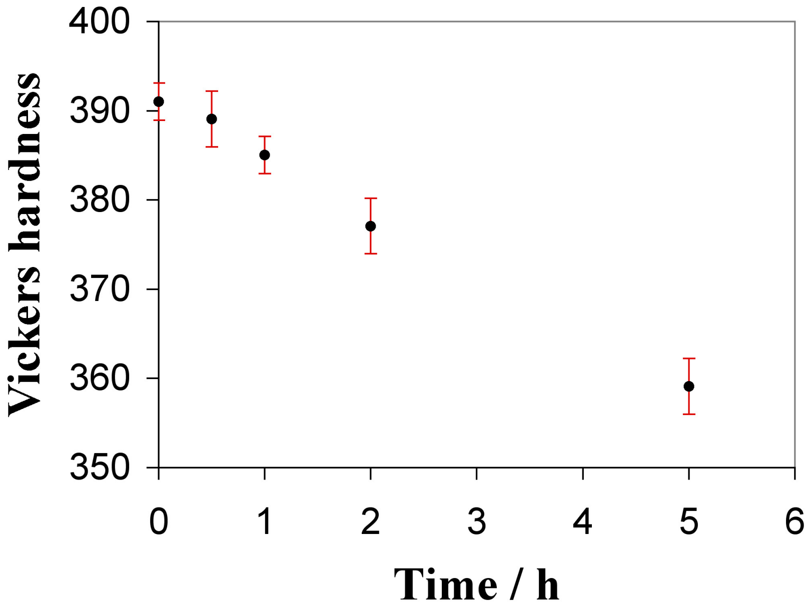

Figure 5.6: Variation of hardness (measured using 30 kg load) with tempering time at 450°C.

the Morié fringes. Intensive electron microscopy studies were carried out in order to identify the type of carbides. Figure 5.14 shows carbide precipitated on the austenite film after tempering for 1 h. The electron diffraction pattern in Figure 5.15, taken from the tempered retained austenite film in a sample after tempering at 450°C for 2 h, reveals the presence of cementite carbide. In both the Figures the carbides have been observed to precipitate at the interface between ferrite and retained austenite.

5.4.5 Stability of Retained Austenite

Transmission electron microscopy of samples which were tempered at 450°C and then cooled to ambient temperature revealed both tempered and untempered martensite, which could be distinguished easily by checking for the presence or absence of cementite precipitation. An example of untempered martensite after tempering for 30 min is shown in Figure 5.16, illustrating the twinned martensite typical of transformation from high–carbon austenite [15]. Further evidence of martensitic twins after tempering for 1 h is illustrated in Figure 5.17. It is evident that tempering destabilises the austenite due to

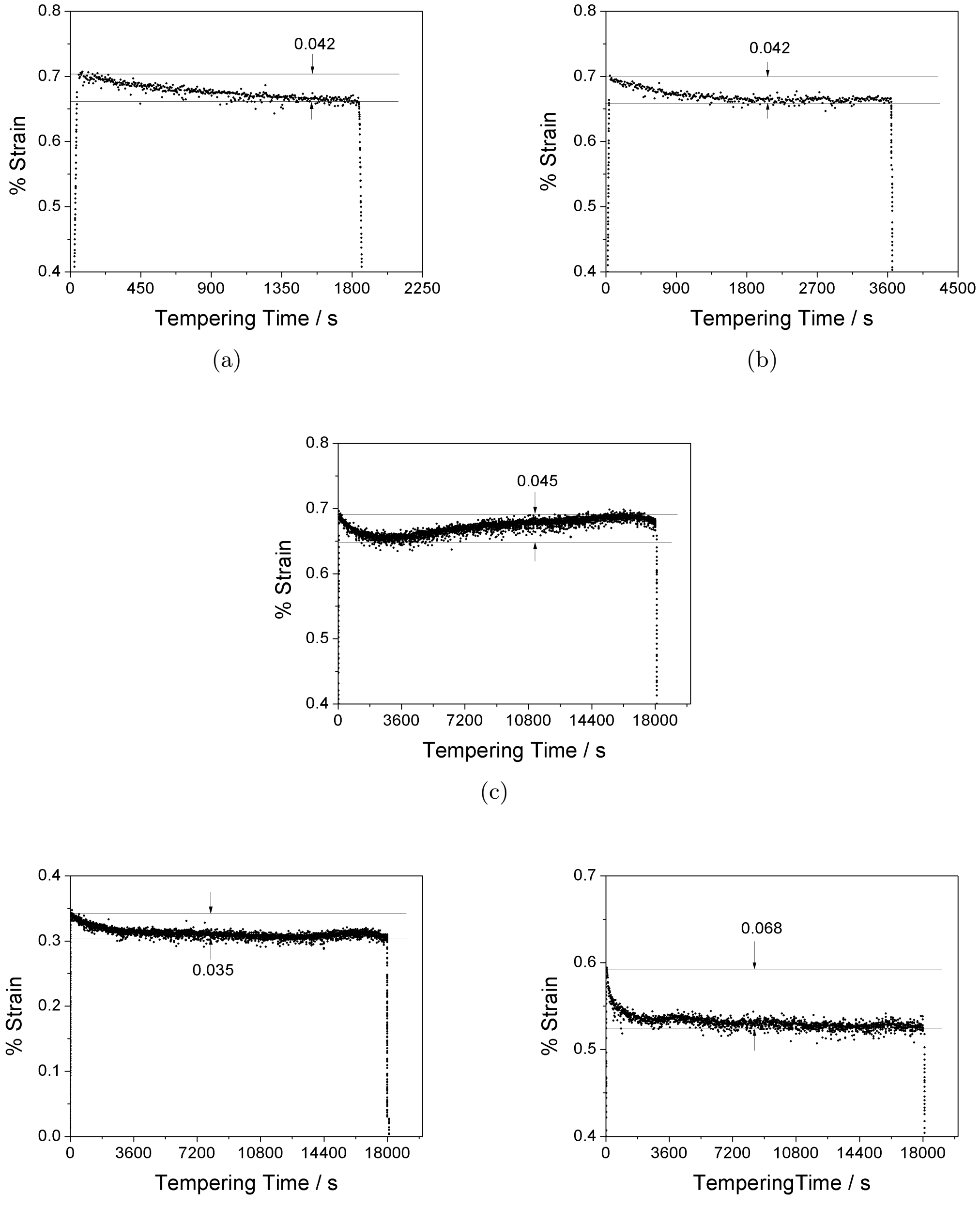

(a) (b)

(c)

(d) (e)

Figure 5.7: Dilatometric curves obtained during tempering at 450°C for tempering times of (a) 30 min, (b) 1 h and (c) 5 h. (d) Tempered at 250°C, 5 h. (e) Dilatation curve during tempering of a fully martensitic sample tempered at 450°C.

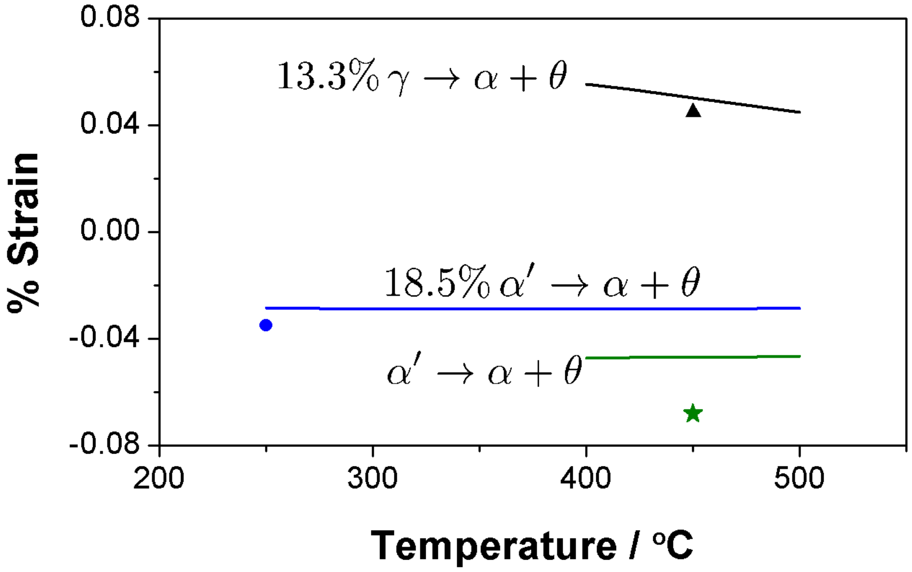

Figure 5.8: The calculated strains for the decomposition of a microstructure containing 13.3% of retained austenite containing 0.67 wt% C, due to the tempering of a microstructure containing 18.5% martensite containing 0.67 wt% C, and of a fully martensitic sample containing 0.22 wt% C. The points near each line represent experimental measurements.

the local reduction in carbon concentration following the precipitation of cementite, so that some of it transforms into untempered martensite on cooling.

5.5 Discussion

The characterisation experiments all indicate a sequence during heat treatment at 450°C, in which martensite tempers relatively rapidly, but followed by the decomposition of the austenite into a mixture of cementite and ferrite. The initial stage in the decomposition of the austenite is the precipitation of cementite, with the formation of ferrite occurring some one hour after the beginning of the tempering reaction.

It has been possible in the dilatometric experiments to clearly separate the contraction due to the tempering of martensite, and the expansion due to the formation of cementite and ferrite from austenite. The calculated strain due to austenite decomposition using Equation 5.2 was found to be 0.0502% for an initial austenite fraction of 0.133,

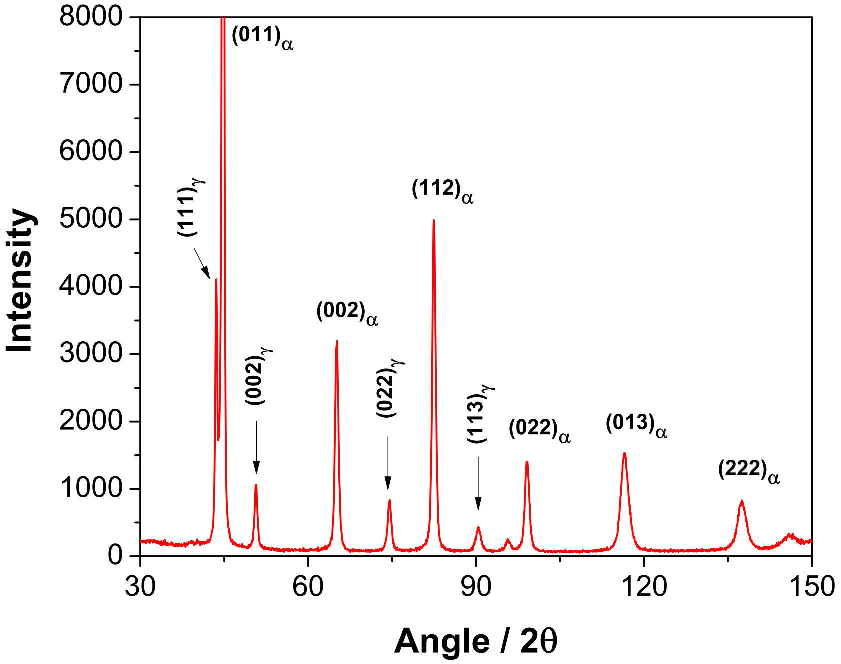

(a)

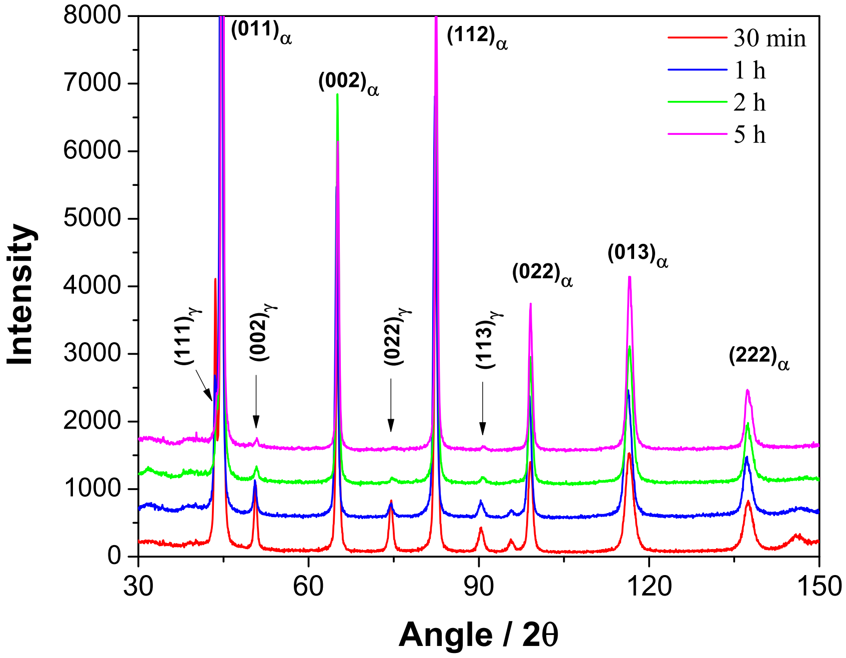

(b)

Figure 5.9: X–ray diffraction experiments. (a) Following isothermal transformation at 390°C. (b) Isothermal transformation followed by tempering at 450°C.

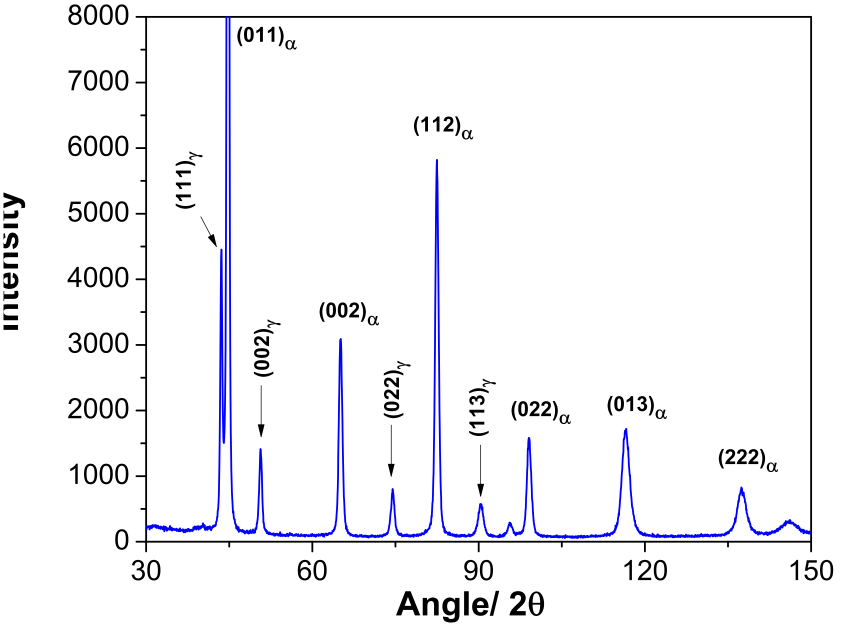

(a)

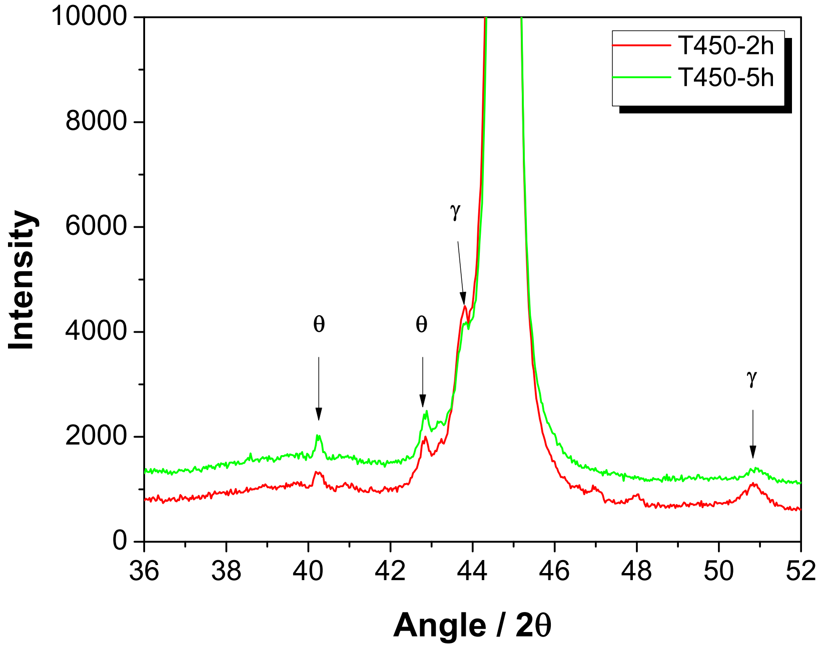

(b)

Figure 5.10: (a) X–ray diffraction pattern after tempering for 5 h at 250°C. (b) Diffraction patterns focusing on low θ, after tempering for 2 h and 5 h at 450°C.

t/min	T/°C	γ/%	Error(±)	a_γ/Å	Error(±)	a_α/Å	Error(±)
0	-	13.3	0.4	3.6031	3E-4	2.8667	3E-4
30	450	4.2	0.2	3.5959	3E-4	2.8671	9E-5
60	450	1.8	0.3	3.5888	2E-4	2.866	7E-5
120	450	1.3	0.3	3.5880	3E-4	2.8654	7E-5
300	450	0	NA	NA	NA	2.8648	7E-5
300	250	12.9	0.4	3.6042	2E-4	2.8665	1E-4

Table 5.1: Summary of the X-ray diffraction analysis.

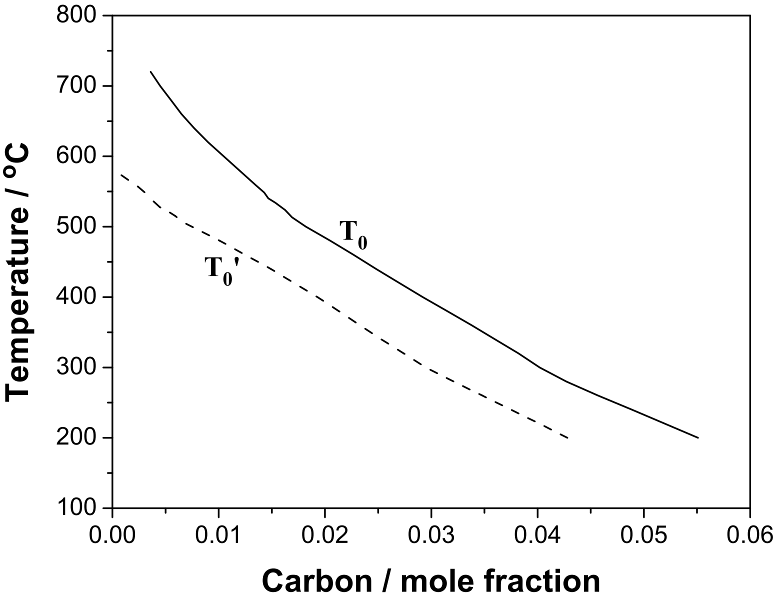

Figure 5.11: Variation of T_0 and $T_0^{'}$ carbon with carbon content.

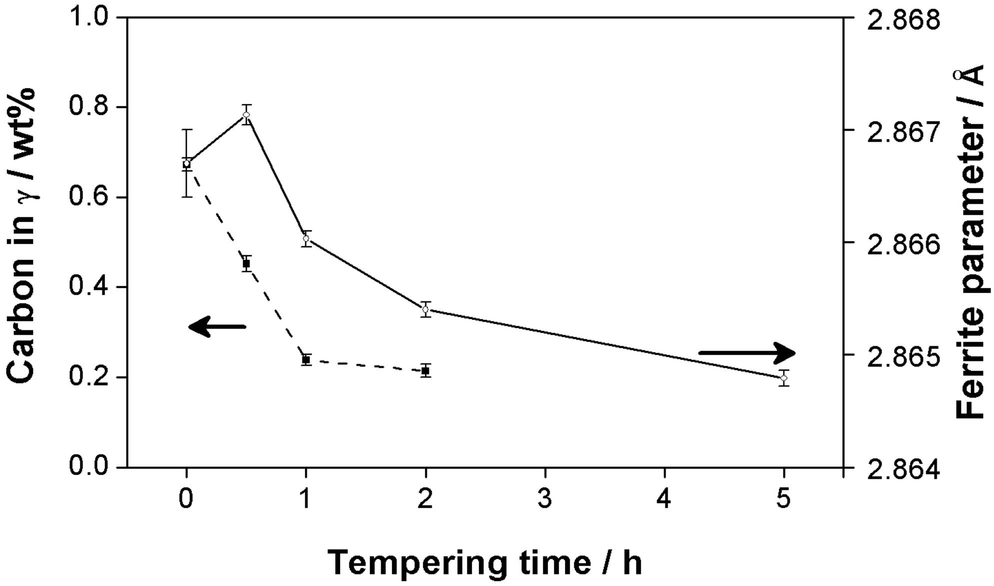

Figure 5.12: Carbon concentration in austenite and lattice parameter of ferrite as a function of the tempering time at 450°C.

which is consistent with the measured strain during tempering at 450°C (Figure 5.7).

For martensite tempering the calculated strain using Equation 5.6 for a fully martensitic sample was 0.047% whereas that determined experimentally was closer to 0.068%, as shown in Figure 5.7e. The calculation is, however, very sensitive to the initial and final lattice parameters of the martensite. In the case of tempering at 250°C, where the volume fraction of initial martensite was calculated using the thermodynamic model to be $V_{\alpha'}^{25} = 0.185$, the calculated percent strain was 0.035% which is close to the measured strain of 0.0285% (Figure 5.8).

An important outcome from the present work is that the early stages of tempering (time less than one hour) do not lead to ferrite formation, as indicated by the contraction evident in the dilatometric curves. Nevertheless, tempering leads to a dramatic decrease in the amount of retained austenite measured on the tempered samples at room temperature. This is because of the precipitation of minute quantities of cementite from the austenite, which leads to a decrease in its carbon concentration and hence the forming of untempered martensite on cooling to ambient temperature. This untempered martensite has been unambiguously identified using transmission electron microscopy.

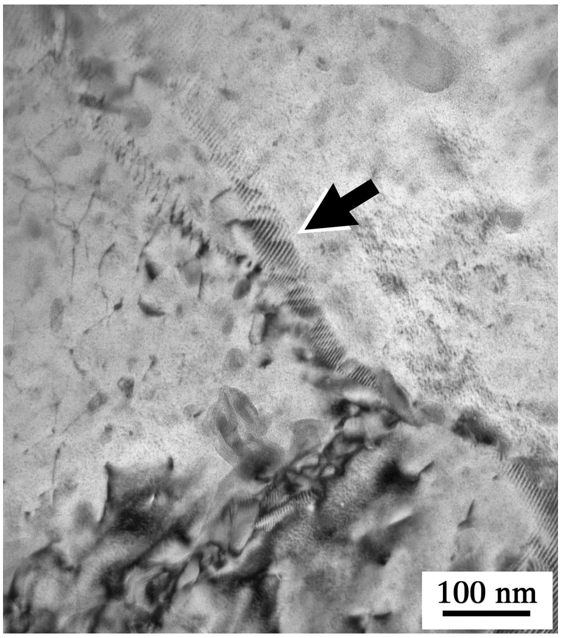

Figure 5.13: Transmission electron micrograph showing Morié fringe (arrowed) in the tempered specimen, tempered for 2 h at 450°C.

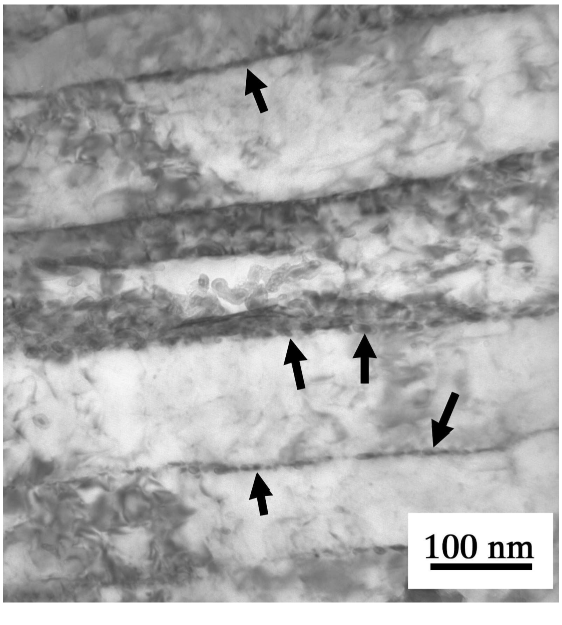

Figure 5.14: Transmission electron micrograph showing precipitation of carbide (arrow marked) on the austenite film after tempering for 1 h 450°C.

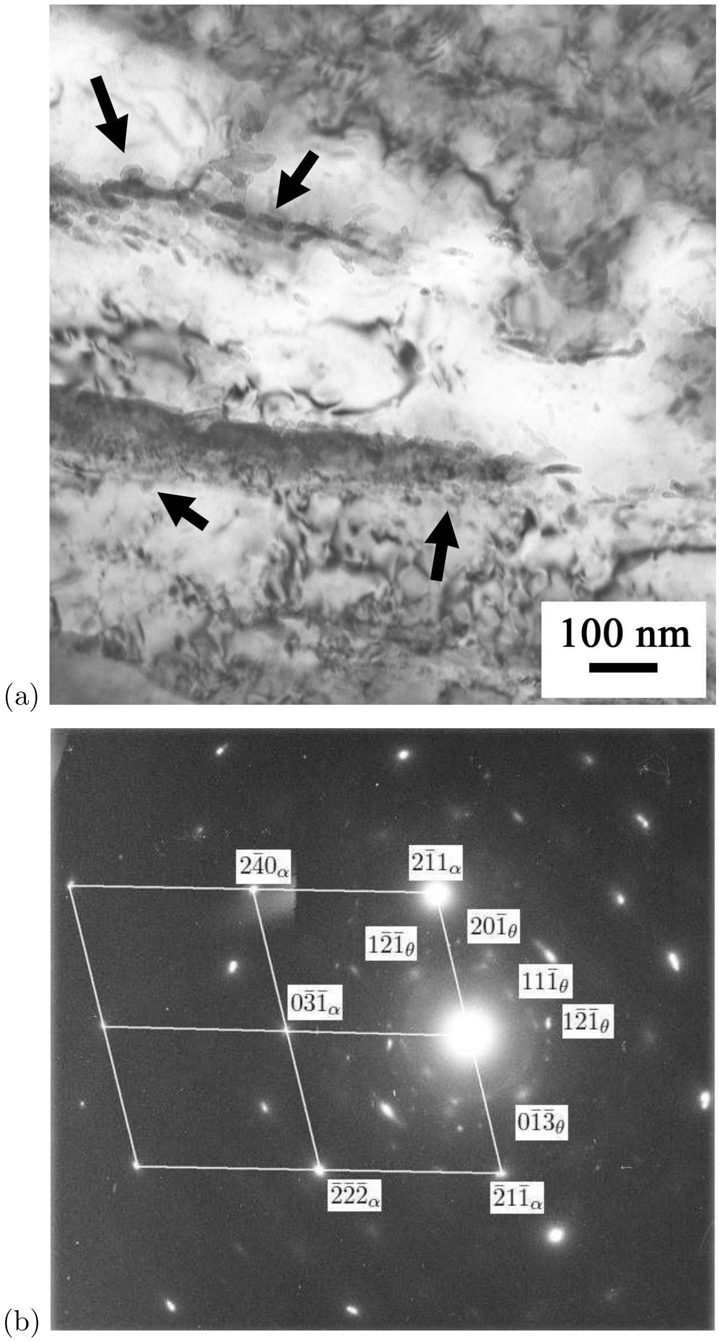

Figure 5.15: (a) Transmission electron micrograph, with the lower half showing austenite containing containing fine cementite particles (arrowed) following tempering at 450°C for 2 h. The upper half shows a thinner austenite film which has decomposed. (b) Electron diffraction pattern obtained from the tempered austenite region.

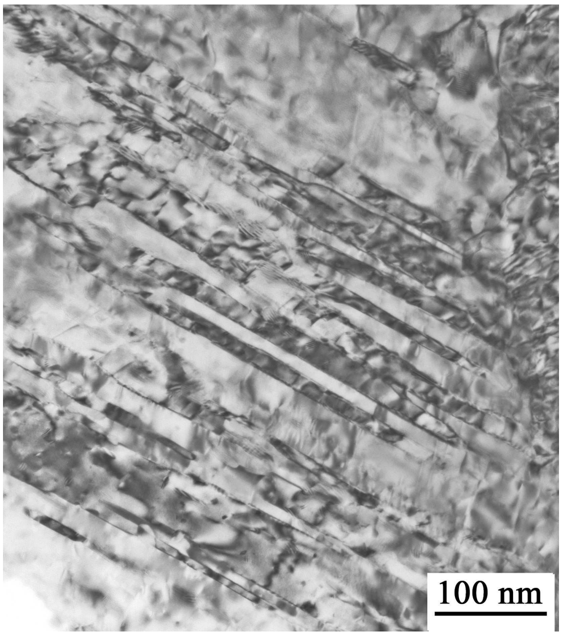

Figure 5.16: Transmission electron microscope image of martensitic twins in a sample tempered at 450°C for 30 min.

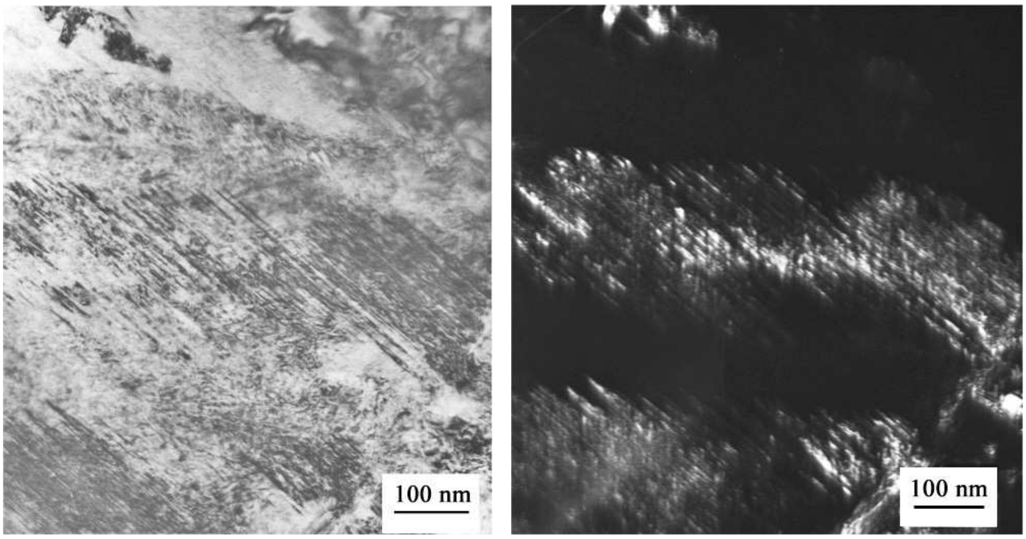

(a)

(b)

Figure 5.17: Bright and dark field transmission electron microscope images of untempered martensite (showing twins) in a sample tempered at 450°C for 1 h.

Finally, it is notable that Cameron in 1956 [161] noted that in an EN40C steel containing retained austenite, tempering followed by cooling to room temperature resulted in an increase in hardness. He described this as the "conditioning" of the austenite, and concluded that tempering resulted in a reduction in the carbon content of the austenite so that it transformed on cooling, thus leading to the increase in hardness. We have presented here evidence for the detailed mechanism, but the conclusions reached in the present work are essentially identical.

5.6 Summary

The tempering behaviour of a mixture of bainitic ferrite, retained austenite and martensite has been studied using a variety of characterisation techniques. The tempering experiments were carried out mostly at a temperature above the isothermal transformation temperature used to generate the original microstructure. A clear and novel picture has emerged for these conditions, on the events leading to the loss of stability of retained austenite present prior to tempering.

It appears that for the circumstances studied, there are two separable stages, the first involving the tempering of martensite and the precipitation of minute quantities of cementite from supersaturated austenite. This latter process makes the austenite sufficiently unstable to martensitic transformation on cooling, leading to a dramatic loss in the quantity of retained austenite measured at room temperature. The second stage involves the transformation of the austenite at the tempering temperature into ferrite and further quantities of carbides.

Chapter 6

In Situ TEM Observation of Austenite Decomposition

6.1 Introduction

With the development of ferrite-bainite dual phase steels [3], the application of bainite as a microstructural constituent has increased, for example in the manufacture of rail steels and car bodies. The microstructure, which consists of fine plates of bainitic ferrite separated by carbon enriched regions of austenite is also critical for many applications. Apart from galvanizing/ galvannealing application, an identical situation may arise during welding when the retained austenite present in the heat affected zone may well be tempered or transformed in to other products. Very little information is known about the decomposition of retained austenite in steels subject to tempering [162, 163], especially when it comes to γ present in a bainitic structure. An attempt has therefore been made to investigate the decomposition mechanism of retained austenite in a transmission electron microscope during tempering.

6.2 Experimental Procedure

The Fe-Mn-Si steel was used for this study. Heat treatments were carried out in a *Thermecmaster* thermomechanical simulator using the schedule described below. The details of this instrument has described in Section 4.2.

Austenitization was carried out by heating the specimen at 10°C s^{-1} to 930°C and held for 30 min in the vacuum chamber. Samples were then cooled to 390°C at 10°C s^{-1} using helium gas, for isothermal transformation to bainite for 2 h. After the isothermal transformation the samples were quenched to room temperature at 10°C s^{-1} using a helium jet. The heat treatment is illustrated schematically in Figure 4.2a.

The specimens for *in situ* TEM observation came from the isothermally transformed materials in a *Thermecmaster*. The specimens were prepared for transmission electron microscopy using the method described in Section 4.10. The specimens were then observed in a JEOL 200CX (200 kV) TEM. The specimens were tempered in the *built in* hot chamber mounted inside the TEM instrument. For this, the specimens were heated up to the tempering temperature and held for different time periods to observe the change in the structure and then cooled down to room temperature. Two different tempering temperatures, 420°C and 450°C, were maintained for *in situ* tempering.

6.3 Results

After isothermal transformation, microstructural characterisation was carried out as presented in Section 5.4. It's very hard to distinguish retained austenite from martensite using optical microscopy, although it is expected some martensite must be present in the material, so further effort was made to distinguish this from austenite. After thorough study it was possible to distinguish between austenite and martensite in an optical micrograph using colour contrast. Fig 6.1a shows retained austenite (bright yellow region) and martensite (brown etching region) surrounded by bainite sheaves obtained after isothermal transformation of Fe-Mn-Si steel at 390°C for 2 h.

Figure 6.2a shows a transmission electron micrograph of the specimen after isothermal transformation. The retained austenite film can be observed in the micrograph and confirmed from diffraction pattern (Figure 6.2b). This sample was heated to the tempering temperature of 450°C inside the TEM chamber. It was not possible to maintain the same heating rate of 10°C s^{-1} within the TEM sample holder because of instrumental limitations. The temperature of the sample reached 450°C in 20 min. Figure 6.3a shows the same retained austenite film after 5 min of tempering. The austenite has started to decompose as the thickness of the film has reduced. The film has further shrunk after 10 min of tempering (Figure 6.3b). After 20 min of tempering the film reduced to small area as shown in Figure 6.3c. The austenite film is difficult to distinguish after 30 min of tempering (Figure 6.3d). After 45 min the film was apparently decomposed completely. After holding for 1 h, the sample was allowed to cool to room temperature. Figure 6.4a

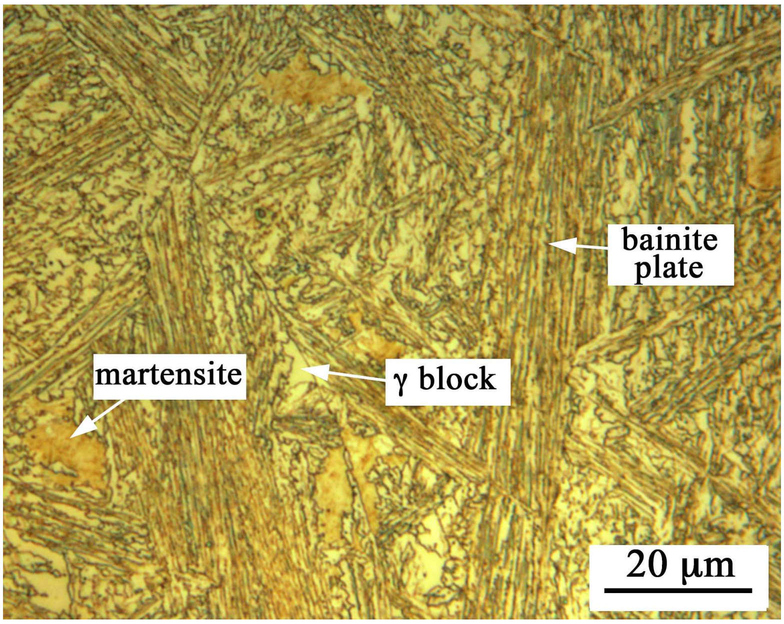

Figure 6.1: Fe-Mn-Si steel: (a) Optical micrograph showing retained austenite and martensite (grey region) surrounded by bainite sheaves after isothermal transformation at 390°C for 2 h.

shows the micrograph at room temperature, the array of precipitates can be observed in the ferrite matrix. The selected area diffraction pattern (Figure 6.4b) from the same region reveals that the precipitate is cementite. At the same time no evidence of retained austenite was observed from the diffraction pattern.

In a different specimen, which was subjected to *in situ* tempering at 420°C for 2 h, twinned martensite was present after isothermal transformation and cooling to ambient temperature, shown in Figure 6.5a. During heating but before reaching the tempering temperature of 420°C, the martensite started to temper. It is reasonable that it should temper at this temperature [15, 17]. Figure 6.5b shows the same location of Figure 6.5a tempered during heating at 300°C. When the sample reached the tempering temperature of 420°C, the martensite twins had disappeared completely, concluding the tempering of martensite phase.

After repeated efforts, transformation to martensite has been captured in the microstructure during cooling of the tempered austenite region. Figure 6.6a shows the area (arrowed) where blocky retained austenite was present in the untempered microstruc-

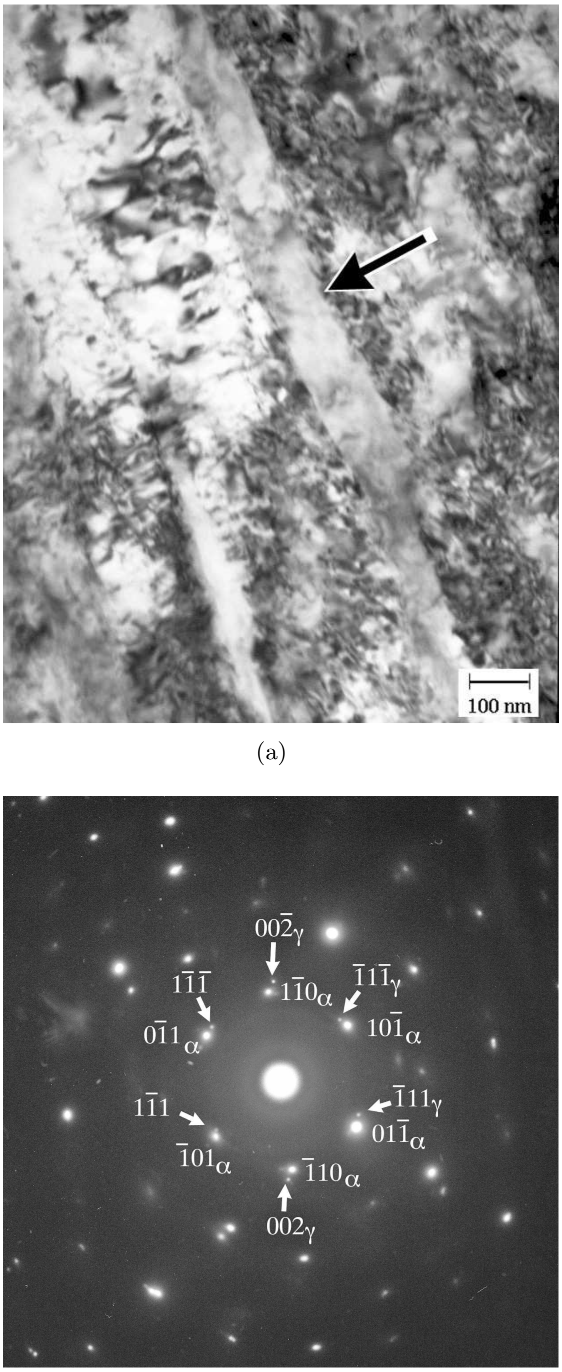

(a)

(b)

Figure 6.2: (a) Transmission electron micrograph of a sample transformed at 390°C for 2 h. The arrow marks a film of retained austenite. (b) Selected area diffraction pattern from the austenite region.

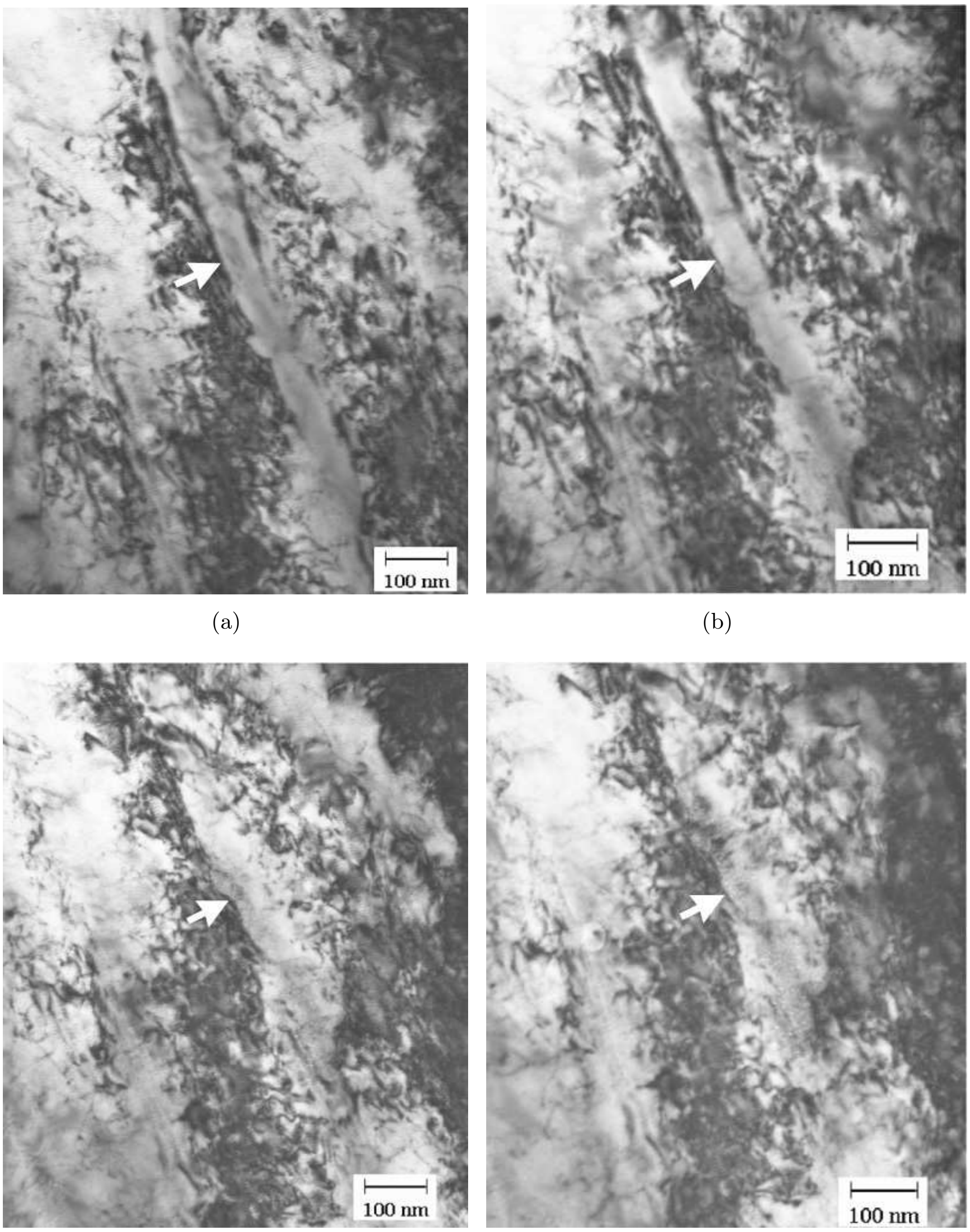

(a) (b)

(c) (d)

Figure 6.3: Transmission electron micrographs of samples tempered at 450°C for (a) 5 min, (b) 10 min and (c) 20 min and (d) 30 min.

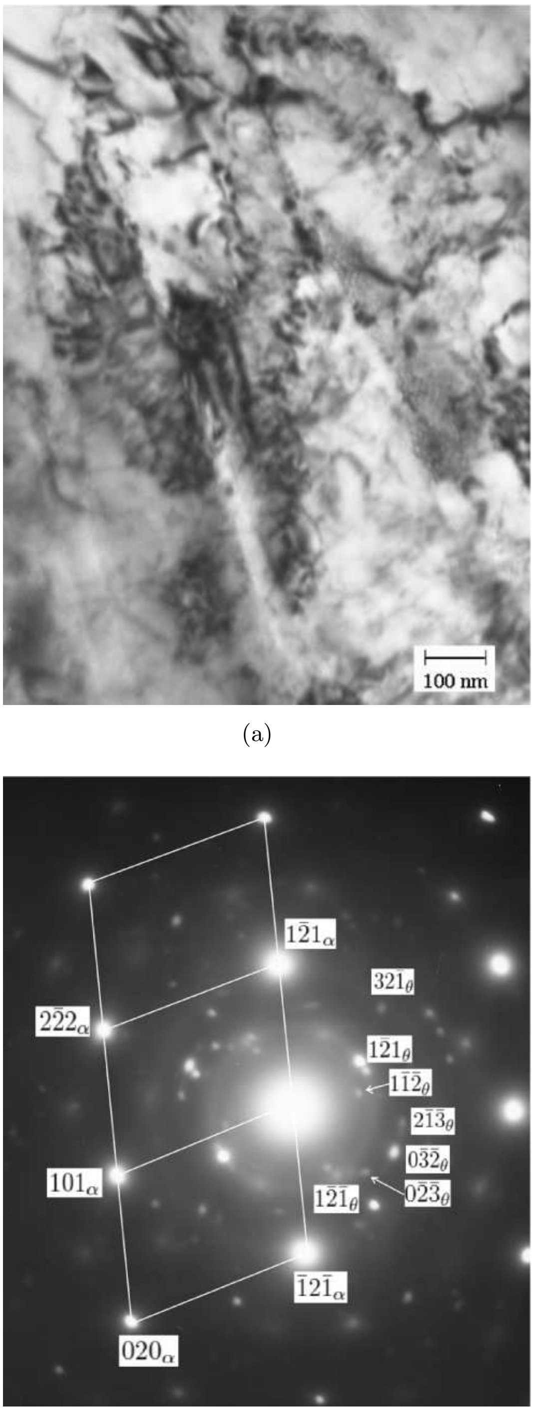

(a)

(b)

Figure 6.4: (a) Transmission electron micrograph of a sample cooled to room temperature after tempering at 450°C for 1 h. (b) Electron diffraction pattern obtained from the tempered austenite region showing presence of cementite particles.

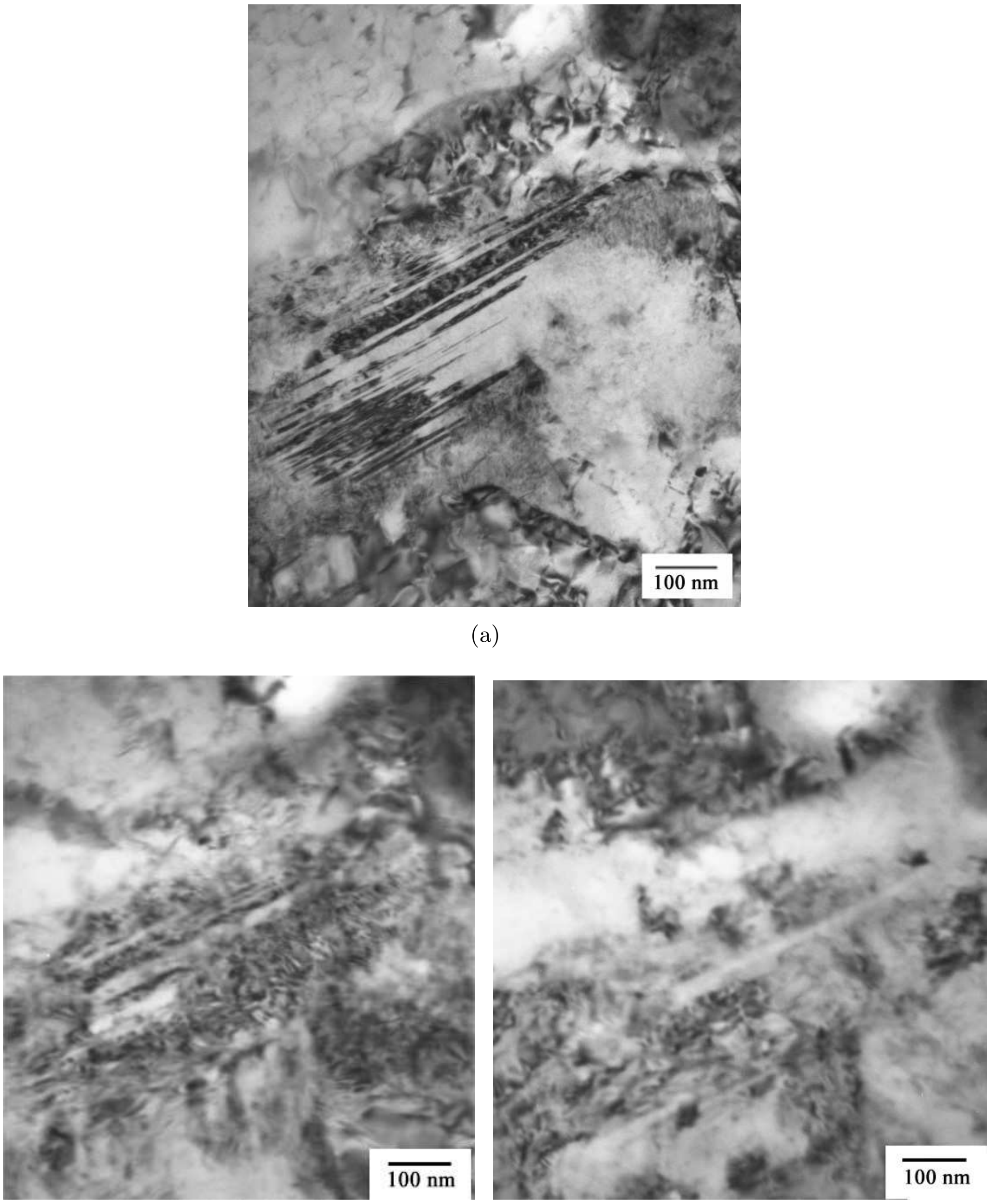

(a)

(b)

(c)

Figure 6.5: Transmission electron micrographs of a sample (a) showing martensitic twins after isothermal transformation at 390°C for 2 h, (b) during the heating at 300°C and (c) after reaching to 420°C.

ture. After tempering at 450°C for 30 min, the specimen was cooled to room temperature. At room temperature twinned martensite was observed in the area where the blocky austenite was initially present (Figure 6.6b). This observation strengthens the theory that unstable austenite transforms into martensite during cooling from the tempering temperature [164]. The formation of precipitates reduces the carbon content of the austenite which therefore becomes unstable and transforms to martensite during cooling.

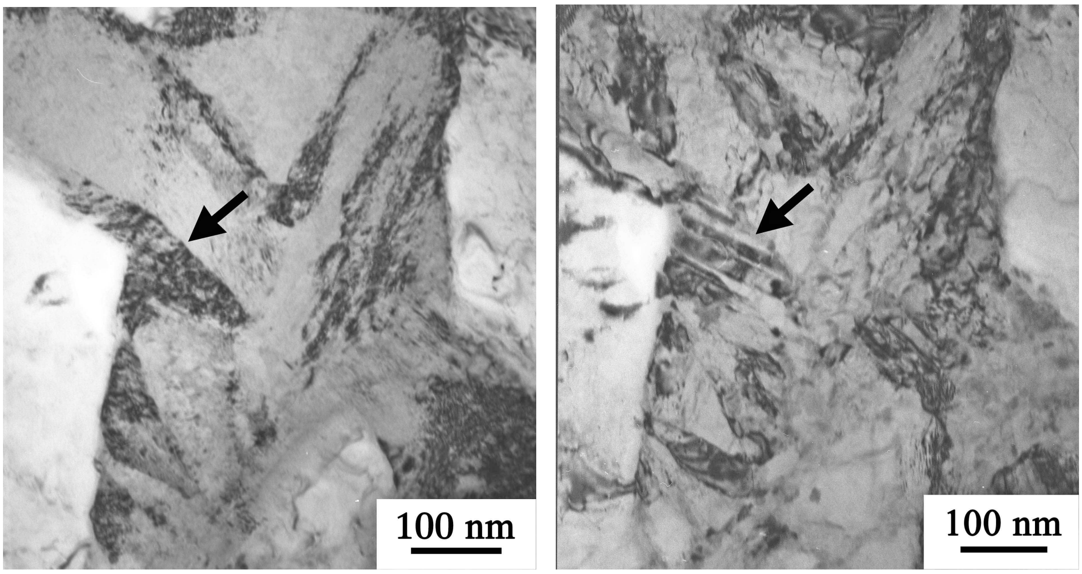

(a) (b)

Figure 6.6: (a) Transmission electron micrograph of blocky retained austenite before tempering (arrowed), (b) Martensitic twins have formed in the area of tempered blocky retained austenite during cooling after being tempered at 450°C for 30 min.

6.4 Discussion

The experimental steel provided an opportunity to study the decomposition behaviour upon tempering because during the bainitic reaction carbides do not form. Hence the precipitation of carbides in this case is independent of that of bainitic ferrite, and can be achieved subsequently by tempering. The structure obtained after isothermal transformation is upper bainite consisting of ferrite plates separated by retained austenite films and blocks.

The decomposition of retained austenite can be observed *in situ* during tempering in the transmission electron microscope. The thickness of the retained austenite film measured from the micrograph, shown in Figure 6.2, was 100±8 nm. During the heating cycle of the tempering process at 450°C, the austenite started to decompose. After a short tempering time of 5 min, the thickness of the austenite film reduced to 50±5 nm indicating decomposition progressed. It is interesting to note that the surrounding area of the austenite film shows signs of recovery via a reduction in strain contrast. The decomposition occurred from both sides of the austenite film and along the α/γ interface. The α/γ interface can be identified by dark contrast. Cementite precipitation was identified in the location where the retained austenite film was originally present. ϵ carbide could not be debated but it has been shown that it is not always a precursor to the precipitation of cementite even during the decomposition of retained austenite [8]. The decomposition mechanism of retained austenite film can be described by the movement of the α/γ interface. The ferrite thus formed has the same orientation as the ferrite around the γ film.

This study supports the theory for austenite decomposition discussed in Chapter 5, where it was claimed that during tempering retained austenite becomes unstable once the precipitation starts and transforms to martensite during cooling to ambient temperature (refer Figure 6.6).

6.5 Summary

This study reveals the decomposition mechanism of retained austenite during tempering which occurs by the movement of α/γ interface and precipitation of cementite along the interface. There is no new ferrite orientation generated by the decomposition of austenite, rather the adjacent bainitic ferrite expands to consume the austenite. These results reinforce the conclusion drawn on the decomposition of retained austenite during cooling.

Chapter 7

In Situ Synchrotron Study of Austenite Stability

7.1 Introduction

Among the different non-destructive methods for the analysis of microstructural features of materials, synchrotron radiation is extensively used for investigating chemical, biological, geological and physical systems and for characterising new materials. Modern synchrotron X-ray sources are proficient to study the heat treatment process *in situ* from the bulk material [165, 166]. This explicates the materials behavior during heat treatment or after heat treatment during cooling. The advantage of high energy X-rays from synchrotron is the large penetration and high intensity. As a result, greater information is available towards structural characterisation on a crystallite scale thus enabling changes in lattice parameters to be analysed [167].

In this chapter *in situ* X-ray diffraction measurements at a synchrotron source were performed to monitor the stability of retained austenite in a bainitic steel during tempering and subsequent cooling. In these measurements, the volume fractions of morphologically different austenite were obtained and the carbon concentrations were monitored as a function of tempering time.

7.2 Experimental Procedure

The Fe–0.39C–4.09Ni–2.05Si alloy described in Chapter 4 was heat-treated in the *Thermecmaster* thermomechanical simulator, using cylindrical samples of 12 mm in length and 8 mm diameter. Austenitisation was carried out in a vacuum (2×10^{-4} torr) by heating from ambient temperature at 10°C s^{-1} to 880°C and holding for 30 min. To obtain the required mixture of bainitic ferrite and retained austenite, isothermal transformation was carried out at 380°C for 2 h, followed by quenching to room temperature. An advantage of this alloy is that there is no carbide precipitation during the bainitic transformation, permitting the decomposition of austenite to be studied beginning with just a two phase mixture. The schematic of this heat treatment is presented in Figure 4.2b.

Following isothermal transformation, some samples were tempered at 400°C for 30 to 120 min for conventional X-ray measurements as described in Chapter 4. Another set of samples was tempered *in situ* using the European Synchrotron Radiation Facility (ESRF) in Grenoble, France. For this purpose cylindrical samples of 10 mm length and 0.8 mm diameter were machined from isothermally transformed materials.

7.2.1 Synchrotron X-ray Diffraction

Samples which were pre-treated to contain a mixture of bainitic ferrite and retained austenite were tempered at 400°C *in situ* using a hot air blower while being exposed to high-energy X-rays with a monochromatic wavelength of 0.50247 Å and a beam size of 10 mm horizontal × 0.6 mm vertical. The temperature in the blower was calibrated with a platinum specimen, following lattice expansion. The Swiss-Norwegian Beam Line BM01 at the European Synchrotron Radiation Facility (ESRF) in Grenoble, France was used for this purpose. A robust 2-circle diffractometer was available for high resolution powder diffraction measurements (Figure 7.1). Each circle has a high precision encoder mounted directly on the rotation axis. This Bragg–Brentano diffractometer works in a transmission geometry. The 13 element Ge detector has 6 fast counting chains to have for each analysis, six complete patterns collected simultaneously, with an offset in $2\theta = 1.1°$, in order to reduce the total data collection time to a minimum.

Diffraction spectra for each sample were collected at room temperature prior to tempering at 400°C for further collection of spectra. In both cases the Full Width Half Maximum (FWHM) resolution was 0.01°. The 2θ ranges were 9 to 37.5° at ambient temperature and 11.5 to 22.5° during tempering with a total acquisition time of 5 min for each spectrum. Heating and cooling were performed rapidly by moving the rotating sample above the air blower. A reference sample of silicon (NIST SRM-640c) was used to calibrate the instrument and the peak-broadening functions for the integrations. The diffraction data were analyzed using the Rietveld method [154, 155] as implemented in the program package MAUD (Materials Analysis Using Diffraction) [168, 169].

Three separate tempering sequences were carried out as shown in Figure 7.2, all with the tempering temperature fixed at 400°C. Treatments–I and II involved two stages, the first consisting of 30 and 45 min of tempering respectively, followed by quenching to room temperature where diffraction data were also collected. The purpose was to observe the change in the carbon content of retained austenite after partial martensitic transformation during cooling [164]. In the second stage, the samples were reheated to the tempering temperature and held for the specified period. Finally the samples were quenched to room temperature. In treatment–III there was no interruption during the period of 180 min, afterwards the sample was quenched to room temperature.

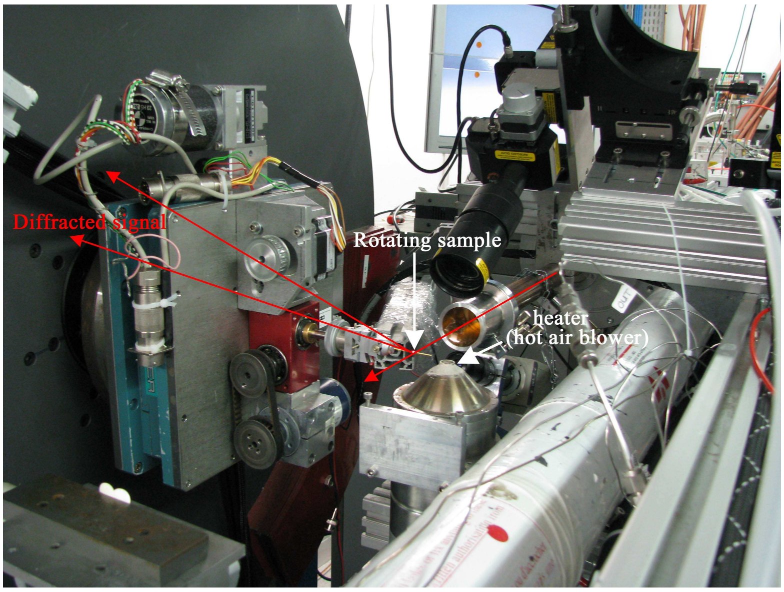

Figure 7.1: Sample assembly mounted at beam line BM01 with hot air blower positioned underneath.

7.3 Results

After isothermal transformation from austenite, the microstructure consists of a mixture of bainitic ferrite and carbon-enriched retained austenite, as shown in Figure 7.3. This structure was then tempered within the synchrotron instrument with data collected

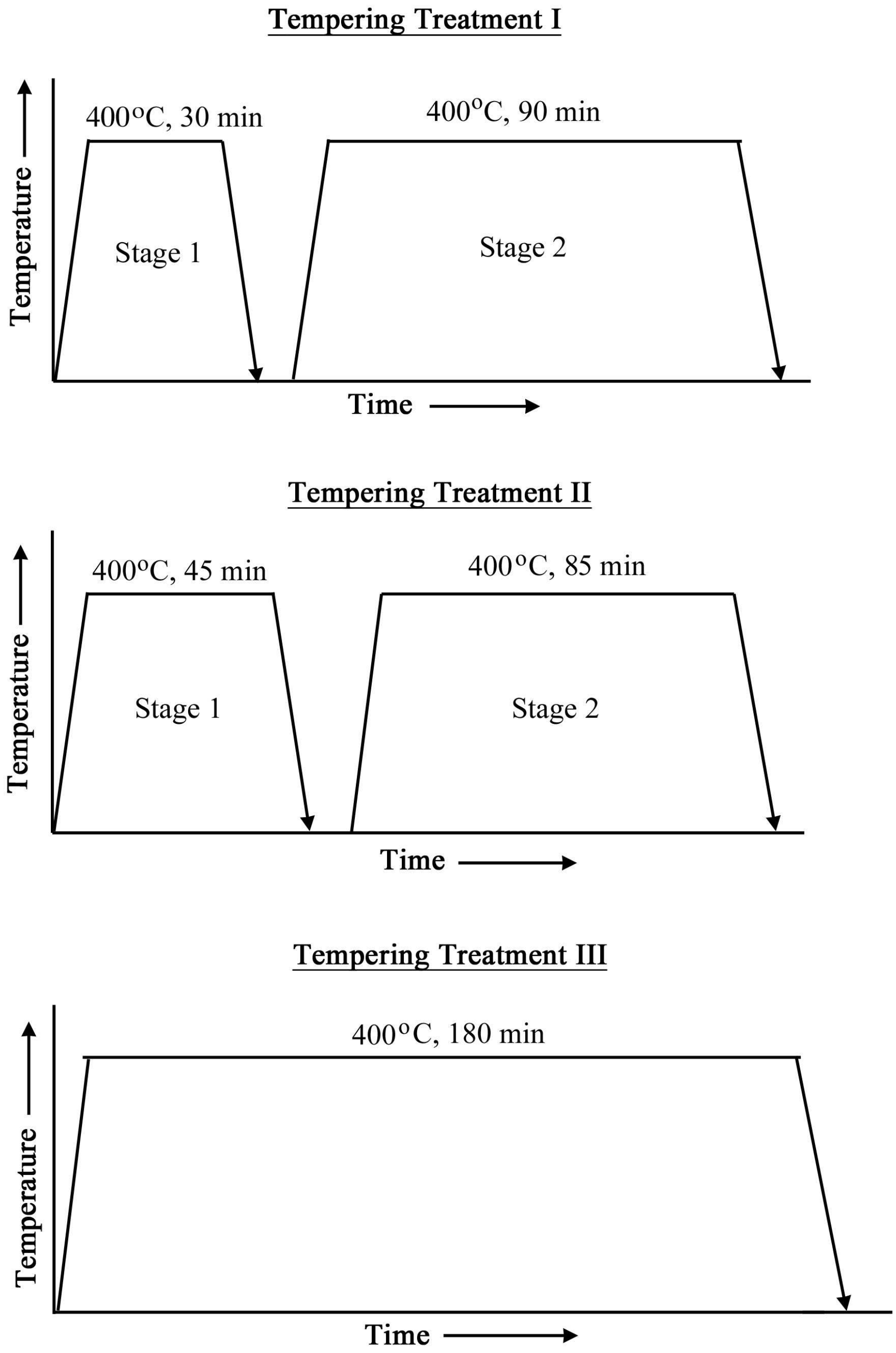

Figure 7.2: Schematics of the tempering treatments carried out using synchrotron X-ray radiation at ESRF, Grenoble. Arrows indicate quenching to room temperature.

every five minutes. Figure 7.4 shows the change in retained austenite content during tempering. The zero tempering time corresponds to the sample in its isothermally transformed state with the austenite content measured at room temperature, to be 0.19. This graph also shows low-energy X-ray diffraction data for comparison purposes. There is a revealing discrepancy in the results using two different techniques. To investigate further the sample after being tempered in the synchrotron was characterised using low-energy X-rays; this information is also plotted and is consistent with the sample tempered in a furnace rather than the synchrotron. SEM was used to check whether there was any de-carburization at the surface of the sample exposed in the synchrotron following tempering treatment–I. The observed structure is shown in Fig 7.5, which shows no evidence of de-carburization given the uniformity of the microstructure across its section.

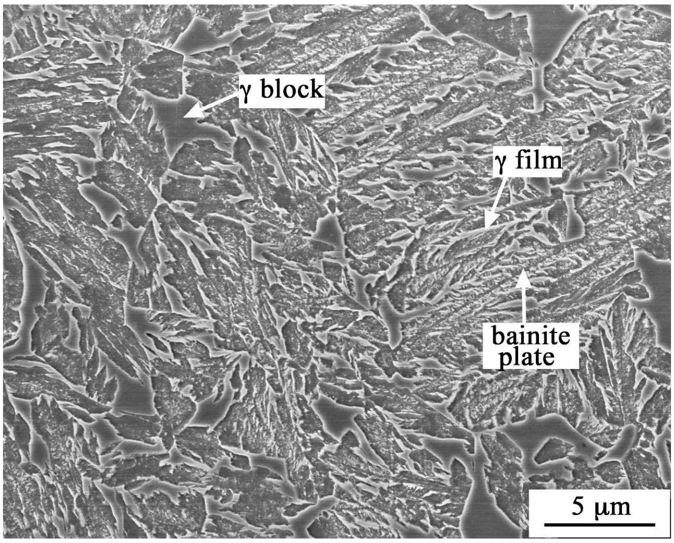

Figure 7.3: Scanning electron micrograph obtained following isothermal transformation at 380°C for 2 h showing mixed microstructure of bainitic ferrite and retained austenite.

The austenite contribution in the microstructure comes from both the untransformed blocks and thin films, the latter being entrapped between the bainite plates. The two kinds of austenite differ in terms of crystallite size and lattice strain and can be separated in X-ray diffraction patterns. The change in volume of both the forms of austenite during tempering treatment–I are plotted in Figure 7.6. The plot shows that blocky austenite always maintains a larger volume fraction as compared with the films. The volume

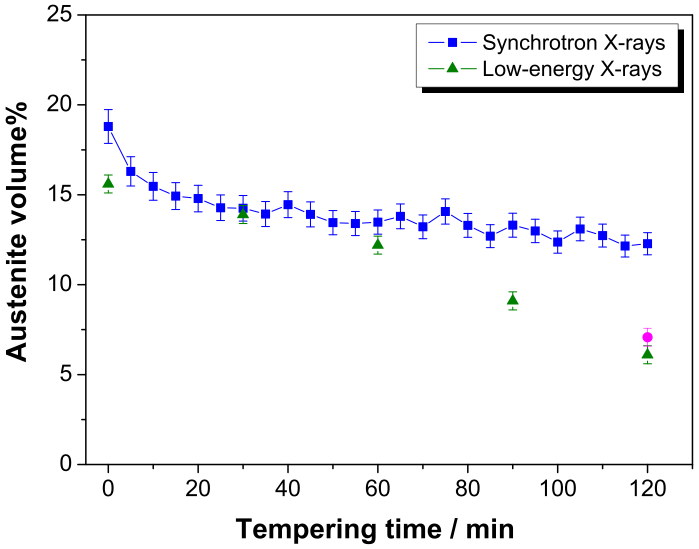

Figure 7.4: Measured volume% of retained austenite as a function of tempering time after tempering treatment–I , obtained by synchrotron radiation (blue square) and low-energy X-rays (green triangles). Standard X-ray measurement for the sample after the tempering treatment–I using synchrotron diffractometer is shown by the magenta circle.

fraction of both blocky and film austenite has decreased with the progress of tempering, but this reduction is gradual for the blocky constituent whereas there is sharp decrease in fraction of the film type in the initial stage, after which there is little change. Similarly volume% of both the austenite variants were analysed during treatment–II (Figure 7.7). The trend is very similar with treatment–1. The only difference with the earlier graph is that here both the constituents reduce gradually as the tempering time elapses. The deconvolution of individual constituents of the austenite intensity is sensitive to the profile fitting.

The lattice parameter of untransformed austenite at the transformation temperature T was calculated from the room temperature (298 K) value using the thermal expansion coefficient, e_γ:

$$a_\gamma^T = a_\gamma^{298}\,[1 + e_\gamma(T - 298)] \tag{7.1}$$

where T is the temperature in K and a_γ represents the lattice parameter of austenite. The thermal expansion coefficient of austenite considered in these calculations was e_γ=2.065 × 10^{-5} K^{-1}. The carbon content of retained austenite was calculated using the relationship between lattice parameter and chemical composition reported by Dyson and

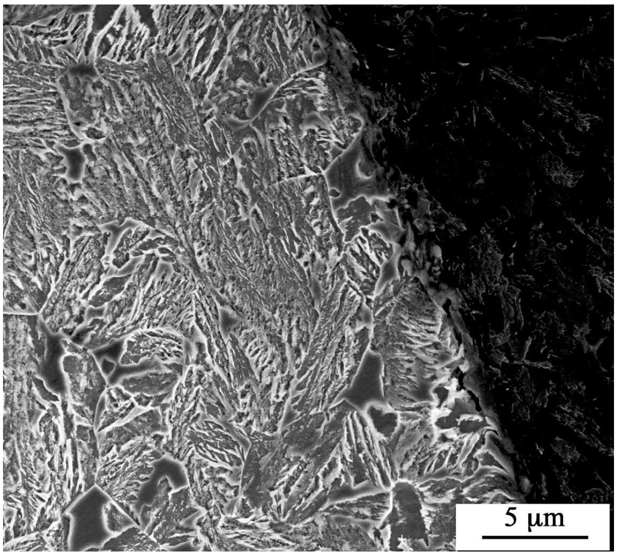

Figure 7.5: Scanning electron micrograph showing microstructure at the edge of the sample after tempering treatment–I.

Holmes [157]. This expression has been selected as being the most complete in terms of the contribution of different solutes to the austenite lattice parameter and its use has been validated due to reasonable agreement with atom probe measurements [53, 62, 170, 171].

The carbon contents of both film and blocky austenite during tempering treatment-I are presented in Figure 7.8a. It shows that the film austenite contains more carbon than the blocky counterpart. It also is important to notice that the average carbon level for both the constituents remain constant throughout the tempering process. A similar plot after tempering treatment–II (Figure 7.8b) shows that although there are apparent fluctuations within the uncertainty limits during the tempering process, the mean carbon concentration of film and blocks remain constant of 1.9 wt% and 1.6 wt% respectively after both the treatments (I and II). Higher carbon in film austenite corresponds to a greater driving force for the precipitation of carbides. This can be deduced from the difference between the equilibrium concentrations given by the extended γ/θ and γ/α boundaries. As a result, austenite films decompose more easily than the blocky constituents, which have higher volume in the microstructure. The T_0 carbon for the studied steel at 400°C is 0.8 wt%, calculated using a method published elsewhere [129, 150]. The carbon content of the retained austenite (both the constituents) is higher

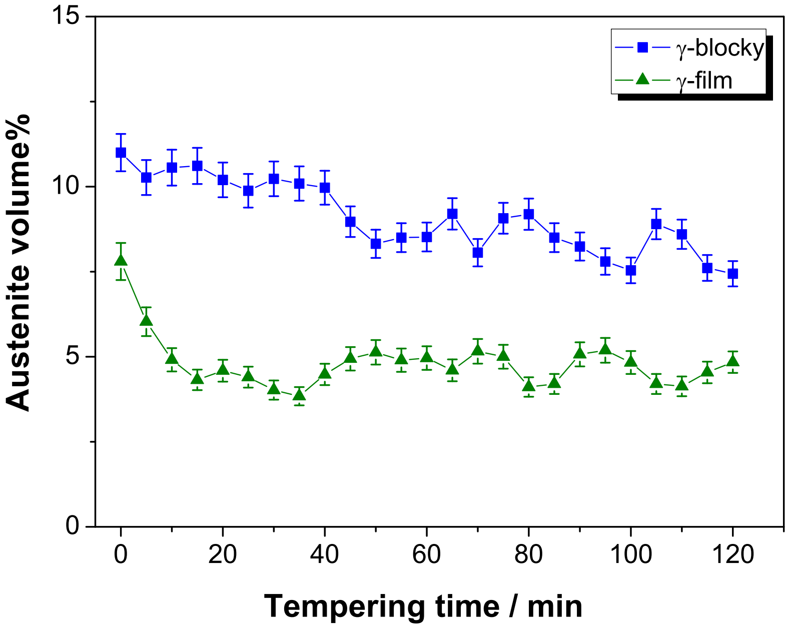

Figure 7.6: Change in volume% of austenite constituents measured during tempering treatment–I.

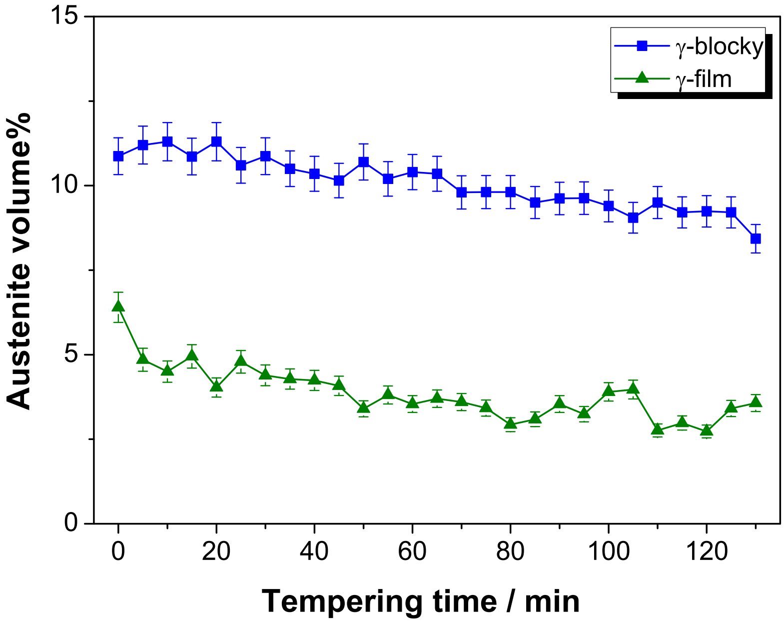

Figure 7.7: Change in volume% of austenite constituents measured during tempering treatment–II.

than the T_0 carbon. This is consistent with the theory that after isothermal bainitic transformation the excess carbon from supersaturated bainitic ferrite is rejected into the residual austenite and accumulates in the austenite, thereby allowing it to be retained at room temperature [42]. The retained austenite when reheated started to decompose at 400°C but the carbon content never fall below T_0.

During tempering treatments I and II, the specimens were quenched to room temperature after stage 1. Figure 7.8 shows that on both the occasions the carbon content of film and blocky austenite has increased from the value measured at 400°C before and after quenching. This is only possible when the unstabilised austenite transforms to martensite during cooling, results in increase in carbon content of the remaining austenite [164]. The room temperature results after stage 2 also show similar behavior because there is still 12.3 volume% of austenite retained in the structure.

The progress of transformation during *in situ* tempering can be accomplished through the change in total austenite content, Figure 7.9. The decomposition reaction is sluggish after 1 h, as a result the amounts of austenite remained in the structure are similar following treatments II and III.

High-energy X-ray diffraction patterns of untempered material and after tempering for 30 min and 120 min, obtained at room temperature, are shown in Figure 7.10. The effect of tempering can be observed from the (002) peak of austenite. Low-energy X-ray results are shown in Figure 7.11, which shows faster reduction of austenite volume though the decrease in austenite peaks intensity. After isothermal transformation the material contained 0.16±0.01 and 0.19±0.01 volume fraction of austenite measured using low and high-energy X-ray diffraction respectively.

The microstructure after tempering is shown in Figure 7.12a. The amount of austenite retained in the structure after 2 h of tempering was 12.3 volume%. The blocky austenite can be clearly observed in the microstructure primarily at the grain boundaries, it may be noted that the blocky austenite present in the structure in larger volume as described in Figures 7.6 and 7.7. Transmission electron microscopy examination revealed the presence of cementite particles in the tempered specimen. Figure 7.13a shows cementite precipitates at the grain boundaries and the corresponding electron diffraction pattern confirms the cementite phase.

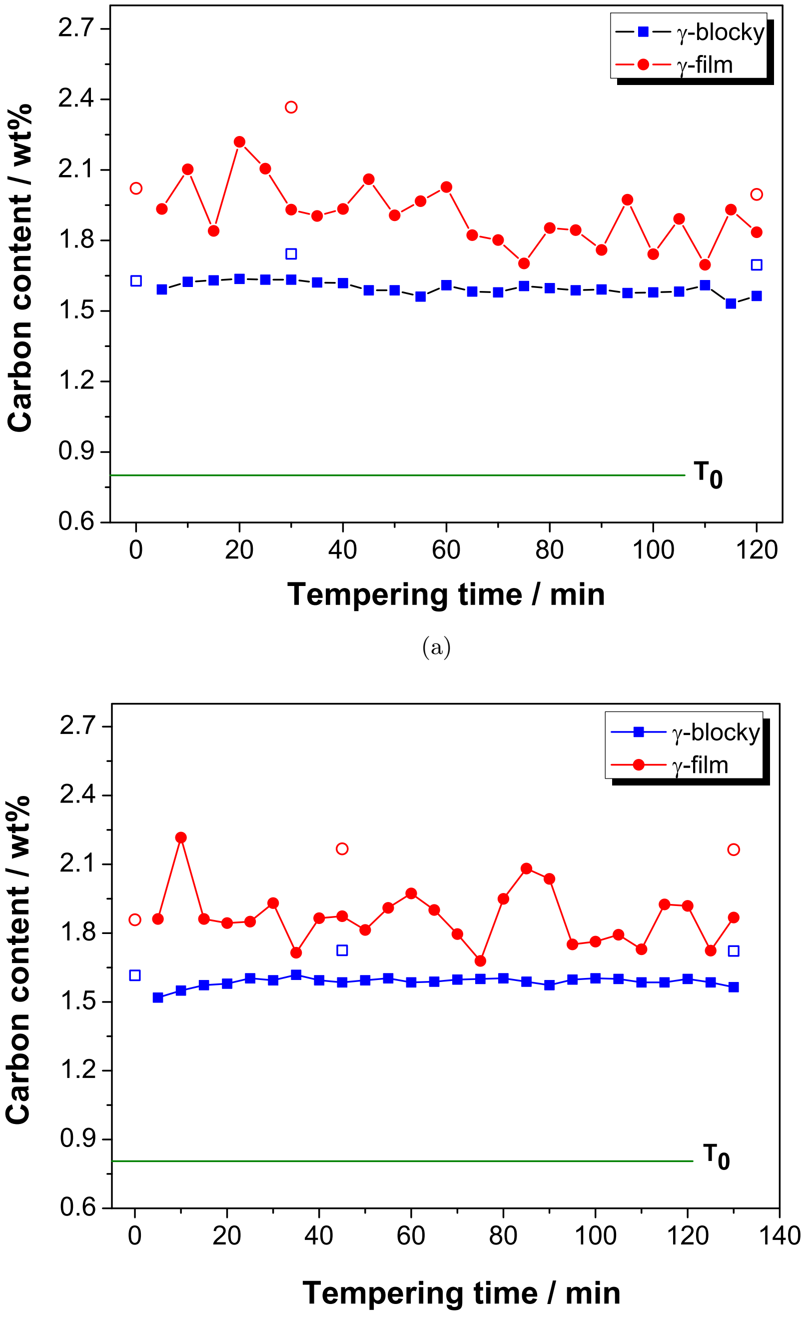

(a)

(b)

Figure 7.8: Carbon content of retained austenite obtained during *in situ* tempering for (a) treatment–I and (b) treatment–II. Open markers represent the results from room temperature measurements. T_0 curve calculated for the studied steel [150].

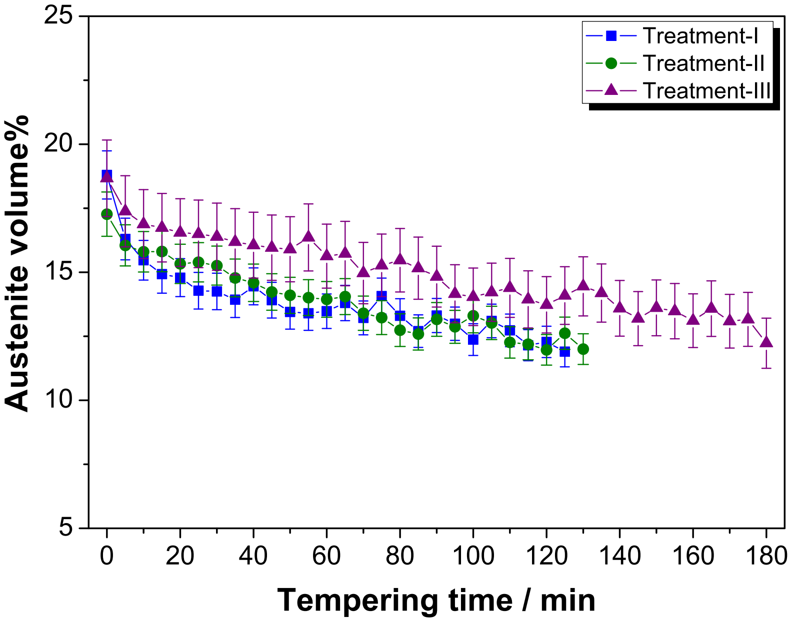

Figure 7.9: Measured volume% of retained austenite as a function of tempering time for three different tempering treatments.

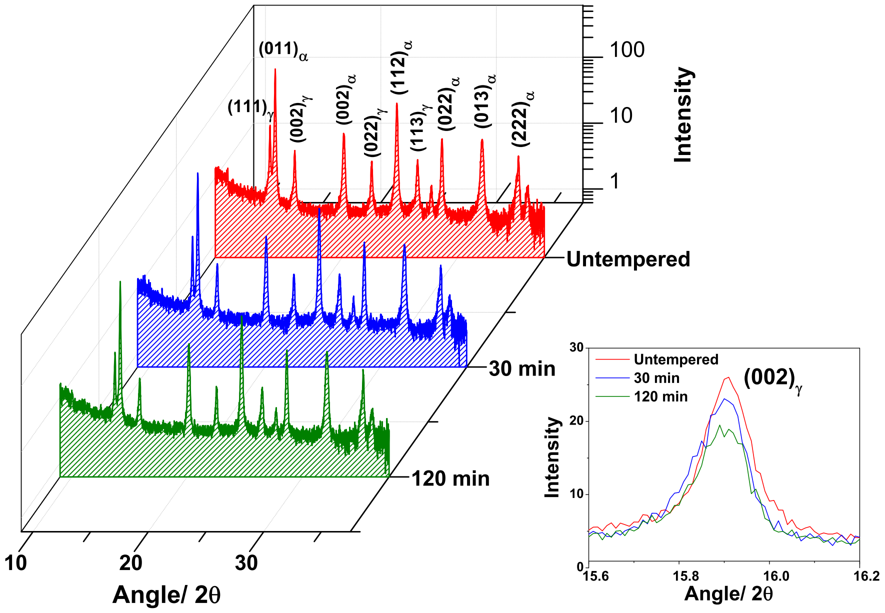

Figure 7.10: The plot showing synchrotron X-ray diffraction results after tempering treatment–I measured at room temperature.

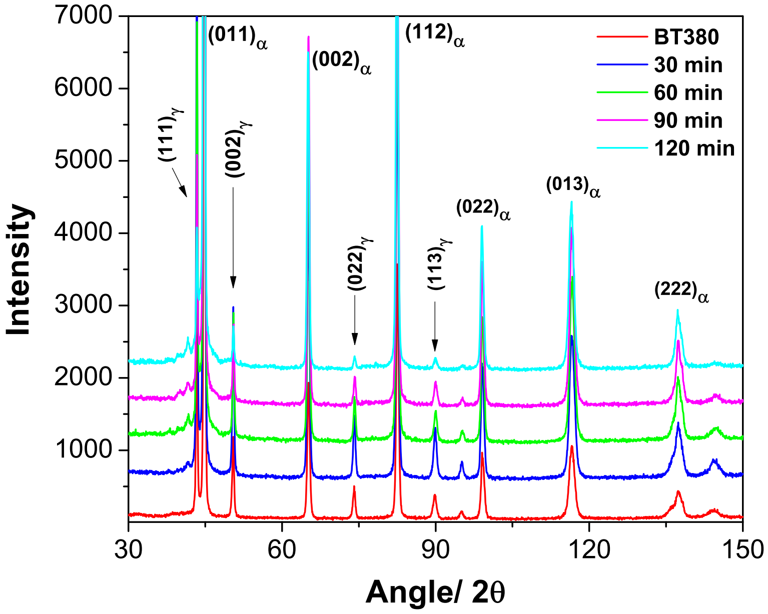

Figure 7.11: Results of low-energy X-ray diffraction. Isothermal transformation at 390°C (BT380) and followed by tempering at 400°C for different durations.

7.4 Discussion

Low energy X-ray radiation and synchrotron radiation were used to study the Fe-Ni-Si steel subjected to tempering. Synchrotron radiation, characterised by its high spatial resolution and flux density, was demonstrated to yield microstructural information that was not resolvable by conventional X-ray. There is a major discrepancy between the low-energy and high-energy X-ray diffraction data (Figure 7.4), with the former underestimating the fraction of austenite when the two results are compared. The synchrotron data were collected at the tempering temperature with one interruption (for treatments–I and II) when the sample was cooled down to room temperature. In contrast, the low-energy data were collected after cooling each sample from the tempering temperature to room temperature. The amounts of V_γ determined at 400°C were higher as compared those measured at room temperatures. It is estimated that the penetration depth of X-rays in Fe(γ) with CuKα target varies from 0.5-1.7 μm for the angle of incidence (2θ) between 20°-150° [172]. In case of synchrotron radiation the depth of penetration lies in the range of 68 to 75 μm for the wavelength of 0.5 Å [173]. It is possible, therefore,

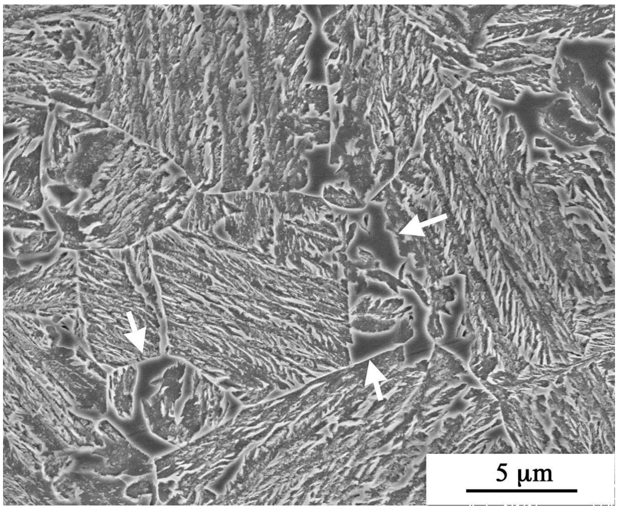

(a)

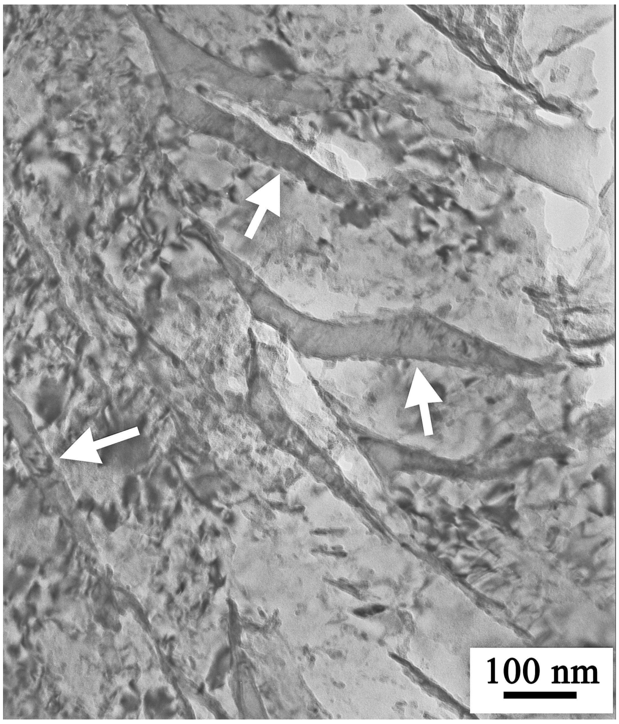

(b)

Figure 7.12: (a) Scanning electron micrograph of the tempered sample after tempering treatment–I, showing retained austenite (arrowed) present in the microstructure even after 2 h of tempering. (b) Corresponding transmission electron micrograph showing retained austenite marked with arrows.

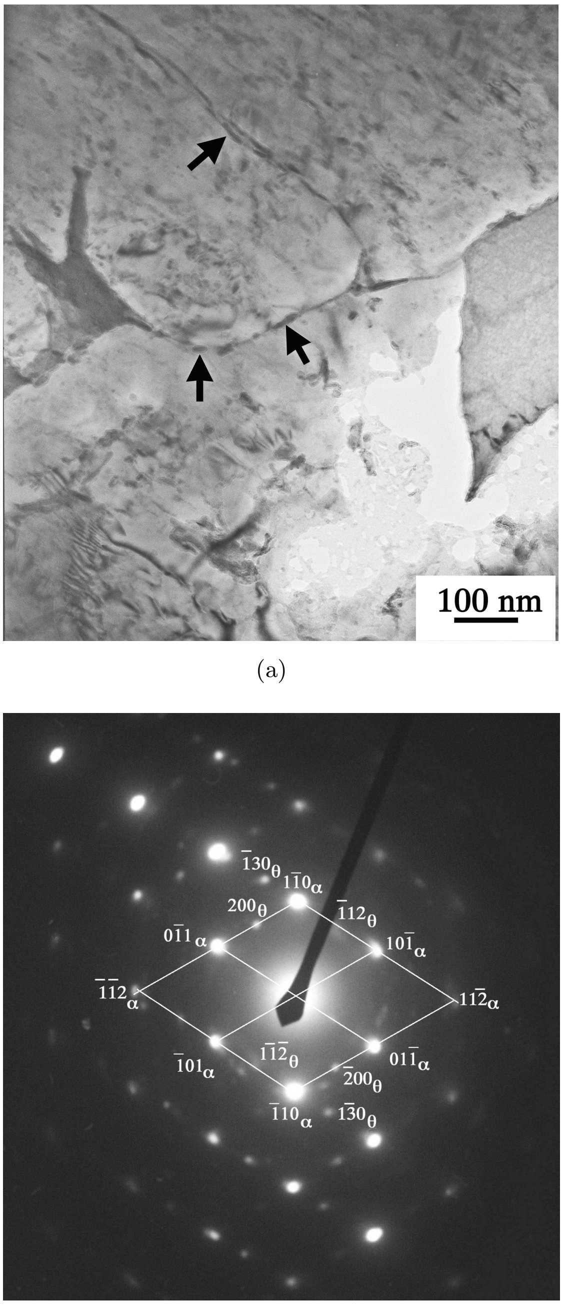

(a)

(b)

Figure 7.13: (a) Transmission electron micrograph showing precipitation of fine cementite particles (arrowed) in the tempered specimen, tempered using *Thermecmaster* at 400°C for 30 min. (b) Electron diffraction pattern obtained from the precipitates.

that the underestimation in the low–penetration experiments comes from the decomposition of retained austenite in the proximity of the free surface, an effect which would be masked in the synchrotron experiments which sample a greater depth.

To test this hypothesis, the conventional X-ray samples were further chemically polished and V_γ was measured again. This resulted in an increase in the measured values of retained austenite content. The discrepancy between the two kinds of experiments vanished for an annealing time of 30 min, but not for longer periods at 400°C. This is because during tempering, the precipitation of carbides reduces the stability of the austenite so that on cooling, some of this transforms into martensite [164]. In the experimental alloy, cementite precipitation has been observed in the specimen after a short tempering time of 30 min (Figure 7.13). The room temperature measurements after 30 min and 45 min for treatment–I and treatment–II respectively revealed an increase in carbon content due to the formation of martensite and subsequent enrichment of carbon in the retained austenite. This is consistent with existing theory [174].

The work reveals two new pieces of information, first that conventional experiments using X-ray diffraction may in some cases mislead due to surface effects, and secondly, the comparison reinforces the conclusion (Chapter 5) that there is some decomposition of the residual austenite, which exists at 400°C, into martensite on cooling to ambient temperature. This effect is most prominent at the surface of the sample, and hence the effect is less pronounced when dealing with synchrotron samples.

7.5 Summary

Experiments were carried out with the aim of determining the change in volume% and chemical composition of retained austenite under thermal load. High-energy synchrotron X-ray radiation has been used to analyze the decomposition behavior *in situ*. This result successfully demonstrates the change in volume% of individual constituents of austenite phase present in the microstructure after bainitic transformation. The blocky austenite can accommodate less carbon as compared with film type. As a result, blocky austenite is shown to be more stable under thermal load and present even after long tempering treatments. This study further strengthens the theory that following the precipitation of cementite, the remaining austenite becomes unstable to transform into martensite during cooling.

Chapter 8

Tempering Behaviour of Fe-Mn-Si and Fe-Ni-Si Steels

8.1 Introduction

The purpose of tempering is to reduce the brittleness associated with hardening and to produce defined physical properties within the steel. Besides reducing brittleness, tempering also softens the steel. That is unavoidable and the amount of hardness that is lost depends on the temperature that the steel is heated to during the tempering process. That is true for all steels except those which secondary harden where tempering increases the hardness when alloy carbides are able to precipitate [175, 176]. In some cases, tempering may not be deliberate such as during galvanizing or galvannealing, where the materials get momentarily exposed to elevated temperatures. In this chapter, the tempering behavior of the two bainitic Fe-Mn-Si and Fe-Ni-Si steels are compared. The effects of tempering are discussed in terms of microstructural changes and non-uniform strain; an attempt has been made to correlate these changes with the amount of austenite decomposed.

8.2 Experimental Procedure

The chemical compositions and the manufacturing routes of the studied steels have been elaborated in Section 4.1. All the heat treatments were carried out in a *Thermecmaster* thermomechanical simulator using cylindrical samples, 12 mm in length and 8 mm diameter as described in Section 4.2.

The specimens for optical microscopy, electron microscopy and X-ray diffraction were cut out from the heat treated samples. X-ray diffraction measurements were carried out using a Philips vertical diffractometer with unfiltered CuK$_\alpha$ radiation using the parameters described in Section 4.8. Peak positions and phases were identified using X'Pert HighScore Plus software. The volume fraction of retained austenite was determined using Rietveld refinement [140, 142]. In case of microstrain analysis the PROFIT software package was used for profile fitting and thereby to obtain the information regarding peak position, width and intensity. Lanthanum hexaboride (LaB_6) was used to calibrate the instrumental broadening of diffraction peaks.

Transmission electron microscopy was carried out using a JEOL 2000FX (200 kV) transmission electron microscope. Apart from thin foils, carbon extraction replicas were used to characterise the carbides in the Fe-Mn-Si steel subjected to tempering, the details of which has been depicted in Section 4.10.

Orientation imaging of grains was carried out using the electron backscattered diffraction (EBSD) technique. The measurement was carried out on the direction perpendicular to rolling direction, over a field of 486 × 364 μm for true representative sampling. The sample preparation and instrumental techniques have been described in Section 4.9.

8.3 Results

The prior austenite grain size was revealed using thermal etching of grain boundaries, as shown in Figure 4.3. The mean linear intercept of prior austenite grain size of thermally etched samples of the Fe-Mn-Si and Fe-Ni-Si steels are 51.8±2.6 μm and 28.2±1.4 μm respectively.

The amount of austenite remaining at the isothermal transformation temperature after the bainitic transformation is known as residual austenite and this can be estimated using the T_0 curve of the phase diagram [42]. During cooling from the transformation temperature to room temperature, some of the austenite decomposes to martensite and the quantity can be estimated by applying the Koistinen and Marburger Equation [159] as described in Section 5.4. Table 8.1 shows the phase fractions of two different alloys following isothermal transformation. The austenite volume fractions measured using X-ray diffraction after the isothermal transformation were 0.13±0.01 and 0.16±0.01 for the Fe-Mn-Si and Fe-Ni-Si steels respectively and are consistent with the calculations in Table 8.1.

Volume fraction	Fe-Mn-Si steel	Fe-Ni-Si steel
Residual austenite	$V_\gamma^{390} = 0.32$	$V_\gamma^{380} = 0.44$
Martensite	$V_{\alpha'}^{20} = 0.19$	$V_{\alpha'}^{20} = 0.27$
Retained austenite	$V_\gamma^{20} = 0.13$	$V_\gamma^{20} = 0.17$

Table 8.1: Volume fractions of different phases calculated from T_0 plot. The superscripts indicate the temperature in degrees celcius.

8.3.1 Effect of Tempering on Microstructural Characteristics

After isothermal transformation the microstructure consists of bainitic ferrite, retained austenite and a quantity of martensite. The individual microstructures of both alloys following isothermal transformation were presented in Chapters 5 and 7.

Figure 8.1 illustrates the microstructures of the Fe-Mn-Si steel. The sample tempered at 420°C for 1 h is shown in Figure 8.1a; retained austenite can be observed in the microstructure along with the "decomposed region". This is an area which transformed from retained austenite as the consequence of tempering. Figure 8.2 shows higher resolution micrographs of the decomposed region. The transmission electron micrograph is presented in Figure 8.3, confirming the presence of austenite films. It is difficult to find retained austenite in the structure after 10 h of tempering (Figure 8.1b) since X-ray diffraction indicated only 3 % of this phase.

Some typical optical micrographs of the Fe-Ni-Si steel following tempering treatments are presented in Figure 8.4. Tempering at 400°C for 30 min leaves the ferrite fraction essentially unchanged with a minor reduction of austenite, but after 1 h a tempered bainitic structure can be be observed. With gradual progress of tempering the retained austenite disappeared from the microstructure. The presence of only tempered bainite and decomposed ferrite after 5 h of tempering indicates the end of the tempering process.

Fig 8.5 shows the evolution of the austenite volume fraction as a function of heat treatment, determined using X-ray diffraction on samples cooled to room temperature following tempering. The data are also plotted as isothermal transformations in Figure 8.6 which shows that kinetics of decomposition are much faster in the Ni-containing alloy, which will be explained later using thermodynamic calculations.

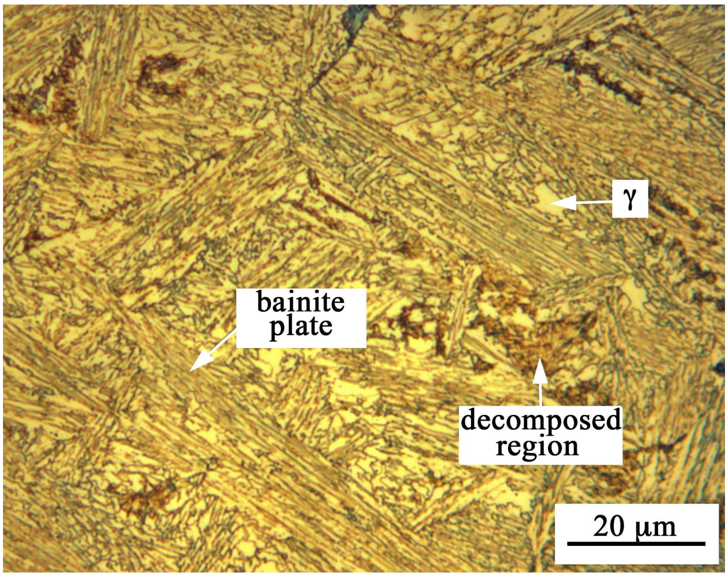

(a)

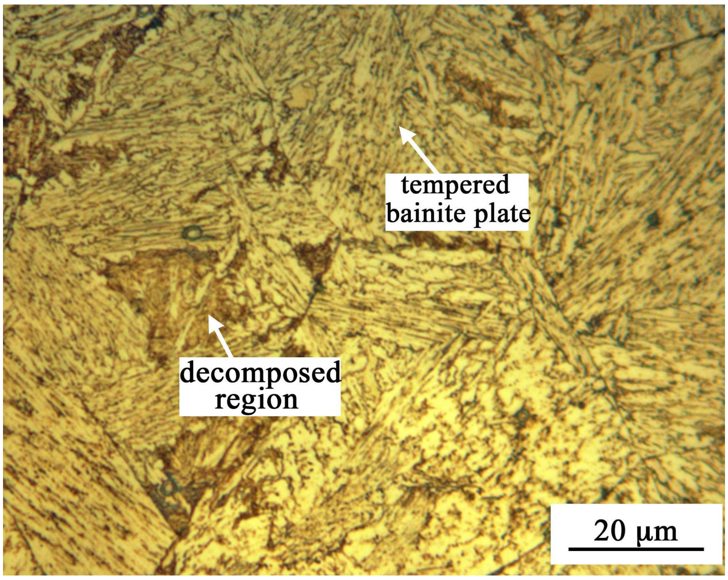

(b)

Figure 8.1: Fe-Mn-Si steel: (a) Optical micrograph showing retained austenite (bright) surrounded by bainite sheaves after tempering at 420°C for 1 h. (b) Optical micrograph showing tempered bainite and decomposed region (brown) after tempering for 10 h at 420°C.

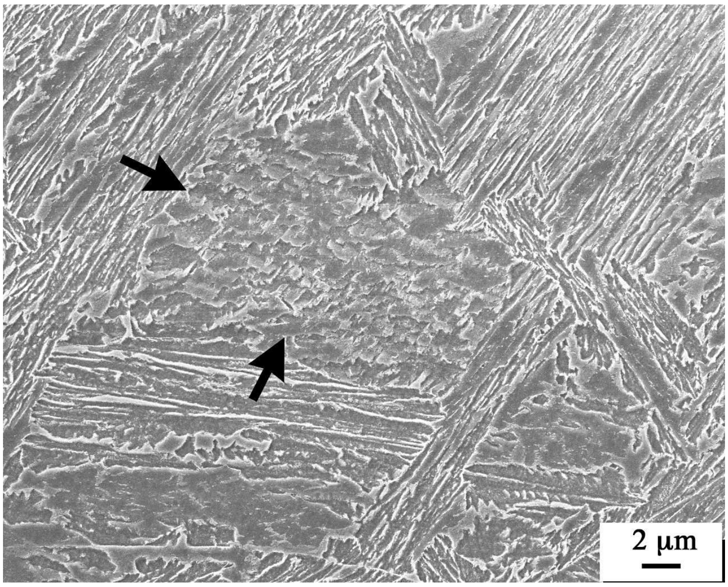

(a)

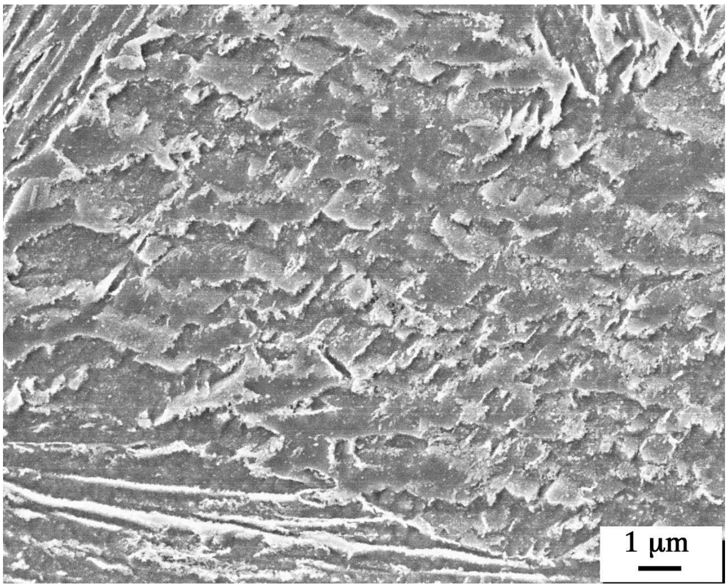

(b)

Figure 8.2: Fe-Mn-Si steel: (a) Scanning electron micrograph showing decomposed region after tempering for 5 h at 420°C. (b) Magnified decomposed region shown in (a).

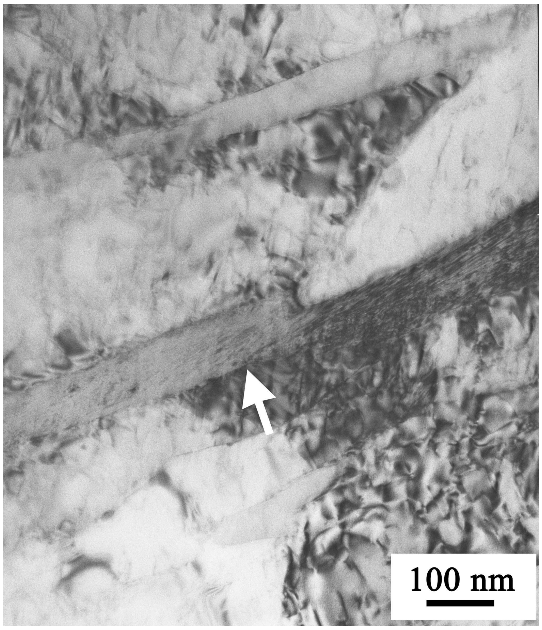

(a)

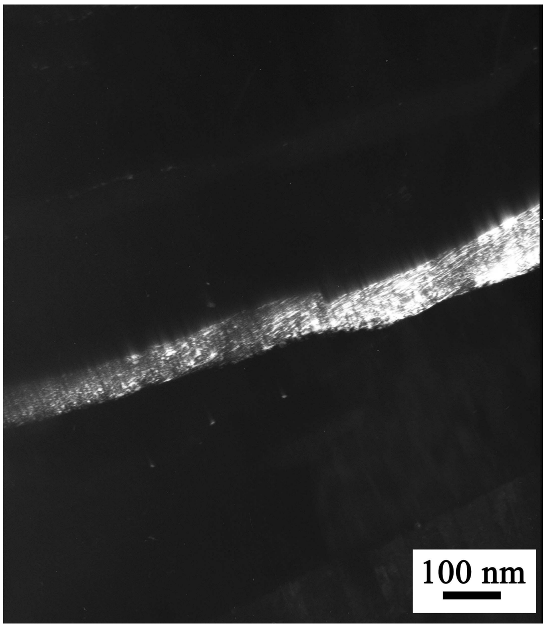

(b)

Figure 8.3: (a) Transmission electron micrograph showing retained austenite (arrowed) in the structure after tempering at 420°C for 1 h. (b) Dark field image of the austenite film using a {111} reflection.

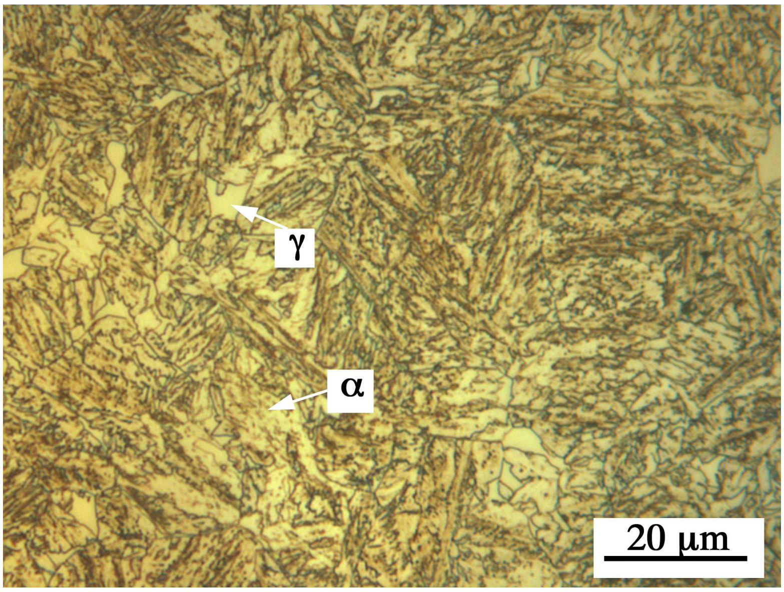

(a)

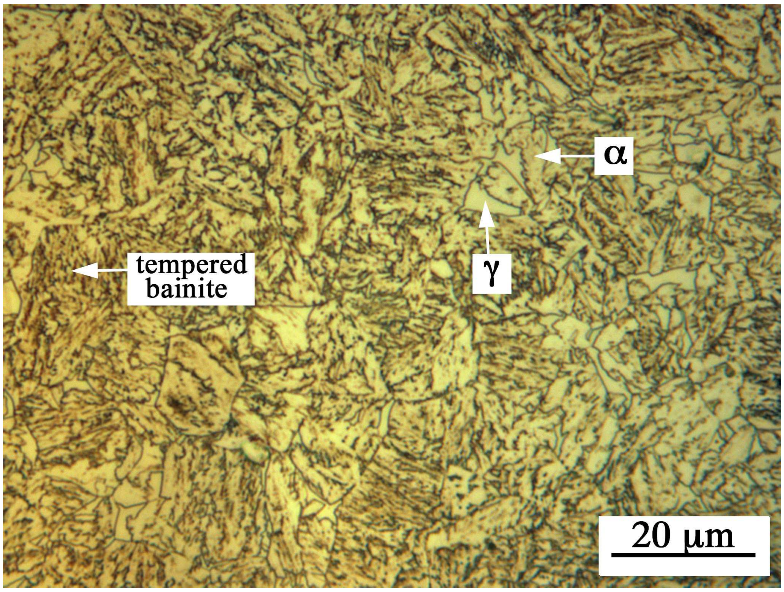

(b)

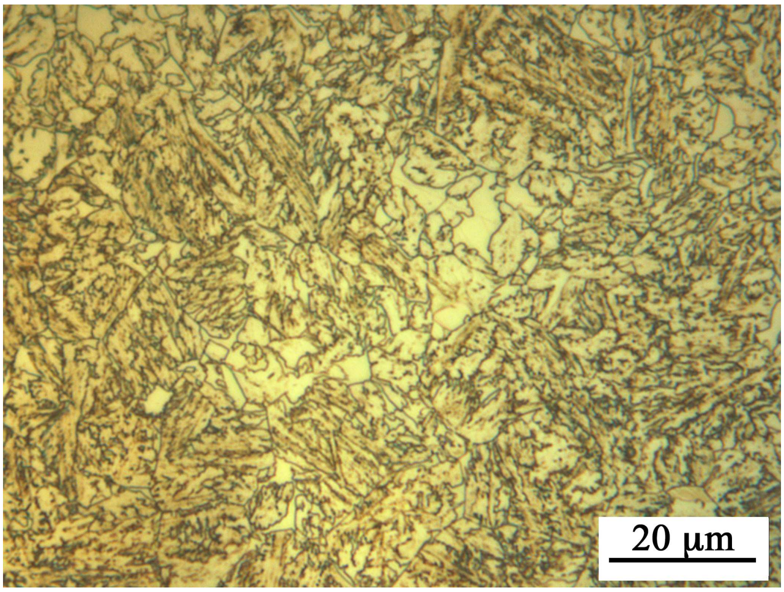

(c)

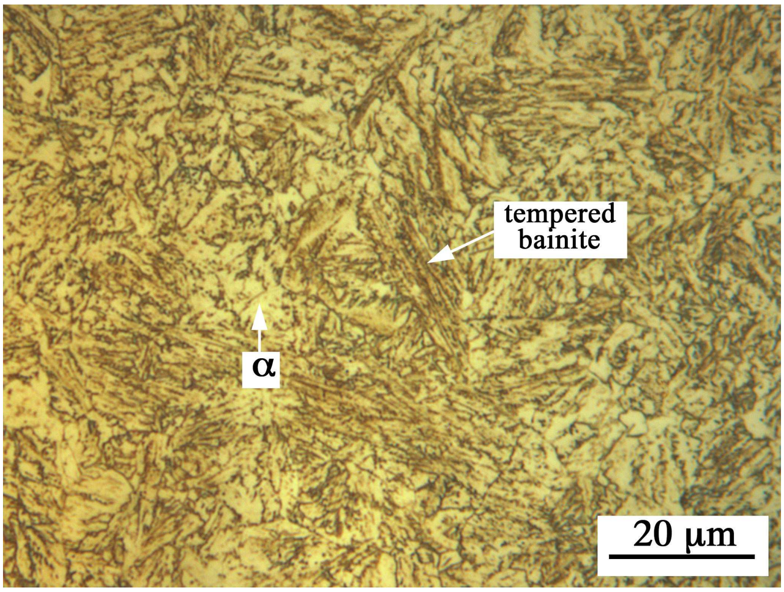

(d)

Figure 8.4: Fe-Ni-Si steel: Optical micrograph showing retained austenite (bright) and transformed ferrite (grey region) (α) surrounded by bainite sheaves after tempering at 400°C for (a) 30 min, (b) 1 h and (c) 2 h. (d) Optical micrograph showing tempered bainite and transformed ferrite after tempering for 5 h at 400°C.

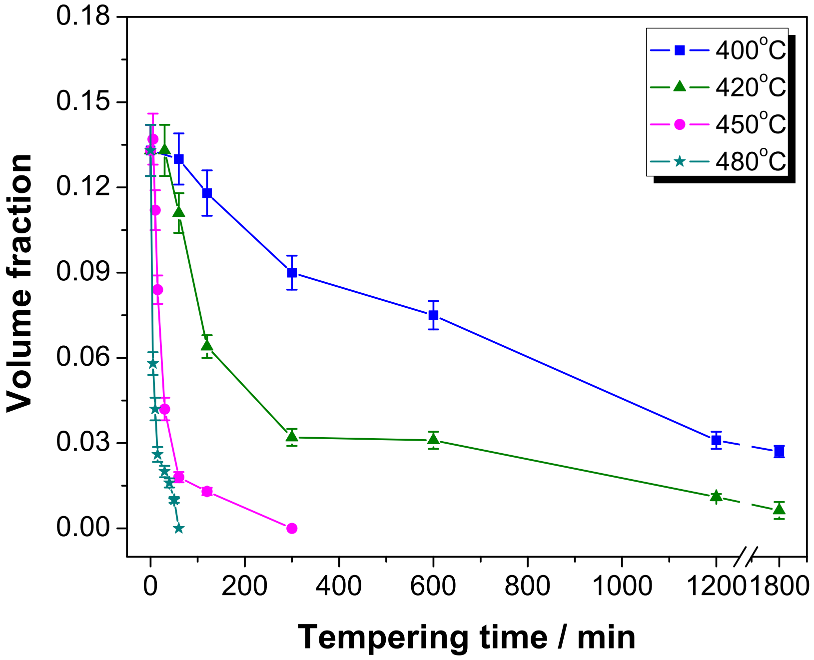

(a)

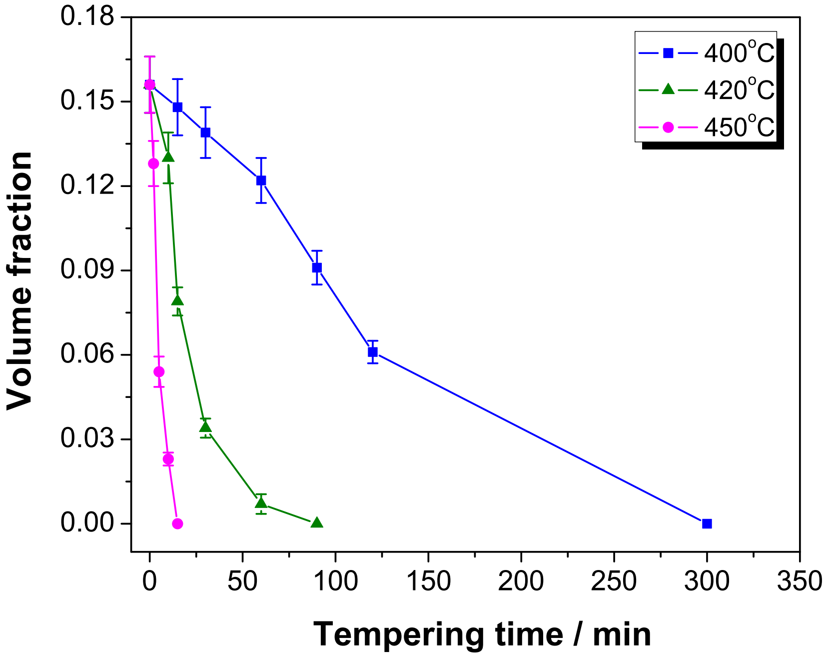

(b)

Figure 8.5: Effect of tempering on the retained austenite volume fraction measured at ambient temperature for (a) the Fe-Mn-Si and (b) the Fe-Ni-Si steels.

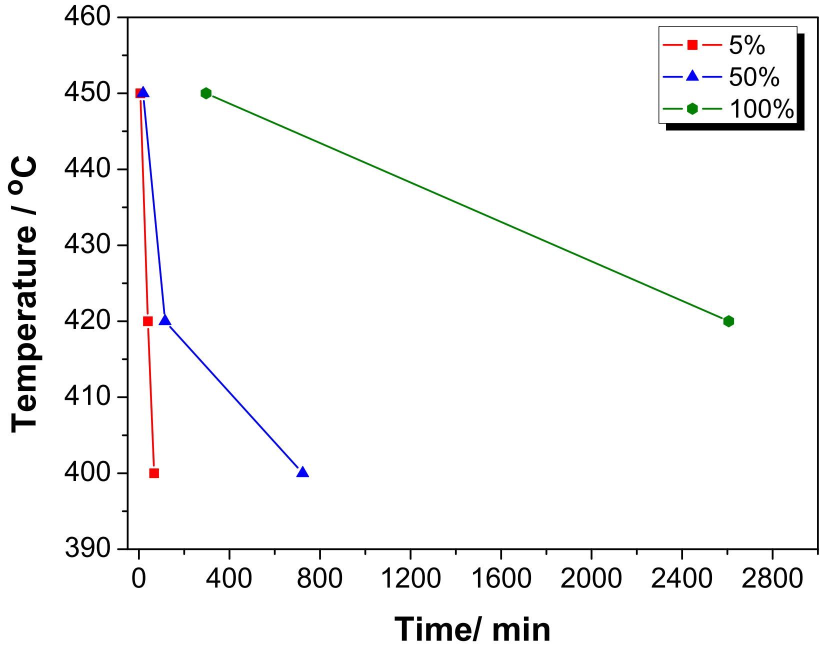

(a)

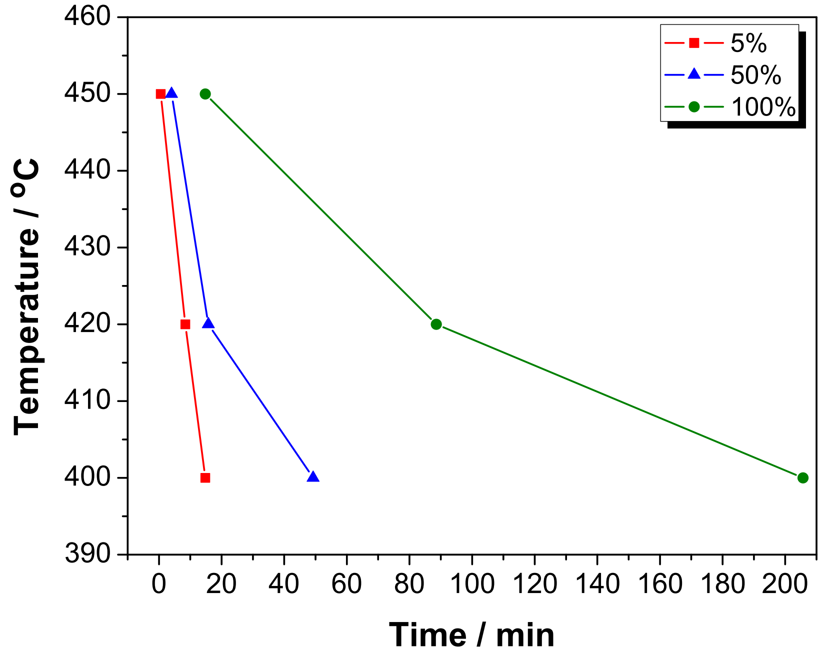

(b)

Figure 8.6: Isothermal transformation diagram for retained austenite decomposition for (a) the Fe-Mn-Si and (b) the Fe-Ni-Si steels.

8.3.2 Effect of Tempering on Hardness

Fig 8.7 shows the variation of hardness due to tempering. Not surprisingly the Fe-Ni-Si steel shows rapid reductions in hardness consistent with the kinetics of microstructural change described in previous section. Grange and Baughman [177] had shown that the Mn-containing steel poses 5 to 7 times more resistance to martensite tempering as compared with Ni-containing steel when the carbon content is within the range of 0.2 to 0.85 wt%. The initial increase in hardness of Mn containing steel is due to the formation of a significant amount of martensite. So the decrease in hardness because of softening was actually compensated by that increase. Subsequently the austenite transforming to ferrite and cementite causes a reduction in hardness. In the Ni added steel after rapid transformation in the initial stages, which is evident from the rapid decrease in hardness, the change in hardness is minimal at later stages.

8.3.3 Precipitation of Carbides During Tempering

Specific low angle X-ray diffraction scans were carried out to characterise the carbides after tempering. Figure 8.8 shows the diffraction data for the Fe-Ni-Si steel after tempering at 400°C and 420°C for different periods. The presence of ϵ-carbide after shorter duration of tempering is clear for both the tempering temperatures. With the progress of tempering, the ϵ-carbide transformed, as expected, to more stable cementite. This is similar to what is found in the martensite tempering [25, 87, 103]. The precipitation of epsilon carbide during tempering of bainite has been reported recently [178]. The scans were also conducted for Fe-Mn-Si steel, as presented in Section 5.4.3, although apart from cementite no other carbide was revealed.

Transmission electron microscopy was used to characterise the carbides after tempering of the Fe-Ni-Si steel. Figure 8.9a shows the tempered structure where ϵ-carbide formed during tempering. Figure 8.9b shows, consistent with X-ray diffraction, the corresponding electron diffraction pattern of ϵ-carbide. Extensive transmission electron microscope results failed to detect ϵ-carbide in the tempered Fe-Mn-Si steel. Carbon extraction replicas were made from the tempered Fe-Mn-Si steel but were not successful in extracting the extremely fine carbides, which are only 5-15 nm in width (Figures 5.14 and 5.15). The epsilon carbides were even finer than this. It is possible that the precipitates are coherent with the matrix, which would explain why they could not be

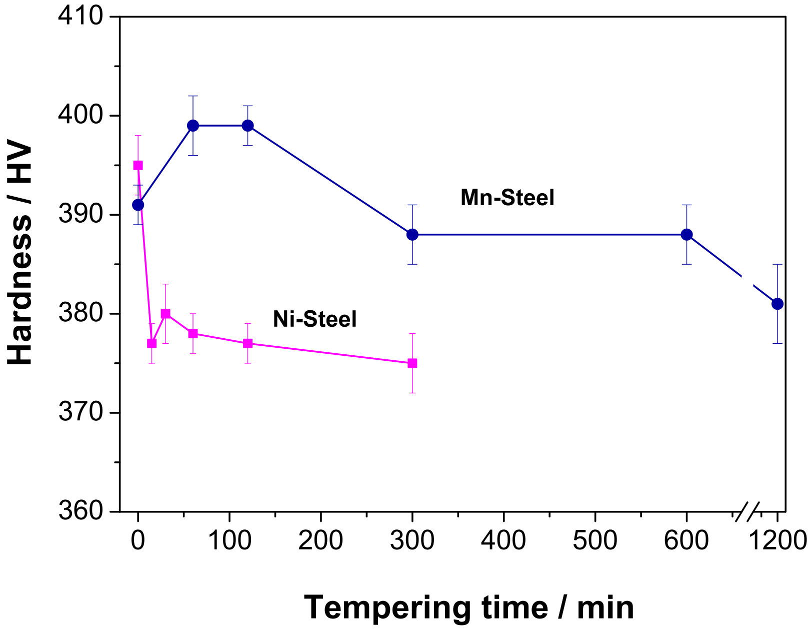

(a)

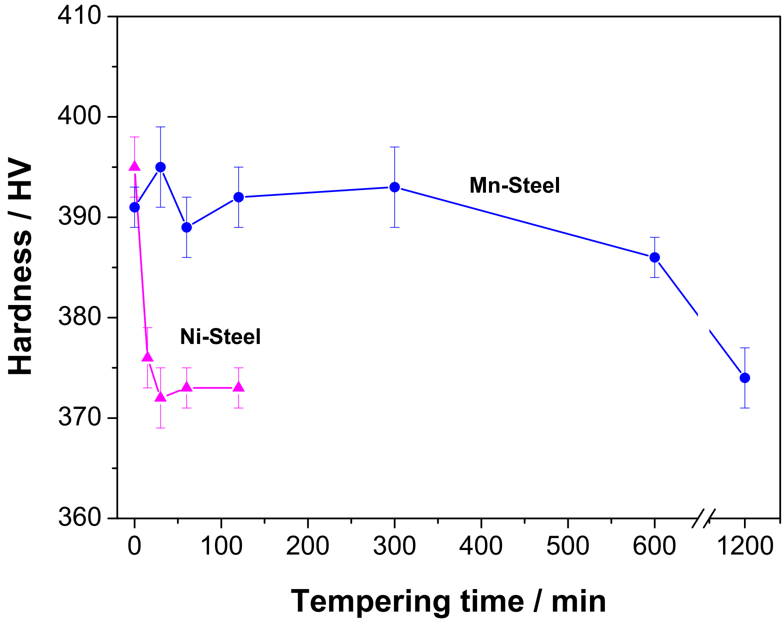

(b)

Figure 8.7: Variation of Vickers hardness with tempering time (a) 400°C and (b) 420°C.

extracted.

The Fe-Mn-Si steel tempered at 450°C for 2 h contained cementite revealed by X-ray diffraction (Section 5.4.3) and transmission electron microscopy of thin foils (Section 5.4.4). Extraction residue from this material was also analysed using X-ray diffraction to confirm the presence of carbide particles. Figure 8.10 shows the diffraction pattern after X-ray analysis indicating the cementite peaks. The diffraction pattern analysis of the filter paper was also carried out to identify any peak arising by itself.

8.3.4 Microstrain and Dislocation Density

The effect of crystallite size, microstrain and instrumental broadening can be separated conveniently if the peaks are Lorentzian or Gaussian shaped. For Lorentzian peaks the measured breadth, β_m [138]:

$$\beta_m = \beta_{inst} + \beta_{size} + \beta_{strain} \tag{8.1}$$

and for Gaussian peaks the following applies [138]:

$$\beta_m^2 = \beta_{inst}^2 + \beta_{size}^2 + \beta_{strain}^2 \tag{8.2}$$

where β_{inst}, β_{size}, β_{strain} are the contributions from instrumental broadening, crystallite size and microstrain respectively on the measured breadth. Corrections for instrumental broadening were obtained by using Lanthanum hexaboride (LaB_6), which has almost zero sample broadening.

Broadening due to size and strain components can be separated by plotting $\beta\cos\theta$ as function of $\sin\theta/\lambda$ with the implicit assumption that peaks shapes are Lorentzian. This plot is known as Williamson-Hall plot [179]. The resultant line breadth β_r=(β_m–β_{inst}) can be obtained from [180]:

$$\beta_r = 4\xi \tan\theta + \frac{K_s\lambda}{D\cos\theta} \tag{8.3}$$

where β_r is in radians, ξ is the effective lattice microstrain, θ is the Bragg angle, K_s is the shape factor, λ is the wavelength of the radiation used and D is the crystallite size.

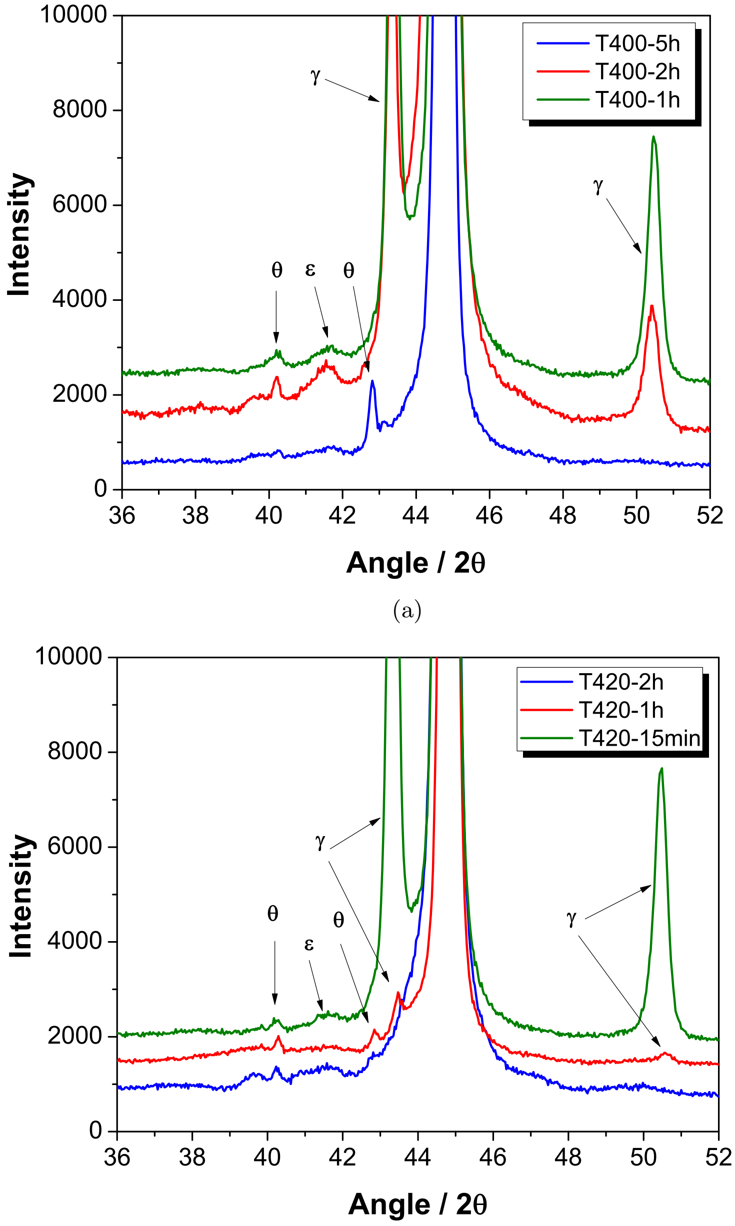

(a)

(b)

Figure 8.8: X-ray diffraction patterns from Fe-Ni-Si steel focusing on low θ, after tempering at (a) 400°C and (b) 420°C.

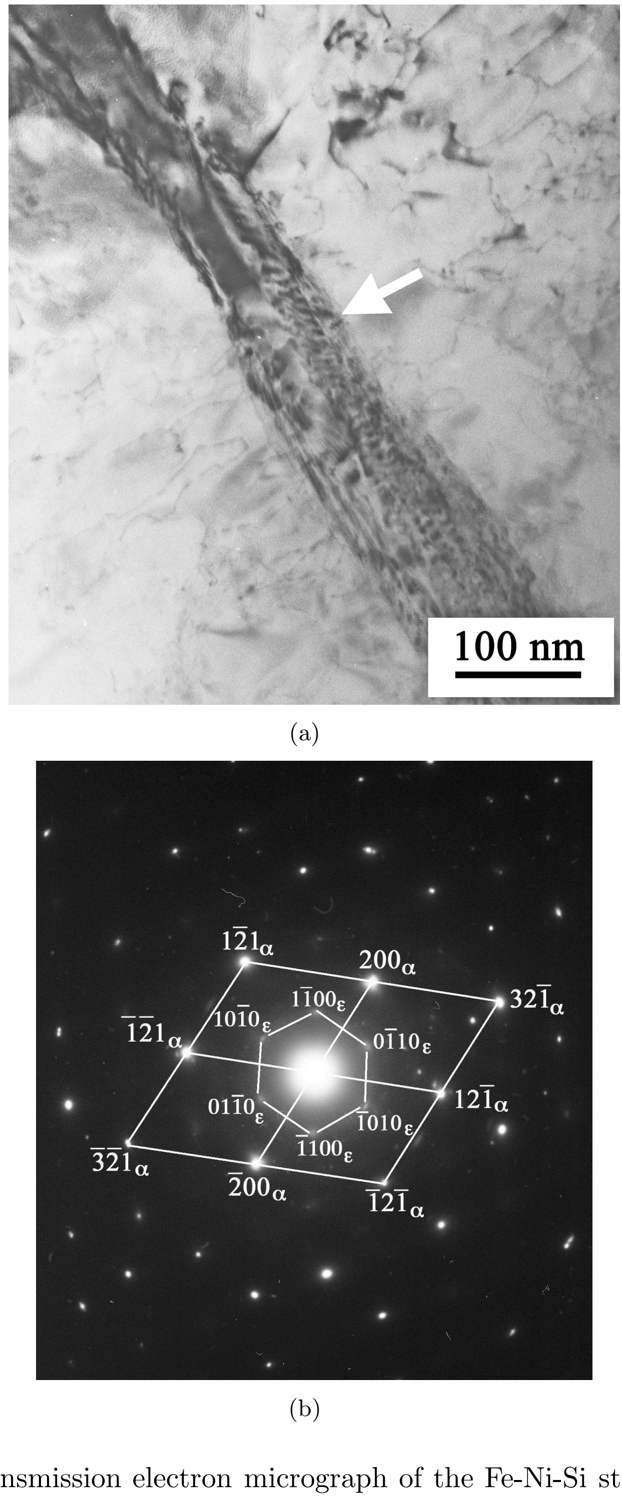

(a)

(b)

Figure 8.9: (a) Transmission electron micrograph of the Fe-Ni-Si steel showing epsilon carbide (arrowed) in the transformed austenite region after tempering at 400°C for 2 h. (b) Electron diffraction pattern of epsilon carbide in a ferritic matrix.

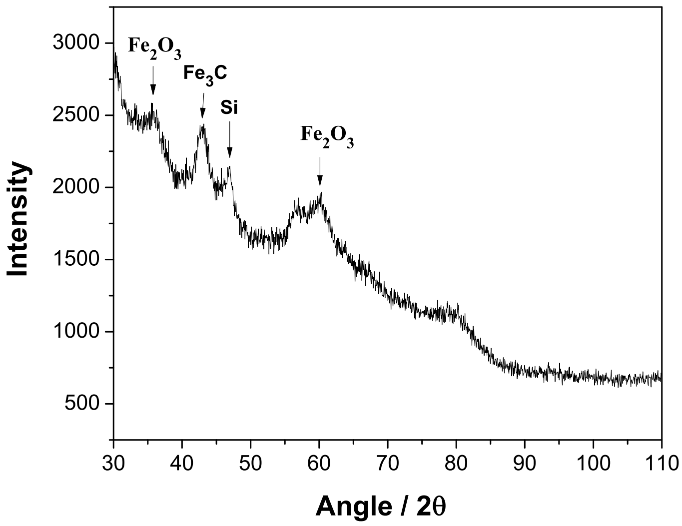

Figure 8.10: X-ray diffraction analysis of the extracted residue of Fe-Mn-Si steel after tempering at 450°C for 2 h.

The value of K_s varies from 0.89 to 1 depending upon whether β_m is the full width at half maximum (FWHM) or the integral breadth and the assumptions about peak profile and crystallite shape. Since the integral breadth was considered, K_s was taken as 1. Hence, Equation 8.3 can be re-written as:

$$\frac{\beta_r \cos\theta}{\lambda} = \frac{1}{D} + 4\xi \frac{sin\theta}{\lambda} \tag{8.4}$$

If strain broadening is the important contribution then $\beta_r \cos\theta$ is a linear function of $\sin\theta$. Plotting Equation 8.4 gives a Williamson-Hall plot where the intercept of the fitted straight line with the y axis yields the inverse of the crystallite size and from the slope microstrain can be obtained if the strain distribution is isotropic. Figure 8.11 shows a Williamson-Hall plot for the Fe-Mn-Si steel after isothermally transforming the material at 390°C for 2 h. If size broadening is the only significant contribution to peak width, then $\beta_r \cos\theta/\lambda$ is a constant for all peaks i.e. its Williamson-Hall plot would be a horizontal line.

When lattice microstrains and fine crystallite size induce Gaussian peak shape, the resultant line breadth can be obtained by adding the square of the constituents:

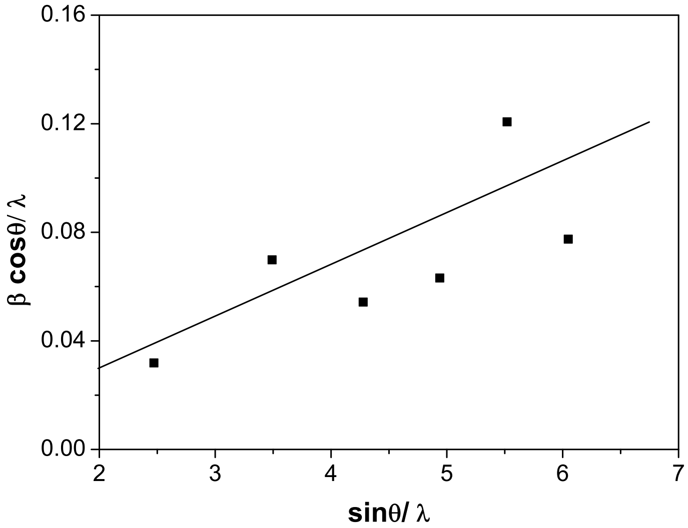

Figure 8.11: Williamson-Hall plot of the Fe-Mn-Si steel after isothermally transformed at 390°C for 2 h.

$$\beta_r^2 = (4\xi \tan\theta)^2 + \left(\frac{K_s\lambda}{D\cos\theta}\right)^2 \tag{8.5}$$

Line profiles were fitted to a pseudo-Voigt function using the Philips PROFIT software package. The package allowed a flexible control over the refinement process and provided a high degree of accuracy in profile fitting. The pseudo-Voigt function can be represented as:

$$p - V = \eta L + (1 - \eta)G \tag{8.6}$$

where L is the Lorentzian component, G is the Gaussian component and η is the mixing parameter. During the profile fitting procedure, η was refined to capture the weights of both components L and G in each peak width. This refinement yielded an excellent fit; almost all peak shapes observed were a mix of Lorentzian and Gaussian functions.

Dislocation densities and information about dislocation arrangements from the X-ray studies were deduced by Gay, Hirsch and Kelly [181]. They considered materials in terms of particles of size x which are separated by a single wall of edge or screw dislocations. Thus the dislocation density in the boundaries was expressed as:

$$D_s = \varphi/bx \tag{8.7}$$

where φ is the angle between two particles and b is the Burgers vector. The values of φ and x extracted from Debye-Scherrer rings of X-ray photograph. The dislocation density, however, calculated through this methods underestimates the actual density in the materials. It was assumed that dislocations are randomly arranged, which is unlikely when regular array of dislocations may present in the annealed materials.

Williamson and Smallman [182] overcame this difficulty by calculating dislocation densities from the line profile of X-ray measurement where breadth of the strain distribution, ξ, was deduced from the Williamson and Hall plot (Figure 8.11). The dislocation density thus calculated from the strain broadening is [182]:

$$\rho = \frac{k}{F}.\frac{\xi^2}{b^2} \tag{8.8}$$

where $k = 6\pi E(A/\mu)\ln(r/r_0)$ and varies between 2 to 25. Here E is Young's modulus, factor A depends on the shape of strain distribution, μ is shear modulus, F is interaction factor among dislocations, b is the Burgers vector of the dislocation, r is the radius of the crystal containing dislocation and r_0 is the integration limit.

A more exact calculation of k which does not involve any of the above assumptions is possible by using the results of Wilson [183] for the broadening by a screw dislocation. This calculation gives k=14.4 for body-centred cubic metals with b along <111> directions. The value of F is assumed to be 1. Hence for the calculation of the dislocation density of bainitic ferrite, Equation 8.8 becomes:

$$\rho = 14.4\,\frac{\xi^2}{b^2} \tag{8.9}$$

The Burgers vector used for the present study was 2.47×10^{-10} m [182].

The non-uniform strain of the bainitic ferrite was measured from X-ray analysis after isothermal transformation and during different stages of tempering treatments. Line profiles of {110}, {002}, {112}, {022}, {013} and {222} peaks of bainitic ferrite were taken into account. The measured non-uniform strain of the isothermally transformed specimen and tempered specimens of Fe-Mn-Si alloy are plotted in Figure 8.12. It is seen that at the beginning of tempering the strain drops drastically from that of the untempered state and this was identified for both the tempering temperatures. The rate

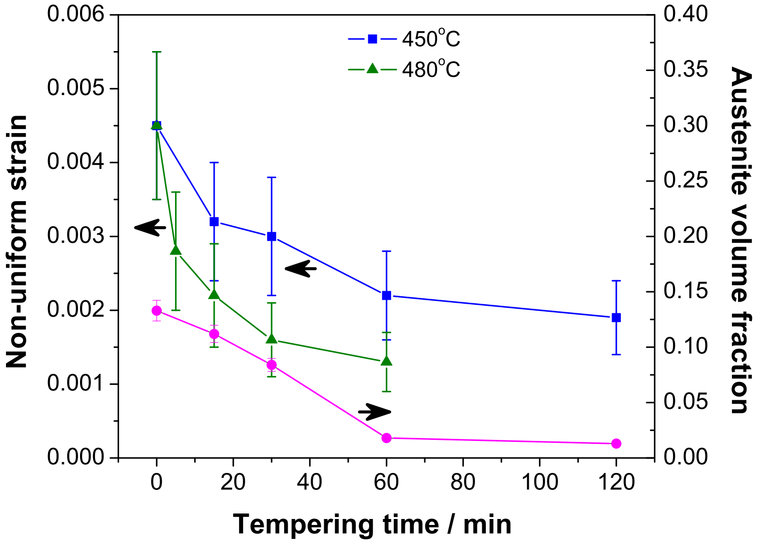

Figure 8.12: Non-uniform strain measured using X-ray analysis for the Fe-Mn-Si alloy before and after tempering at 450°C and 480°C. The austenite volume fraction was measured from specimens tempered at 450°C.

of decrease was sluggish after the initial events at 450°C and eventually after 60 min the change in strain is relatively constant. This can be correlated with the fact that until 60 min the rate of reduction of austenite volume fraction is uniform but after 60 min the austenite retained in the materials was negligible. At 480°C the decrease in strain is much faster because of higher tempering temperature. There is clear correlation between the non-uniform strain in the bainitic ferrite and the amount of austenite present in the microstructure.

A similar conclusion can also be drawn from Figure 8.13 which shows non-uniform strain in the Fe-Ni-Si steel specimens before and after tempering at 400°C and 420°C. The austenite volume fraction, obtained at 400°C, follows a similar trend with the non-uniform strain measured at the same temperature. This graph also shows the rapid decrease in strain at the initial stage of tempering.

The estimated dislocation densities for different tempering conditions are shown in Figures 8.14 and 8.15 of the Fe-Mn-Si and Fe-Ni-Si steels respectively. The dislocation density, measured using X-ray peak broadening analysis, of the isothermally transformed specimens were $4.8 \pm 1.2 \times 10^{15}\,\mathrm{m}^{-2}$ for the Fe-Mn-Si steel and $4.4 \pm 1.0 \times 10^{15}\,\mathrm{m}^{-2}$ for the Fe-Ni-Si steel. As expected, the results show a tendency to decrease dislocation den-

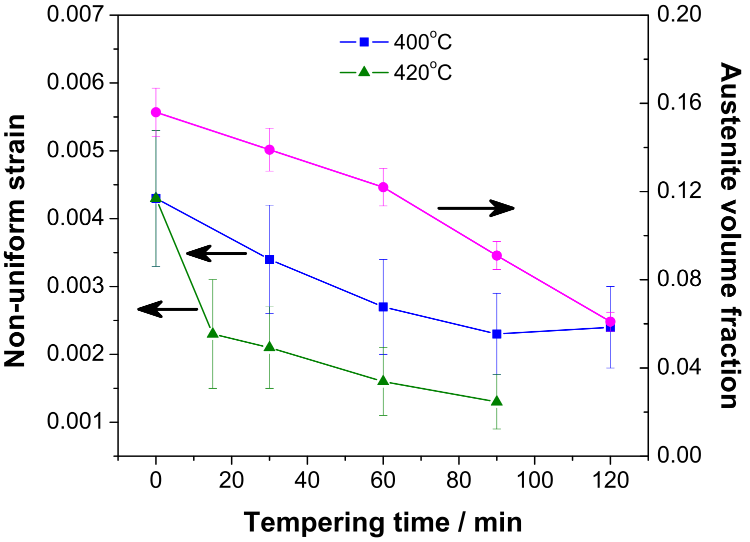

Figure 8.13: Non-uniform strain measured using X-ray analysis for the Fe-Ni-Si alloy before and after tempering at 400°C and 420°C. The austenite volume fraction was measured from specimens tempered at 400°C.

sity following tempering treatment. In the Fe-Mn-Si steel after tempering for 120 min at 450°C, the dislocation density drops down from $4.8 \pm 1.2 \times 10^{15}\,\mathrm{m}^{-2}$ to $8.5 \pm 2.2 \times 10^{14}\,\mathrm{m}^{-2}$. The interesting observation is that the dislocation density of the Fe-Mn-Si steel after tempering for 60 min at 480°C was $4.0 \pm 1.2 \times 10^{14}\,\mathrm{m}^{-2}$ which was same with the Fe-Ni-Si steel after tempering for 90 min at 420°C, in both the specimens the austenite was decomposed completely. This further supports the conclusion that dislocation density in bainitic ferrite depends on the austenite retained in the microstructure.

8.4 Electron Backscattered Diffraction

The specimen from the Fe-Ni-Si steel after isothermal transformation was used for electron backscattered diffraction (EBSD) analysis. To measure the phase fraction from the crystallographic contrast a field of 486 × 364 μm was scanned with a step size of 0.5 μm. The volume fractions of bainitic ferrite and retained austenite measured were 0.93±0.05 and 0.07±0.01 respectively. The volume fraction of austenite measured using X-ray diffraction is significantly larger than measured by this method. This is because the austenite films were not resolved (Figure 5.2). EBSD has some limitations to identify

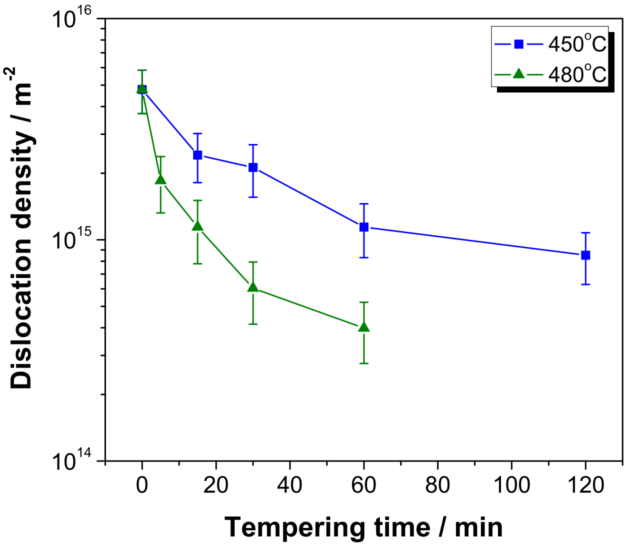

Figure 8.14: Dislocation density measured at 450°C and 480°C during different stages of tempering for the Fe-Mn-Si alloy.

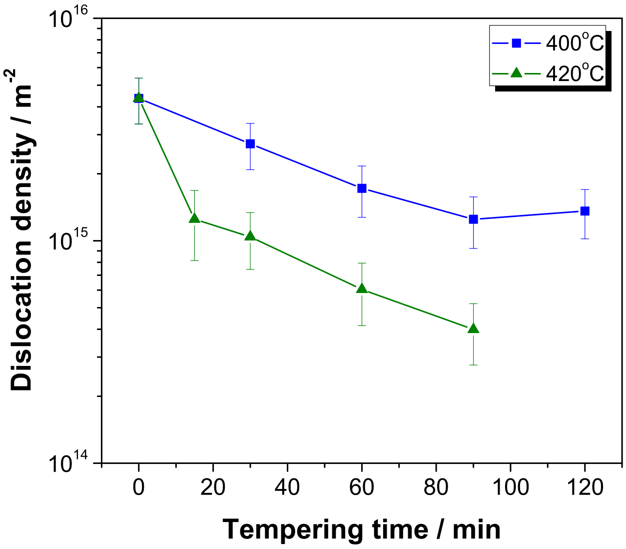

Figure 8.15: Dislocation density measured at 400°C and 420°C during different stages of tempering for the Fe-Ni-Si alloy.

fine features of less than 50 nm [184]. Moreover to determine grain or subgrain size from EBSD map, the minimum pixel step size to be considered. It was shown that to obtain an accuracy of 10% at least 5 pixels per grain are required and for an accuracy of 5%, a minimum of ∼8 pixels per grain size required [185]. Therefore, it can be concluded that EBSD is not an appropriate tool for the present purpose where microtexture is not an issue.

8.5 Discussion

The tempering behaviours of the two bainitic steels, Fe-Mn-Si and Fe-Ni-Si, have been discussed. Hardness tests show the Fe-Mn-Si steel is more resistant to tempering as compared to the Ni added steel and the hardness remains constant in the latter grade throughout the tempering process after the initial drop.

Tempering introduces different types of carbides in the microstructure, which were characterised using various techniques. Among the methods, X-ray diffraction and transmission electron microscopy were the most useful. Cementite is the only carbide formed in the Fe-Mn-Si steel whereas in the Ni-added steel both cementite and ϵ-carbide were formed as a result of tempering. Manganese was reported to decrease the rate of carbon diffusion in ferrite, therefore, delays the precipitation of the ϵ carbide [186]. But, Pacyna [187] claimed this may not be true and proposed that large concentrations of carbon and manganese are required for ϵ carbide precipitation. In further work, Pacyna [188] showed that nickel enhances ϵ carbide precipitation during tempering. It was also observed that epsilon carbide did not form during the tempering of a martensite containing 0.2 wt% carbon or less [88, 103]. The present study is consistent with this observation for the decomposition of retained austenite. The metastable ϵ-carbide transformed to stable cementite during the tempering process, as seen during the tempering of martensite [25, 87, 103].

Through experimental analysis it was observed that the austenite decomposition kinetics are much faster in the Ni-added steel compared with the Mn-added steel irrespective of the transformation temperatures (Figures 8.5 and 8.6). In order to understand the thermodynamics of the transformation, the driving force for the formation of ferrite and cementite together from the carbon-enriched austenite was calculated using MT-DATA, as shown in Figure 8.16a. Surprisingly, the driving force for the decomposition of austenite is large in the Mn-steel although this alloy showed slower transformation kinetics. To further clarify the fact, the driving force for the formation of cementite alone was calculated, shown in Figure 8.16b. This plot shows that the driving force for the formation of cementite is much higher in the Ni-containing steel compared with the Mn-added steel. This indicates that cementite formation is faster in the Ni-added steel because of higher driving force. Cementite formation naturally leads to a reduction in the carbon content of the system. Figure 8.16a described the equilibrium mixture of both the phases, whereas formation of cementite controls the kinetics of the decomposition reaction. Hence it can be concluded that because of early precipitation of cementite particles, the decomposition kinetics are faster in the Ni-added steel. In Chapter 5, similar postulation was derived for the decomposition of retained austenite, where it was observed that cementite formed first during tempering of Mn-added steel. The thermodynamic calculations confirm this fact.

It has been possible to determine the non-uniform strain during austenite decomposition from the X-ray diffraction results. The peak shapes were considered as Lorentzian type for this analysis since the estimated strains for both Lorentzian and Gaussian peak shapes were very similar. Dislocation density can also be formulated from the non-uniform strain using a numerical method. Non-uniform strain and dislocation density were measured for both the alloys and the effects of tempering on these parameters were studied. As expected, tempering has been shown to reduce the non-uniform strain and dislocation density in the materials. It is possible that the changes in non-uniform strain may be correlated with the change in retained austenite content during the tempering process. This was observed in both the alloys.

8.6 Summary

The changes that occur during the tempering of a mixture of bainitic ferrite, carbon-enriched retained austenite and martensite have been studied using different techniques for two different alloys. An in-depth study of the precipitation behavior during tempering was carried out for the two bainitic alloys. Epsilon carbide was formed as a precursor of cementite in the Fe-Ni-Si steel, whereas this sequence was not observed in the Mn-added steel. The kinetics of austenite decomposition has been observed to be much faster in the Ni-containing steel compared to the Mn-containing steel. Early precipitation of

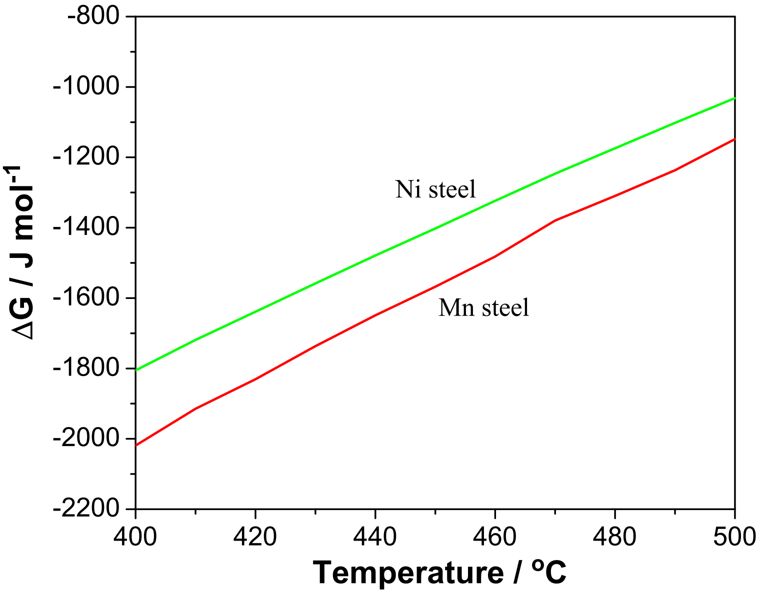

(a)

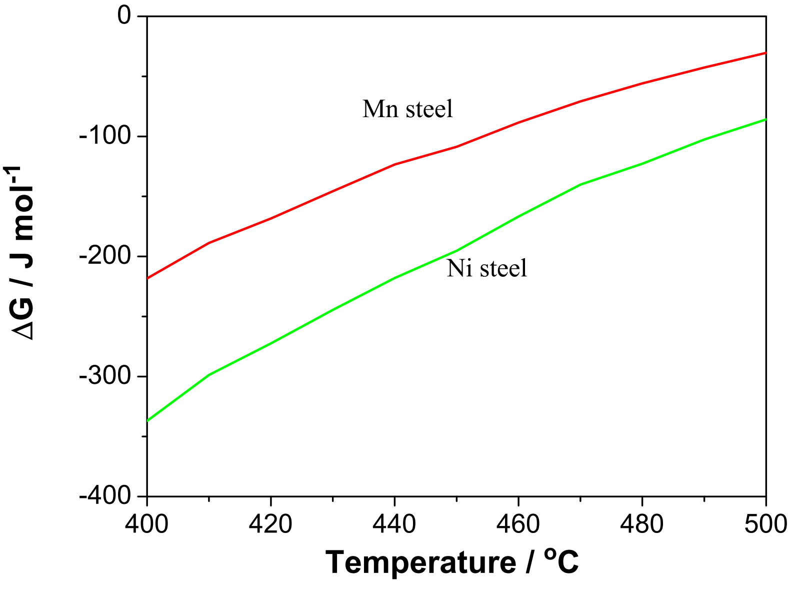

(b)

Figure 8.16: Driving force for the formation of (a) ferrite and cementite together and (b) cementite alone from carbon-enriched retained austenite under equilibrium condition. Retained austenite carbon contents of the Mn steel and the Ni steel are 0.7 wt% and 1.41 wt% respectively.

cementite controls the kinetics of the decomposition reaction. The measurement of non-uniform strain and dislocation density from the X-ray diffraction peaks broadening were discussed and the effects of tempering on these parameters were explained in terms of the austenite decomposition.

Chapter 9

Kinetics of Austenite Decomposition

9.1 Introduction

The effect of tempering on the stability of retained austenite has been discussed in Chapters 5 to 8. The retained austenite decomposes into ferrite and cementite. Some metastable carbides were formed but are eventually replaced by stable cementite. In order to generalise the results, a theory is developed and presented here to describe the overall transformation kinetics of austenite decomposition during tempering of mixtures of bainitic ferrite and retained austenite. The model takes as its inputs the appropriate compositions and thermodynamic data and estimates the volume fractions of the decomposition products as a function of time and temperature. There are only two fitting parameters, the interfacial energy and the number density of nucleation sites. Given these fitting parameters, it was decided to neglect the fact that metastable carbides precede cementite. The method truly is general and sufficiently robust to deal with multiple reactions but each additional carbide phase would introduce two further fitting parameters and reduce the ability of the method.

9.2 Model for Nucleation

The reaction modelled is as follows:

$$\gamma_R \rightarrow \alpha + \theta$$

where γ_R is the retained austenite. The nucleation rate for ferrite/cementite is given from classical nucleation theory (Section 3.2.1) as

$$I = N_V \frac{kT}{h} \exp\left(-\frac{G^* + Q}{RT} \right) \tag{9.1}$$

where the activation energy barrier to nucleation G^* is given by

$$G^* = \frac{16\pi\sigma_{\alpha\beta}^3}{3\Delta G_V^2} \tag{9.2}$$

To evaluate the nucleation rate it is necessary to determine the number of nucleation sites per unit volume, N_V, the interfacial energy per unit area, σ, and the driving force for nucleation ΔG_V. The activation energy, Q, for both ferrite and cementite was assumed to be 200 kJ mol^{-1}.

9.2.1 Chemical Free Energy Change for Nucleation

The composition of the retained austenite is given by the T_0 curve same as in the experiments used to generate the starting mixture of bainitic ferrite and austenite, the isothermal heat treatment was long enough to prevent the reaction to stop (Figure 9.1). The ultimate, expected volume fractions of ferrite and cementite were calculated from the extended $(\gamma+\theta)/\gamma$ and $(\gamma+\alpha)/\gamma$ phase boundaries using the lever rule. The driving force for the formation of ferrite and cementite during the decomposition of retained austenite was calculated using MTDATA, ferrite was calculated under para-equilibrium conditions. Figure 9.2 shows the driving force as a function of the tempering temperature for the independent formation of ferrite and cementite. The free energy change for cementite formation is less in the Mn-added steel because of the lower carbon content. The equilibrium volume fractions of the phases at different temperatures are illustrated in Figure 9.3.

9.3 Growth Model

Growth of ferrite and cementite were characterised by paraequilibrium i.e. only carbon can diffuse, since the temperatures involved are too low to permit substitutional solutes to be mobile [178]. The low transformation temperature is also responsible for the low mobility of the iron atoms [189]. The growth is therefore solely controlled by the diffusion of carbon in austenite.

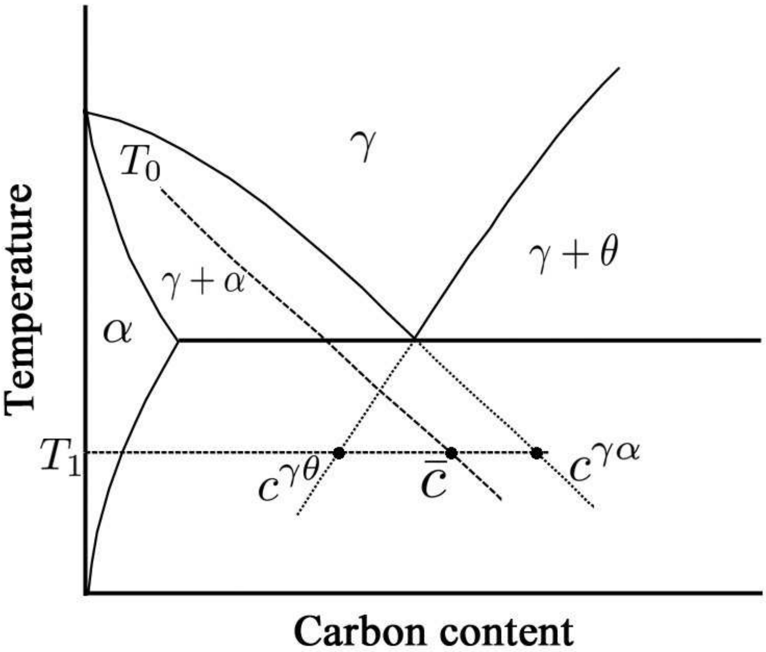

Figure 9.1: Schematic representation of the Fe-C equilibrium phase diagram with a T_0 curve superimposed.

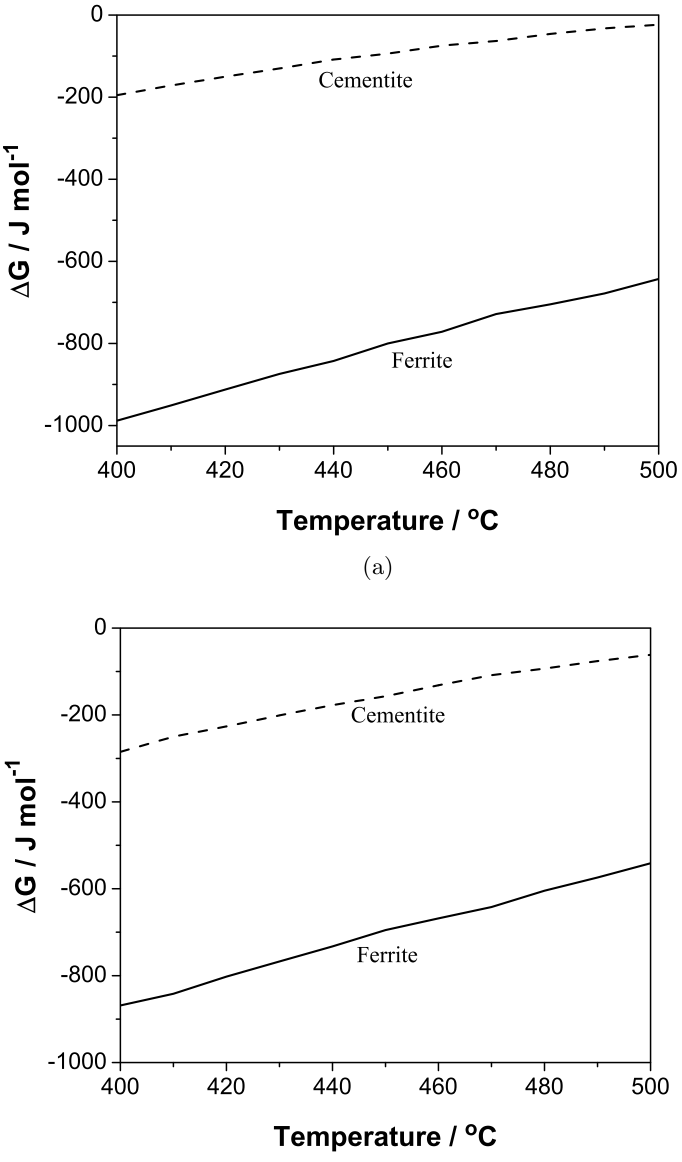

(a)

(b)

Figure 9.2: Driving force, ΔG, for given phase formation (calculated using MTDATA) for (a) the Fe-Mn-Si steel (0.7 wt%C) and (b) the Fe-Ni-Si steel (1.41 wt%C). Ferrite was calculated under para-equilibrium conditions.

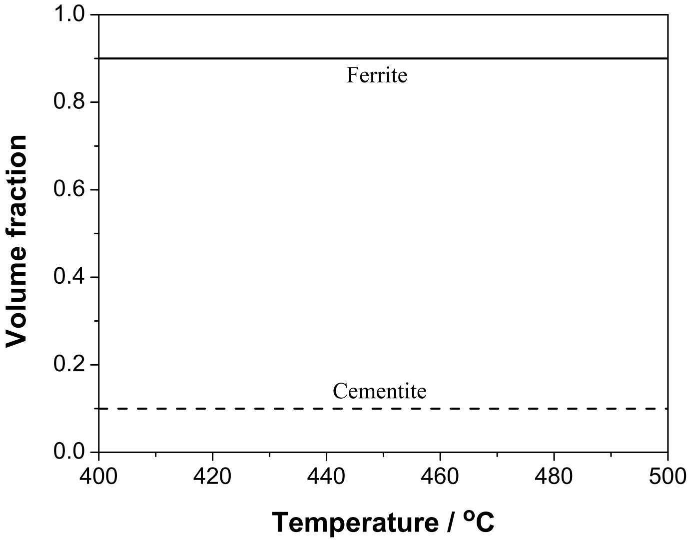

(a)

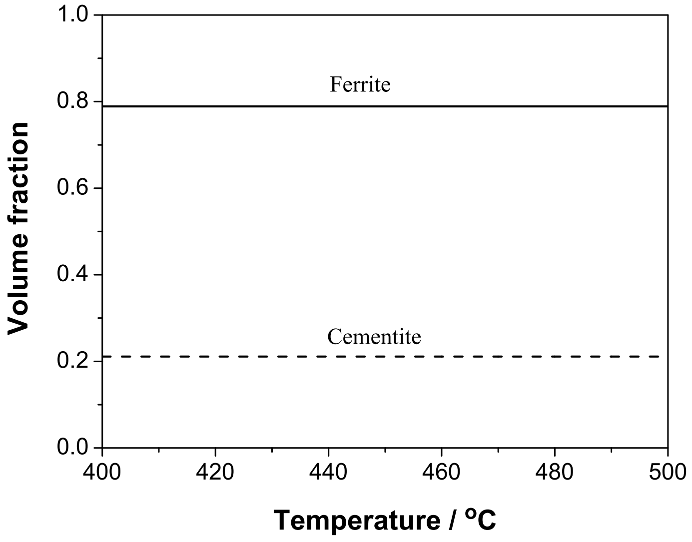

(b)

Figure 9.3: Volume fraction of phases in thermodynamic equilibrium as function of temperature (calculated using MTDATA) for (a) the Fe-Mn-Si steel (0.7 wt%C) and (b) the Fe-Ni-Si steel (1.41 wt%C).

For the austenite to ferrite transformation the concentrations at the interfaces can be obtained from the diagram, as shown in Figure 9.4.

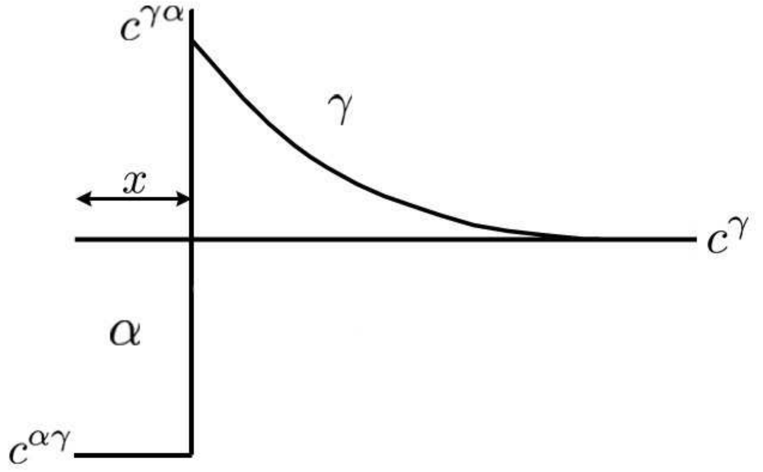

Figure 9.4: Distribution of carbon at the α/γ interface, where x is the precipitate size.

In the present case, both ferrite and cementite particles were initially assumed to grow isotropically so they can be represented by spheres of radius

$$r = \psi(t-\tau)^{1/2} \tag{9.3}$$

where ψ is the three-dimensional parabolic rate constant and an individual region may form after a time interval $t = \tau$. For the growth of cementite,

$$\psi = \frac{2^{\frac{1}{2}} D^{\frac{1}{2}} (\overline{c} - c^{\gamma\theta})^{\frac{1}{2}}}{(c^{\theta\gamma} - c^{\gamma\theta})^{\frac{1}{4}} (c^{\theta\gamma} - \overline{c})^{\frac{1}{4}}} \tag{9.4}$$

where $\overline{c}$ is the mean carbon content of austenite, $c^{\gamma\theta}$ is the carbon content in the austenite in equilibrium with cementite and $c^{\theta\gamma}$ is the carbon content of cementite in equilibrium with austenite. The volume of an individual particle at a time $t-\tau$ is given by

$$V = \frac{4}{3}\pi\psi^3(t-\tau)^{\frac{3}{2}} \tag{9.5}$$

For austenite to cementite transformation the concentrations at the interfaces follow the diagram as shown in Figure 9.5.

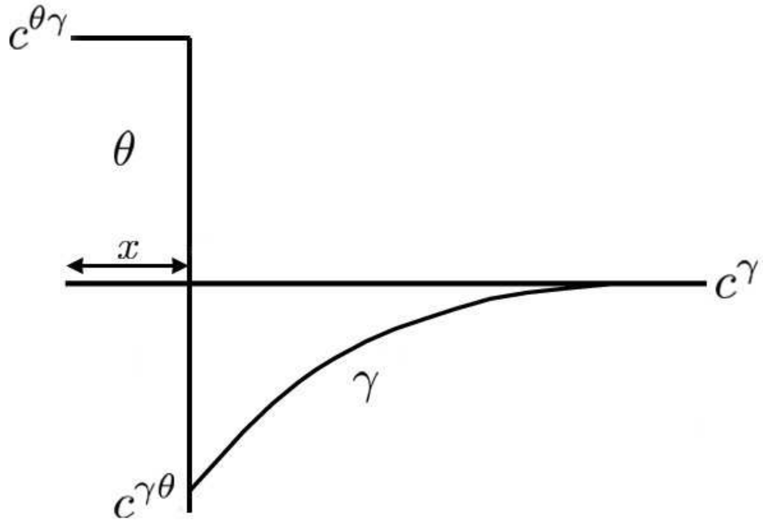

Figure 9.5: Distribution of carbon at the θ/γ interface.

The real volume fractions of ferrite and cementite were calculated from the extended volume concept, as discussed in Section 3.4. The increase in real volumes of ferrite and cementite can be expressed in terms of extended volume by [125, 190]:

$$dV_\alpha = \left(1 - \frac{V_\alpha + V_\theta}{V}\right) dV_e{}^{\alpha} \tag{9.6}$$

$$dV_\theta = \left(1 - \frac{V_\alpha + V_\theta}{V}\right) dV_e{}^{\theta} \tag{9.7}$$

where V^α and V^θ are real volumes of ferrite and cementite respectively whereas $V_e{}^\alpha$ and $V_e{}^\theta$ are the extended volumes. These are coupled equations which must be solved simultaneously.

9.3.1 Diffusion of Carbon

The diffusivity of carbon in austenite is dependent on its concentration. To account for this, Trivedi and Pound [121] proposed a weighted average diffusivity $\overline{D}$ which for the ferrite growth from austenite is given by

$$\overline{D} = \frac{1}{c^{\gamma\alpha} - \bar{c}} \int_{\bar{c}}^{c^{\gamma\alpha}} D\{c, T\}\, dc \tag{9.8}$$

where $D\{c,T\}$, the composition dependent diffusivity of carbon in austenite, $\bar{c}$ is the average carbon content of the alloy and $c^{\gamma\alpha}$ is the maximum permissible carbon content in the austenite at the transformation interface.

Siller and Mclellan [191] developed the theory for $D\{c,T\}$ where T is the absolute temperature:

$$D\{c,T\} = D'\zeta\{\delta\} \tag{9.9}$$

where δ is the atom fraction of carbon and D' is a temperature dependent but carbon concentration independent term which can be expressed as [192]:

$$D' = \frac{kT}{h}\exp(-\frac{\Delta F^*}{kT})\frac{\lambda^2}{3\gamma_m} \tag{9.10}$$

where k is Boltzmann's constant, h is Planck's constant, ΔF^* is the activation free energy which is independent of composition and temperature and represents the difference in free energy between the 'activated complex' and the 'reactants' when each is in its standard state at the temperature of 'reaction', γ_m is the activity coefficient of the activated complex and assumed constant and λ is the distance between the $\{002\}$ austenite planes. Bhadeshia [193] has derived $\Delta F^*/k$ as $21230\,\mathrm{K}^{-1}$ and $\ln(3\gamma_m/\lambda^2) = 31.84$.

Siller and Mclellan [194] showed that the concentration dependent part of Equation 9.9 is given by:

$$\zeta\{\delta\} = \Omega\left|1 + \frac{z(1+\delta)}{1-\left(\frac{z}{2}+1\right)\delta + \frac{z}{2}\left(\frac{z}{2}+1\right)(1-\sigma)\delta^2}\right| + (1+\delta)\frac{d\Omega}{d\delta} \tag{9.11}$$

where z is the coordination number of the octahedral interstitial site in the austenite lattice and Ω is the activity of carbon.

9.4 Overall Transformation Kinetics

The diffusion controlled growth of spherical particles is parabolic in all directions. Hence each dimension of the growing particle increases in proportion to the square root of time (Section 3.3.2). Considering growth to occur in a small increment of time, Δt, the change in the extended volume of spherical particles, ΔV_1^e, for the first increment of time, Δt_1, is given by [190]:

$$\Delta V_1^e = (I_1 V \Delta t_1)(C\psi_1^3 \Delta t_1^{\frac{3}{2}}) \tag{9.12}$$

where $C = 4\pi/3$ and the numerical subscripts identify the sequence of time increments, I_1 is the nucleation rate after the first increment of time and V is the volume of retained austenite. The two terms on the right designate the number of particles nucleated and the contribution of each particle to the extended volume, respectively.

After the second time interval, Δt_2, the change in extended volume, ΔV_2^e, can be written as:

$$\Delta V_2^e = (I_2 V \Delta t_2)(C\psi_2^3 \Delta t_2^{\frac{3}{2}}) + \frac{3}{2} I_1 V \Delta t_1 C \psi_2^3 (\Delta t_1 + \Delta t_2)^{\frac{1}{2}} \Delta t_2 \tag{9.13}$$

where I_2 is the nucleation rate after second time interval and the second term on the right is the contribution due to the increase in the size of particles which were nucleated in the first time interval. Since the time intervals are of equal size, the equation can be written as:

$$\Delta V_2^e = CV\Delta t^{\frac{5}{2}} \psi_2^3 \left[I_2 + \frac{3}{2} I_1 \sqrt{2} \right] \tag{9.14}$$

Therefore, after generalising, the corresponding change in extended volume for the m th time increment, ΔV_m^e, can be given by [190]:

$$\Delta V_m^e = CV\Delta t^{\frac{5}{2}} \psi_m^3 \left[I_m + \frac{3}{2}\sqrt{2} I_{m-1} \dots\dots\dots + \frac{3}{2}\sqrt{m} I_1 \right] \tag{9.15}$$

For each interval, the increase in extended volume, ΔV_j^e, for a specific phase, j, is converted to a corresponding change in actual volume, ΔV_j, allowing for the coexistence of n phases:

$$\Delta V_j = \left(1 - \frac{\sum_{i=1}^{n} V_i}{V} \right) \Delta V_j^e \tag{9.16}$$

where V_i is the real volume of the i th phase at the time t. The instantaneous value of ΔV_j, together with corresponding changes in the volumes of the other $n-1$ phases, can be used to calculate the total volume of each phase at the time $t + \Delta t$ in a computer implemented numerical procedure by writing

$$V_{j,t+\Delta t} = V_{j,t} + \Delta V_j \quad for\ j\ = 1, 2...n \tag{9.17}$$

so that a plot of the fraction of each phase can be obtained as a function of time. $V_{j,t+\Delta t}$ is the new volume of j phase after time $t + \Delta t$ and $V_{j,t}$ is the volume after time t. The growth and nucleation rates can also be updated during this step, should they have changed because of solute enrichment in the untransformed parent materials. This procedure is repeated for all the intervals from $t = 0 \rightarrow t_f$, at which time the final volume is output along with the time. The accuracy of the iterative procedure will depend on the step size which is used. Reasonable accuracy was obtained with the step size of 20 s. Reducing the step size further will not lead any improvement in the accuracy.

9.5 Predictions Using the Model

The volume fractions of the decomposition products, ferrite and cementite, were estimated using this model. Figure 9.6 shows the change in volume fractions of these phases after tempering of Fe-Ni-Si steel at 400°C. The initial volume fraction of retained austenite for this alloy was 0.19±0.01, measured using synchrotron X-ray radiation (Chapter 7). For each phase incorporated into the model there are two parameters to be adjusted to fit the experimental results. These are the nucleation site density and interfacial energy for nucleation. The parameters used for this model are listed in Table 9.1. The final volume fraction of cementite predicted using the model was 0.03 and of ferrite was 0.16 after 7 h of tempering.

Parameters	Ferrite	Cementite
Nucleation sites per unit volume, m^{-3}	2.01E+16	7.6E+18
Interfacial energy with austenite, $J\,m^{-2}$	0.035	0.012

Table 9.1: Input parameters for the model

The volume fractions of untransformed austenite both predicted and experimental are also shown in Figure 9.6. The measured amount of austenite decreased sharply at first, followed by a reduction in rate and then a further sharp reduction. The model also shows a stepwise reduction at the initial stage due to the rapid nucleation and growth of cementite (Figure 9.6) but still not fast enough compared with the experimental data. Figure 9.7 shows that the nucleation of ferrite started at the very initial stages, which

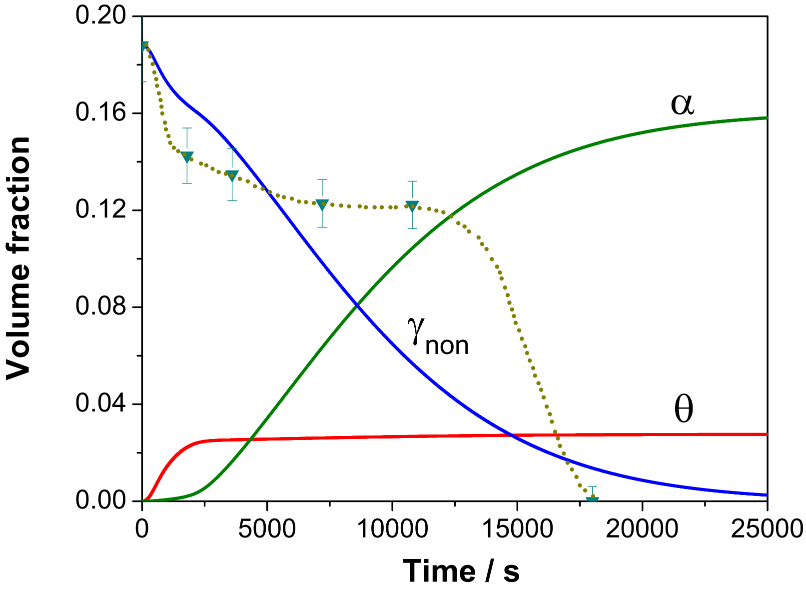

Figure 9.6: Predicted volume fractions of α and θ, non-transformed austenite (γ_{non}) and experimental results of Fe-Ni-Si alloy during tempering at 400°C.

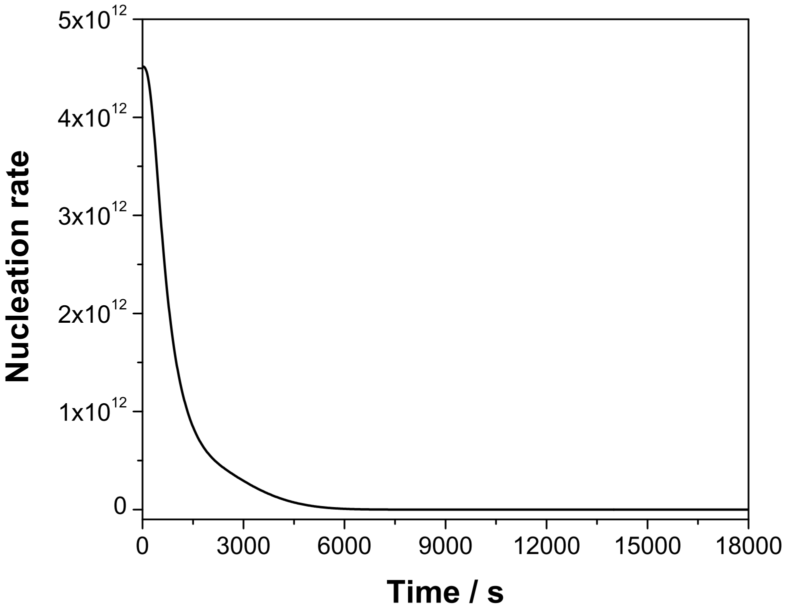

Figure 9.7: For the Fe-Ni-Si alloy, predicted volume fractions of untransformed γ after tempering at 400°C shown as continuous line whereas the experimental results are shown in as discrete points. The experimental data collected at 400°C.

from the work presented in the previous chapters indicates may not be true in reality. Figures 9.8, 9.9, 9.10 and 9.11 provide some examples of different fitting parameters used to match with the experimental results, but none of these predicted results synchronised with the experimental data. The experimental results suggest that the major ferrite formation takes place after some precipitation of cementite has occurred. The nucleation and diffusional growth theory depicted in Chapter 3 appears to be irrational for the formation of ferrite during tempering of retained austenite. Hence the present model could not explain the observed decomposition phenomenon.

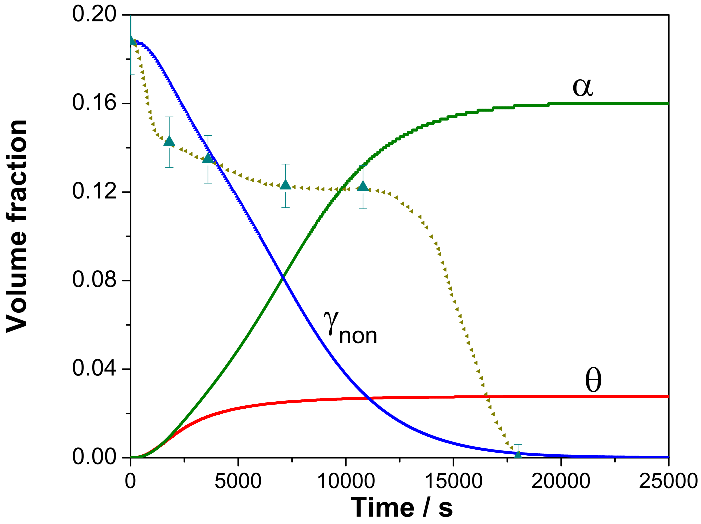

Figure 9.8: Predicted volume fractions of α and θ, non-transformed austenite (γ_{non}) and experimental results of the Fe-Ni-Si alloy during tempering at 400°C. Parameters used: for ferrite $N_V^\alpha = 5.39 \times 10^{16}\,\mathrm{m}^{-3}$ and $\sigma_{\gamma\alpha} = 0.035\,\mathrm{J\,m}^{-2}$, for cementite $N_V^\theta = 6.09 \times 10^{17}\,\mathrm{m}^{-3}$ and $\sigma_{\gamma\theta} = 0.012\,\mathrm{J\,m}^{-2}$.

The volume fractions of ferrite, cementite and untransformed austenite for the Mn-containing steel have been predicted using the model, shown in Figure 9.12. The same parameters used for this prediction are listed in Table 9.1. The prediction shows that the kinetics are faster in this alloy when compared with the Ni-containing steel (Figure 9.6). However the experimental results contradict this prediction. The results obtained from X-ray diffraction measurements at room temperature (Figures 8.5 and 8.6) indicated that the kinetics for austenite decomposition in Ni-steel were much faster compared with the Mn-steel. Hence it can be interpreted that the present model is unrealistic in terms

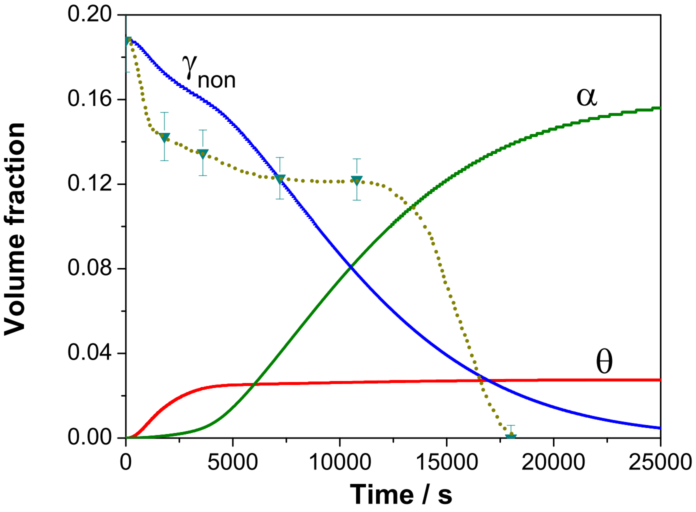

Figure 9.9: Predicted volume fractions of α and θ, non-transformed austenite (γ_{non}) and experimental results of the Fe-Ni-Si alloy during tempering at 400°C. Parameters used: for ferrite $N_V^{\alpha} = 1.66 \times 10^{15}\,\mathrm{m}^{-3}$ and $\sigma_{\gamma\alpha} = 0.028\,\mathrm{J\,m}^{-2}$, for cementite $N_V^{\theta} = 1.82 \times 10^{18}\,\mathrm{m}^{-3}$ and $\sigma_{\gamma\theta} = 0.012\,\mathrm{J\,m}^{-2}$.

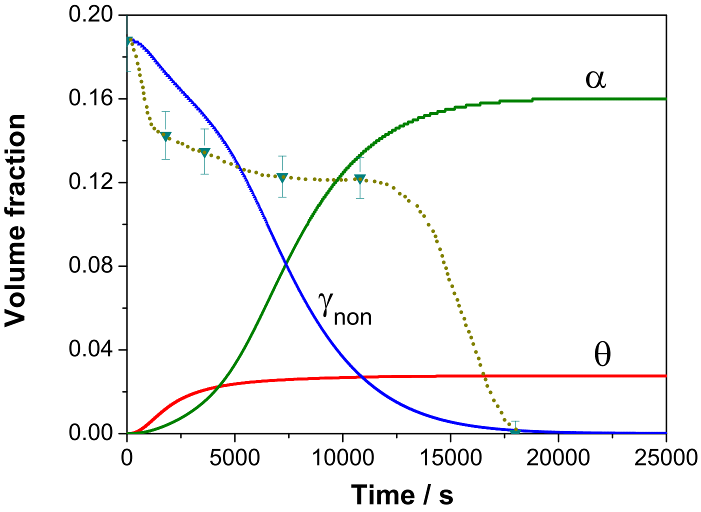

Figure 9.10: Predicted volume fractions of α and θ, non-transformed austenite (γ_{non}) and experimental results of the Fe-Ni-Si alloy during tempering at 400°C. Parameters used: for ferrite $N_V^{\alpha} = 2.85 \times 10^{15}\,\mathrm{m}^{-3}$ and $\sigma_{\gamma\alpha} = 0.023\,\mathrm{J\,m}^{-2}$, for cementite $N_V^{\theta} = 1.41 \times 10^{18}\,\mathrm{m}^{-3}$ and $\sigma_{\gamma\theta} = 0.018\,\mathrm{J\,m}^{-2}$.

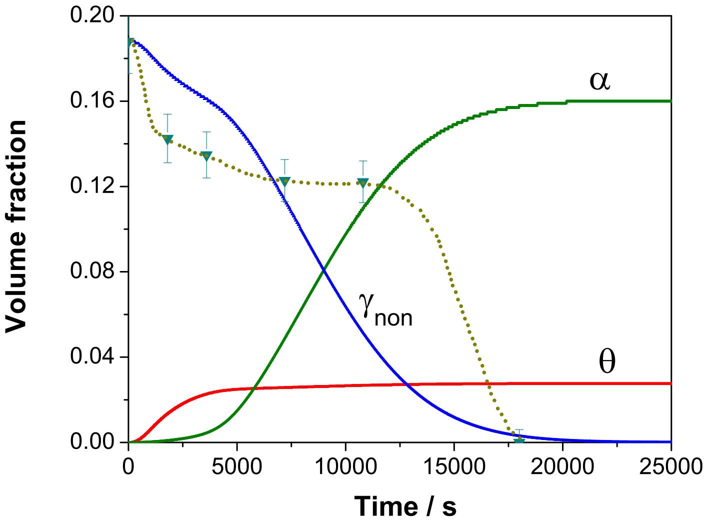

Figure 9.11: Predicted volume fractions of α and θ, non-transformed austenite (γ_{non}) and experimental results of the Fe-Ni-Si alloy during tempering at 400°C. Parameters used: for ferrite $N_V^{\alpha} = 3.07 \times 10^{14}\,\mathrm{m^{-3}}$ and $\sigma_{\gamma\alpha} = 0.009\,\mathrm{J\,m^{-2}}$, for cementite $N_V^{\theta} = 1.54 \times 10^{18}\,\mathrm{m^{-3}}$ and $\sigma_{\gamma\theta} = 0.018\,\mathrm{J\,m^{-2}}$.

of nucleation and diffusion controlled growth of ferrite. It has explained in Chapter 8 (Figure 8.16) that the driving force for the formation of ferrite and cementite together is higher for the Mn-steel, which is also consistent with the model although in reality both the phases are not forming simultaneously.

It can be concluded that the austenite decomposition reaction during tempering cannot be interpreted by the model described, with the discrepancy probably arising in the model for ferrite. Because the ferrite formation did not start at the initial stages with cementite but occurred at later stages, after which it grows very rapidly. As supported by this model and also discussed in Chapter 5, cementite particles formed at the early stages of the reaction. Rapid precipitation of cementite at the initial stages has also been explained from thermodynamic calculations in Chapter 8. These carbides were precipitated at the γ/α boundary and their sizes are as small as 2-5 nm. These fine carbides impinge the boundaries [195] and therefore the movement of the boundaries becomes restricted. It is evident from the *in situ* TEM observations (Section 6.4) that during the austenite decomposition the orientation of the old ferrite and the transformed ferrite remained the same. Hence the growth of the ferrite takes place by movement of

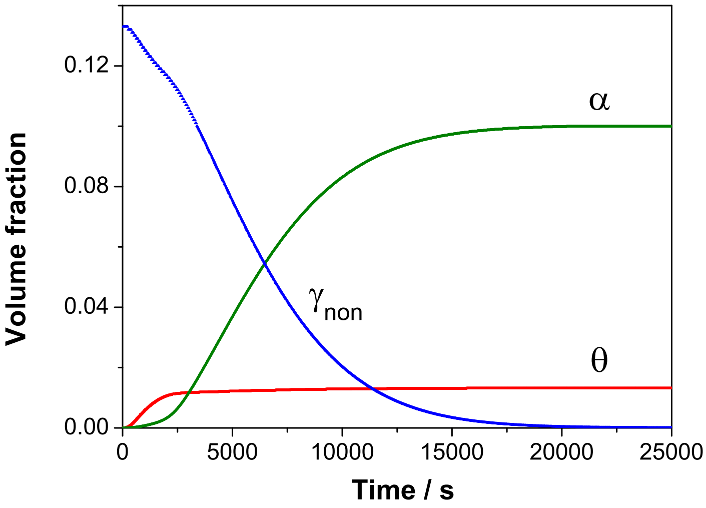

Figure 9.12: Predicted volume fractions of α, θ and non-transformed austenite (γ_{non}) of the Fe-Mn-Si alloy during tempering at 400°C.

the α/γ boundary instead of by nucleation of new ferrite. This can only be possible if the tiny cementite particles, which pin the γ/α boundaries, coarsen so the α/γ interphases bow between the particles. The explanation of growth theory in Figure 9.4 appears to be unrealistic for the decomposition of retained austenite. It is likely that ferrite growth at this transformation temperature is controlled by a displacive mechanism, which can explain the faster transformation at the later stage. Sandvik [32] showed that secondary bainitic ferrite can form from the carbon depleted austenite region by displacive transformation.

This issue can be addressed using the theory for the prediction of mechanical stabilisation, which was proposed by Chatterjee and co-workers [196]. In mechanical stabilization, the α/γ interface motion is blocked by plastic deformation debris present in the austenite rather than by the carbide particles relevant here. According to this theory, the onset of mechanical stabilisation can be predicted by balancing the force which drives the motion of the interface against the resistance of the dislocation debris. In the present system the inter-particle distance, which would have to exceeded before the γ/α boundary becomes mobile, can be estimated using this theory.

The mean stress, τ, required to force the dislocations to bow around the particles is given by [197]:

$$\tau = \frac{Gb}{8\pi(1-\nu)l} \tag{9.18}$$

where G is the shear modulus, ν the Poisson's ratio, b is the magnitude Burgers vector and l is the distance between the adjacent cementite particles.

The stress, τ_T, that drives the motion of the interface is originated from the chemical free energy change, ΔG, of transformation and is expressed by [198]:

$$\tau_T = \phi\Delta G \tag{9.19}$$

where ϕ is a constant generally assumed as unity [196] and ΔG is the chemical driving force, defined in this case as $\Delta G = G_\gamma - G_\alpha$.
Hence l can be determined by equating Equations 9.18 and 9.19:

$$l = \frac{Gb}{8\pi(1-\nu)\phi\Delta G} \tag{9.20}$$

The parameters used for this calculation are listed in Table 9.2.

Parameter	Value
Shear modulus of austenite	18×10^{10} Pa
Poisson' s ratio	0.27
Burgers vector	2.52×10^{-10} m

Table 9.2: Parameters to calculate critical inter-particle distance.

The inter-particle spacing must exceed the critical distance l to permit ferrite to form. The minimum inter-particle distances are listed in Table 9.3. The critical distance increases with increasing temperature as the value of ΔG decreases for the ferrite formation. Figure 9.13a shows the structure after 1 h of tempering at 400°C, which reveals that cementite particles are closely distributed in rows along the γ/α boundaries with inter-particle spacings less than 2 nm. After 5 h of tempering (Figure 9.13b) the non-uniformity in the distribution of cementite particles, which is associated with the coarsening of particles, can be observed. It can be estimated that the inter-particle spacing has increased to 12±4 nm after 5 h of tempering, which is higher than the 1 h sample and also more than the critical spacing required for boundary migration at this temperature. In another sample, which was tempered at the same temperature for 30 min (refer Figure 7.13 in Chapter 7) indicates that the carbides are finer than the 5 h sample as well as close to each other. Moreover, it can also be observed that between 1 h and 5 h of tempering, the precipitate size has increased to double. All these experimental evidences indicate that cementite particles have coarsened during prolonged tempering and also the inter-particle spacing has increased. Therefore, it can be concluded that the microstructural evidence supports the postulate that ferrite growth was possible in this materials due to the coarsening of cementite particles, which helped the γ/α boundary to migrate.

Tempering temperature, °C	ΔG, $\mathrm{J\,mol^{-1}}$	Inter-particle distance, nm
400	1229	6.5
420	1093	7.3
450	894	8.9

Table 9.3: Minimum inter-particle distance calculated at different tempering temperatures and the corresponding driving force for the Fe-Ni-Si alloy.

9.6 Summary

An attempt has been made to mathematically model the decomposition of the carbon-enriched retained austenite into a mixture of cementite and ferrite. Both of the product phases were, in the first instance, teated to evolve by nucleation and paraequilibrium carbon-diffusion controlled growth of spherical particles. The calculations were based on an overall transformation kinetics theory which permits simultaneous transformation to more than one phase, and in a numerical scheme which allows both hard and soft impingement to be taken into account. Each product phase required two fitting parameters, the energy of the interface in contact with austenite, and the number density of nucleation sites.

It was not possible to correctly represent the measured changes in the austenite content for any reasonable choice of fitting parameters.

The analysis is useful in demonstrating that the decomposition processes considered are not representative of what happens in reality. This is because there are inconsistencies:

(i) that with all combinations of fitting parameters, the calculations indicated significant

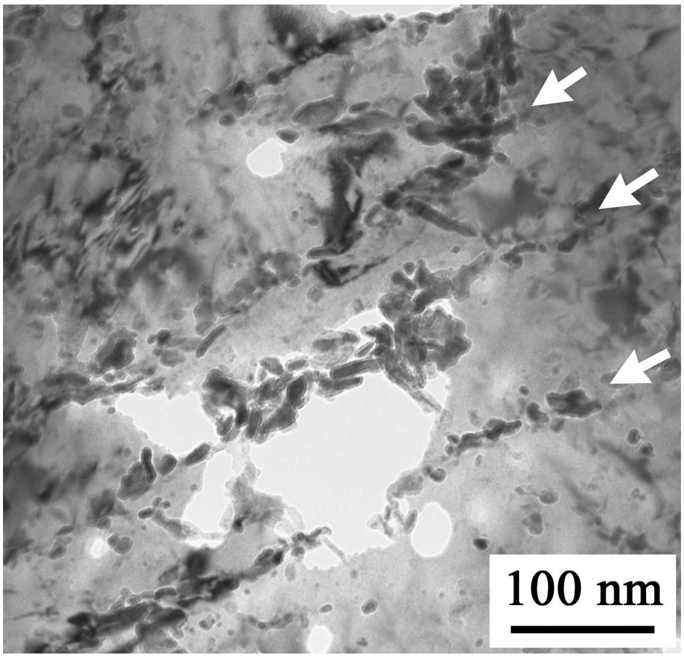

(a)

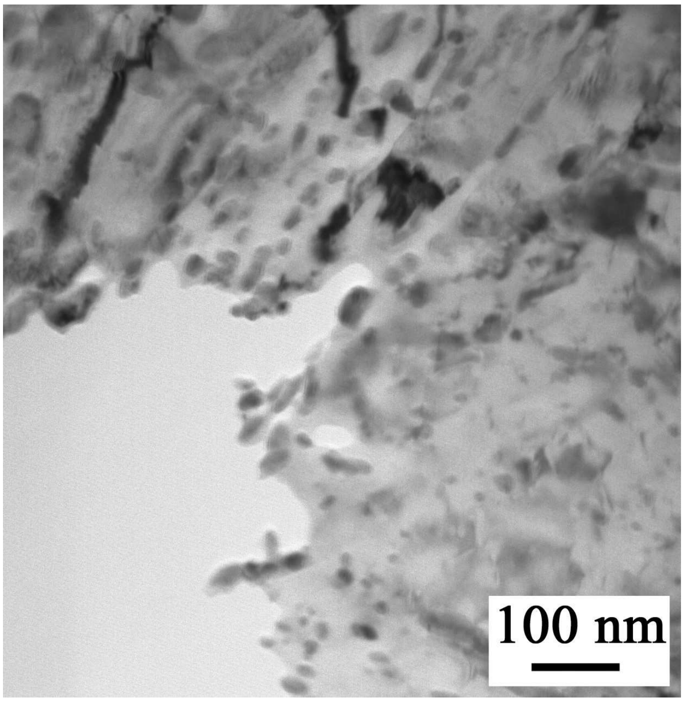

(b)

Figure 9.13: Transmission electron micrograph of the Fe-Ni-Si steel after tempering at 400°C for (a) 1 h (arrows indicate carbide precipitation along the γ/α boundary) and (b) 5 h showing inter-particle spacing and size of the carbide particles have increased during prolonged tempering.

ferrite formation at the early stages of tempering. Experiments on the other hand, show clear evidence that cementite precipitates first.

(ii) it is not reasonable to model the nucleation of ferrite by nucleation theory. The experimental evidence is that existing bainitic ferrite simply grow.

(iii) the growth of ferrite at temperatures as low as 400°C cannot be assumed to be diffusion controlled [32, 189].

An alternative explanation, the details of which have not been quantitatively modelled is that the existing α/γ interfaces can only glide when the cementite particles, which precipitate at the boundaries, coarsen sufficiently to unpin the interfaces. The austenite then decomposes relatively rapidly as indicated by experiments.

Chapter 10

General Conclusions and Future Work

The alloys studied offered a useful combination of microstructures consisting of bainitic ferrite, retained austenite and some martensite. This was achieved by the addition of silicon and other hardenability enhancing elements. The silicon, as expected, suppressed the formation of cementite during isothermal transformation, and hence enabled some austenite to be retained and studied without any interference from the presence of carbides.

Transmission electron microscopy and dilatometry led to the conclusion that during annealing, martensite tempers first followed by the decomposition of retained austenite into cementite and ferrite. This again is expected since carbon supersaturated ferrite is much less stable than the austenite. Dilatometric analysis was used to distinguish quantitavely the contraction due to martensite tempering and the expansion due to austenite decomposition. The resolution of the *Thermecmaster* was not sufficient to identify the small changes in dimensions during later stages of tempering when the austenite volume fraction was minimal.

The formation of martensite during cooling from the annealing temperature was first identified using transmission electron microscopy, which revealed untempered martensite. This places a new light on interpretations based on the measurement of retained austenite content made at ambient temperature. These results were also verified using synchrotron X-ray radiation where austenite decomposition at the annealing temperature can be unambiguously distinguished from that occurring during subsequent cooling.

In situ synchrotron radiation has proven to be a better characterization technique to study the decomposition of retained austenite. This method enabled the measurement of the true amount of retained austenite during the course of tempering. The lattice parameters and carbon contents of the individual constituents of austenite can at the same time be estimated and, with certain assumptions, it can be concluded that film type austenite has more carbon than that which is blocky and less stable under thermal load.

Defects cause heterogeneous strains. The non-uniform strain and dislocation densities were estimated from the broadening of X-ray diffraction peaks. For this analysis, peak shapes were considered as Lorentzian since the estimated strains for both Lorentzian and Gaussian peak shapes were similar. The tempering process showed a systematic reduction of dislocation densities which is expected from this heat treatment. There is a linear correlation between the dislocation densities with the amount of retained austenite present in the structure. The dislocation densities, obtained before tempering, are consistent with the literature and useful since no information of this kind is available in the context of tempered bainitic steel. However, the absolute values of the dislocation densities should be verified by direct observation.

Metastable carbides have been observed in the Ni-containing steel but not in the Mn alloys because of low carbon in the latter case. High carbon along with high manganese is a requirement for the precipitation of metastable carbides. However, there is not much literature available to justify this conclusion. Hence further research is suggested to prove the individual contributions of Mn and Ni towards the formation of carbide sequences.

The present study revealed that the kinetics of austenite decomposition of the Ni-containing steel are faster as compared with the Mn rich steel. This contradicts expectations from thermodynamic calculations on the decomposition of austenite simultaneously into ferrite and cementite under equilibrium conditions. In these circumstances kinetics of the nickel alloy should be slower. The explanation for this lies in the discovery that the tempering process begins with the precipitation of cementite alone from the carbon-enriched austenite. The early formation of cementite has been confirmed using the transmission electron microscopy and is consistent with thermodynamic estimates. A kinetic model developed for the decomposition of carbon enriched retained austenite, based on the nucleation and diffusion controlled simultaneous growth of the ferrite and cementite, could not reproduce the experimental results. In reality, rapid precipitation of cementite occurred at the initial stages of tempering while ferrite formation began subsequently. Moreover, experimental observations also showed that new ferrite does not form, rather that existing bainitic ferrite grows at the expense of austenite. The ferrite growth is then controlled primarily by movement of the γ/α boundary. The cementite particles which precipitated at the γ/α interface restrict the movement of the γ/α interfaces by pinning them. After prolonged tempering, the carbide particles coarsen, permitting the existing γ/α interfaces to advance and consume austenite, by a mechanism which is displacive.

Proposed future research:

- The measurement of non-uniform strains from the peak width broadening and the interpretation of the latter in terms of dislocation densities needs detailed direct verification. Transmission electron microscopy can be used to measure the true Burgers vector for the similar microstructures.
- Limited information is available on the stability of individual austenite constituents subjected to mechanical load. Future work should investigate these relations. The effect of pre-strain on the tempering behaviour of bainite and retained austenite would be interesting since there is some relevance in the context of TRIP-aided steels.
- The shortfall of the present work, because of time limitations, arises in cases where metastable carbides precipitate prior to the equilibrium cementite. There are few thermodynamic data available for many of the transition carbides, and their mechanisms of formation are also ill understood. In future work it would be interesting to study high-carbon alloys, where the likelihood of transition carbides is much greater, to see whether the kinetic models require major adaptation. Such a study should focus on mechanisms, so that the strain energy and non-equilibrium compositions can be characterised and understood in order to implement the physically based kinetic theory.

Appendix A

Computer Program - Transformation Strain

Program MAP_TRANS_STRAIN

A.1 Provence of Source Code

A. Saha Podder, Phase Transformations Group, Department of Materials Science and Metallurgy, University of Cambridge, Cambridge, UK.

A.2 Purpose

To calculate the transformation strain during decomposition of austenite, where the transformation of austenite into ferrite and carbide as well as tempering of martensite have been incorporated in the calculation.

A.3 Specification

This is a self-contained program written in C.

A.4 Description

The program reads chemical compositions of the alloy, volume fractions of different phases and the transformation temperature. It then calculates the strain generated in the material due to transformation.

A.5 References

1. A. Saha Podder, PhD Thesis. University of Cambridge, 2011.

2. A. Saha Podder and H. K. D. H. Bhadeshia, “Thermal stability of austenite retained in bainitic steels’, Materials Science & Engineering A, vol. 527, 2010, pp 2121-2128.

A.6 Parameters

Input parameters

XBAR - carbon content in wt%
MN - Manganese content in wt%
SI - Silicon content in in wt%
NI - Nickel content in wt%
CR - Chromium content in wt%
MO - Molybdenum content in wt%
V - Vanadium content in wt%
TC - Transformation temperature in ^{o}C
VGI - Initial volume fraction of austenite
VAI - Initial volume fraction of martensite
VAF - Final volume fraction of ferrite
VCF - Final Volume fraction of cementite

Output parameters

S - Transformation strain

A.7 Program Listing

```
#include <stdio.h>
#include <stdlib.h>
#include <math.h>

double FE, XBAR, MN, SI, NI, CR, MO, V;
double VAI, VAF, VCI, VCF, VGI, AA, AA1, AC1, AC2, AC3;
```

```
double AG, AAT, AAT1, AC1T, AC2T, AC3T, AGT, AAA, AAC, AAAT, AACT;
double EXA, EXC, EXG, TC, T, SG, SM;
double mol_fraction();

int main(void)
{
printf(``Enter Steel Chemistry in wt%:\n");
printf(``Carbon: ");
scanf(``%lf",&XBAR);
printf(``Manganese: ");
scanf(``%lf",&MN);
printf(``Silicon: ");
scanf(``%lf",&SI);
printf(``Nickel: ");
scanf(``%lf",&NI);
printf(``Chromium: ");
scanf(``%lf",&CR);
printf(``Molybdenum: ");
scanf(``%lf",&MO);
printf(``Vanadium: ");
scanf(``%lf",&V);
printf(``Transformation Temperature in C: ");
scanf(``%lf",&TC);
T= TC + 273;
printf(``Initial Vol frac of Austenite: ");
scanf(``%lf",&VGI);
printf(``Initial Vol frac of Martensite: ");
scanf(``%lf",&VAI);
printf(``Final Vol frac of Ferrite: ");
scanf(``%lf",&VAF);
printf(``Final Vol frac of Cementite: ");
scanf(``%lf",&VCF);

if (VGI > 0)
{
AG= 0.3573 + 0.0033*XBAR + 0.000095*MN − 0.00002*NI + 0.00006*CR
+0.00031*MO+0.00018*V;
printf(``AG= %lf\n", AG);
printf(``Carbon content of transformed ferrite (wt%): ");
scanf("%lf",&XBAR);
mol_fraction();
EXA= 0.00001244;
EXG= 0.00002065;
```

```
EXC= 6.0*pow(10,-6)+(3.0*pow(10,-9)*(T-273.0))+(1.0*pow(10,-11)*
pow((T-273.0),2.0));
AC1= 0.45246;
AC2= 0.50885;
AC3= 0.67423;
AAT= AA*(1.0 + EXA*(T-298.0));
AGT= AG*(1.0 + EXG*(T-298.0));
AC1T= AC1*(1.0 + EXC*(T-298.0));
AC2T= AC2*(1.0 + EXC*(T-298.0));
AC3T= AC3*(1.0 + EXC*(T-298.0));
SG=0;
SG= ((2.0*VAF*pow(AAT,3.0) + (VCF*AC1T*AC2T*AC3T)/3.0
-VGI*pow(AGT,3.0))/(3.0*VGI*pow(AGT,3.0)))*VGI;
printf(''Strain due to austenite decomposition= %lf\n\n", SG);
}
else
{
printf(''Carbon content of martensite (in wt%): ");
scanf(''% lf",&XBAR);
mol_fraction();
AA1=AA;
EXA= 0.00001244;
EXG= 0.00002065;
EXC= 6.0*pow(10,-6) + (3.0*pow(10,-9)*(T-273.0))
+ (1.0*pow(10,-11)*pow((T-273.0),2.0));
AC1= 0.45246;
AC2= 0.50885;
AC3= 0.67423;
//calculation of lattice parameter of martensite
AAA= AA1-0.0038*XBAR;
AAC= AA1+0.0054*XBAR;
printf(''Lattice parameter of martensite:\n");
printf(''AAA= %lf\n", AAA);
printf(''AAC= %lf\n", AAC);
AAAT= AAA*(1.0 + EXA*(T-298.0));
AACT= AAC*(1.0 + EXA*(T-298.0));
AGT= AG*(1.0 + EXG*(T-298.0));
AC1T= AC1*(1.0 + EXC*(T-298.0));
AC2T= AC2*(1.0 + EXC*(T-298.0));
AC3T= AC3*(1.0 + EXC*(T-298.0));
printf(''Carbon content in transformed ferrite (in wt%): ");
scanf(''% lf",&XBAR);
mol_fraction();
```

```
AAT= AA*(1.0 + EXA*(T-298.0));
SM = ((6.0*VAF*pow(AAT,3) + (VCF*AC1T*AC2T*AC3T)
- (6.0*VAI*AAAT*AAAT*AACT))/(3.0*6.0*VAI*AAAT*AAAT*AACT))*VAI;
printf(‘‘Strain due to martensite tempering= %lf\n\n”, SM);
}
}

double mol_fraction()
{
double X_C = 0;
double X_SI = 0;
double X_MN = 0;
double X_CR = 0;
double X_NI = 0;
double X_V = 0;
double X_MO = 0;
double total_moles= 0;
AA=0;
FE = 100-XBAR -MN - SI - CR - NI - MO - V;
total_moles = XBAR/12.01115 + FE/55.847 + SI/28.086 + MN/54.847
+ NI/58.71 + MO/95.94 + CR/51.996 + V/50.9415;
X_C= (XBAR/12.01115)/total_moles;
X_SI= (SI/28.086)/total_moles;
X_MN= (MN/54.847)/total_moles;
X_CR= (CR/51.996)/total_moles;
X_NI= (NI/58.71)/total_moles;
X_V= (V/50.9415)/total_moles;
X_MO= (MO/95.94)/total_moles;
AA= 0.28664 + ((pow((0.28664-0.0279*X_C),2)*(0.28664 + 0.2496*X_C)
-pow(0.28664,3))/(3*pow(0.28664,2))) - 0.003*X_SI + 0.006*X_MN
+ 0.007*X_NI + 0.031*X_MO + 0.005*X_CR + 0.0096*X_V;
return AA;
}
```

Appendix B

Computer Program - Kinetics of Austenite Decomposition

Program MAP_KINETCS_TEMPERING

B.1 Provence of Source Code

A. Saha Podder, Phase Transformations Group, Department of Materials Science and Metallurgy, University of Cambridge, Cambridge, UK.

B.2 Purpose

To calculate the overall transformation kinetics for the decomposition of carbon-enriched retained austenite during isothermal tempering treatment, where simultaneous transformations to both ferrite and cementite have been considered.

B.3 Specification

This is a self-contained program written in C.

B.4 Description

The model uses thermodynamic data (e.g. from MTDATA or Thermo Calc) in terms of free energy and chemical compositions. It then calculates the evolution of volume fractions of ferrite and cementite simultaneously with respect to time and temperature.

B.5 References

1. A. Saha Podder, PhD Thesis. University of Cambridge, 2011.

B.6 Parameters

Input parameters

XBAR - Carbon content in wt%

MN - Manganese content in wt%

SI - Silicon content in in wt%

NI - Nickel content in wt%

CR - Chromium content in wt%

MO - Molybdenum content in wt%

V - Vanadium content in wt%

X_gt - Mole fraction of carbon content of austenite in equilibrium with cementite

X_tg - Mole fraction of carbon content of cementite in equilibrium with austenite

X_ga - Mole fraction of carbon content of austenite in equilibrium with ferrite

X_ag - Mole fraction of carbon content of ferrite in equilibrium with austenite

Xbulk - Bulk carbon content of austenite

TempC - Temperature in celsius

Sigma_ga - Interfacial energy between austenite and ferrite

Sigma_gt - Interfacial energy between austenite and cementite

fa - No. of nucleation sites/unit area

Output parameters

Volume fractions of ferrite and cementite with time

B.7 Program Listing

```
#include <stdio.h>
#include <stdlib.h>
#include <math.h>
#define k 1.3806503E-23
#define h 6.626068E-34
```

```
#define R 8.314472
#define W 8250.0
#define Av 6.0221415E+23
#define PI 3.142857
#define MAXNUM 50000


double a[650][10],I_THETA[MAXNUM],I_ALPHA[MAXNUM];
double FE,XBAR,MN,SI,NI,CR,MO,V,X_mole,X_atom,X_m,X_wt;
double TempC,TempK;
double X_bulk,Xg,X_gt,X_tg,X_ga;
double X_ag,X_atom_aus,X_atom_cem,X_atom_fer;
double ALPHA,DALPHA,up_limit,low_limit,
double EDIFF,DIFF_THETA,DIFF_ALPHA;
double FE_gamma,FE_gamma_theta,FE_gamma_alpha;
double G_dash_theta2,G_dash_theta1,G_dash_theta;
double G_dash_alpha2,G_dash_alpha1,G_dash_alpha,del_G,G_star;
double Nr_theta,Nr_alpha,Gr_theta,Gr_alpha;
double Sigma_gt,Sigma_ga,Rc_theta,Rc_alpha,fa,fb,fc;
double V_theta,V_alpha,V_gamma,V_gamma0;
double dV_theta,dV_alpha,dV_gamma,V_frac_gamma_trans;
double dVe_theta,dVe_alpha,V_EXD_THETA,V_EXD_ALPHA;
double TTT,Ts,Tn,dt,t;
double dY_theta,Y_theta,Y_gamma,Y_gamma0,dR_theta,R_theta;
double mole_fraction(),atom_fraction(),wt_percent();
double alpha(),dalpha(),diffuse(),nrate_theta(),nrate_alpha();

int main(void)
{
FILE *fxauscem,*fxausfer,*fxcemaus,*fxferaus,*fg,*fout;
int i,j,m,n,p,q,r,s,ITN,id;
double J,L1,L2,T_moles;
printf(‘‘Enter Steel Chemistry in wt%:\n”);
printf(‘‘Manganese: ”);
scanf(‘‘%lf”,&MN);
printf(‘‘Silicon: ”);
scanf(‘‘%lf”,&SI);
printf(‘‘Nickel: ”);
scanf(‘‘%lf”,&NI);
printf(‘‘Chromium: ”);
scanf(‘‘%lf”,&CR);
printf(‘‘Molybdenum: ”);
scanf(‘‘%lf”,&MO);
```

```
printf(‘‘Vanadium: ”);
scanf(‘‘%lf”,&V);
printf(‘‘Enter material identification no: ”);
scanf(‘‘%d”,&id);
printf(‘‘Enter temperature in Celcius: ”);
scanf(‘‘%lf”,&TempC);
printf(‘‘Enter transformation time (min): ”);
scanf(‘‘%lf”,&TTT);
TempK = TempC+273;

fxauscem = fopen(‘‘x_aus_cem.txt”,‘‘r”);
fxausfer = fopen(‘‘x_aus_fer.txt”,‘‘r”);
fxcemaus = fopen(‘‘x_cem_aus.txt”,‘‘r”);
fxferaus = fopen(‘‘x_fer_aus.txt”,‘‘r”);
fg = fopen(‘‘free_energy_Ni.txt”,‘‘r”);
fout = fopen(‘‘output_Ni.txt”,‘‘w”);

// reading carbon content of austenite in equilibrium with cementite
for(i=1;i<=602;i++)
{
for(j=1;j<=2;j++)
{
fscanf(fxauscem,‘‘%lf”,&a[i][j]);
if(a[i][j] == TempK)
{
m=i;
n=j+1;
fscanf(fxauscem,‘‘%lf”,&a[m][n]);
XBAR = a[m][n];
}
}
}
mole_fraction();
X_gt = X_mole;
printf(‘‘Mole fraction of X_gt = %.6lE\n\n”,X_gt);

// reading carbon content of cementite in equilibrium with austenite
for(i=1;i<=602;i++)
{
for(j=1;j<=2;j++)
{
fscanf(fxcemaus,‘‘%lf”,&a[i][j]);
if(a[i][j] == TempK)
```

```
{
m=i;
n=j+1;
fscanf(fxcemaus,‘‘%lf”,&a[m][n]);
XBAR = a[m][n];
}
}
}
mole_fraction();
X_tg = X_mole;

// reading carbon content of austenite in equilibrium with ferrite
for(i=1;i<=602;i++)
{
for(j=1;j<=2;j++)
{
fscanf(fxausfer,‘‘%lf”,&a[i][j]);
if(a[i][j] == TempK)
{
m=i;
n=j+1;
fscanf(fxausfer,‘‘%lf”,&a[m][n]);
XBAR = a[m][n];
}
}
}
mole_fraction();
X_ga = X_mole;

// reading carbon content of ferrite in equilibrium with austenite
for(i=1;i<=602;i++)
{
for(j=1;j<=2;j++)
{
fscanf(fxferaus,‘‘%lf”,&a[i][j]);
if(a[i][j] == TempK)
{
m=i;
n=j+1;
fscanf(fxferaus,‘‘%lf”,&a[m][n]);
XBAR = a[m][n];
}
}
```

```
}
mole_fraction();
X_ag = X_mole;

// reading free energy data and average carbon content of gamma
for(i=1;i<10;i++)
{
for(j=1;j<6;j++)
{
fscanf(fg,‘‘%lf”,&a[i][j]);
if(a[i][j] == TempK)
{
m=i;
n=j+1;
fscanf(fg,‘‘%lf %lf %lf %lf %lf”,&a[m][n],&FE_gamma,
&FE_gamma_alpha,&FE_gamma_theta,&T_moles);
XBAR = a[m][n];
}
}
}
mole_fraction();
X_bulk = X_mole;

G_dash_theta2 = FE_gamma_theta - FE_gamma;
G_dash_theta1 = G_dash_theta2/(T_moles*7.255E-6);
G_dash_theta = G_dash_theta1/(X_bulk/X_tg);
G_dash_alpha1 = FE_gamma_alpha - FE_gamma;
G_dash_alpha = G_dash_alpha1/(T_moles*7.255E-6);

//Overall simultaneous transformation kinetics
Ts = TTT*60;
dt = 20;
Tn = Ts/dt;
ITN = Tn;
V_gamma0 = PI*16*12*0.156*(1E-9);
Xg = X_bulk;
V_theta = 0;
V_alpha = 0;
fc = 4*PI/3;
I_THETA[1] =0;
I_ALPHA[1] =0;
nrate_theta();
nrate_alpha();
```

```
fprintf(fout,‘‘Time step (dt) = %.1lf sec”,dt);
fprintf(fout,‘‘Volume of austenite = %.3lE”,V_gamma0);
fprintf(fout,‘‘Time V_theta V_alpha V_gamma_untrans”);

for(p=1;p<=ITN;p++)
{
if(Xg > X_gt && Xg < X_ga)
{
t = p*dt;
V_EXD_THETA = 0;
V_EXD_ALPHA = 0;
X_mole = Xg;
alpha();
dalpha();

//diffusivity calculation for cementite
X_m = Xg;
wt_percent();
XBAR = X_wt;
atom_fraction();
X_atom_aus = X_atom;
up_limit = X_gt;
low_limit = Xg;
diffuse();
DIFF_THETA = EDIFF;

//diffusivity calculation for ferrite
up_limit = X_ga;
low_limit = Xg;
diffuse();
DIFF_ALPHA = EDIFF;

L1 = I_THETA[1]/Nr_theta;
if(L1 >100000)
{
I_THETA[p] = 0;
}
else
{
nrate_theta();
I_THETA[p] = Nr_theta;
}
L2 = I_ALPHA[1]/Nr_alpha;
```

```
if(L2 >100000)
{
I_ALPHA[p] = 0;
}
else
{
nrate_alpha();
I_ALPHA[p] = Nr_alpha;
}
J = p;
Rc_theta = sqrt(2*(Xg-X_gt)*DIFF_THETA)/(pow((X_tg-X_gt),0.25)*
pow((X_tg-Xg),0.25));
Rc_alpha = sqrt(2*(X_ga-Xg)*DIFF_ALPHA)/(pow((Xg-X_ag),0.25)*
pow((X_ga-X_ag),0.25));
for(q=1;q<(p+1);q++)
{
if(q == p)
{
dVe_theta= fc*V_gamma0*pow(dt,2.5)*pow(Rc_theta,3)*I_THETA[q];
dVe_alpha= fc*V_gamma0*pow(dt,2.5)*pow(Rc_alpha,3)*I_ALPHA[q];
}
else
{
dVe_theta = fc*V_gamma0*pow(dt,2.5)*pow(Rc_theta,3)*
I_THETA[q]*1.5*sqrt(J);
dVe_alpha = fc*V_gamma0*pow(dt,2.5)*pow(Rc_alpha,3)*
I_ALPHA[q]*1.5*sqrt(J);
}
V_EXD_THETA = V_EXD_THETA + dVe_theta;
V_EXD_ALPHA = V_EXD_ALPHA + dVe_alpha;
J = J-1;
}
if(p == 1)
{
dV_theta = V_EXD_THETA;
dV_alpha = V_EXD_ALPHA;
}
else
{
dV_theta = (1-((V_theta+V_alpha)/V_gamma0))*V_EXD_THETA;
dV_alpha = (1-((V_theta+V_alpha)/V_gamma0))*V_EXD_ALPHA;
}
V_theta = V_theta + dV_theta;
```

```
V_alpha = V_alpha + dV_alpha;
V_gamma = V_gamma0 - (V_theta+V_alpha);
V_frac_gamma_trans = 1-(V_gamma/V_gamma0);
Gr_theta = Rc_theta/(2*sqrt(t));
Gr_alpha = Rc_alpha/(2*sqrt(t));
fprintf(fout,‘‘%lf  %lE  %lE  %lE”,t,V_theta,V_alpha,V_gamma/V_gamma0);
Xg = (X_bulk*V_gamma0-(X_tg*V_theta)-(X_ag*V_alpha))/V_gamma;
}
else
{
fprintf(fout,‘‘V_theta/V_gamma0 = %.5lf  ”,V_theta/V_gamma0);
fprintf(fout,‘‘V_alpha/V_gamma0 = %.5lf  ”,V_alpha/V_gamma0);
fprintf(fout,‘‘Vol percent austenite untransformed = %.5lf  ”,
V_gamma*100/V_gamma0);
exit(0);
}
}
fprintf(fout,‘‘V_theta/V_gamma0 = %.5lf  ”,V_theta/V_gamma0);
fprintf(fout,‘‘V_alpha/V_gamma0 = %.5lf  ”,V_alpha/V_gamma0);
fprintf(fout,‘‘vol percent austenite untransformed = %.5lf  ”,
V_gamma*100/V_gamma0);
fclose(fxauscem);
fclose(fxausfer);
fclose(fxcemaus);
fclose(fxferaus);
fclose(fg);
fclose(fout);
}

//*****************************************************
//CALCULATION OF MOLE FRACTION

double mole_fraction()
{
double X_C,X_SI,X_MN,X_CR,X_NI,X_V,X_MO,total_moles;
FE = 100-XBAR -MN - SI - CR - NI - MO - V;
total_moles = (XBAR/12.01115)+(FE/55.847)+(SI/28.086)
+(MN/54.847)+(NI/58.71)+(MO/95.94)+(CR/51.996)+(V/50.9415);
X_C=  (XBAR/12.01115)/total_moles;
X_SI= (SI/28.086)/total_moles;
X_MN= (MN/54.847)/total_moles;
X_CR= (CR/51.996)/total_moles;
X_NI= (NI/58.71)/total_moles;
```

```
X_V=  (V/50.9415)/total_moles;
X_MO= (MO/95.94)/total_moles;
X_mole = X_C;
return X_mole;
}
//*******************************************************
//CALCULATION OF ATOM FRACTION

double atom_fraction()
{
double X_C,X_SI,X_MN,X_CR,X_NI,X_V,X_MO,X_FE,total_atoms;
FE = 100-XBAR -MN - SI - CR - NI - MO - V;
X_C =  (XBAR/12.01115)*Av;
X_SI = (SI/28.086)*Av;
X_MN = (MN/54.847)*Av;
X_CR = (CR/51.996)*Av;
X_NI = (NI/58.71)*Av;
X_V =  (V/50.9415)*Av;
X_MO = (MO/95.94)*Av;
X_FE = (FE/55.847)*Av;
total_atoms = X_SI + X_MN + X_CR + X_NI + X_NI + X_V + X_MO + X_FE;
X_atom = X_C/total_atoms;
return X_atom;
}
//********************************************************
//CALCULATION OF WT% FROM MOLE FRACTION

double wt_percent()
{
double total_moles;
total_moles = 55.847*((100/55.847)+SI*((1/28.086)-(1/55.847))
+MN*((1/54.847)-(1/55.847))+NI*((1/58.71)-(1/55.847))
+MO*((1/95.94)-(1/55.847))+CR*((1/51.996)
-(1/55.847))+V*((1/50.9415)-(1/55.847)))/(55.847-55.847*X_m
+12.01115*X_m);
X_wt = X_m*total_moles*12.01115;
return X_wt;
}
```

```
//**********************************************************
//CALCULATION OF ALPHA

double alpha()
{
double LCG,AJ,DG,EG;
AJ = 1.0-exp(-W/(R*TempK));
if(X_mole <= 1.0E-10)
{ALPHA = log(1.0E-10);}
else
{
DG = sqrt(1.0-2.0*(1.0+2.0*AJ)*X_mole+(1.0+8.0*AJ)*X_mole*X_mole);
EG = 5.0*log((1.0-2.0*X_mole)/X_mole) + 6.0*W/(R*TempK) +
(38575.0-13.48*TempK)/(R*TempK);
LCG = EG+6.0*log((DG-1.0+(3.0*X_mole))/(DG+1.0-(3*X_mole)));
ALPHA = exp(LCG);
}
return ALPHA;
}
//**********************************************************
//CALCULATION OF DALPHA

double dalpha()
{
double AJ,DG,DDG;
AJ = 1.0-exp(-W/(R*TempK));
DG = sqrt(1.0-2.0*(1.0+2.0*AJ)*X_mole + (1.0+8.0*AJ)*X_mole*X_mole);
DDG = (0.5/DG)*(-2.0-4.0*AJ+2.0*X_mole+16.0*AJ*X_mole);
DALPHA = -((10.0/(1.0-2.0*X_mole))+(5.0/X_mole))+6.0*((DDG+3.0)/
(DG-1.0+3.0*X_mole)-(DDG-3.0)/(DG+1.0-3.0*X_mole));
return DALPHA;
}
//**********************************************************
//CALCULATION OF DIFFUSIVITY

double diffuse()
{
int i,step;
double F,L,z,p,q,RS,RP,sum1,sum2,SIGMA,SAI,D_dash,DIFF,THETA;
double c[250];
F = 21230.0;
L = 1/exp(31.84);
z = 12;
```

```
step = 50;
THETA = X_atom_aus;
q = step;
p = (up_limit-low_limit)/q;
sum2=0;
for(i=0;i<=step;i++)
{
SIGMA = 1.0-exp(-W/(k*TempK));
RS = (1.0+((z*(1.0+THETA))/(1.0 -((z/2.0)+1.0)*THETA
+ (z/2.0)*((z/2.0)+1.0)*(1.0 -SIGMA)*pow(THETA,2.0))));
SAI = ALPHA*RS + (1.0+THETA)*DALPHA;
RP = exp(-F/TempK);
D_dash=(k/h)*TempK*RP*L;
DIFF = D_dash*SAI;
c[i] = DIFF;
THETA = THETA+p;
}
for(i=1;i<step;i++)
{
   sum2 = sum2 + c[i];
}
sum1 = c[0] + c[step];
EDIFF = (sum1 + 2*sum2)/(2*q*10000);
return EDIFF;
}
//*******************************************************
//CALCULATION OF NUCLEATION RATE FOR CEMENTITE

double nrate_theta()
{
double Q,Sv,Nv,lamda,ab;
fa = 1.14E+12;
fb = 16*PI/3;
Q = 200000;
Sigma_gt = 0.012;
Sv = 2/(3E-7);
Nv = fa*Sv;
lamda = (V_theta/V_gamma0)/((Xg-X_gt)/(X_tg-X_gt));
del_G = (1-lamda)*G_dash_theta*(X_tg-X_gt)/(Xg-X_gt);
G_star = fb*Av*pow(Sigma_gt,3)/(del_G*del_G);
Nr_theta = Nv*(k*TempK/h)*exp(-(G_star+Q)/(R*TempK));
return Nr_theta;
}
```

```
//*******************************************************
//CALCULATION OF NUCLEATION RATE FOR FERRITE

double nrate_alpha()
{
double Q,Sv,Nv,lamda,ab;
fa = 3.02E+09;
fb = 16*PI/3;
Q = 200000;
Sigma_ga = 0.035;
Sv = 2/(3E-7);
Nv = fa*Sv;
lamda = (V_alpha/V_gamma0)/((X_ga-Xg)/(X_ga-X_ag));
del_G = (1-lamda)*G_dash_alpha*(X_ga-X_ag)/(X_ga-Xg);
G_star = fb*Av*pow(Sigma_ga,3)/(del_G*del_G);
Nr_alpha = Nv*(k*TempK/h)*exp(-(G_star+Q)/(R*TempK));
return Nr_alpha;
}
```

Bibliography

[1] E. S. Davenport and E. C. Bain. Transformation of austenite at constant subcritical temperature. *Transactions Materials Society AIME*, 90:117–154, 1930.

[2] K. J. Irvine and F. B. Pickering. Low carbon bainitic steels. *Journal of Iron and Steel Institute*, 187:292–309, 1957.

[3] A. Saha Podder, D. Bhattacharjee, and R. K. Ray. Effect of martensite on the mechanical behavior of ferrite–bainite dual phase steels. *ISIJ International*, 47:1058–1064, 2007.

[4] H. K. D. H. Bhadeshia. High performance bainitic steels. *Materials Science Forum*, 500-501(63-74), 2005.

[5] H. K. D. H. Bhadeshia. Bulk nanocrystalline steel. *Ironmaking and Steelmaking*, 32:405–410, 2005.

[6] H. K. D. H. Bhadeshia. *Bainite in Steels.* IOM communications Ltd, London, UK, 2001.

[7] H. K. D. H. Bhadeshia and D. V. Edmonds. Bainite in silicon steels: new composition-property approach part I. *Metal Science*, 17:411–419, 1983.

[8] H. K. D. H. Bhadeshia and D. V. Edmonds. The bainite transformation in a silicon steel. *Metallurgical and Materials Transactions A*, 10A:895–907, 1979.

[9] B. P. J. Sandvik. The bainite reaction in Fe-Si-C alloys: the primary stage. *Metallurgical and Materials Transactions A*, 13A:777–787, 1982.

[10] W. S. Owen. Effect of silicon on the kinetics of tempering. *Transactions ASM*, 46:812–829, 1954.

[11] W. S. Owen. The carbide phase in iron carbon silicon alloys. *Journal of Iron and Steel Institute*, 167:117–120, 1951.

[12] M. Takahashi and H. K. D. H. Bhadeshia. A model for the microstructure of some advanced bainitic steels. *Transactions Japan Institute of Metals*, 32:689–696, 1991.

[13] J. Wang and S. van der Zwaag. Stabilization mechanisms of retained austenite in transformation-induced plasticity steel. *Metallurgical and Materials Transactions A*, 32A:1527–1539, 2001.

[14] F. G. Caballero, H. K. D. H. Bhadeshia, K. J. A. Mawella, D. G. Jones, and P. Brown. Very strong low temperature bainite. *Materials Science and Technology*, 18:279–284, 2002.

[15] C. J. Barton. The tempering of a low carbon internally twinned martensite. *Acta Metallurgica*, 17:1085–1093, 1969.

[16] D. Kalish and M. Cohen. Structural changes and strengthening in the strain tempering of martensite. *Materials Science and Engineering*, 6:156–166, 1970.

[17] F. H. Samuel and A. A. Hussein. Tempering of medium and high carbon martensites. *Metallography*, 15:391–408, 1982.

[18] Y. H. Lee and R. C. Voight. The hardenability of ductile irons. *Transactions AFS*, 97:915–938, 1989.

[19] L. Cheng, C. M. Brakman, B. M. Korevaar, and E. J. Mittemeijer. The tempering of iron-carbon martensite, dilatometric and caloriometric analysis. *Metallurgical and Materials Transactions A*, 19A:2415–2426, 1988.

[20] M. J. Van Genderen, M. Isac, A. Bottger, and E. J. Mittemeijer. Aging and tempering behavior of Iron-Nickel-Carbon and Iron-Carbon martensite. *Metallurgical and Materials Transactions A*, 28A:545–561, 1997.

[21] M. Jung, S. J. Lee, and Y. K. Lee. Microstructural and dilational changes during tempering and tempering kinetics in martensitic medium carbon steel. *Metallurgical and Materials Transactions A*, 40A:551–559, 2009.

[22] M. Perez, C. Sidoroff, A. Vincent, and C. Esnouf. Microstructural evolution of martensitic 100Cr6 bearing steel during tempering: From thermoelastic power measurements to the prediction of dimensional changes. *Acta Materialia*, 57:3170–3181, 2009.

[23] H. K. D. H. Bhadeshia and D. V. Edmonds. Tempered martensite embrittlement: Role of retained austenite and cementite. *Metal Science*, 13:325–334, 1979.

[24] H. K. D. H. Bhadeshia. The lower bainite transformation and the significance of carbide precipitation. *Acta Metallurgica*, 28:1103–1114, 1980.

[25] Y. Ohmori and I. Tamura. Epsilon carbide precipitation during tempering of plain carbon martensite. *Metallurgical and Materials Transactions A*, 23A:2737–2751, 1992.

[26] J. Deliry. Noveau carbure de fer transformation bainitique dans les aciers au carbone silicium. *Mémoires Scientifiques Revue de Métallurgie*, 62:527–550, 1965.

[27] J. Pomey. Revenu de la martensite et reaction bainitique inferieure: Cas des aciers au carbone-silicium et des aciers au carbone. *Mémoires Scientifiques Revue de Métallurgie*, 63:507–532, 1966.

[28] R. F. Hehemann. *Phase Transformations*. ASM, Metal Park, Ohio, 1970.

[29] D. H. Huang and G. Thomas. Metallography of bainitic transformation in silicon containing steels. *Metallurgical and Materials Transactions A*, 8A:1661–1674, 1977.

[30] S. A. Sajjdi and S. M. Zebarjad. Isothermal transformation of austenite to bainite in high carbon steels. *Journal of Materials Processing Technology*, 189:107–113, 2007.

[31] W. Pitsch. Der orientierungszusammenhang zwischen zementit und austenit. *Acta Metallurgica*, 10:897–900, 1962.

[32] B. P. J. Sandvik. The bainite reaction in Fe-Si-C alloys: the secondary stage. *Metallurgical and Materials Transactions A*, 13A:789–800, 1982.

[33] G. N. Haindemenopoulos and A. N. Vasilakos. Modeling of austenite stabilty in low-alloy triple-phase steels. *Steel Research*, 67:513–519, 1996.

[34] X. D. Wang, B. X. Huang, Y. H. Rong, and L. Wang. Microstructures and stability of retained austenite in TRIP steels. *Materials Science and Engineering A*, A438-440:300–305, 2006.

[35] N. Luzginova, L. Zhao, and J. Sietsma. Evolution and thermal stabily of retained austenite in SAE 52100 bainitic steel. *Materials Science and Engineering A*, A 448:104–110, 2007.

[36] M. Y. Sherif, C. García-Mateo, T. Sourmail, and H. K. D. H. Bhadeshia. Stability of retained austenite in TRIP-assisted steels. *Materials Science and Technology*, 20:319–322, 2004.

[37] I. B. Timokhina, P. D. Hodgson, and E. V. Pereloma. Effect of microstructure on the stability of retained austenite in transformation-induced-plasticity steels. *Metallurgical and Materials Transactions A*, 35A:2331–2341, 2004.

[38] W. Shi, Lin Li, B. C. DeCooman, Patrick Wollants, and Chun xia YANG. Thermal stability of retained austenite in TRIP steel after different treatments. *Journal of Iron and Steel Research International*, 15:61–64, 2008.

[39] A. Kammouni, W. Saikaly, M. Dumont, C. Marteau, X. Bano, and A. Charai. Effect of the bainitic transformation temperature on retained austenite fraction and stability in Ti microalloyed TRIP steels. *Materials Science and Engineering A*, 518:89–96, 2009.

[40] K. Sugimoto, N. Usui, M. Kobayashi, and S. Hashimoto. Effects of volume fraction and stability of retained austenite on ductility of TRIP-aided dual phase steels. *ISIJ International*, 32:1311–1318, 1992.

[41] H. J. Jun, S. H. Park, S. D. Choi, and C. G. Park. Decomposition of retained austenite during coiling process of hot rolled TRIP aided steels. *Materials Science and Engineering A*, 379:204–209, 2004.

[42] H. K. D. H. Bhadeshia and D. V. Edmonds. Mechanism of bainite formation in steel. *Acta Metallurgica*, 28:1265–1273, 1980.

[43] H. K. D. H. Bhadeshia. A rationalisation of shear transformations in steels. *Acta Metallurgica*, 29:1117–1130, 1981.

[44] R. F. Hehemann, K. R. Kinsman, and H. I. Aaronson. A debate on the bainite reaction. *Metallurgical and Materials Transactions A*, 3A:1077–1094, 1972.

[45] I. Stark, G. D. W. Smith, and H. K. D. H. Bhadeshia. The element redistribution associated with the 'incomplete reaction phenomenon' in bainitic steels: An atom probe investigation. In G. W. Lorimer, editor, *Phase Transformations '87*, pages 211–215, London, 1988. Institute of Metals.

[46] K. Tsuzaki, A. Kodai, and T. Maki. Formation mechanism of bainitic ferrite in an Fe-2 pct Si -0.6 pct C alloy. *Metallurgical and Materials Transactions A*, 25A:2009–2016, 1994.

[47] B. Josefsson and H. O. Andrén. Atom probe field ion microscopy of bainitic transformation in 2.25Cr-1Mo weld metal. *Materials Science and Technology*, 7:849–851, 1991.

[48] H. K. D. H. Bhadeshia. Bainite: an atom-probe study of the incomplete reaction phenomenon. *Acta Metallurgica*, 30:775–784, 1982.

[49] J. M. Oblak and R. F. Hehemann. *Transformations and Hardenability in Steels.* Climax Molybdenum, Ann Arbor, MI, 1967.

[50] F. B. Pickering. *Transformations and Hardenability in Steels.* Climax Molybdenum Company, Ann Arbor, MI, USA, 1967.

[51] H. K. D. H. Bhadeshia and J. W. Christian. Bainite in steels. *Materials Science and Technology*, 21A:767–797, April 1990.

[52] E. Swallow and H. K. D. H. Bhadeshia. High resolution observations of displacements caused by bainitic transformation. *Materials Science and Technology*, 12:121–125, 1996.

[53] F. G. Caballero, M. K. Miller, S. S. Babu, and C. Garcia-Mateo. Atomic scale observations of bainite transformation in a high carbon high silicon steel. *Acta Materialia*, 55:381–390, 2007.

[54] F. G. Caballero, C. García-Mateo, M. J. Santofimia, M. K. Miller, and C. Garcia de Andres. New experimental evidence on the incomplete tansformation phenomenon in steel. *Acta Materialia*, 57:8–17, 2009.

[55] L. C. Chang and H. K. D. H. Bhadeshia. Microstructure of lower bainite formed at large undercoolings below bainite start temperature. *Materials Science and Technology*, 12:233–236, 1996.

[56] H. I. Aaronson and C. Wells. Sympathetic nucleation of ferrite. *Transactions AIME*, 206:1216–1223, 1956.

[57] J. M. Oblak, R. H. Goodenow, and R. F. Hehemann. Morphology of bainite in hypoeutectoid steels. *Transactions of the Materials Society of AIME*, 230:258–259, 1964.

[58] M. Takahashi and H. K. D. H. Bhadeshia. Model for transition from upper to lower bainite. *Materials Science and Technology*, 6:592–603, 1990.

[59] E. Kozeschnik and H. K. D H. Bhadeshia. Influence of silicon on cementite precipitation in steels. *Materials Science and Technology*, 24, no. 3:343–347, 2008.

[60] L. J. Habraken and M. Economopolus. *Transformations and Hardenability in Steels.* Climax Molybdenum, Ann Arbor, MI, USA, 1967.

[61] L. J. Habraken. *Physical properties of martensite and bainite.* Special Report 93, The Iron and Steel Institute, London, 1965.

[62] C. García-Mateo, F. G. Caballero, and H. K. D. H. Bhadeshia. Development of hard bainite. *ISIJ International*, 43:1238–1243, 2003.

[63] L. C. Chang. Microstructures and reaction kinetics of bainite transformation in Si-rich steels. *Materials Science and Engineering A*, A368:175–182, 2004.

[64] A. G. Alten and P. Payson. *Transactions ASM*, 45:498–531, 1953.

[65] J. Gordine and I. Codd. The influence of silicon up to 1.5 wt% on the tempering characteristics of a spring steel. *Journal of Iron and Steel Institute*, pages 461–467, 1968.

[66] L. Zhu, D. Wu, and X. Zhao. Effect of silicon content on the austenite decomposition. *Journal of Iron and Steel Research International*, 13:57–60, 2006.

[67] R. L. Houillier, G. Begin, and A. Dube. A study of the particularities of austenite during the formation of bainite. *Metallurgical Transactions*, 2:2645–2653, 1971.

[68] H. K. D. H. Bhadeshia. Bainite in silicon steels: new composition-property approach part ii. *Metal Science*, 17:420–425, 1983.

[69] I. Tamura, T. Maki, and H. Hato. Morphology of strain-induced martensite and trip in Fe-Ni-Cr alloy. *Transactions of the Iron and Steel Institute of Japan*, 10:163–172, 1970.

[70] O. Matsumura, Y. Sakuma, and H. Takechi. Enhancement of elongation by retained austenite in intercritical annealed 0.4C-1.5Si-0.8Mn steel. *Transactions of the Iron and Steel Institute of Japan*, 27:570–579, 1987.

[71] P. J. Jacques, E. Girault, Ph. Harlet, and F. Delannay. The develepment of cold rolled TRIP assisted multiphase steels. Low Si TRIP assisted multiphase steels. *ISIJ International*, 41:1061–1067, 2001.

[72] R. Harrison. The influence of silicon on nickel steel. *Journal of Iron and Steel Institute*, 124:261–282, 1931.

[73] G. Poulachen, M. Dessoly, C. Le. Calvez, J. L. Lebrun, V. Prunet, and I. S. Jawahir. An investigation of the influence of sulphide inclusions on tool-wear in high speed milling of tool steels. *Wear*, 250:334–343, 2001.

[74] G. King, R. A. Jarman, and P. Judson. The effect of manganese and nickel on the room temperature tensile characteristics of ferritic weld metal. Technical report, Thames Polytechnic Report, April 1989.

[75] A. M. Hall. *Nickel in Iron and Steel.* John Wiley and Sons, New York, N. Y.,USA, 1954.

[76] J. R. Davis, editor. *Alloying: understanding the basics.* ASM International, Materials Park, OH, first edition, December 2001.

[77] R. W. K. Honeycombe and H. K. D. H. Bhadeshia. *Steels: microstructure and properties.* Edward Arnold, London, UK, 1995.

[78] S. B. Singh and H. K. D. H. Bhadeshia. Estimation of bainite plate-thickness in low-alloy steels. *Materials Science and Engineering A*, A245:72–79, 1998.

[79] C. Mack. *Proceeding Cambridge Philosophical Society*, 52:246, 1956.

[80] G. Langford and M. Cohen. Calculation of cell size strengthening of wire-drawn iron. *Metallurgical and Materials Transactions A*, 1A:1478, 1970.

[81] H. K. D. H. Bhadeshia. Theoritical analysis of changes in cementite composition during tempering of bainite. *Materials Science and Technology*, 5:131–137, 1989.

[82] N. Udompongsanon and D. W. Borland. Note on the transition from lath to plate martensite. *Journal of Australian Institute of Metals*, 19:56–58, 1974.

[83] T. George, E. R. Parker, and R. O. Ritchie. Susceptibility to hydrogen attack of a thick section 3Cr1Mo1Ni pressure-vessel steel-role of cooling rate. *Materials Science and Technology*, 1:198–208, 1985.

[84] R. M. Horn and R. O. Ritchie. Mechanisms of tempered martensite embrittlement in low alloy steel. *Metallurgical Transactions A*, 9A:1039–1053, 1978.

[85] H. K. D. H. Bhadeshia and D. V. Edmonds. Bainite in silicon steels: a new composition property approach II. *Metal Science*, 17(420-425), 1983.

[86] V. T. T. Miihkinen and D. V. Edmonds. Tensile deformation of two experimental high-strength bainitic low-alloy steels containing silicon. *Materials Science and Technology*, 3(432-440), 1987.

[87] G. R. Speich and W. C. Leslie. Tempering of steel. *Metallurgical and Materials Transactions A*, 3A:1043–1054, 1972.

[88] C. S. Roberts, B. L. Averbach, and M. Cohen. The mechanism and kinetics of the first stage of tempering. *Transactions ASM*, 45:576, 1953.

[89] C. Wells, W. Batz, and R. F. Mehl. Diffusion coefficient of carbon in austenite. *Transactions AIME*, 188:553–560, 1970.

[90] K. Sugimoto, M. Misu, M. Kobayashi, and H. Shirasawa. Effect of second phase morphology on retained austenite morphology and tensile properties in a TRIP aided dual phase steel sheet. *ISIJ International*, 33:775–782, 1993.

[91] A. Z. Hanzaki, P. D. Hodgson, and S. Yue. Retained austenite characteristics in thermomechanically processed Si-Mn transformation-induced plasticity steels. *Metallurgical and Materials Transactions A*, 28A:2405–2414, 1997.

[92] B. S. Lement, B. L. Averbach, and M. Cohen. Microstructural changes on tempering iron-carbon alloys. *Transactions ASM*, 46:851, 1954.

[93] B. S. Lement, B. L. Averbach, and M. Cohen. Further study of microstructural changes on tempering iron-carbon alloys. *Transactions ASM*, 47:291, 1955.

[94] G. B. Olson and M. Cohen. Stages of aging and tempering of ferrite martensites. *Metallurgical and Materials Transactions A*, 14A:1057–1065, 1983.

[95] K. Han, M. J. Van Gendere, A. Bottger, H. W. Zandbergen, and E. J. Mittemeijer. Initial stages of Fe-C martensite decomposition. *Philosophical Magazine A*, 81:741–757, 2001.

[96] E. Tekin and M. H. Richman. An electron microscopical study of the tempering of tungsten high speed steels. *Metallography*, 3:327–335, 1970.

[97] W. Steven and K. Balajiva. The influence of minor elements on the isothermal embrittlement of steels. *Journal of Iron and Steel Institute*, 193:141–152, 1959.

[98] B. C. Edwards, H. E. Bishop, J. C. Riviere, and B. L. Eyre. An AES study of temper embrittlement in a low alloy steel. *Acta Metallurgica*, 24:957–967, 1976.

[99] Y. Imai. Phases in quenched and tempered steels. *Transactions Japan Institute of Metals*, 16:721–734, 195.

[100] W. K. Choo and R. Kaplow. Mossbauer measurements on the aging of iron-carbon martensite. *Acta Metallurgica*, 21:725–732, 1973.

[101] Y. Hirotsu and S. Nagakura. Crystal structure and morphology of the carbide precipitated from martensite high cabon steel during the first stage of tempering. *Acta Metallurgica*, 20:645–655, 1972.

[102] S. Nagakuraa, Y. Hirotsu, M. Kusunoki, T. Suzuki, and Y. Nakamura. Crystallographic study of the tempering of martensite carbon steel by electron microscopy and diffraction. *Metallurgical and Materials Transactions A*, 14A:1025–1031, 1983.

[103] S. Matas and R. F. Hehemann. Retained austenite and tempering of martensite. *Nature*, 187:685–686, 1960.

[104] B. K. Jha and N. S. Mishra. Microstructural evolution during tempering of a multiphase steel containing retained austenite. *Materials Science and Engineering A*, A263:42–55, 1998.

[105] K. H. Jack. Structural transformations in the tempering of high carbon martensitic steels. *Journal of Iron and Steel Institute*, 169:26–36, 1951.

[106] E. J. Fasiska and G. A. Jefrey. On the cementite structure. *Acta Cryatalography*, 19:463–471, 1965.

[107] J. Liu and C. P. Luo. Precipitation behavior of the lower bainitic carbide in a medium carbon steel containing Si, Mn and Mo. *Materials Science and Engineering A*, A403-440:153–157, 2006.

[108] H. L. Yakel. Crystal structures of stable and metastable iron-containing carbides. *International Materials Reviews*, 30:17–40, 1985.

[109] P. J. Clemm and J. C. Fisher. The influence of grain boundaries on the nucleation of secondary phases. *Acta Metallurgica*, 3:70–73, 1955.

[110] J. W. Cahn. The kinetics of grain boundary nucleated reactions. *Acta Metallurgica*, 4:449–459, 1956.

[111] A. T. W. Kempen, F. Sommer, and E. J. Mittemeijer. The kinetics of the austenite-ferrite phase transformation of Fe-Mn: differential thermal analysis during cooling. *Acta Materialia*, 50:3545–3555, 2002.

[112] F. Liu, F. Sommer, and E. J. Mittemeijer. Kinetics of the abnormal austenite–ferrite transformation behaviour in substitutional fe-based alloys. *Acta Materialia*, 52:2549–2560, 2004.

[113] C. Zener. Equilibrium relations in medium alloy steels. *Transactions AIME*, 167:513–534, 1946.

[114] C. Zener. Theory of diffusion. In R. Maurer W. Shockley, J. H. Holloman and F. Seitz, editors, *Imperfections in nearly perfect crystals*, pages 289–314, New York, 1952. John Wiley and Sons Inc.

[115] C. Zener. Theory of growth of spherical precipitates from solid solution. *Journal of Applied Physics*, 20:950–953, 1949.

[116] J. W. Christian. *The Theory of Transformations in metals and Alloys*, volume Part 1. Pergamon Press, Oxford, second edition, 1975.

[117] R. Trivedi. Growth of dendritic needles from a supercooled melt. *Acta Metallurgica*, 18:287–296, 1970.

[118] R. Trivedi. The role of interfacial free energy and interface kinetics during the growth of precipitate plates and needles. *Metallurgical and Materials Transactions A*, 1A:921–927, 1970.

[119] G. P. Ivantsov. Temperature field around spheroidal, cylindrical and acicular crystal growing in a supercooled melt. *Doklady Akademii Nauk SSSR*, 58:567–569, 1947.

[120] M. Hillert. The role of interfacial energy during solid state phase transformations. *Jernkontorets Ann*, 141:757–789, 1957.

[121] R. Trivedi and G. M. Pound. Effect of concentration dependent diffusion coefficient on the migration of interphase boundaries. *Journal of Applied Physics*, 38:3569–3576, 1967.

[122] M. Avrami. Kinetics of phase change 1. *Journal of Chemical Physics*, 7:1103–1112, 1939.

[123] M. Avrami. Kinetics of phase change 2. *Journal of Chemical Physics*, 8:212–224, 1940.

[124] M. Avrami. Kinetics of phase change 3. *Journal of Chemical Physics*, 8:177–184, 1941.

[125] S. J. Jones and H. K. D. H. Bhadeshia. Kinetics of the simultaneous decomposition of austenite into several transformation products. *Acta Materialia*, 45:2911–2920, 1997.

[126] S. M. Hodson. *MTDATA-Metallurgical and Thermomechanical Databank*. National Physical Laboratory, Teddington, U.K., 1989.

[127] K. W. Andrews. Empirical formulae for the calculation of some transformation temperatures. *Journal of Iron and Steel Institute*, 203:721–727, 1965.

[128] G Krauss. *Steels - Processing, Structure and Performance.* ASM International, Materials Park, Ohio, 2005.

[129] H. K. D. H. Bhadeshia. Thermodynamic analysis of isothermal transformation diagrams. *Metal Science*, 16:159–165, 1982.

[130] http://www.msm.cam.ac.uk/phase-trans/map/.

[131] H. K. D. H. Bhadeshia and D. V. Edmonds. Thermodynamic extrapolation and the Ms temperature of substitutionally alloyed steels. *Metal Science*, 15(178-180), 1981.

[132] C. G. de Andrés, F. G. Caballero, C. Capdevila, and D. San Martin. Revealing austenite grain boundaries by thermal etching: advantages and disadvantages. *Materials Characterization*, 49:121–127, 2002.

[133] R. T. DeHoff and F. N. Rhines. *Quantitative Microscopy.* McGraw-Hill, New York, USA, 1968.

[134] R. Jenkins and R. L. Snyder. *Introduction to X-ray powder diffractometry powder diffractometry.* John Wiley and Sons, New York, USA, 1996.

[135] A. J. C. Wilson. Geiger counter X-ray spectometer- influence of size and absorption coefficient of specimen on position and shape of powder diffraction maxima. *Journal of Scientific Instruments*, 27:321–325, 1950.

[136] C. Dong, F. Wu, and H. Chen. Correction of zero shift in powder diffraction patterns using the reflection-pair method. *Journal of Applied Crystallography*, 32:850–853, 1999.

[137] M. U. Cohen. Precision lattice constants from X-ray powder photographs. *Review of Scientific Instruments*, 6:68–74, 1935.

[138] B. D. Cullity and S. R. Stock. *Elements of X-ray diffraction.* Prentice Hall, New Jercy, USA, third edition, 1996.

[139] G. S. Smith and R. L. Snyder. A criterion for rating powder diffraction patterns and evaluating the reliability of powder-pattern indexing. *Journal of Applied Crystallography*, 12:60–65, 1979.

[140] R. A. Young, editor. *The Rietveld Method, IUCr Monographs on Crystalography, Vol. 5.* Oxford University Press, New York, USA, 1993.

[141] R. J. Hill and C. J. Howard. Quantitative phase analysis from neutron powder diffraction data using the Rietveld method. *Journal of Applied Crystallography*, 20:467–474, 1987.

[142] L. B. McCusker, R. B. Von Dreele, D. E. Cox, D. Louer, and P. Scardi. Rietveld refinemet guidelines. *Journal of Applied Crystallography*, 32:36–50, 1999.

[143] D. B. Williams and C. B. Carter. *Transmission electron microscopy.* Plenum Publishing Corporation, New York, N. Y., USA, 1996.

[144] W. W. Gerberich, G. Thomas, E. R. Parker, and V. F. Zackay. Metastable austenites: decomposition and strength. In *Second International Conference on Strength of Metals and Alloys*, pages 894–899, Ohio, USA, 1970. ASM International.

[145] E. R. Parker. Interrelations of compositions, transformation kinetics morphology and mechanical properties of alloy steels. *Metallurgical and Materials Transactions A*, 8A:1025–1042, 1977.

[146] E. Dorazil, B. Barta, E. Munsterova, L. Stransky, and A. Huvar. High strength bainitic ductile cast iron. *AFS International Cast Metals Journal*, 22(52-62), 1982.

[147] P. J. Jacques. Transformation-induced plasticity for high strength formable steels. *Current Opinion in Solid State and Materials Science*, 8:259–265, 2004.

[148] B. C. De Cooman. Structure–properties relationship in TRIP steels containing carbide-free bainite. *Current Opinion in Solid State and Materials Science*, 8:285–303, 2004.

[149] P. G. Self, H. K. D. H. Bhadeshia, and W. M. Stobbs. Lattice spacings from lattice fringes. *Ultramicroscopy*, 6(29-40), 1981.

[150] http://www.msm.cam.ac.uk/map/steel/programs/mucg46-b.html.

[151] J. R. Yang and H. K. D. H. Bhadeshia. The bainite to austenite transformation. In G. W. Lorimer, editor, *Phase Transformations '87*, pages 365–373, 1988.

[152] J. R. Yang and H. K. D. H. Bhadeshia. Continuous heating transformation of bainite to austenite. *Materials Science and Engineering A*, 131:99–113, 1991.

[153] F. G. Caballero, C. García-Mateo, and C. G. de Andrés. Dilatometric study of reaustenitisation of high silicon bainitic steels: Decomposition of retained austenite. *Metallurgical and Materials Transactions A*, 46A:581–586, 2005.

[154] H. M. Rietveld. A profile refinement method for nuclear and magnetic structures. *Journal of Applied Crystallography*, 2:65–71, 1969.

[155] R. A. Young and D. B. Wiles. Profile shape functions in Rietveld refinements. *Journal of Applied Crystallography*, 15:430–438, 1982.

[156] H. Stuart and N. Rindley. Thermal expansion of cementite and other phases. *Journal of Iron and Steel Institute*, 204:711–717, 1966.

[157] D. J. Dyson and B. Holmes. Effect of alloying additions on the lattice parameter of austenite. *Journal of Iron and Steel Institute*, 277:469–474, 1970.

[158] H. K. D. H. Bhadeshia, S. A. David, J. M. Vitek, and R. W. Reed. Stress induced transformation to bainite in Fe-Cr-Mo-C pressure vessel steel. *Materials Science and Technology*, 7:686–698, 1991.

[159] D. P. Koistinen and R. E. Marburger. A general equation prescribing te extent of the austenite-martensite transformation in pure iron carbon alloys and plain carbon steels. *Acta Metallurgica*, 7:59–60, 1959.

[160] M. Peet, S. S. Babu, M. K. Miller, and H. K. D. H. Bhadeshia. Three-dimensional atom probe analysis of carbon distribution in low-temperature bainite. *Scripta Materialia*, 50:1277–1281, 2004.

[161] J. A. Cameron. Its conditioning in En40C steel, and its occurrence in other B.S. En steels. *Journal of Iron and Steel Institute*, 194:260–267, 1956.

[162] G. T. Nazarenko. Decomposition range for retained austenite in carbon steels during tempering. *Metal science and heat treatment*, 1:29–31, 1959.

[163] B. B. Vinikur, M. V. Belous, S. E. Kondratyuk, and L. A. Semenova. Isothermal phase diagram of residual austenite in tempering. *Metal science and heat treatment*, 28:621–624, 1986.

[164] A. Saha Podder and H. K. D. H. Bhadeshia. Thermal stability of austenite retained in bainitic steels. *Materials Science and Engineering A*, 527:2121–2128, 2010.

[165] H. J. Stone, H. K. D. H. Bhadeshia, and P. J. Withers. In situ monitoring of weld transformations to control weld residual stresses. *Materials Science Forum*, 571-572:393–398, 2008.

[166] H. Dai, J. A. Francis, H. J. Stone, H. K. D. H. Bhadeshia, and P. J. Withers. Characterising phase transformations and their effects on ferritic weld residual stresses with X-rays and neutrons. *Metallurgical and Materials Transactions A*, 39A:3070–3078, 2008.

[167] H. J. Stone, M. J. Peet, H. K. D. H. Bhadeshia, P. J. Withers, S. S. Babu, and E. D. Specht. Synchrotron X-ray studies of austenite and bainitic ferrite. *Proceedings of Royal Scociety*, 464:1009–1027, 2008.

[168] L. Lutterotti, S. Matthies, H. R. Wenk, A. S. Shultz, and J. W. Richardson. Combined texture and structure analysis of deformed limestone from time-of-flight neutron diffraction spectra. *Journal of Applied Physics*, 81:594–600, 1997.

[169] Maud package: http://www.ing.unitn.it/ maud/.

[170] C. García-Mateo, M. Peet, F. G. Caballero, and H. K. D. H. Bhadeshia. Tempering of hard mixture of bainitic ferrite and austenite. *Materials Science and Technology*, 20:814–818, 2004.

[171] C. García-Mateo and F. G. Caballero. The role of retained austenite on tensile properties of steels with bainitic microstructures. *Materials Transactions*, 46:1839–1846, 2005.

[172] M. J. Marques, J. Pina, A. M. Dias, J. L. Lebrun, and J. Feugeas. X-ray diffraction characterization of ion-implanted austenitic stainless steel. *Surface and Coating Technology*, 195:8–16, 2005.

[173] M. Dudley, J. Wu, and G. D. Yao. Determination of penetration depths and analysis of strains in single crystals by white beam synchrotron X-ray tomography in grazing Bragg-Laue geometries. *Nuclear Instruments and Methods in Physics Research*, B40/41:388–392, 1989.

[174] H. K. D. H. Bhadeshia. Carbon content of retained austenite in quenched steels. *Metal Science*, 17:151–152, 1983.

[175] M. Wang, Y. Wang, and F. Sun. Tempering behavior of a semi-high speed steel containing nitrogen. *Materials Science and Engineering A*, 438-440:1139–1142, 2006.

[176] F. Pan, P. Ding, S. Zhou, M. Kang, and D. V. Edmonds. Effect of silicon additions on the mechanical properties and microstructure of high speed steels. *Acta Materialia*, 45(11):4703–4712, 1997.

[177] R. A. Grange and R. W. Baughman. Hardness of tempered martensite in carbon and low alloy steels. *Transactions of the ASM*, 48:165–191, 1956.

[178] F. G. Caballero, M. K. Miller, C. García-Mateo, C. Capdevila, and S. S. Babu. Redistribution of alloying elements during tempering of a nanocrystalline steel. *Acta Materialia*, 56:188–199, 2008.

[179] G. K. Williamson and W. H. Hall. X-ray line broadening from filed aluminium and wolfram. *Acta Metallurgica*, 1:22–31, 1953.

[180] W. H. Hall. X-ray line broadening in metals. *Proceedings of the Physical Scociety*, A62:741–743, 1949.

[181] P. Gay, P. B. Hirsch, and A. Kelly. The estimation of dislocation densities in metals from X-ray data. *Acta Metallurgica*, 1:315–319, 1953.

[182] G. K. Williamson and R. E. Smallman. Dislocation densities in some annealed and cold worked metals from measurements on the X-ray Debye-Scherrer spectrum. *Philosophical Magazine*, 1:34–46, 1956.

[183] A. J. C. Wilson. The diffraction of X-rays by distorted crystal aggregates. IV. Diffraction by a crystal with an axial screw dislocation. *Acta Crystallography*, 5:318–322, 1952.

[184] E. Demir, D. Raabe, N. Zaafarani, and S. Zaefferer. Investigation of the indentation size effect through the measurement of the geometrically necessary dislocations beneath small indents of different depths using EBSD tomography. *Acta Materialia*, 57:559–569, 2009.

[185] F. J. Humphreys. Review grain and subgrain characterisation by electron backscatter diffraction. *Journal Materials Science*, 36:3833–3854, 2001.

[186] T. Malkiewicz. *Metaloznawstwo stopow zelaza.* PWN, Warszawa-Krakow, Poland, 1976.

[187] J. Pacyna, A. Jedrzejewska-Strach, and M. Strach. The effect of manganese and silicon on the kinetics of phase transformations during tempering - Continuous Heating Transformation (CHT) curves. *Journal of Materials Processing Technology*, 64:311–318, 1997.

[188] G. Zajac and J. Pacyna. The kinetics of phase transformations during tempering in structural steels with nickel. In *13th International scientific conference on achievements in mechanical and materials engineering*, pages 719–722, Gliwice-Wisia, Poland, 2005.

[189] J. W. Christian and D. V. Edmonds. The bainite transformation. In A. R. Marder and J. I. Goldstein, editors, *Phase Transformations in Ferrous Alloys*, pages 293–325, NY, 1984. The metallurgical society of AIME.

[190] J. D. Robson and H. K. D. H. Bhadeshia. Modelling precipitation sequences in power plant steels. Part 1 - Kinetic theory. *Materials Science and Technology*, 13:631–639, 1997.

[191] R. H. Siller and R. B. McLellan. Application of first order mixing statistics to the variation of the diffusivity of carbon in austenite. *Metallurgical Transactions*, 1:985–988, 1970.

[192] J. C. Fisher, J. H. Hollomon, and D. Turnbull. Kinetics of the austenite to martensite transformation. *Metals Transactions*, 185:691–700, 1949.

[193] H. K. D. H. Bhadeshia. Diffusion of carbon in austenite. *Metal Science*, 15:477–479, 1981.

[194] R. B. McLellan and W. W. Dunn. A quasichemical treatment of interstitial solid solutions: its application to carbon in austenite. *Journal of Physics and Chemistry of Solids*, 30:2631–2637, 1969.

[195] K. Lucke and K. Detrt. A quantitative theory of grain-boundary motion and recrystallization in metals in the presence of imputrities. *Acta Metallurgica*, 5:828–637, 1957.

[196] S. Chatterjee, H. S. Wang, J. R. Yang, and H. K.D. H. Bhadeshia. Mechanical stabilisation of austenite. *Materials Science and Technology*, 22:641–644, 2006.

[197] R. W. K. Honeycombe. *Phase deformation of metals.* Edward Arnold, London, 2nd edition, 1984.

[198] G. B. Olson and M. Cohen. A general mechanism of martensitic nucleation: Part I. *Metallurgical Transactions A*, 7A:1897–1904, 1976.